Structural characterization of antimonide-based metamorphic buffer layers on (001) silicon substrate

Dissertation

zur
Erlangung des Doktorgrades
der Naturwissenschaften
(Dr. rer. nat.)

dem

Fachbereich Physik
der Philipps-Universität Marburg

vorgelegt von

Andrea Ott

aus

Bensheim

Marburg/Lahn, 2016

Vom Fachbereich Physik der Philipps-Universität Marburg
als Dissertation angenommen am:
Erstgutachter: Frau Prof. Dr. Kerstin Volz
Zweitgutachter:
Tag der mündlichen Prüfung:
Hochschulkennziffer 1180

Contents

1 Introduction 1

2 Physical Background 5
- 2.1 Fundamentals of semiconductor physics . . . 5
- 2.2 Crystal structures . . . 7
- 2.3 Crystal growth of heterostructures . . . 10
  - 2.3.1 Stability of growth . . . 11
  - 2.3.2 Growth mode of nucleation . . . 13
  - 2.3.3 Heteroepitaxial growth . . . 15
- 2.4 Lattice Defects . . . 17
  - 2.4.1 Point defects . . . 17
  - 2.4.2 Line defects . . . 17
  - 2.4.3 Planar defects . . . 24
- 2.5 Strain . . . 26
- 2.6 Fundamentals of transmission electron microscopy . . . 29
  - 2.6.1 Electron scattering . . . 30
  - 2.6.2 Electron diffraction . . . 32
  - 2.6.3 Magnetic lenses in TEM . . . 38
  - 2.6.4 Contrast in (S)TEM . . . 44

3 Experimental Methods 49
- 3.1 Metal organic vapor phase epitaxy . . . 49
- 3.2 Atomic force microscopy . . . 51
- 3.3 X-ray diffraction . . . 51
  - 3.3.1 Rocking-curve measurements . . . 53
  - 3.3.2 Reciprocal space maps . . . 55
- 3.4 Transmission electron microscopy . . . 57
  - 3.4.1 Sample preparation . . . 57
  - 3.4.2 Optics of a transmission electron microscope . . . 58
  - 3.4.3 Conventional dark-field and weak-beam imaging . . . 61
  - 3.4.4 Convergent beam electron diffraction . . . 63
  - 3.4.5 High-resolution TEM . . . 65
  - 3.4.6 High-angle annular dark-field STEM . . . 66
  - 3.4.7 Simulation of HAADF images . . . 67

3.4.8 Theoretical strain mapping 70
3.4.9 Strain mapping by geometric phase analysis and peak pairs analysis 72

4 Results and discussion 75
4.1 Growth optimization of Sb-based buffer layers 75
4.1.1 Pseudomorphic growth of Sb-based buffer layers on InP-substrate . 75
4.1.2 Metamorphic growth of Sb-based buffer layers on GaP/Si pseudo-substrate 77
4.1.3 Variation of growth parameters 96
4.1.4 Intentional growth of pseudomorphic interlayer 101
4.1.5 Pulsed growth of Ga(PSb) on GaP/Si 104
4.1.6 InP interlayer 112
4.1.7 Summary of the growth optimization of Sb-based buffer layers . . 117
4.2 Structural investigation of GaSb, Ga(PSb) and Ga(AsSb) islands on GaP 119
4.2.1 GaSb/GaP interface - Comparison of simulation and experiment . 120
4.2.2 Ga(PSb)/GaP interface 134
4.2.3 Ga(AsSb)/GaP interface 139
4.2.4 Summary of the structural investigation of GaSb, Ga(PSb) and Ga(AsSb) islands on GaP 142

5 Summary and Outlook 145

6 Zusammenfassung 149

Bibliography 153

List of acronyms

ADF annular dark-field

a.u. arbitrary units

AFM atomic force microscopy

Al aluminum

AP absorptive potential

APBs anti-phase boundaries

Ar argon

BF bright-field

BFP back focal plane

Bi bismuth

C carbon

CBED Convergent beam electron diffraction

CCD charge-coupled device

ccp cubic closed-packed

CL camera length

CMOS complementary metal–oxide–semiconductor

DF dark-field

DP diffraction pattern

EELS electron energy loss spectroscopy

EDX energy dispersive X-ray spectroscopy

fcc face-centered cubic

FEG field emission gun

FM	Frank van der Merwe
FME	flow rate modulated epitaxy
FT	Fourier transform
FWHM	full width at half maximum
Ga	gallium
Ga(AsSb)	gallium arsenide antimonide
(GaIn)As	gallium indium arsenide
GaP	gallium phosphide
Ga(PSb)	gallium phosphide antimonide
GaSb	gallium antimonide
GPA	geometric phase analysis
H	hydrogen
H_2	molecular hydrogen
H_2O	water
HAADF	high-angle annular dark-field
hcp	hexagonal closed-packed
HEMT	high-electron-mobility transistor
HRTEM	high-resolution transmission electron microscopy
InAs	indium arsenide
InP	indium phosphide
MD	molecular dynamics
MFC	mass flow controller
MOVPE	metal organic vapor phase epitaxy
ML	monolayer
μm	micrometer
N_2	molecular nitrogen

nm	nanometer
O	oxygen
P	phosphorous
PC	pressure controller
PCTF	phase contrast transfer function
PIPS	precision ion polishing system
PE	primary electron
$\mathbf{p_P}$	partial pressure
PP	peak pairs
Sb	antimony
rms	root mean square
RSM	reciprocal space map
Sb	antimony
SE	secondary electron
SEM	scanning electron microscopy
SF	stacking fault
Si	silicon
SiC	silicon carbid
SiGe	silicon germanium
SK	Stranski-Krastanow
STEM	scanning transmission electron microscopy
(S)TEM	(scanning) transmission electron microscopy
TBAs	tert-butylarsenic
TBP	tert-butylphosphine
TD	threading dislocation
TDS	thermal diffuse scattering

TEGa triethylgallium

TEM transmission electron microscopy

TESb triethylantimony

UHV ultra-high vacuum

VW Volmer Weber

WB weak-beam

XRD X-ray diffraction

1 Introduction

The use of computers, mobile devices and other electronic equipment and their continuous improvement is taken for granted in our modern society today. The first computers were built in the 1940's [1]. Within the lifetime of a human being, they became faster, smaller, cheaper, more powerful, and more reliable. Today, computers and other electronic devices vastly impact nearly every aspect of our lives. They are used privately and at the workplace, in economy, medicine, administration, and science for communication, data processing, simulations, monitoring and controlling of machines, presentations or designing, just to name a few examples.

The rapid evolution of computers and development of other electronic devices is based on the invention of the transistor as well as integrated circuits (IC) by Kilby [2] and Noyce [3] in 1959. ICs connect a large number of electronic components such as transistors, diodes, resistors or capacitors on a single chip leading to a lower production cost and increasing the performance due to faster switching and lower power consumption compared to circuits that wire up discrete components. The first ICs had only few transistors of micrometer sizes connected on one chip. This number rapidly increased, especially after the invention of the complementary metal–oxide–semiconductor (CMOS) process by Wanlass in 1963 [4] that lead to a denser packing and miniaturization of the components. In 1965, Gordan Moore predicted [5] the invention of personal computers, mobile devices and automatic controls for cars due to a minimum component cost in integrated circuits increasing by a factor two per year. In 1975, Moore [6] reformulated his observation as a doubling of complexity every two years. This became famous as "Moore's law" with its most popular formulation of "a doubling of the number of transistors on integrated circuits every two years", becoming a driving force in the semiconductor industry ever since [7]. The "International Technology Roadmap for Semiconductors" [8] has been established by experts in the semiconductor industry to predict and coordinate future developments and set benchmark goals. However, during the last years, this progress has slowed down [9–11], since further downscaling in the CMOS technology becomes more difficult. The latest microprocessors from Intel (E5-2699 v4) are fabricated with a 14 nm technology in the order of 10^9 transistors per die [12]. There is an foreseeable end to the further miniaturization of the silicon/silicon dioxide CMOS technology due to fundamental physical limits but also for economical reasons [7, 8].

In order to continue this successful journey of technological improvement, new materials need to be investigated. In the long term, this means the introduction of new information processing systems beyond CMOS. However, in the mid-term perspective, the "International Technology Roadmap for Semiconductors" is aiming for "More Moore" [8] by integrating new high-mobility III-V channel materials into the CMOS technology. The advantages of these high-electron-mobility transistor (HEMT) compared to the complementary metal-oxide-semiconductor field-effect transistors based on silicon/silicon dioxide are lower noise levels and higher switching speeds that allows the operation at higher frequencies. Hereby, n-doped (GaIn)As or InAs are very promising candidates, since their effective electron masses are much lower than in silicon (Si), leading to much higher electron mobilities [13]. As indicated in figure 1.1, the electron mobility of Si is with 1400 cm^2/Vs much lower than 7000- 18000 cm^2/Vs for n-doped gallium indium arsenide ((GaIn)As) and 20000 - 30000 cm^2/Vs for indium arsenide (InAs), respectively. The integration of these channel materials into the silicon-based CMOS-technology requires the implementation of a buffer layer between the Si substrate and the channel material to overcome the mismatch of their lattice constants.

Figure 1.1 is a plot of the band gaps of different semiconductor materials in dependence on their lattice constants. The figure shows that (GaIn)As has a much higher lattice constant than Si and can be grown lattice-matched to InP substrate. InAs is nearly lattice matched to GaSb. In order to integrate the high-mobility channel layers into the silicon-based CMOS technology, it is necessary to grow a buffer layer between the exact (001) silicon substrate and the active channel layer to overcome the lattice mismatch between these heterogeneous materials. However, the CMOS technology demands for buffer layers in a very high quality with low defect densities. Otherwise, the defects will act as scattering and/or recombination centers for electrons and holes reducing the mobilities of the charge carriers. Additionally, the buffer layers should be as thin as possible to be able to integrate these components onto the die within a reasonable scale. Therefore, graded buffer layers [14, 15] with thicknesses up to one micrometer are unreasonable.

(GaIn)As high-mobility field-effect transistors (HEMTs) are already grown successfully on InP substrate [17, 18]. Therefore, it would be beneficial to transfer these high mobility channel layers with a lattice constant of InP onto the silicon substrate using a metamorphic buffer layer with the suitable lattice constant. The graph 1.1 demonstrates that larger lattice constants are achieved by using crystal structures with large atoms. Hereby, antimony (Sb) is very suitable. In this study, two different antimonide-based buffer layers will be explored, gallium arsenide antimonide (Ga(AsSb)) and gallium phosphide antimonide (Ga(PSb)). They are drawn into the figure as blue arrows. Using the right composition, Ga(PSb) and Ga(AsSb) can be grown with the lattice constant of InP onto the exact silicon substrate.

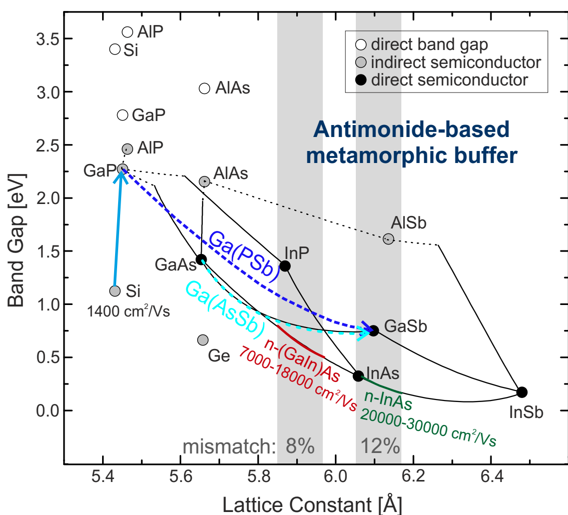

Figure 1.1: The band gap in eV of various semiconductor materials in dependence on the lattice constant in Å. Black circles mark the direct semiconductors. The indirect semiconductors are drawn as gray circles while their corresponding direct band gaps are also shown as white circles. The values taken from [16]. The arrows indicate the investigated buffer layers of this study, Ga(PSb) and Ga(AsSb) as well as the GaP buffer layer grown between the Sb-based layer and Si-substrate. The electron mobilities of Si, (GaIn)As, and InAs are reported in the graph in cm^2/Vs.

However, the growth will not take place directly on the silicon substrate but a GaP/Si pseudosubstrate. This gallium phosphide (GaP) buffer layer is introduced between the Si substrate and the Sb-based buffer layer in order to overcome the formation of anti-phase domains that arise during the growth of polar III/V-materials on the non-polar silicon substrate [19]. The Ga(PSb) and Ga(AsSb) layers will be grown as metamorphic buffer layers without step grading the composition. The large lattice mismatch of 8.1 % will introduce misfit strain. It is the aim of this study, to optimize the growth conditions so the buffer layers relax by forming network of misfit Lomer dislocations at the interface without introducing a high density of other defects such as threading dislocations, stacking faults or twins. The investigation of these structures from the nanometer down to the atomic scale will be conducted by transmission electron microscopy. Additionally, the formation of misfit dislocations at the Ga(PSb)/GaP and Ga(AsSb)/GaP interfaces will be compared to the binary material system GaSb/GaP. GaSb has an even higher lattice constant with a 12 % lattice mismatch to silicon. It could act as a suitable buffer layer for InAs channel layers.

In the following, this thesis is divided into four parts. Chapter 2 will give an overview of the fundamental physics that is necessary to describe the investigated material system with its problems during growth due to strain and the formation of defects as well as the interaction of the material with electrons or x-rays that have been used for the investigation. Chapter 3 introduces the methods that have been used for sample growth using metal

organic vapor phase epitaxy (MOVPE) and sample characterization by atomic force microscopy (AFM), X-ray diffraction (XRD) and transmission electron microscopy (TEM). In TEM, a wide range of operation modes have been applied, from conventional weak-beam imaging, Convergent beam electron diffraction (CBED), high-resolution transmission electron microscopy (HRTEM) to high-angle annular dark-field (HAADF) in scanning transmission electron microscopy. The results and discussion of these investigations is presented in chapter 4, which is divided into two sections. The first section presents the results on the growth optimization of Ga(AsSb) and Ga(PSb) buffer layers on GaP/Si pseudosubstrate with the main focus on the latter. The second section studies the interfaces of GaSb, Ga(PSb) and Ga(AsSb) to GaP at the beginning of their island-like growth. Finally, chapter 5 summarizes the presented results and gives a short outlook on future work.

2 Physical Background

This chapter introduces the basic physical background about crystalline semiconductors and their interacting with electrons that is necessary to understand the growth and characterization of the material systems in this study. The first section 2.1 deals with the physical properties of semiconductors. The following section 2.2 introduces the periodic arrangement of the atoms in the studied crystalline Sb-based semiconductors grown on a GaP/Si pseudosubstrate, while crystal growth is explained in section 2.3. Since the investigated materials have very different lattice constants, strain as well as lattice defects are addressed in sections 2.5 and 2.4. Section 2.6 discusses the physical background of the TEM, where the interaction of the electrons with the investigated materials as well as the imaging with magnetic lenses are explained.

2.1 Fundamentals of semiconductor physics

In most textbooks, e.g. [20–22], semiconductors are defined as materials which have a small enough band gap, usually up to 3.5 eV, so that electrons from the valence band can overcome the energy difference to the conducting band at finite temperatures due to deviations from the Fermi-Dirac distribution. At 0 Kelvin, the valence band is the last full, while the conduction band is the first empty band and their energy difference defines the band gap in semiconductors and isolators. The electrical resistivity of semiconductors ranges over several orders of magnitude from $10^{-4} - 10^{7} \Omega m$ [21].

In semiconductors, not only the electrons in the conduction bands are contributing to the conductivity but also the holes in the valence band, which are acting as positive charge carriers. The intrinsic conductivity of semiconductors is temperature dependent and can be changed easily by intentionally doping the material with impurity atoms that are supplying additional charge carriers. The dopant atoms determine weather the semiconductor becomes n-conductive due to a majority of electrons or p-conductive due to a majority of holes as charge carriers. The electronic band structure can be described by quantum-mechanically considerations as a result of the overlap of the wave functions of the single atoms in a solid [20]. The electronic band structures are characterized in dependence on the wavevector $\mathbf{k}$ in momentum space. A distinction is made between direct and indirect semiconductors. Direct semiconductors have the valence band maximum and conduction band minimum at the Γ-point where $\mathbf{k} = 0$ while indirect semiconductors

have the extrema at different positions as illustrated in figure 2.1. In the latter case, transitions between valence and conduction band by absorbing or emitting a photon with the energy of the band gap $\hbar\omega_g = E_g$ can only take place in cooperation with a phonon in order to preserve the conservation of energy and quasimomentum as shown in figure 2.1. This process is statistically much more unlikely than the direct transition so that indirect semiconductors such as Silicon or GaP are less effective for optoelectronic applications than direct semiconductors such as GaAs or GaInAs.

Figure 2.1 depicts the band structures of an direct (a) and indirect (b) semiconductor showing the direct and indirect transition of an electron from the valence band maximum to the conduction band minimum creating a hole in the valence band. The indirect transition requires the participation of a photon with energy $\hbar\Omega$.

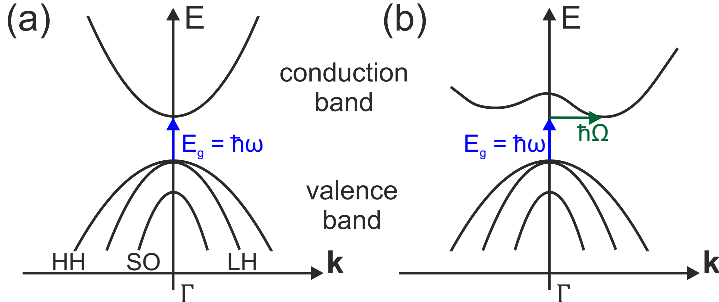

Figure 2.1: Schematic illustration of an direct (a) and indirect (b) semiconductor. The valence band shows the three energetically highest bands, the heavy hole (HH), light hole (LH) and split-off (SO) band. The arrow indicate the transition of an electron from the valence band maximum to the conduction band minimum.

The band structures are drawn as parabolic functions, which is an approximation of the band structure close to the highly symmetric Γ-point. Of course, real band structures are much more complicated. This simplified picture only serves as illustration and can be justified by the fact that the excited electrons relax very quickly to their band extrema. The curvature of the bands define the effective mass m^* of the charge carriers. In the one-dimensional parabolic approximation this is

$$\frac{1}{m^*} = \frac{1}{\hbar}\left(\frac{\partial^2 E}{\partial k^2}\right)^{-1} . \tag{2.1}$$

The valence bands in the figure are represented by the three energetically highest bands, the split-off (SO) band and the heavy-hole (HH) and light-hole (LH) bands, which are degenerated at the Γ-point. The heavy hole band has a larger curvature than the light hole band so that the effective mass of the holes is larger (heavier). The split-off band is non-degenerated to the other two bands and has a lower energy due to the spin-orbit interaction.

The effective mass determines the charge carrier mobility μ through an inversely proportional relationship

$$\mu = \frac{q * \bar{\tau}}{m^*} , \qquad (2.2)$$

where q is the charge of the carrier and $\bar{\tau}$ the mean scattering time between two scattering events. The carrier mobility defines in turn the electrical conductivity σ by

$$\sigma = \sigma_n + \sigma_p = ne\mu_n + ne\mu_p , \qquad (2.3)$$

where e is the elemental charge, μ_n and μ_p the electron and hole mobilities, and n and p the electron and hole densities, respectively.

2.2 Crystal structures

The investigated Sb-based layers and the GaP/Si pseudosubstrate are crystalline materials with a high periodicity in the atomic arrangement. A perfect crystal is defined as the infinite, periodic, three-dimensional arrangement of atoms or identical groups of atoms (all in the same orientation) that are called a basis, into a point lattice, the Bravais lattice. The periodicity or translation from one Bravais lattice point to the next can be described by the translation vector $\mathbf{R}$

$$\mathbf{R} = u\mathbf{a}_1 + v\mathbf{a}_2 + w\mathbf{a}_3, \quad u,v,w = \text{integer} , \qquad (2.4)$$

where $\mathbf{a}_1$, $\mathbf{a}_2$ and $\mathbf{a}_3$ are three linear independent basic vectors. These basis vectors define the volume elements of the lattice, the so-called unit cells with a volume V_c of

$$V_c = \mathbf{a}_1(\mathbf{a}_2 \times \mathbf{a}_3) . \qquad (2.5)$$

There are 14 different Bravais lattices that describe all possible translational symmetries. Their unit cells are displayed in figure 2.2. The Bravais lattices are grouped by common lattice parameters, i.e. the angles and lattice constants (the magnitudes of the basis vectors). The different crystal symmetries affect physical properties, such as ductility, cleavage, electronic band structure, and optical transparency.

In order to describe the interactions of the lattice with other particles such as electrons or x-rays, it is necessary to define the Bravais lattice in k-space. This is the reciprocal lattice, which transforms a set of lattice planes in real lattice into a point in reciprocal space and vice versa. The reciprocal lattice vector $\mathbf{g} = h\mathbf{b}_1 + k\mathbf{b}_2 + l\mathbf{b}_3$ is defined by the reciprocal basis vectors in accordance to the translation vector $\mathbf{R}$ so that

$$\mathbf{g} \cdot \mathbf{R} = n, \quad n = \text{integer} \qquad (2.6)$$

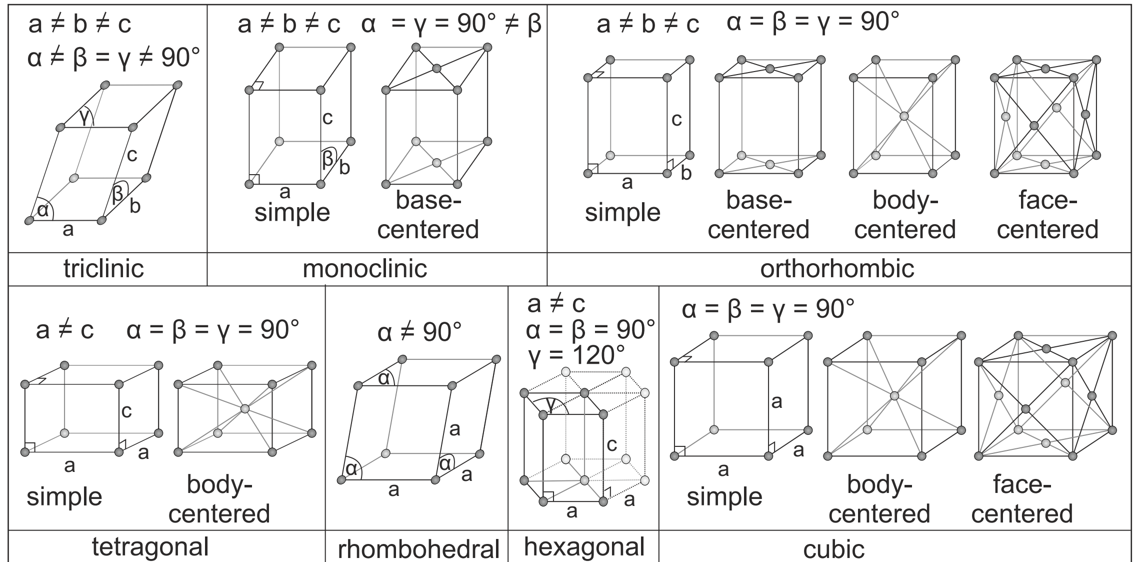

Figure 2.2: The 14 Bravais lattices. [23]

and

$$\mathbf{a}_i \cdot \mathbf{b}_j = \delta_{ij} \quad \text{with } i,j = 1,2,3 \text{ and } \delta_{ij} = \begin{cases} 1 & \text{if } i = j \\ 0 & \text{if } i \neq j \end{cases} . \tag{2.7}$$

This defines the reciprocal basis vectors to

$$\mathbf{b}_1 = \frac{\mathbf{a}_2 \times \mathbf{a}_3}{\mathbf{a}_1 \cdot (\mathbf{a}_2 \times \mathbf{a}_3)} = \frac{\mathbf{a}_2 \times \mathbf{a_3}}{V_c} , \tag{2.8}$$

where cyclic permutation of the indices 1,2,3 gives all three linear independent reciprocal basis vectors and V_c defines the volume of the unit cell. The indices h,k,l of the reciprocal lattice vector $\mathbf{g}$ define the corresponding set of lattice planes in real space. The distance d_{hkl} between the lattice planes is then defined by the inverse absolute value of the reciprocal lattice vector

$$d_{hkl} = \frac{1}{|\mathbf{g}|} \overset{cubic}{=} \frac{a_0}{\sqrt{h^2 + k^2 + l^2}} . \tag{2.9}$$

The lattice planes and directions of the lattices can be described by the Miller indices notation system. The Miller indices of a set of lattice planes are formed by determining the intersection of one lattice plane with the coordinate axis of the the basis vectors $\mathbf{a_1}, \mathbf{a_2}, \mathbf{a_3}$ in one unit cell. In the next steps, the common factors are canceled out, the reciprocal values are formed and the result is multiplied with the lowest common multiple of the denominator. At this point, three integers that label that plane in the unit cell and the reciprocal lattice vector $\mathbf{g}$ are obtained. These triplets are notated in (hkl) brackets for a particular set of lattice planes, and {hkl} brackets for general planes. Negative values are

marked by a bar, $\bar{h}$, and an intersection in infinity is defined by a 0. Particular directions can be described by [uvw] brackets, which translate into $u\mathbf{a_1} + v\mathbf{a_2} + w\mathbf{a_3}$. The direction [hkl] is only perpendicular to (hkl) planes in cubic lattice structures. General directions referring to a set of directions, e.g. [001],[010],[100], [$\bar{1}$00]...are notated as <uvw>. The three most important lattice planes for later investigations, (001), (110) and (111), are shown in figure 2.3.

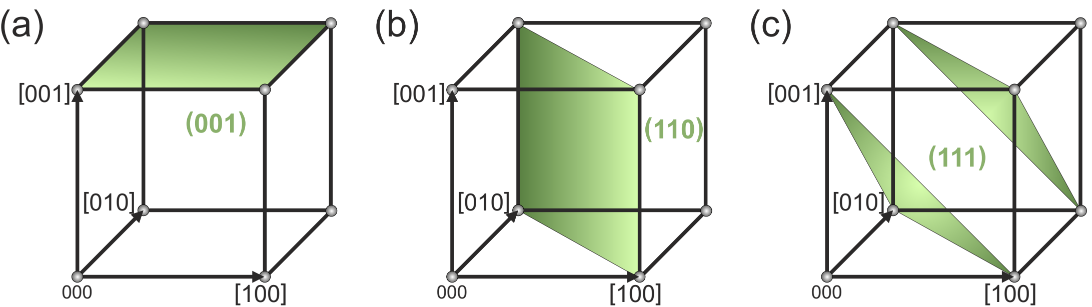

Figure 2.3: (a) (001) (b) (110) and (c) (111) lattice planes in a simple cubic unit cell. The three lattice vectors [100], [010] and [001] are marked by arrows in the unit cells.

In figure 2.2, the most important lattice for this study is the face-centered cubic (fcc) lattice. The fcc lattice is, like the hexagonal lattice, most closely packed. When stacking close-packed atomic planes in three dimensions there are two possible ways to do this, as shown in figure 2.4. The hexagonal closed-packed (hcp) crystal has a stacking of {001} atomic planes in the order ABABAB. The fcc cubic closed-packed (ccp) crystal has a stacking of {111} atomic planes in the order of ABCABCABC, where each atomic plane is rotated by 30° towards the previous plane and the same letter, for example A, denotes the same orientation.

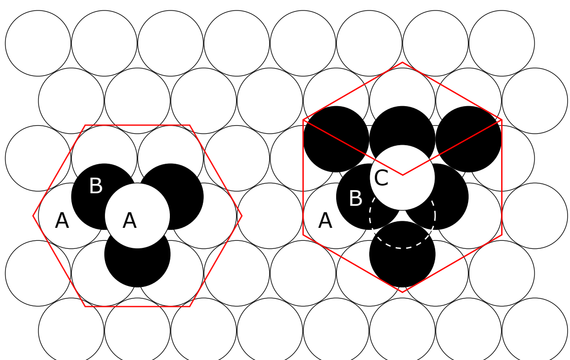

Figure 2.4: The hexagonal close packing (hcp) on the left and the cubic closed packing (ccp) on the right. [24]

The fcc lattice is the base for the studied structures of this study: Si, GaP and the Sb-based buffer layers Ga(PSb), Ga(AsSb) and GaSb. Si crystallizes in the diamond structure, which is a fcc lattice with a two atomic basis in the unit cell, one group IV atom at (0, 0, 0) and the other one at ($\frac{a}{4}$, $\frac{a}{4}$, $\frac{a}{4}$), where a is the lattice constant. The

corresponding structure is shown in figure 2.5 (a). The two atomic basis is marked by their positions. Each atom has four neighbors that are forming a tetrahedron around it. The bonds between the atoms therefore have a 109.5° angle to each other and are purely covalent with an sp^3-hybridization. The polyatomic GaP and Sb-based buffer layers crystallize in the zinc blende structure that has the same atomic configuration as the diamond structure, but the two group IV atoms of the basis are a group III and group V atom, as shown in 2.5 (b). The group III and group V atoms each form a fcc sublattice which are displaced by $(\frac{a}{4}, \frac{a}{4}, \frac{a}{4})$ to each other. The atom bonds also show a sp^3-hybridization, however, these III-V compound bounds have not a purely covalent but also an ionic character.

Since the TEM samples will be prepared in <110> direction, the corresponding projections are displayed in figure (c). The image shows the dumbbell structure that can be observed along the <110> viewing directions. The polarity of the dumbbell is defined by the upper atom of the dumbbell in the [001] growth direction. A Ga-polar dumbbell defines the [110] projection and a P-polar dumbbell the perpendicular [$\bar{1}$10] direction.

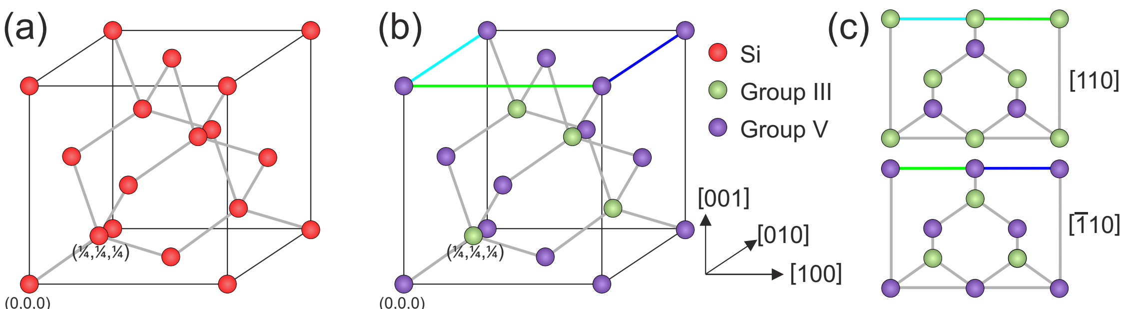

Figure 2.5: (a) Diamond and (b) zinc blende structure. Si atoms are displayed in red, group III atoms in green and group V atoms in violet. The two atoms of the basis are marked by their positions at (0, 0, 0) and $(\frac{a}{4}, \frac{a}{4}, \frac{a}{4})$. Image (c) shows the Ga-polar [110] projection (upper image) and the P-polar [$\bar{1}$10] projection (lower image) of the zinc blende structure. The corresponding upper edges of the (110) and ($\bar{1}$10) lattice planes in the unit cell of the zinc blende structure in (b) and its projection in (c) are marked by blue and green color, respectively.

2.3 Crystal growth of heterostructures

The investigated crystalline samples in this study have been grown by MOVPE. Epitaxy refers to the deposition of a crystalline layer onto a single crystalline substrate, that determines the orientation of the layer grown on top of it. The technical aspects of MOVPE will be described in section 3.1. This section is used to give a theoretical background on the topic and point out the challenges in the epitaxy of heterostructures such as the investigated III/V-compounds. An extensive overview on metal organic vapor

phase epitaxy has been published by Stringfellow [25].

The growth of heterostructures is much more challenging than homoepitaxy where the epitaxial layer is the same material as the substrate. However, it offers a much wider range of applications due to the possibility of changing the band structure and introducing new properties such as a different electronic transport or optoelectronic transitions. These advantages are only be accessible with a high crystalline quality of the structures that can only be achieved by optimal growth conditions. As the name suggests, the growth in MOVPE not only depends on the incorporation of the desired atoms into the crystal but also on the mass transport of the metal organic compounds to the crystal, their decomposition, the reactions of the residual organic groups, and the desorption and transport of the reaction products. The incorporation of the atoms into the crystal is governed by the adsorption, chemisorption, diffusion and chemical reactions of the atoms on the surface, and desorption from the substrate. The decomposition of the organometallic compounds, which are named precursors, does not necessarily occur in the gas phase but might take place by reactions on the surface in the presence of chemical radicals of other precursors or surface atoms. The partial pressure ($\mathrm{p_P}$) of the precursors in the gas phase is several orders of magnitude higher than the equivalent equilibrium partial pressures which makes the epitaxial growth a non-equilibrium process with the possibility to grow metastable materials.

2.3.1 Stability of growth

The stability criteria that defines whether the composition of a material is stable at a certain growth temperature is the Gibbs free energy G. The Gibbs energy is a thermodynamic potential that is defined by the internal energy U, the intensive variables temperature T and pressure p as well as the extensive variables entropy S and volume V through

$$G(p,T) = U + pV - TS = H - TS\ , \tag{2.10}$$

where H is the enthalpy so that G is also often mentioned as Gibbs enthalpy. Negative Gibbs enthalpy differences of a chemical reaction with isobar and isothermal conditions are exergonic processes that can take place spontaneously. Positive Gibbs free energy differences describe endergonic reactions that can only take place under energy supply. The partial derivative of the Gibbs free energy with respect to the number of particles (or number of moles) N_i of the ith chemical component defines the chemical potential μ_i of this component to

$$\mu_i = \left(\frac{\partial G}{\partial N}\right)^i\ . \tag{2.11}$$

The Gibbs free energy for a system with two components A and B has its energetically most stable state at the minimum of G, at thermodynamic equilibrium, where the chemical potential of the two components are equal to each other $\mu_A = \left(\frac{\partial G}{\partial N}\right)^A = \left(\frac{\partial G}{\partial N}\right)^B = \mu_B$. For a stable composition of $A_{1-x}B_x$, the Gibbs enthalpy in dependence on the extensive parameters N should exhibit a positive, concave curvature, i.e. $\frac{\partial^2 G}{\partial N^2} > 0$. Figure 2.6 (a) illustrates the Gibbs free energy G for three different temperatures in dependence on the composition x of a binary solid $A_{1-x}B_x$. The second graph demonstrates the dependence of the temperature T on the composition and can be derived from (a).

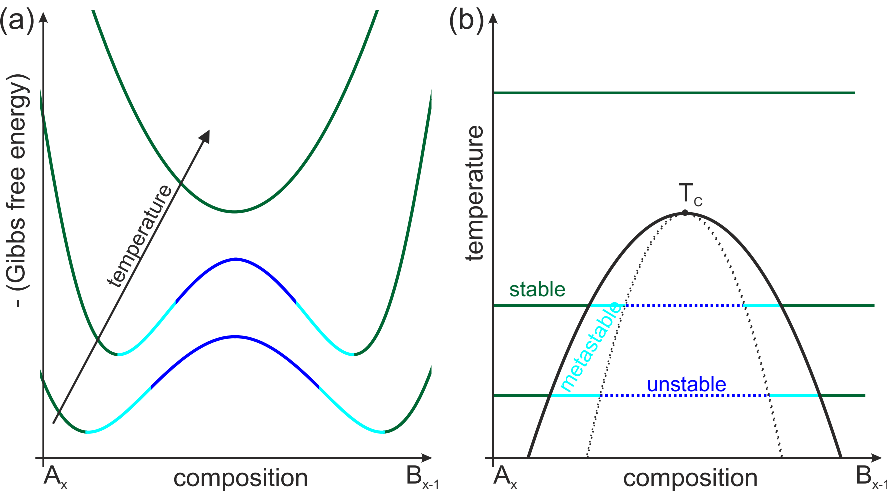

Figure 2.6: (a) Schematic curves of the negative Gibbs free energy in dependence on the composition x of the material $A_{1-x}B_x$ for different temperatures. (b) Corresponding curves of graph (a) showing the dependence of the temperature on the composition. There are three different regimes: stable (green), metastable (orange) and unstable (blue) growth conditions that are separated by the binodal (undashed) and spinodal (dashed) curves. T_c is the citical temperature above which only stable growth will take place.

The topmost green curve in (a) displays a parabola curve for which the stability criteria of a positive curvature is fulfilled. Therefore, the temperature dependent second graph in (b) shows that it is possible to grow the material at every composition at this temperature. The corresponding curve is displayed as a green line. The other two curves in (a) are W-shaped curves. Each curve has two minima between which a phase transition might occur. Between the two minima, there is a maximum and two turning points, where $\frac{\partial^2 G}{\partial N^2} = 0$. The curvature between the two turning points is negative so the stability criteria is not fulfilled for this section of the curve. This means, that the corresponding compositions are unstable so a continuous phase separation into the compositions of the minima will occur. This will lead to a reduction of the Gibbs free energy. However, there exists an activation barrier that needs to be overcome for the phase separation, e.g. by increasing the temperature. The unstable regimes are plotted in a blue color in both graphs. The turning points that confine the unstable regime in (a), define the spinodal

curve in (b). In the temperature dependent graph, the spinodal is plotted with a black dashed line. The third regime in the Gibbs enthalpy dependent graph, between the minima and the turning points, define the metastable regime, plotted in an bright blue color. The metastable state is confined by the spinodal and the binodal curves in the temperature dependent graph in (b). The binodal curve is plotted with a continuous black line. It marks the transition between the matastable and stable growth and is defined by the minima in (a).

With increasing temperature, the miscibility gap of the metastable and unstable regime becomes smaller until the critical temperature T_c, at which the growth becomes completely stable, is reached. The critical temperature is different for each material system and depends on the difference of lattice constants of A and B, $T_c \propto (\Delta a)^2 = (a_A - a_B)^2$. For very high T_c, it is necessary to grow in the metastable regime at lower temperatures and non-equilibrium growth conditions in order to grow certain compositions at all.

The non-equilibrium growth conditions are realized by partial pressures in the gas phase that are much higher than the according equilibrium partial pressures. For the growth of III/V-compounds, it is important to note that the equilibrium p_P of the group V species is higher than the group III species. This results in an incongruent evaporation, where the desorption of the group V atoms from the surface is higher than the desorption of the group III atoms so it is necessary to offer the group V precursors in excess. This means that the V/III ratio, defined by $V/III = \frac{\sum p_P(groupV)}{\sum p_P(groupIII)}$, should be larger than one. Since both species are necessary for the growth of a III/V-compound, the epitaxial growth is determined by the group III fluxes. The growth rate then depends on the the group III flux as well as the temperature. If the temperatures are too low, the decomposition of the precursors will govern the growth rate since the metal organic chemicals need certain activation energies that can be supplied by sufficiently high temperatures. These temperatures depend strongly on the different precursors and the growth rate decreases linearly with 1/T in that regime. If all the precursors are decomposed, the growth rate will be determined by the mass transport of the chemicals to the surface. This is independent of the temperature since it only depends on the diffusion in the gas phase. However, the growth temperature should not be chosen too high, because in this case the growth rate will drop again due to the higher desorption from the surface.

2.3.2 Growth mode of nucleation

The epitaxial growth can be classified into three fundamental growth modes that are depicted schematically in figure 2.7. The growth mode is determined by the surface energy of the substrate γ_S in comparison to the surface energies of the epitaxial layer γ_L and the interface energy [26] of the two materials γ_i under equilibrium conditions [27]. The

Frank van der Merwe (FM) growth mode [28] is a layer-by-layer growth, where the second monolayer (ML) does not grow before the coverage of the substrate is completed. In case of III/V-compounds, the layers are actually bilayers, not monolayers. This 2D-nucleation will take place if $\gamma_S > \gamma_L + \gamma_i$. The growth starts with an island nucleation, where the islands grow together to form a complete layer that is serving as a substrate for the next layer as illustrated in 2.7 (a). At non-equilibrium conditions, a pseudo-FM growth can be obtained when the surface diffusion length $l_{sd}(t)$ within the time t to deposit one ML coverage is approximately equal to the hopping distance a [29]. The surface diffusion length

$$l_{sd}(t) = \sqrt{D_{sd} t} \tag{2.12}$$

is defined by the surface diffusion coefficient D_{sd}. The surface diffusion depends on the hopping distance a, the hopping attempt frequency ν, the surface diffusion activation energy E_{sd} and the surface temperature T through

$$D_{sd}(t) = a^2 \nu e^{\frac{-E_{sd}}{k_B T}} \ . \tag{2.13}$$

The condition for the deposition of one ML within the time t depends on the deposition rate R through $Rt = 1/a^2$. In combination with two previous equations for the diffusion length and coefficient, this gives

$$R = a^{-2} \nu e^{\frac{-E_{sd}}{k_B T}} \ , \tag{2.14}$$

where $l_{sd} \approx a$. However, the diffusion length should be larger than the terraces between the surface steps. Otherwise the adatoms favor the incorporation at these steps and a transition from the 2D growth to a step flow growth will take place. This can be avoided by providing a substrate with large enough terraces due to a lower off-orientation of the wafer, or by decreasing the growth temperature, which decreases the diffusion length according to 2.13.

If the substrate surface energy is too small so that $\gamma_S < \gamma_L + \gamma_i$, a homogenous wetting will be energetically unfavorable. This causes a three-dimensional island-like growth mode, which leads to a roughening of the interface. This island-like nucleation is known as Volmer Weber (VW) growth mode [30] and is illustrated in figure 2.7 (c). The thermodynamic argument for the island formation is based on the surface tension γ_i that stays the same for growing layer A on B and vice versa. If A forms a wetting layer on B because $\gamma_B > \gamma_A + \gamma_i$ then B will not wet A because $\gamma_A > \gamma_B + \gamma_i$.

The intermediate growth mode between complete wetting (FM) and island formation (VW) is the Stranski-Krastanow (SK) growth mode [31] shown in 2.7 (b). It usually takes place for pseudomorphic growth with a high compressive strain. The SK growth starts off with a complete wetting of the substrate displaying a 2D growth for the first few ML until a critical thickness is reached. At this point, the growth mode transitions to an island-like 3D growth to lower the total energy. In non-equilibrium growth conditions it is possible to suppress this transition by decreasing the growth temperature so that the diffusion length will be reduced and the growth takes place only at localized equilibrium that avoids the formation equilibrium shapes [29]. After a few MLs, the system returns to homoepitaxial growth conditions at which FM growth can take place spontaneously.

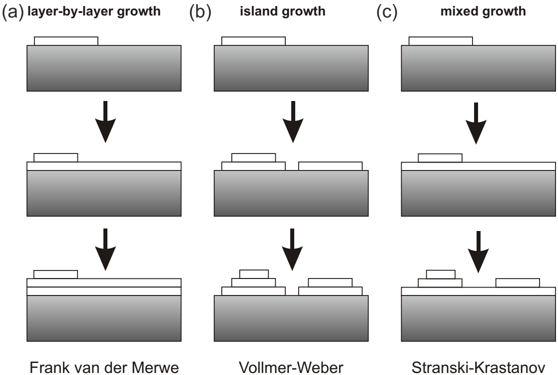

Figure 2.7: Schematic illustration of (a) Frank van der Merwe (b) Stranski-Krastanow and (c) Volmer Weber growth, modified from [32].

2.3.3 Heteroepitaxial growth

Heteroepitaxial growth can be distinguished into lattice-matched, pseudomorphic and metamorphic growth [33] that are depicted schematically in figure 2.8. The lattice-matched growth, see figure 2.8 (a), takes place when growing an epitaxial layer of the same lattice constant as the substrate. For homoepitaxy this is always the case. During pseudomorphic growth, the in-plane lattice constant of the epitaxial layer a_L is adapted to the lattice constant of the substrate a_S by tetragonal distortion as illustrated in 2.8 (b). This generates strain in the material and will be discussed further in the following section 2.5. If $a_L > a_S$, as drawn in 2.8 (b), the lattice spacing d of the epitaxial layer will be elongated in growth direction and compressed in the growth plane resulting in compressive strain. The opposite case, growing a layer with $a_L < a_S$ takes place under tensile strain (not shown here). During metamorphic growth, the lattice constant of the epitaxial layer is undistorted or relaxed to its natural value. The mismatch of the lattice constants is accommodated by misfit dislocations at the interface due to the additional lattice planes

of the material with the smaller lattice constant depicted in 2.8 (c). They will be discussed further in the following section 2.4 on lattice defects.

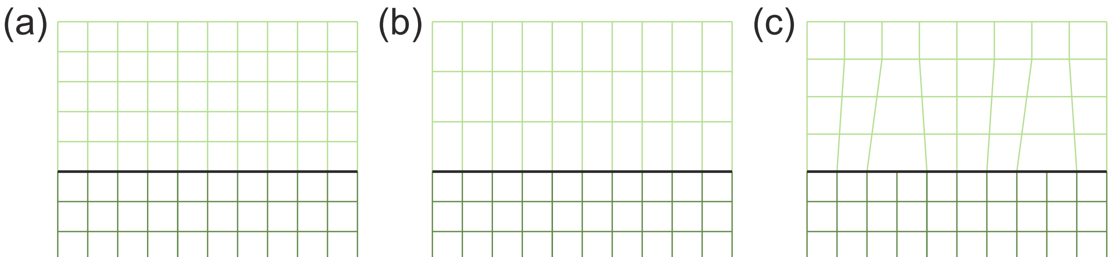

Figure 2.8: Schematic illustration of (a) lattice-matched (b) pseudomorphic and (c) metamorphic growth. Modified from [33].

Whether heteroepitaxy is taking place as pseudomorphic or metamorphic growth will depend on the lattice mismatch between the epitaxial layer and the substrate as well as the layer thickness. This will also define the growth mode that have been described in the last paragraph.

The lattice mismatch [34], or misfit, is defined by the difference in lattice constants in relation to the lattice constant of the substrate

$$mf = \frac{\Delta a}{a_0} = \frac{a_L - a_S}{a_S} = \frac{a_L}{a_S} - 1\,. \tag{2.15}$$

The lattice constants of the compound materials can be determined by the lattice parameters of its two components if the pure constituents have the same crystal structure as the compound. This heuristic observation is known as Vegard's law [35]:

$$a_{A_xB_{1-x}} = xa_A + (1-x)a_B\,. \tag{2.16}$$

This law can be applied for most III/V-compound materials, since they crystallize in zinc blende structure. The lattice constant for the investigated Ga(PSb) and Ga(AsSb) layers can be determined by the according binary lattice constants:

$$\begin{aligned} a_{Ga(P_xSb_{1-x})} &= xa_{GaP} + (1-x)a_{GaSb} \\ a_{Ga(As_xSb_{1-x})} &= xa_{GaAs} + (1-x)a_{GaSb} \end{aligned} \tag{2.17}$$

Pseudomorphic growth can only take place for very low lattice mismatches [28, 34, 36] and can therefore not be expected for the investigated material systems. Additionally, pseudomorphic growth can only be achieved if the layer thickness does not exceed a certain critical thickness h_c at which the strained pseudomorphic layer becomes thermodynamically unstable and relaxes by the formation of misfit dislocations [28, 37, 38]. Misfit dislocations are a certain kind of lattice defects that will be explained in the following section.

2.4 Lattice Defects

For thermodynamic reasons, a real crystal is never perfect and these imperfections in periodicity are described as defects. They can be beneficial as there are certain defects that can improve mechanical, optical, or electrical properties. However, in most cases the opposite is true and a large number of grown-in defects are highly unfavorable as they degrade the performance and lifetime of the materials [39].

2.4.1 Point defects

Point defects are zero-dimensional defects in the lattice that can be distinguished into vacancies, interstitials, antisites, and impurities.

Vacancy and interstitial defects

Vacancies are missing atoms in the crystal lattice that would be occupied by an atom in a perfect crystal while interstitial defects are atoms that are located in between lattice sites of a perfect crystal.

Antisite defects

Antisites defects can only occur in crystal structures with more than one sort of atom, because they are caused by atoms that occupy lattice sites on the wrong sublattice, e.g. a P atom on a Ga atom position in the GaP zinc blende structure.

Impurity defects

Impurities, also called substitutional defects, are foreign atoms incorporated into lattice either on purpose, for example as donor or acceptor atoms to increase the charge carrier density, or during growth as an undesirable defects that degrades the material, for example oxygen or carbon atoms from organic rest groups in MOVPE.

2.4.2 Line defects

Line defects are dislocations because the atomic distortions in the crystal structure that form a dislocation lie along a line, the thus defined dislocation line. If the dislocation can relieve misfit strain (equation 2.15), it can be called a misfit dislocation. Misfit dislocations are generated at the interface to the strained layer as already illustrated in figure 2.8 (c) in section 2.3.
Dislocations extending through the layer to the surface or the following interface are threading dislocation. They are often attached to misfit dislocations [40–42].

Dislocation characteristics

The dislocation line defines the dislocation line vector **l**. However, a dislocation cannot be characterized by the direction of the dislocation line alone, but the direction and magnitude of the lattice distortion due to dislocation also play an import role. The measure for the lattice distortion can be obtained from the Burgers construction [43]. Therefore, a lattice that contains a dislocation is compared to a perfect lattice without dislocation as illustrated in figure 2.9. In the first step, a closed circuit, that connects the lattice points some distance away from the dislocation, is drawn clockwise around the dislocation as shown in figure 2.9 (a). In the second step, this circuit is transferred to a perfect lattice of the same type and orientation as depicted in image (b). Due to the missing dislocation in the perfect crystal, the circuit is open. The lattice vector that connects the starting and end point of this open circuit is the Burgers vector **b**.

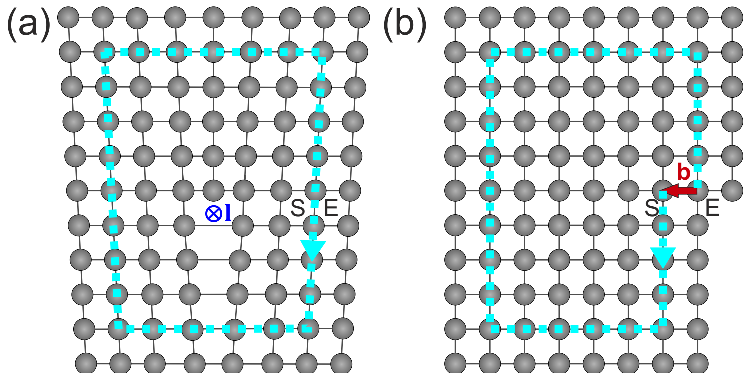

Figure 2.9: (a) Burgers circuit around an dislocation caused by the additional half lattice plane in the upper part of the crystal. The dislocation line is marked by the red cross and vector **l**, the start and end of the circuit by the letters S and E. (a) Burgers circuit of (a) transferred into a perfect lattice of the same type and orientation. The Burgers vector **b** connects the start and end of the circuit.

The elastic energy per unit length of a dislocation proportional to the square of its Burgers vector and will determine the stability of the dislocation as well as how much strain will be relieved when forming a misfit dislocation at the interface during heteroepitaxial growth [44]

$$E_{disl} \propto b^2 \,. \tag{2.18}$$

The misfit is only relieved by the Burgers vector component in the plane normal to the dislocation line [29].

The different types of dislocations are defined by the location of the Burgers vector in relation to the line vector. There are two types of pure dislocations, edge dislocations

and screw dislocations. All other kinds of dislocations are mixed type dislocations which exhibit characteristics of both.

Screw dislocations

Screw dislocations have dislocation lines parallel to their Burgers vector, $\mathbf{b} \parallel \mathbf{l}$. Therefore, they are not misfit dislocations. The distorted lattice planes follow a helical path around the dislocation line. The structure of a screw dislocation can be visualized by making a cut along a half plane of the perfect crystal up to the dislocation line, moving the lattice planes by the Burgers vector in direction of the dislocation line and slipping the crystal back together as shown in figure 2.10.

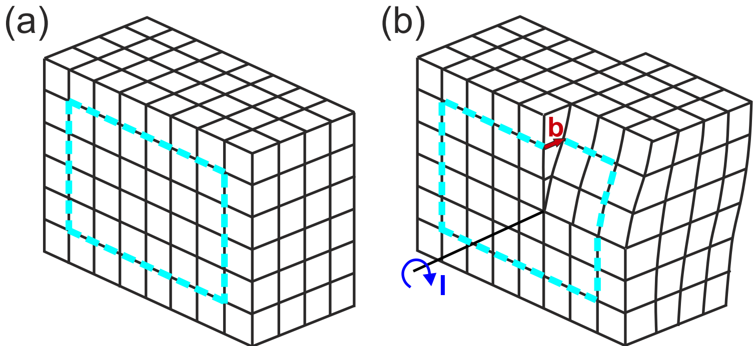

Figure 2.10: (a) Perfect lattice with Burgers vector circuit (b) Screw dislocation with Burgers vector **b** parallel to its dislocation line **l**.

Edge dislocations

Edge dislocations are defined by Burgers vectors that are perpendicular to their dislocation line, $\mathbf{b} \perp \mathbf{l}$. Therefore, edge dislocations are also mentioned as 90° dislocations. They occur due to the introduction of additional incomplete lattice planes into the crystal as already shown in the figures 2.9 and 2.8 (c). The dislocation lines are located at the edges of the extra half lattice planes.

In fcc, zinc blende and diamond structures grown in (001) direction, the additional lattice planes forming a 90° dislocation are two intersecting $\{111\}$ planes in $<110>$ directions with a resulting Burgers vector of $\pm\frac{a}{2}[110]$ or $\pm\frac{a}{2}[\bar{1}10]$. These edge dislocations can be generated by the reaction of two dislocations that are arising from inserting only one

additional lattice plane, for example $(1\bar{1}1)$ lattice planes with Burgers vectors $\frac{a}{2}[011]$ and $\frac{a}{2}[10\bar{1}]$ so

$$\frac{a}{2}[011] + \frac{a}{2}[10\bar{1}] = \frac{a}{2}[110]\,. \tag{2.19}$$

The resulting 90° dislocation, which is now consisting of two additional intersecting $(1\bar{1}1)$ planes, lowers the elastic energy of the crystal better than the two single dislocations and is therefore more efficient for strain relaxation. This reaction has been first described for fcc structures by Lomer [45], which is why these 90° dislocations are also known as Lomer dislocation.

60° dislocations

The single dislocations originating from only one additional {111} lattice plane are mixed type dislocations with a screw component in <110> and an edge component in <112> direction. They are referred to as 60° dislocations because their Burgers vector is forming a 60° angle to their dislocation line as shown in figure 2.11 (a). The edge component is usually split into a tilt component and misfit strain relieving component along <110> directions. The misfit relieving component $\mathbf{b}_{misfit}$ perpendicular to the dislocation line is smaller than the corresponding component of an edge dislocation where $\mathbf{b}_{misfit} = \mathbf{b}$. This is the reason why 90° dislocations are much more efficient for strain relaxation than 60° dislocations. Image (b) shows the <110> Burgers vector of the eight possible 60° dislocations with a [110] dislocation line in (001) projection. The continuously drawn vectors point out of the (001) plane and dashed vectors point into it. The four 60° dislocations on the left relieve tensile strain, the four dislocations on the right relieve compressive strain [46].

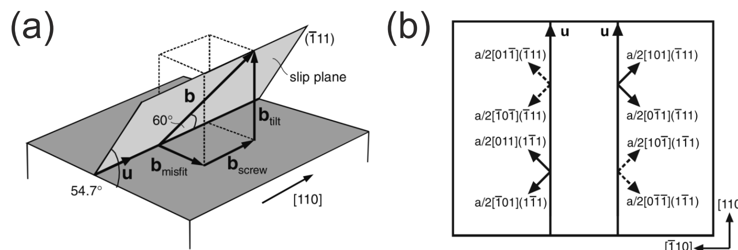

Figure 2.11: (a) Schematic representation of dislocation line and Burgers vector of a 60° dislocation in [110] direction. The Burgers vector **b** is split into its components: $\mathbf{b} = \mathbf{b}_{screw} + \mathbf{b}_{tilt} + \mathbf{b}_{misfit}$. (b) (001) projection of the eight possible 60° dislocations in [110] direction. The continuously drawn vectors point out of the (001) plane and dashed vectors point into it. Modified from [46].

Partial dislocations

If the Burgers vector of a dislocations is not a lattice vector, the dislocation will be called a partial dislocation. Partial dislocations are generated by the dissociation of a perfect dislocation into partial dislocations so that the Burgers vectors of these partials are generally smaller than the lattice vector. These partial dislocations will then have a lower energy, which makes their formation energetically favorable according to Frank's rule [47] explained in the following.

Frank and Nicholas [47] formulated a stability criteria for dislocations based on the dependence of the energy per unit length on the Burgers vector shown in equation 2.18. When a Burgers vector $\mathbf{b}_1$ of a dislocation is equal to the sum of two other possible Burgers vectors $\mathbf{b}_2$ and $\mathbf{b}_3$, so $\mathbf{b}_1 = \mathbf{b}_2 + \mathbf{b}_3$, the dissociation of the dislocation according to $\mathbf{b}_1 \rightarrow \mathbf{b}_2 + \mathbf{b}_3$ will take place if $b_1^2 > b_2^2 - b_3^2$. According to Nabarro [44], this will lower the total energy that is proprortional to the square of the Burgers vector (see equation 2.18). If $b_1^2 < b_2^2 - b_3^2$ then the dissociation is unstable because it will cost energy.

For the reaction of two dislocation with Burgers vectors $\mathbf{b}_2$ and $\mathbf{b}_3$ to a new dislocation with Burgers vector $\mathbf{b}_1$ according to $\mathbf{b}_2 + \mathbf{b}_3 \rightarrow \mathbf{b}_1$, as described by Lomer in equation 2.19, the opposite criteria must be fulfilled as pointed out by Hornstra [48]. In this case, it should be $b_1^2 < b_2^2 + b_3^2$, in order to create a stable dislocation with a lower total energy.

The reaction of two 60° dislocations to a Lomer dislocation and the dissociation into partial dislocations show that the dynamics of dislocations is very important for the generation of dislocations and will therefore be explained in more detail in the following section.

Dynamics of dislocations

Dislocations play a crucial role for the plastic deformation of crystalline materials. Plastic deformation results from the glide of specific planes over their neighboring atomic planes by breaking and reforming all connecting bonds during this process. Dislocations already have broken bond so their movement in the crystals requires a much lower energy than moving a plane in a perfect crystal. The glide (or slip) planes of the dislocations contain the Burgers vector $\mathbf{b}$ as well as the dislocation line $\mathbf{l}$.

Since $\mathbf{b} \parallel \mathbf{l}$ for screw dislocations, any plane can be considered as a glide plane. For mixed type or edge dislocations, there is only one distinct glide plane. In the fcc, diamond and zinc blende structures, these are the most closely packed and most widely spaced $\{111\}$ lattice planes because their shear stress during motion is the lowest [33, 39]. Hirth and Lothe [49] distinguished between two different kinds of $\{111\}$ glide planes. The difference

is illustrated in figure 2.12 displaying the [111] stacking sequence of the diamond lattice in $(01\bar{1})$ projection with its dumbbell structure.

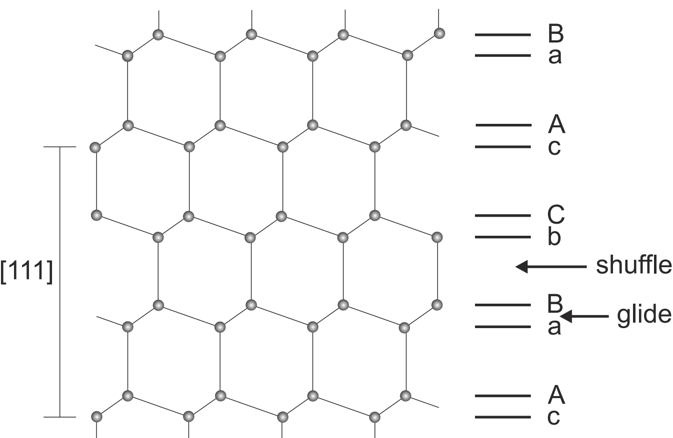

Figure 2.12: Diamond lattice in $(01\bar{1})$ projection illustrating the stacking of the (111) planes to define the "‘shuffle"’ and "‘glide"’ slip planes. Modified from [50]

The stacking sequence in diamond or zinc blende in $(01\bar{1})$ projection is AaBbCcAaBbCc. The first type of slip planes are shuffle sets between, for example, "B" and "b" atomic planes between the dumbbells as displayed in 2.12. The second type of slip planes are glide sets between, for example, "a" and "B" planes of atoms within the dumbbells. They are named glide sets since Hirth and Lothe expected that these planes could move more easily without having to "‘shuffle"’ the atoms during the glide process.

During the glide process, the dislocation is moved only by bond breaking, so mass transport of point defects is unnecessary. The opposite is true for the climb process that takes place during the motion out of the glide plane by extending or contracting the extra half planes of 60° or edge dislocations through diffusion of point defects [39].

Dynamics of partial dislocations

The dissociation of a perfect dislocation into partial dislocation has been first described by Heidenreich and Shockley [51] for so-called Shockley partials with $\frac{a}{6} < 112 >$ Burgers vectors. Additionally, Frank [52] proposed the existence of partial dislocations with $\frac{a}{3} < 111 >$ Burgers vectors. These Frank partials are sessile dislocations that cannot glide because the are not lying in but normal to {111} planes. They can move only by diffusion climb processes while Shockley partial can glide since they are lying in {111} planes. The Shockley partial dislocation glide apart because they repel each other due to their parallel Burgers vectors. This gives rise to a stacking fault (SF) (see subsection 2.4.3) in between the partials [39, 47] as illustrated in figure 2.13 for two Shockley partials enclosing a stacking fault. Frank partials enclose SFs that arise due to the disorder in the

lattice plane stacking as described in subsection 2.4.3, [39].

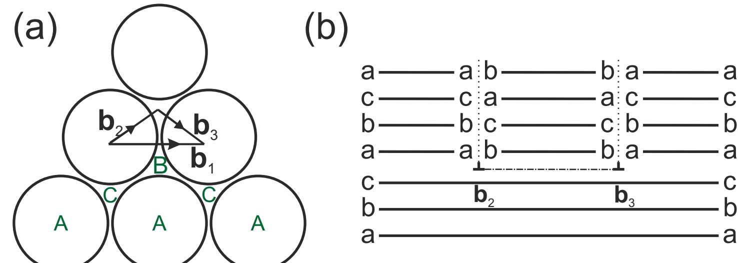

Figure 2.13: (a) Dissociation of perfect dislocation with Burgers vector $\mathbf{b}_1 = \frac{a}{2}[110]$ into two Shockley partial dislocations with Burgers vectors $\mathbf{b}_2 = \frac{a}{6}[211]$ and $\mathbf{b}_3 = \frac{a}{6}[121]$ according to $\mathbf{b}_1 \rightarrow \mathbf{b}_2 + \mathbf{b}_3$ in a fcc lattice. (b) The two Shockley partials (viewed in (110) projection and symbolized by a $\perp$ symbol) enclose a stacking fault. [39].

Structure of dislocations

A careful consideration concerning the core structure of these dislocations has first been conducted by Hornstra for the diamond lattice [48]. He described possible atomic arrangements for screw, edge, 60°, and partial dislocations with different numbers of free or "dangling" bonds. According to Hornstra, edge dislocations in the zinc blende or diamond lattice exist in two different atomic configurations. The first type of edge dislocations are composed of rings of five and seven atoms, where the extra half {111} lattice planes with one dangling end on shuffle planes planes which is why they were named shuffle set dislocation. The corresponding glide set dislocations consist of eight-atom rings with an inner atom with two dangling bonds in the glide plane. In the case of edge dislocation at the interface between polyatomic materials such as the investigated Ga(PSb)/GaP interface, there exist two different configurations of the respective shuffle and the glide set dislocations due to the polarity of GaP that can alter the termination of the additional half {111} lattice plane. 60° dislocations also end with one dangling bond at the extra half plane and can easily glide on {111} planes. Experiments have shown that the 60° dislocations occur always in glide set as well as shuffle set configuration [39]. The two different structures can be transformed into each other by stress dependent climb processes [50, 53].

Generation of misfit dislocations

The generation of misfit dislocations results from the lattice mismatch strain during growth. Their creation is facilitated by thermal energy provided by the growth temperature and by the occurrence of defects in the material. These defects can be free edges of monolayers or islands, vacancies, interstitials, and, predominately, grown-in threading dislocation (TD)

or TD full- or half-loops [29]. Since 60° dislocations can glide easily on the {111} planes, they are the main source for the formation of misfit dislocations at the interface [54]. They can be generated from grown-in threading dislocations that glide on {111} planes to the edges of a ML or island and form a misfit dislocation in between. This is illustrated in figure 2.14 A. However, the density of grown-in TD is generally too low the relieve the strain in this way. Additional TDs can be generated as half-loops on the surface that glide on the {111} planes to the interface to form misfit dislocations in between [38] as illustrated figure 2.14 B. In this way a network of misfit dislocations is formed at the interface between the substrate and the thereby relaxed layer.

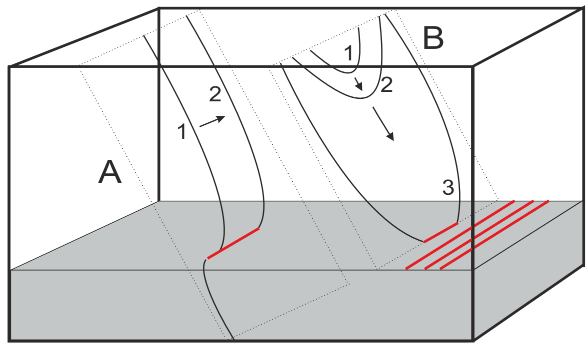

Figure 2.14: Model to describe the generation of misfit dislocations (red lines) at the interface. (A) shows the glide of threading dislocation (black line) forming misfit dislocations during this process. (B) illustrates the formation of dislocation half-loops at the surface that glide to the interface to form misfit dislocations is this way. Modified from [54] in [55].

As already described by Lomer (equation 2.19), the 60° dislocations can react to form a perfect edge dislocations if they lie within the same glide plane or, more specifically, if their Burgers vectors have opposite screw components. Burgers vectors with parallel screw component will lead to the formation of closely spaced 60° dislocation pairs [38, 56–58].

2.4.3 Planar defects

Planar defects extend over a long range in the crystal. They occur inevitable in any real crystal in form of surfaces. Due to the finite size of real crystals, the infinite translational symmetry is broken. For this reason, interfaces to all kinds of volume defects or crystallographic disorder are considered as planar defects.

Stacking faults

Stacking faults (SF) occur from a deviation from the stacking sequence and are most common in the closed-packed ccp and hcp crystal structures. If the stacking sequence is missing a crystallographic plane, for example ABCABABC in the ccp structure, the stacking fault will be an intrinsic stacking fault. In case of an additional lattice plane, for

example ABCABACABC in ccp, it is an extrinsic stacking fault. The investigated zinc blende structure in this study can also contain stacking faults, however, the disordered {111} lattice plane consists of a double atomic plane with a group III and group V atom, respectively. Stacking faults have a certain formation enthalpy per unit area giving rise to a stacking-fault energy that depends on the material [59, 60] and provides strain relaxation. As described in before in section 2.4.2, stacking faults can arise due do the dissociation of a 60° dislocation into Shockley partials that repel each other due to their parallel Burgers vectors [61]. Another reason for the occurrence of the stacking disorder are point defects like interstitials and impurities [62] as well as too rapid growth rates [63, 64]. These grown-in stacking faults are enclosed by sessile Frank partial dislocations [65].

Grain and twin boundaries

Grain boundaries occur in polycrystalline materials that consist of a multitude of crystallites or grains. These grains have different orientations to each other and are separated by grain boundaries. The grain sizes can range from nanometers to millimeters. Second phase grains not only have grain boundaries due to different crystal orientations but also due to compositional changes. Twin boundaries are similar to grain boundaries as they also occur between regions of different crystal orientations, however, they can also occur in single crystals. Their formation is similar to stacking faults. The difference is a disorder of the stacking sequence over a long range. Due to their low energy interfaces they are generated easily during growth.

Domain boundaries

Domain boundaries occur between regions that have the same crystallographic orientation but have different domains of aligned electric dipoles (ferroelectric domains) or aligned magnetic moments (ferromagnetic domains) as well as different phases of lattice site occupation. This means, that the polarity in these anti-phase domains (APD) is reversed compared to the neighboring region. Since these antiphase boundaries (APB) are of importance for this study, they will be discussed further.

Antiphase domains

APB can arise during the growth of a polar material, such as GaAs [66], InP [67, 68] or GaP [69], on a non-polar, elemental semiconductor such as silicon. They are generated at mono-atomic steps because the polarity will change at the step if there is a wetting of the first ML as demonstrated in figure 2.15. The antiphase boundaries are characterized by wrong bonds between two neighboring group III or group V atoms as indicated by the black dotted lines in 2.15. This means that the antiphase boundary is not charge neutral. Figure 2.15 shows that the direction of the APB is not set for one certain lattice

direction and will determine the charge of the antiphase boundary. Image (a) shows a charge neutral {110}-interface while (b) and (c) display group III-rich and group V-rich {111}-interfaces, respectively. However, in a real crystal, APBs are not limited to those three cases and can also run along other lattice planes. Previous work by Beyer [69] has shown that for GaP on exact Si (001), it is possible to grow APB that have an anisotropic shape viewed along the <110> directions. In $[\bar{1}10]$ projection, the APB are charge neutral {110}-interfaces as in 2.15 (a) while in [110] direction, they have kinks and lie on {112}- and {111}-planes. This means that these ABD are self-annihilating and do not reach the surface like APD with {110}-interfaces only.

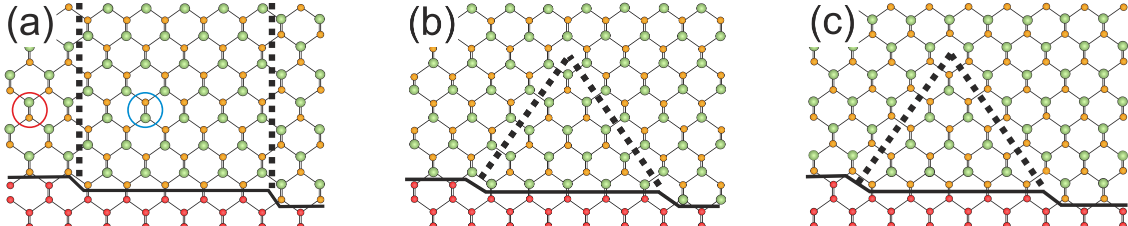

Figure 2.15: Simplified model of antiphase domains: (a) charge neutral {110}-interface, (b) group III-rich {111}-interface and (c) group V-rich {111}-interface. Si atoms are displayed in red, group III atoms in green and group V-atoms in orange. Modified from [69]

2.5 Strain

As described in the previous sections, strain plays a crucial role for epitaxial growth. It not only has an severe influence on the growth mode and crystal quality, strain can also effect the band gap structure of a material by changing the position of the bands and band off-sets as well as their curvature as described for example in [70–73]. In consequence, the electrical and optical properties of the materials will be changed as well.

For a continuous elastic material, strain is closely related to stress that occurs in reaction to external forces such as temperature or pressure or lattice mismatch during heteroepitaxy [34, 39, 74]. Strain is a measure for the deformation, while stress is a measure of the internal force per unit cross sectional area of the material. The forces acting on a cubic crystal are either tangential τ_{ij} or normal σ_i to the surfaces $i = x,y,z$ for all three directions. The resulting stress on the crystal can then be described by a second rank tensor σ_{ij} with nine components

$$\sigma = \begin{pmatrix} \sigma_x & \tau_{xy} & \tau_{xz} \\ \tau_{xy} & \sigma_y & \tau_{yz} \\ \tau_{xz} & \tau_{yz} & \sigma_z \end{pmatrix} , \tag{2.20}$$

where $\tau_{ij} = \tau_{ji}$ due to symmetry reasons. An elastic material will deform under stress. Infinitesimal stresses cause a linearly proportional strain that depends on the elastic stiffness of the material. This relationship between stress σ and strain ε is described by Hooke's law that assumes that the forces causing the stress are in direct proportion with the extension or compression of a material as long as the force does not exceed the elastic limit after which the deformation becomes irreversible. The elastic stiffness is a material dependent property that can be described by a rank four tensor $\underline{\underline{C}}$ with $3 \times 3 \times 3 \times 3 = 81$ entries so

$$\underline{\underline{\sigma}} = \underline{\underline{C\varepsilon}} \,. \tag{2.21}$$

The deformation of a material can be described by a displacement field $\mathbf{u}$ that defines the distortion from the ideal lattice by a second rank distortion tensor to

$$e_{ij} = \frac{\partial \mathbf{u}_i}{\partial x_j} \,, \quad \text{where } i,j = 1,2,3 \,. \tag{2.22}$$

The elastic strain tensor is then defined by the normal elastic strains $\varepsilon_{ii} = e_{ii}$ and shear elastic strains $\varepsilon_{ij} = (e_{ij} + e_{ji})$, where $i,j = x,y,z$ for cubic crystals, to

$$\varepsilon = \begin{pmatrix} \varepsilon_{xx} & \varepsilon_{xy} & \varepsilon_{xz} \\ \varepsilon_{yx} & \varepsilon_{yy} & \varepsilon_{yz} \\ \varepsilon_{zx} & \varepsilon_{zy} & \varepsilon_{zz} \end{pmatrix} \,. \tag{2.23}$$

This definition is valid for layers grown on (001) orientation. For other orientations, equation 2.23 needs to be rotated to the appropriate direction.

The strain and stress tensor in equation 2.21 can be symmetrized. Since $\varepsilon_{ij} \neq \varepsilon_{ji}$, the non-diagonal entries are averaged by $\frac{1}{2}(e_{ij} + e_{ji})$ for each ε_{ij} and ε_{ji} so that only 6 variables are left for the stress and strain tensor and the stiffness tensor only has 36 element. In the Voigt notation [75], the symmetric matrices become vectors with 6 columns, where the indices are reduced to 1-6 instead of xx, yy, zz, yz, xz, xy. Due to the high symmetry in cubic crystals, the stiffness tensor has only three independent stiffness constants, c_{11}, c_{12}, and c_{44}. Equation 2.21 can then be written as

$$\begin{pmatrix} \sigma_1 \\ \sigma_2 \\ \sigma_3 \\ \sigma_4 \\ \sigma_5 \\ \sigma_6 \end{pmatrix} = \begin{pmatrix} c_{11} & c_{12} & c_{12} & 0 & 0 & 0 \\ c_{12} & c_{11} & c_{12} & 0 & 0 & 0 \\ c_{12} & c_{12} & c_{11} & 0 & 0 & 0 \\ 0 & 0 & 0 & c_{44} & 0 & 0 \\ 0 & 0 & 0 & 0 & c_{44} & 0 \\ 0 & 0 & 0 & 0 & 0 & c_{44} \end{pmatrix} \cdot \begin{pmatrix} \varepsilon_1 \\ \varepsilon_2 \\ \varepsilon_3 \\ \varepsilon_4 \\ \varepsilon_5 \\ \varepsilon_6 \end{pmatrix} \tag{2.24}$$

for a cubic crystal in (001) orientation. Moreover, a cubic crystal does not have any shear stress and the stress at the free surface z (the perpendicular growth direction) vanishes so $\sigma_3 = \sigma_4 = \sigma_5 = \sigma_6 = 0$. Under these conditions, the solution of this linear system of equations in 2.24 then is

$$\varepsilon_1 = \varepsilon_2 \tag{2.25}$$

$$\varepsilon_3 = -2\frac{c_{12}}{c_{11}}\varepsilon_1 \tag{2.26}$$

$$\varepsilon_4 = \varepsilon_5 = \varepsilon_6 = 0\,. \tag{2.27}$$

Equations 2.25-2.27 show that the strain in the growth plane is equal for the two orthogonal in-plane directions 1 and 2. The strain ε_3 in the perpendicular growth direction depends on the in-plane strain as a function of the material dependent stiffness constants c_{11} and c_{12}. Due to the linear relationship in Hook's law, the stiffness constants of compound materials can also be calculated by Vegards law, substituting the stiffness constants for the lattice constant in equation 2.16. In the following, the in-plane component will be denoted with $\|$ sign and the component in growth direction with a $\perp$ sign. The parallel component is the mean value of the the two in-plane components. For the in-plane strain, this means $\varepsilon_\| = \frac{\varepsilon_1+\varepsilon_2}{2}$.

During pseudomorphic growth, the in-plane lattice spacing $d_\|$ accommodates the natural lattice constant a_L to the lattice constant of the substrate a_S. This deformation introduces elastic strain in the layer that is defined as in-plane strain $\varepsilon_\|$ in a similar manner as the misfit in equation 2.15 to

$$\varepsilon_\| = \frac{\Delta a}{a_L} = \frac{a_L - a_S}{a_L} = 1 - \frac{a_S}{a_L}\,. \tag{2.28}$$

During metamorphic growth or when the pseudomorphic layer growth exceeds the critical thickness, plastic relaxation occurs due to the formation of misfit dislocations at the interface. The in-plane lattice spacing $d_\|$ starts to relax towards the natural layer constant. Depending on the degree of relaxation, the in-plane lattice spacing $d_\|$ takes a value between the lattice constant of the substrate a_S and the natural lattice constant of the un-strained layer a_L [34]. The plastic relaxation is then defined as

$$R = \frac{d_\| - a_S}{a_L - a_S} \times 100\%\,. \tag{2.29}$$

Additionally, the residual strain [76] can be defined with respect to the natural lattice constant as

$$\varepsilon_i^{res} = \frac{d_i - a_L}{a_L} \quad i = \perp, \| \quad . \tag{2.30}$$

Plastic strain ε_p is defined in the same way as elastic strain by the distortion tensor $e_{ij} = \frac{\partial \mathbf{u}_i}{\partial x_j}$ (equation 2.22). It can also be considered as the difference between the misfit and elastic strain

$$\varepsilon_p = mf - \varepsilon \, . \tag{2.31}$$

A completely relaxed layer with $R = 100\%$ only has misfit strain and no elastic strain since the in-plane lattice spacing is relaxed to the natural layer constant.

For partially relaxed layers, with $0\% < R < 100\%$, the lattice spacings d_i are tetragonal distorted in dependence of equation 2.26. By substituting $\varepsilon_{\parallel}^{res} = \frac{d_{\parallel} - a_L}{a_L}$ and $\varepsilon_{\perp}^{res} = \frac{d_{\perp} - a_L}{a_L}$ in equation 2.26 [76], the layer constant a_L can be determined to

$$a_L = \frac{c_{11}}{c_{11} + 2c_{12}} d_{\perp} + \frac{2c_{12}}{c_{11} + 2c_{12}} d_{\parallel} = \frac{c_{11}}{c_{11} + 2c_{12}} (d_{\perp} - d_{\parallel}) + d_{\parallel} \, . \tag{2.32}$$

This equation can be solved for known lattice spacings of compound materials if Vegard's law is considered for a_L and the stiffness constants c_{11} and c_{12}.

2.6 Fundamentals of transmission electron microscopy

Transmission electron microscopy is a very versatile usable instrument to investigate the sample structure, crystallography, chemical composition, strain or defects of materials on the micrometer to atomic scale, depending on the chosen operation technique [77, 78]. The interaction of the highly accelerated electrons with the analyzed material can be described by regarding the electron either as a wave to explain diffraction and imaging in low and high resolution in conventional TEM or as a particle to interpret the high-angle annular dark-field (HAADF) images in STEM as well as analytical methods such as energy dispersive X-ray spectroscopy. Due to the high acceleration voltage and low beam current, the electron beam interaction with the specimen can be considered as one electron at a time and is therefore often described as a self interference of the incoming electron. The incident electron beam is scattered by the thin specimen either elastically without energy loss or inelastically with some measurable energy loss. The second distinction made for the scattering process is whether it is coherent or incoherent, so whether the phase relationship between the incident and scattered wave are preserved or not. The imaging in conventional TEM can be explained by coherent, elastic scattering into low angles, because the incident electrons interact with the screened atom cores of the specimen. The scattering in HAADF is considered as an almost elastic, incoherent scattering, where the incident electrons pass close to the nucleus and are deflected into high angles, which is similar to Rutherford scattering.

2.6.1 Electron scattering

The scattering intensity is defined by the scattering cross section σ, which depends on the effective target area of the scatterer and the probability of interaction. However, the incident electron is much smaller than the scattering atom so that the electron interacts with only a small area of the total cross section and is scattered into a particular increment in the solid angle Ω in this process. Therefore, the differential scattering cross section $\frac{d\sigma}{d\Omega}$ has to be considered. The scattering intensity is defined by the square of the absolute scattering factor $f(\mathbf{k}, \mathbf{k}_0)$, that depends on the incident wavevector $\mathbf{k_0}$ and outgoing wavevector $\mathbf{k}$, so that

$$\frac{d\sigma}{d\Omega} = |f(\mathbf{k}, \mathbf{k}_0)|^2 \,. \tag{2.33}$$

Rutherford investigated the scattering of α-particles from a thin gold foil [79] and hence concluded on the existence of nuclei. He also calculated the differential cross section between the nuclei and α-particles to:

$$\frac{d\sigma_R}{d\Omega} = \frac{e^4 Z^2}{16(4\pi\varepsilon_0 E_0)^2} \frac{1}{sin^4(\theta)} \,. \tag{2.34}$$

In case of an incident electron inside a scattering potential $V(\mathbf{r})$, the scattering factor can be calculated from the corresponding Schrödinger equation

$$-\frac{\hbar^2}{2m}\nabla^2\psi(\mathbf{r}) + V(\mathbf{r})\psi(\mathbf{r}) = E\psi(\mathbf{r}) \,. \tag{2.35}$$

The incoming electrons are treated as a plane wave $\Psi_{inc} = e^{2\pi i \mathbf{k_0 r}}$ that are scattered at the atom at position $\mathbf{r}'$. The plane wave will be the general solution to the Schrödinger equation 2.35, if $k_0^2 \equiv \frac{2mE}{\hbar^2}$. The scattered wave function is a special solution, so that $\Psi_{tot} = \Psi_{inc} + \Psi_{scatt}$. The scattered wave function can be obtained by transforming the differential Schrödinger equation to an integral equation using a Green's function $G(\mathbf{r}', \mathbf{r})$. The scattered wave is a spherical wave, which has its origin at the scattering atom $\mathbf{r}'$ as illustrated in figure 2.16.

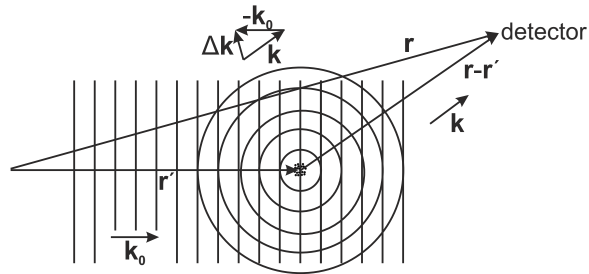

Figure 2.16: Position vectors and wavevectors for electron scattering, from [78].

$$\Psi_{scatt}(\mathbf{r}) = \frac{2m}{\hbar^2}\int V(\mathbf{r}')\Psi(\mathbf{r}')G(\mathbf{r}',\mathbf{r})d^3\mathbf{r}' = \frac{2m}{\hbar^2}\int V(\mathbf{r}')\Psi(\mathbf{r}')\frac{-1}{4\pi}\frac{e^{2\pi ik|\mathbf{r}-\mathbf{r}'|}}{|\mathbf{r}-\mathbf{r}'|}d^3\mathbf{r}' \quad (2.36)$$

Two approximations are made to solve this equation. The first Born approximation assumes that the incident plane wave is undamped and scattered only once so that it can be applied for $\Psi(\mathbf{r}')$ in equation 2.36. The second approximation takes the detector far from the scatterer so that plane waves can be expected to arrive at the detector, where $\mathbf{k}$ is aligned parallel to $(\mathbf{r}-\mathbf{r}')$ (see figure 2.16) and $\mathbf{r}' \ll \mathbf{r}$ so that $|\mathbf{r}-\mathbf{r}'| \approx |\mathbf{r}|$ in the denominator of $G(\mathbf{r}')$. Taking into account the definition $\Delta\mathbf{k} \equiv \mathbf{k_0} - \mathbf{k}$, the solution for the scattered wave can be approximated to

$$\begin{aligned}\Psi_{scatt}(\mathbf{r}) &\simeq -\frac{m}{2\pi\hbar^2}\int V(\mathbf{r}')e^{2\pi i\mathbf{k}_0\cdot\mathbf{r}'}\frac{e^{2\pi i\mathbf{k}\cdot(\mathbf{r}-\mathbf{r}')}}{|\mathbf{r}|}d^3\mathbf{r}' \\ &= -\frac{m}{2\pi\hbar^2}\frac{e^{2\pi i\mathbf{k}\cdot\mathbf{r}}}{|\mathbf{r}|}\int V(\mathbf{r}')e^{-2\pi i\Delta\mathbf{k}\cdot\mathbf{r}'}d^3\mathbf{r}'\,.\end{aligned} \quad (2.37)$$

The scattering factor is now defined as the Fourier transform of the scattering potential $V(\mathbf{r})$ that depends only on the difference $\Delta\mathbf{k}$ between the incident and outgoing wavevectors:

$$f(\Delta\mathbf{k}) \equiv -\frac{m}{2\pi\hbar^2}\int V(\mathbf{r}')e^{-2\pi i\Delta\mathbf{k}\cdot\mathbf{r}'}d^3\mathbf{r}'\,. \quad (2.38)$$

The scattering factor is a measure for the strength of the scattering that depends on the scattering atoms. If only the scattering potential of a single atom $V_{at}(\mathbf{r})$ is considered in equation 2.38, the scattering factor $f(\Delta\mathbf{k})$ will be defined as the atomic form factor $f_{el}(\Delta\mathbf{k})$.The atomic form factors can be calculated by using the analytical expressions for small values of $\Delta\mathbf{k}$ from Doyle and Turner [80] that are valid up to 20 nm^{-1}. Weickenmeier and Kohl [81] proposed an empirical analytical expression for larger values of $\Delta\mathbf{k}$.

With the definition of the scattering potential, the scattered part of the wave can be written as a spherical wave that depends on the position $\mathbf{r}$ and the difference of the incoming out scattered wavevectors $\Delta\mathbf{k}$

$$\Psi_{scatt}(\mathbf{r},\Delta\mathbf{k}) = f(\Delta\mathbf{k})\frac{e^{2\pi i\mathbf{k}\cdot\mathbf{r}}}{|\mathbf{r}|}\,. \quad (2.39)$$

The coherent, elastic scattering into low angles occurs due to the scattering of the incident electron at atoms of atomic number Z with a screened Coulomb potential $-\frac{Ze^2}{r}e^{-\mathbf{r}/r_0}$. The Coulomb potential depends on the effective Bohr radius $a_0 = \frac{h^2\varepsilon_0}{\pi me^2}$ with $r_0 = a_0Z^{-1/3}$, where m and e are the mass and elemental charge of the electron, h is the Planck constant and Z the atomic number of the scattering atom. The atomic form factor for the coherent,

elastic scattering can be described by the following equation 2.40 when inserting and evaluating the Coulomb potential into equation 2.38.

$$f_{el}(\Delta\mathbf{k}) = \frac{2Za_0}{4\pi^2(\Delta k)^2a_0^2 + Z^{2/3}} \tag{2.40}$$

However, the intensity of the coherent, elastic scattering depends not on a single atom but on the arrangement of the single atoms and will be discussed as electron diffraction in the next section.

When the incoming high energy electrons are scattered at the nuclei, the screening of the nuclei becomes less important and the electrons are scattered into high angles. Hereby, the difference in the wavevectors becomes large so $\Delta\mathbf{k}^2a_0^2 \gg Z^{2/3}$. Equation 2.40 can be simplified by dropping $Z^{2/3}$ and the differential cross section of equation 2.33 becomes the cross section of Rutherford scattering 2.34 when considering that the difference of the wavevectors $\Delta\mathbf{k}$ depends on the relativistic wavelength λ and scattering angle θ by $\Delta\mathbf{k} = \frac{2sin(\theta)}{\lambda}$ (this will be evaluated in equation 2.51) and the energy $E_0 = \frac{p^2}{2m}$ depends on the wavelength by $\lambda = \frac{h}{p}$ according to de Borglie so that

$$\frac{d\sigma}{d\Omega} = |f_{el}(\Delta\mathbf{k})|^2 = \frac{4Z^2}{(4\pi)^2a_0^2(\Delta k)^4} = \frac{Z^2\lambda^4}{64\pi^4a_0^2}\frac{1}{sin^4(\theta)} = \frac{e^4Z^2}{16(4\pi\varepsilon_0E_0)^2}\frac{1}{sin^4(\theta)}\ . \tag{2.41}$$

However, the screening of the nuclei cannot be omitted completely and is considered by the screening parameter $\theta_0 = \frac{0.117Z^{1/3}}{E_0^{1/2}}$, so that the differential cross-section for the electron scattering at the partly screened nuclei becomes

$$\frac{d\sigma}{d\Omega} = \frac{Z^2\lambda^4}{64\pi^4a_0^2}\frac{1}{[sin^2(\theta) + \theta_0^2]^2}\ . \tag{2.42}$$

2.6.2 Electron diffraction

Electron diffraction occurs due to the elastic coherent scattering of the incoming electrons on the periodically arranged atoms of the crystal and can only be explained by considering the wave nature of the electrons and including more than one scatterer because the interference and phase relationship between the scattered waves from each atom in the crystal have to be taken into account. The elastic coherent scattered wave for one scattering center has been calculated in equation 2.37 using the first Born approximation, which is equivalent to the "kinematical diffraction theory" that also assumes only a single scattering event for each electron. In order to include the superposition of the scattered spherical waves from each atom in the crystal, equation 2.37 has to be modified by choosing the scattering potential $V(\mathbf{r}')$ in dependence of the atom positions which are located at $\mathbf{R_j}$ as illustrated in figure 2.17 (a).

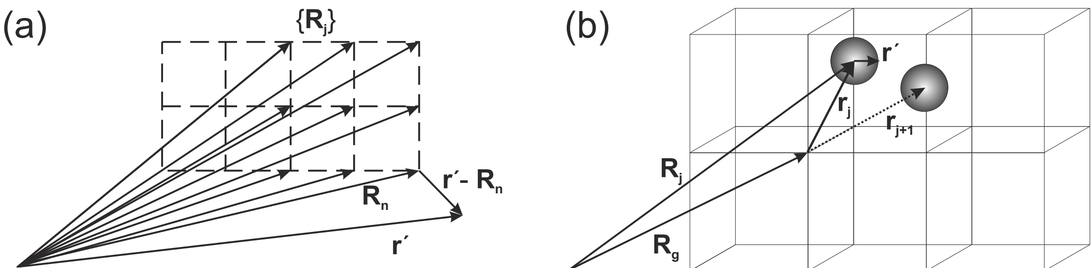

Figure 2.17: (a) The atom positions are at fixed coordinates, $\{\mathbf{R}_j\}$, while the independent vector $\mathbf{r}'$ ranges over all space. The vector $\mathbf{r}' - \mathbf{R}_n$ is the distance between $\mathbf{r}'$ and the nth atom, from[78]. (b) The positions of the centers of atoms in dependence on the translation vector $\mathbf{R_g}$ and the positions $\mathbf{r}_j$ in the unit cell using $\mathbf{R}_j = \mathbf{R_g} + \mathbf{r}_j$, from [69]

$$V(\mathbf{r}') = \sum_{\mathbf{R}_j} V_{at}(\mathbf{r}' - \mathbf{R}_j) \tag{2.43}$$

With the scattering potential of equation 2.43, the scattered wave will result in the following equation 2.44 if defining a new coordinate $\mathbf{r} \equiv \mathbf{r}' - \mathbf{R_j}$.

$$\begin{aligned} \Psi_{scatt}(\mathbf{r}, \Delta\mathbf{k}) &= \frac{-m}{2\pi\hbar^2} \frac{e^{2\pi i \mathbf{k}\cdot\mathbf{r}}}{|\mathbf{r}|} \int \sum_{\mathbf{R}_j} V_{at}(\mathbf{r}' - \mathbf{R}_j) e^{-2\pi i \Delta\mathbf{k}\cdot\mathbf{r}'} d^3\mathbf{r}' \\ &\overset{\mathbf{r}\equiv\mathbf{r}'-\mathbf{R}_j}{=} \frac{e^{2\pi i \mathbf{k}\mathbf{r}}}{|\mathbf{r}|} \sum_{\mathbf{R}_j} \int \frac{-m}{2\pi\hbar^2} V_{at,\mathbf{R}_j}(\mathbf{r}) e^{-2\pi i \Delta\mathbf{k}\cdot(\mathbf{r}+\mathbf{R}_j)} d^3\mathbf{r} \end{aligned} \tag{2.44}$$

The integration is independent from $e^{-2\pi i \Delta\mathbf{k}\cdot\mathbf{R}_j}$ so that the integral corresponds to the definition of the atomic form factor f_{el} in equation 2.38 using the atomic potential $V_{at,\mathbf{R_j}}$ at the positions $\mathbf{R}_j$. In the following, only the angular dependence of $\Psi_{scatt}(\mathbf{r}, \Delta\mathbf{k})$ that defines the direction of scattering will be considered and the amplitude in dependence of the distance $\mathbf{r}$ will be dropped so that

$$\Psi_{scatt}(\Delta\mathbf{k}) = \sum_{\mathbf{R}_j} f_{el}(\mathbf{R}_j) e^{-2\pi i \Delta\mathbf{k}\cdot\mathbf{R}_j} \,. \tag{2.45}$$

Due to the periodicity of the crystal, the atom positions $\mathbf{R}_j$ are defined by the sum of the translation vector $\mathbf{R_g}$ to each unit cell and the vectors $\mathbf{r}_j$ to the atom basis within each unit cell so that $\mathbf{R}_j = \mathbf{R_g} + \mathbf{r}_j$ as illustrated in figure 2.17 (b). When inserting these new crystal coordinates into equation 2.45, it has to be considered that $f_{el}(\mathbf{R}_j)$ is independent from the translation $\mathbf{R_g}$ since the atom basis is the same for all unit cells so that $f_{el}(\mathbf{R}_j) = f_{el}(\mathbf{r_j})$ and

$$\Psi_{scatt}(\Delta\mathbf{k}) = \sum_{\mathbf{R_g}}^{lattice} e^{-2\pi i \Delta\mathbf{k}\cdot\mathbf{R_g}} \sum_{\mathbf{r}_j}^{basis} f_{el}(\mathbf{r}_j) e^{-2\pi i \Delta\mathbf{k}\cdot\mathbf{r}_j} \equiv \mathcal{S}(\Delta\mathbf{k})\mathcal{F}(\Delta\mathbf{k}) \,. \tag{2.46}$$

The two independent sums have been defined to the structure factor $\mathcal{F}$ and the shape factor $\mathcal{S}$. The structure factor sums over all atoms within the unit cell and can be considered as the Fourier transform of the atomic form factor distribution $f_{el}(\mathbf{r}_j)$

$$\mathcal{F}(\Delta\mathbf{k}) \equiv \sum_{\mathbf{r}_j}^{unitcell} f_{el}(\mathbf{r}_j) e^{-2\pi i \Delta\mathbf{k}\cdot\mathbf{r}_j} \tag{2.47}$$

The shape factor $\mathcal{S}$ depends on the size of the crystal since it sums over all lattice sites in the Bravais lattice

$$\mathcal{S}(\Delta\mathbf{k}) \equiv \sum_{\mathbf{R_g}}^{lattice} e^{-2\pi i \Delta\mathbf{k}\cdot\mathbf{R_g}} . \tag{2.48}$$

For an infinite perfect crystal, the shape factor correlates to a set of delta function in all three spatial directions so that lattice planes are represented as points in reciprocal space. However, a TEM sample is much thinner along the beam direction so that the shape factor causes an elongation of reciprocal lattice points to rods, referred to as relrods (REciprocal Lattice RODS), along the thin viewing direction.

The intensity of the scattered wave is defined as the square of the absolute value of $\Psi_{scatt}(\Delta\mathbf{k})$ so that:

$$I = |\Psi_{scatt}(\Delta\mathbf{k})|^2 = |\mathcal{S}(\Delta\mathbf{k})|^2 |\mathcal{F}(\Delta\mathbf{k})|^2 . \tag{2.49}$$

Equation 2.45 has shown that Ψ_{scatt} depends on the difference between the incident and scattered wavevectors. The scattering is elastic, which means that the absolute values of $\mathbf{k}_0$ and $\mathbf{k}$ are preserved, namely $\frac{1}{\lambda}$, and the incoming diffraction angle θ is equal to the scattering angle as illustrated in 2.18 (a). Electron diffraction will occur due to constructive interference of the scattered waves from a set of lattice planes (hkl) with a distance d_{hkl}, if the path difference Δl between the diffracted waves is equal to a multiple of the wavelength, $\Delta l = n\lambda$. This condition is commonly known as Bragg's law and is illustrated in figure 2.18 (b).

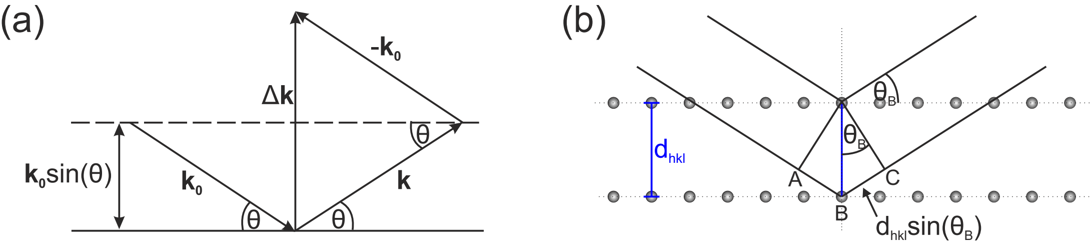

Figure 2.18: (a) Relationship between $\Delta\mathbf{k}$ and θ for elastic scattering, modified from [78]. (b) Bragg scattering occurs at constructive interfence of the scattered wave, i.e. if the path difference $\Delta l = \bar{AB} + \bar{BC} = 2d_{hkl}sin(\theta)$ is equal to a multiple of the wavelength $n\lambda$.

The figure shows that the path difference is $\Delta l = \overline{AB} + \overline{BC} = d_{hkl} sin(\theta) + d_{hkl} sin(\theta)$. The angle for constructive interference is referred to as Bragg angle θ_B so that Bragg's law can be written as

$$n\lambda = 2d_{hkl} sin(\theta_B) \; . \tag{2.50}$$

Bragg's law only depends on the distance between the planes and is independent from the distribution of the atoms on these planes. Considering the geometry of the triangle $\mathbf{k}_0$, $\mathbf{k}$ and $\Delta\mathbf{k}$ in 2.18 (a), an expression for $|\Delta\mathbf{k}|$ can be derived

$$sin(\theta) = \frac{|\Delta\mathbf{k}|/2}{|\mathbf{k}|} \Rightarrow \Delta\mathbf{k} = 2|\mathbf{k}| sin(\theta) \xrightarrow{|\mathbf{k}|=\frac{1}{\lambda}} \Delta\mathbf{k} = \frac{2sin(\theta)}{\lambda} \tag{2.51}$$

Diffraction will occur if the scattering angle is equal to the Bragg angle so that the magnitude of $|\Delta\mathbf{k}|$ can be assigned to a special value, $|\Delta\mathbf{k}_B| = \frac{2sin(\theta_B)}{\lambda}$, which will become Bragg's law if $|\Delta\mathbf{k}_B|$ is equal to the reciprocal lattice plane distance

$$|\Delta\mathbf{k}_B| = \frac{1}{d_{hkl}} \; . \tag{2.52}$$

However, this corresponds to the definition of the reciprocal lattice vector in equation 2.9 so that it can be concluded that

$$\Delta\mathbf{k}_B = \mathbf{g} \; . \tag{2.53}$$

Equation 2.53 is known as the Laue condition that states that diffraction occurs when the difference between the incoming and scattered wavevector $\Delta\mathbf{k}$ is equal to a reciprocal lattice vector $\mathbf{g}$. The Laue condition is equivalent to Bragg's law and can be implemented geometrically by the Ewald construction that is displayed in figure 2.19.

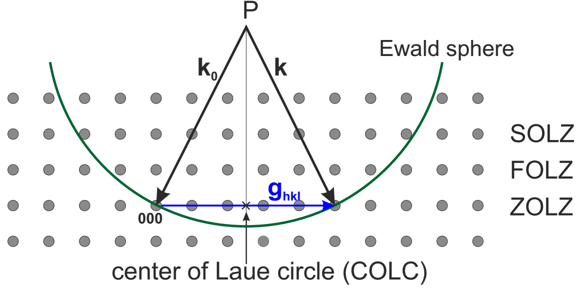

Figure 2.19: Illustration of the Ewald construction. The Laue condition is fulfilled when the Ewald sphere cuts a reciprocal lattice point. The incidence of $\mathbf{k}_0$ also defines the zeroth order Laue zone (ZOLZ). The first order and second order Laue zone (FOLZ, SOLZ) originate from the intersection of the Ewald sphere with higher-indexed reciprocal lattice points modified from [69].

The Ewald construction is a sphere drawn into reciprocal space with a radius of $|\mathbf{k}_0| = |\mathbf{k}| = \frac{1}{\lambda}$. The incident wavevector points to the origin (0 0 0) of the reciprocal space, whereat the origin of $\mathbf{k}_0$ defines the center of the Ewald sphere P, which is not necessarily a reciprocal lattice point. The Laue condition is fulfilled when the Ewald sphere intersects a reciprocal lattice point. The incidence of $\mathbf{k}_0$ also defines the zeroth order Laue zone (ZOLZ). The orthogonal projection of P onto the ZOLZ is defined as the center of Laue circle (COLC). Higher order Laue zones (HOLZ) originate from the intersection of the Ewald sphere with higher-indexed reciprocal lattice points. The higher orders are numbered by first, second, ... order (FOLZ, SOLZ, ...). The diffraction pattern, that can be observed in TEM, is a two dimensional projection of the Ewald sphere in beam direction defined by $\mathbf{k}_0$ on the viewing screen. If the COLC is the center of the diffraction pattern, the sample is in zone-axis orientation.

The reciprocal lattice points are in fact not points but relrods, as described by equation 2.48. This means that the Ewald sphere only needs to intersect the relrod in order to excite the reflection associated with the corresponding reciprocal lattice point. The Laue condition does not need to be fulfilled exactly, which can be accounted by introducing a deviation vector, the excitation error $\mathbf{s}$, to the Laue condition:

$$\varDelta \mathbf{k_B} = \mathbf{g} - \mathbf{s} \,. \tag{2.54}$$

Inserting the revised Laue condition into equation 2.46 for $\varPsi_{scatt}(\varDelta\mathbf{k})$ and considering equation 2.6 with $\mathbf{g} \cdot \mathbf{R_g}$ = integer then the shape factor becomes

$$\mathcal{S}(\mathbf{g} - \mathbf{s}) = \sum_{\mathbf{R_g}} e^{-2\pi i \cdot \text{integer}} e^{+2\pi i \mathbf{s} \cdot \mathbf{R_g}} = \sum_{\mathbf{R_g}} e^{+2\pi i \mathbf{s} \cdot \mathbf{R_g}} = \mathcal{S}(-\mathbf{s}) \,. \tag{2.55}$$

The structure factor can also be rewritten if one considers that $\mathbf{r}_j \cdot \mathbf{s}$ is small, so

$$\mathcal{F}(\mathbf{g} - \mathbf{s}) = \sum_{\mathbf{r}_j} f_{el}(\mathbf{r_j}) e^{-2\pi i (\mathbf{g} - \mathbf{s}) \cdot \mathbf{r}_j} \simeq \sum_{\mathbf{r}_j} f_{el}(\mathbf{r_j}) e^{-2\pi i \mathbf{g} \cdot \mathbf{r}_j} = \mathcal{F}(\mathbf{g}) \,. \tag{2.56}$$

This shows that the shape factor only depends on the excitation error $\mathbf{s}$ and not on the reciprocal lattice vector while the structure factor is independent of the excitation error and only depends on $\mathbf{g}$. The deviation parameter $\mathbf{s}$ is the minimum distance from the Ewald sphere to the reciprocal lattice point. Usually the specimen is tilted in such a way that the thinnest part of the crystal, and therefore the relrods as well as the excitation error, is parallel to the beam direction. The excitation error then becomes $\mathbf{s} = s\mathbf{a_z}$. Therefore,

the shape factor of equation 2.55 can be calculated to 2.57, when considering that the thickness t in in beam direction $\mathbf{a_z}$ contains N_Z unit cells:

$$\begin{aligned} \mathcal{S}(-\mathbf{s}) &= \sum_{n=1}^{N_z} e^{-2\pi i \mathbf{s}\cdot\mathbf{R_g}} = \sum_{n=1}^{N_z} e^{-2\pi i(0+0+sa_z n)} \\ &= \sum_{m=0}^{N_z-1} \left(e^{-2\pi i s a_z}\right)^n \overset{geom.series}{=} \frac{1-e^{-2\pi i s a_z N_z}}{1-e^{-2\pi i s a_z}} \, . \end{aligned} \tag{2.57}$$

The diffracted intensity from a perfect crystal with thickness t can now be calculated within the kinematic approximation from equation 2.49 to

$$I_{\mathbf{g}} = |\mathcal{F}(\mathbf{g})|^2 \mathcal{S}^* \mathcal{S} = |\mathcal{F}(\mathbf{g})|^2 \, \frac{sin^2(\pi s t)}{sin^2(\pi s a_z)} \tag{2.58}$$

using the Euler relations to evaluate $|\mathcal{S}(-\mathbf{s})|^2$.

The structure factor becomes important for lattices with more than one atom in the basis of the unit cell because $\mathcal{F}(\mathbf{g})$ determines the interference between the scattered waves. If the structure factor becomes zero for certain combinations of hkl, the corresponding reflections in the diffraction pattern can be forbidden. Since the investigated materials of this study crystallize in the diamond or zinc blende structure, their structure factors will be evaluated in the following. The diamond structure is the mono-atomic special case of the zinc blende structure so that only the structure factor of the latter has to be calculated. The zinc blende structure is a fcc lattice with a two atomic basis. The group III atom at position (0,0,0) has a atomic form factor of f_{III} and the group V atom with an atomic form factor of f_V is located at $(\frac{1}{4},\frac{1}{4},\frac{1}{4})$ so that equation 2.47 can be split into the structure factor of the fcc lattice and its basis:

$$\mathcal{F}(\mathbf{g}) = \mathcal{F}^{fcc}(\mathbf{g}) \cdot \mathcal{F}^{basis}(\mathbf{g}) \, . \tag{2.59}$$

The atom positions $\mathbf{r}_j$ of the fcc lattice are (0,0,0), $(\frac{1}{2}, 0, \frac{1}{2})$, $(\frac{1}{2},\frac{1}{2},0)$ and $(0, \frac{1}{2},\frac{1}{2})$ so that the fcc structure factor becomes

$$\begin{aligned} \mathcal{F}^{fcc}(\mathbf{g}) &= e^{-2\pi i(0\cdot h+0\cdot k+0\cdot l)} + e^{-\pi i(1\cdot h+1\cdot k+0\cdot l)} + e^{-\pi i(1\cdot h+0\cdot k+1\cdot l)} + e^{-\pi i(0\cdot h+1\cdot k+1\cdot l)} \\ &= 1 + e^{-\pi i(1\cdot h+1\cdot k)} + e^{-\pi i(1\cdot h+1\cdot l)} + e^{-\pi i(1\cdot k+1\cdot l)} \\ &= \begin{cases} 4 & \text{if } h,k,l \quad \text{all even or all odd} \\ 0 & \text{else} \end{cases} \end{aligned} \tag{2.60}$$

and the zinc blende structure factor can be calculated to:

$$\begin{aligned}\mathcal{F}(\mathbf{g}) &= 4\cdot\left(f_{III}e^{-2\pi i(0\cdot h+0\cdot k+0\cdot l)} + f_V e^{-2\pi i(\frac{h}{4}+\frac{k}{4}+\frac{l}{4})}\right)\\ &= 4\cdot\left(f_{III} + f_V e^{-\pi i(\frac{h}{2}+\frac{k}{2}+\frac{l}{2})}\right)\\ &= \begin{cases} 4(f_{III}+f_V) & \text{if} \quad h+k+l=4m\\ 4(f_{III}+if_V) & \text{if} \quad h+k+l=4m+1\\ 4(f_{III}-f_V) & \text{if} \quad h+k+l=4m+2\\ 4(f_{III}-if_V) & \text{if} \quad h+k+l=4m+3\\ 0 & \text{if } h,k,l \quad \text{even and odd}\end{cases}.\end{aligned} \tag{2.61}$$

The structure factor of Si can be obtained when setting $f_{III} = f_V = f_{Si}$ so that the case $h + k + l = 4m + 2$ is forbidden as well.

2.6.3 Magnetic lenses in TEM

Electron lenses in TEM are based on magnetic fields that can either be used to focus a beam of parallel electrons to a point in the focal plane of the lens or to recreate a point in an object to a point in an image. Therefore, magnetic lenses can be considered in analogy to convex lenses of a light microscope, where the beam path can be drawn by ray diagrams that are based on these lens properties. The focusing of the electrons in these magnetic round lenses is based on the Lorentz force that is defined by the cross product of the electron velocity and the magnetic field of the lenses to

$$\mathbf{F} = -e(\mathbf{v}\times\mathbf{B})\,. \tag{2.62}$$

These round lenses are water-cooled ferromagnetic soft-iron polepieces that are magnetized by surrounding copper coils. The strength of the magnetic fields and therefore the deflection and focus of the lenses can be changed by varying the current through the coils. However, these changes are nonlinear so that the magnetic fields of the solenoids of the lenses are difficult to calculate. For symmetry reasons, the magnetic fields of the solenoids are usually treated in cylindrical coordinates r, θ, z. $B_\theta = 0$ because a round lens is defined as a rotationally symmetric optical element. They cause a ray to deviate by an amount proportional to the distance from the optic axis, because the radial component B_r vanishes on the optical axis and increases toward the sides of the polepiece, so the more the electrons travel off axis the more strongly they are deflected. B_z on the other hand is largest at $z = 0$ and decreases with increasing $|z|$. A reflection of B_r across the plane $z = 0$ is antisymmetric leading to a helical beam path through the lenses as shown in figure 2.20. Altogether, this will lead to a decrease of focal length if the lens current increases because B_z as well as v_θ will increase in this case.

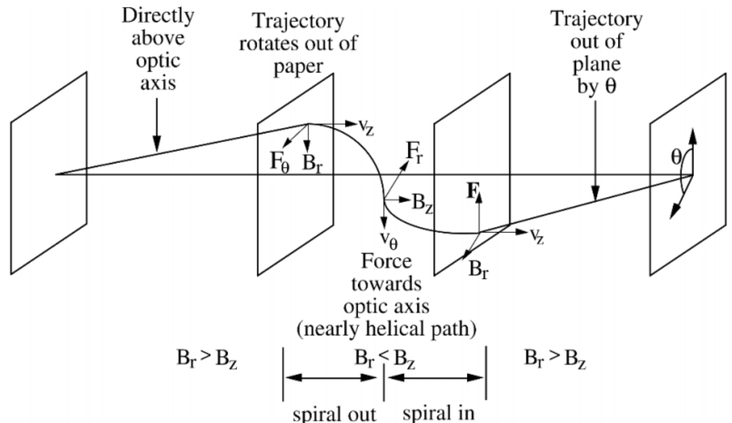

Figure 2.20: Trajectory of an electron through a magnetic lens. [78]

However, Scherzer already showed in 1936 [82] that round, rotationally symmetric lenses in a TEM will inevitably suffer from (spherical) lens aberrations if the lens produces a real image of the object, the fields of the lens system do not vary with time and there is no charge present on the electron-optical axis.

Lens aberrations can be divided into two groups. The coherent or geometric aberrations are caused by the geometry of the electromagnetic field of the lenses that distort the wavefront but retain the coherence. Incoherent aberrations also distort the wavefront but each wave in a different way. They occur due to mechanical and electrical instabilities as well as the energy spread of the source, which is known as chromatic aberration (C_C). Electrons with different kinetic energies have different velocities, which leads to different Lorentz forces and beam path through the magnetic lenses causing an energy dependent focus spread Δ at the optical axis. An energy filter can decrease the energy spread ΔE from the electron source with energy E_0 and therefore the influence of chromatic aberrations, since $\Delta = \frac{\Delta E}{E_0} C_C$ [83].

Figure 2.21 shows that the difference between the geometrically aberrated wavefront to the perfect, spherical, un-aberrated wavefront defines the wave aberration W in dependence on a reciprocal vector $\mathbf{q}$ with the angle θ to the optic axis and the azimuthal angle ϕ around the optic axis. The wave aberration is proportional to the ray aberration δ by

$$\delta \propto \nabla W \,. \tag{2.63}$$

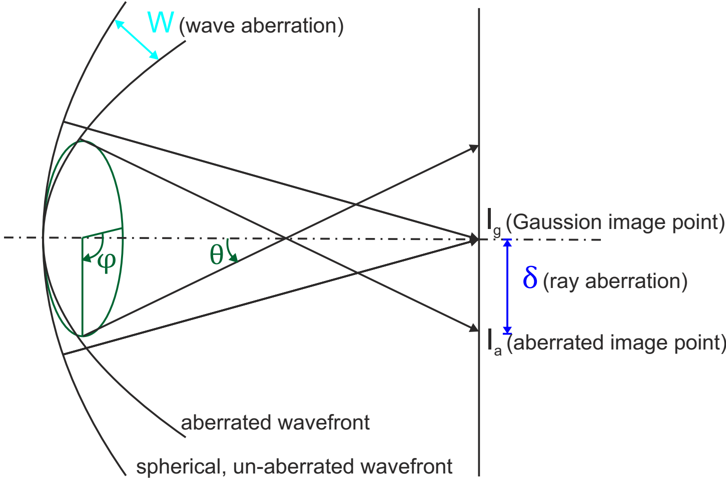

Figure 2.21: Wave W and ray aberration δ in dependence on the radial angle θ and azimuthal angle ϕ. The spherical, un-aberrated wavefront produces Gaussian image point that gets shifted by δ due to the aberrated wavefront. The wave aberration W is the difference between the two wavefronts and defines aberration function. [84]

The ray aberration describes the shift of the Gaussian image point of the un-aberrated wave to the aberrated image point due to the aberration. Additionally, the wave aberration is related to the phase difference $\chi(\mathbf{q})$ through the wavelength λ by

$$\chi(\mathbf{q}) = \frac{2\pi}{\lambda} W(\mathbf{q})\,. \tag{2.64}$$

This phase shift defines the aberration function $B(\mathbf{q}) = e^{i\chi(\mathbf{q})}$ and can be fitted as an polynomial expansion. There exist different expansions of the aberration function with varying notations for the expansion coefficients or rather aberration coefficients. The following two-dimensional expansion of χ in dependence of θ and ϕ is taken from [84], following the notation of Krivanek [85]. It is useful expression for aberrations that nearly vanish close to the optical axis, as it usually the case in the TEM.

$$\begin{aligned}\chi(\theta,\phi) = \frac{2\pi}{\lambda}&(\text{const} + \theta\,(C_{01a}cos(\phi) + C_{01b}sin(\phi))\\ &+ \frac{\theta^2}{2}\,(C_{10} + C_{12a}cos(2\phi) + C_{12b}sin(2\phi))\\ &+ \frac{\theta^3}{3}\,(C_{23a}cos(3\phi) + C_{23b}sin(3\phi) + C_{21a}cos(\phi) + C_{21b}sin(\phi))\\ &+ \frac{\theta^4}{4}\,(C_{30} + C_{34a}cos(4\phi) + C_{34b}sin(4\phi) + C_{32a}cos(2\phi) + C_{32b}sin(2\phi))\\ &+ ...)\end{aligned} \tag{2.65}$$

The expansion coefficients C_{NS} define the different geometrical aberrations, where N gives the radial order and S the azimuthal symmetry, for $S = N+1, N-1, N-3, ...$

and $S \geq 0$. Round aberrations have no azimuthal dependence, so there are no sine or cosine oscillations in ϕ and S is equal to 0. These round aberration include the two most important geometrical aberrations, defocus C_{10} and spherical aberration C_{30}, which are often notated as Δf and C_s. The value of C_s for magnetic lenses is always positive due to the definition of the Lorenz force. Non-round aberrations are represented by the projections C_{NSa} and C_{NSb} of the overall aberration C_{NS} along two orthogonal axes a and b, so that $C_{NS}^2 = C_{NSa}^2 + C_{NSa}^2$. The most important non-round aberrations are twofold (C_{12}) and threefold (C_{23}) astigmatism as well as coma (C_{21}). For a more complete list of aberrations see [84].

Spherical aberration introduces a spread of the focal point along the optical axis because rays with an increasing radial distance from the optic axis are focused more strongly than rays closer to the optical axis, for positive C_s. The minimal enlargement of the focal point is defined as "disc of least confusion". Astigmatism focuses rays with different azimuthal angles in different imaging planes. This introduces a elliptical distortion to the beam. Coma leads to the displacement of concentric circles along a radial line, so a round beam becomes distorted into a comet-shape.

As a consequence of the aberrations, a point (x,y) in the specimen will not be imaged as a point but as an extended region $g(x,y)$ in the image plane. This smearing of the point can be described mathematically by the point-spread function $h(\mathbf{r})$. Two adjoining points of the specimen will create overlapping regions in the image plane. Therefore, the specimen is described by the specimen transfer function $f(\mathbf{r})$, so

$$g(\mathbf{r}) = \int f(\mathbf{r}')h(\mathbf{r} - \mathbf{r}')d\mathbf{r}' = f(\mathbf{r}) \otimes h(\mathbf{r} - \mathbf{r}') \,. \tag{2.66}$$

These three contributing functions can always be expressed in reciprocal space using the corresponding Fourier transformations (FT). Equation 2.66 can then be written as

$$G(\mathbf{q}) = F(\mathbf{q})H(\mathbf{q}) \,, \tag{2.67}$$

where $\mathbf{q}$ is a reciprocal vector, or rather the spatial frequency for a particular direction. $G(\mathbf{q})$, $F(\mathbf{q})$ and $H(\mathbf{q})$ are the FT of $g(\mathbf{r})$, $f(\mathbf{r})$ and $h(\mathbf{r})$.

The point spread function $h(\mathbf{r})$ defines how information in real space is transferred from the specimen to the image, while $H(\mathbf{q})$ describes the information, or rather contrast transfer in reciprocal space [77]. It is therefore known as contrast transfer function CTF. Since the lens aberrations determine the information transfer, the aberration function $B(\mathbf{q}) = e^{i\chi(\mathbf{q})}$ influences the contrast transfer function. However, the image intensity is defined by $I = \Psi\Psi^*$. In consequence, only the the imaginary term of the aberration

function $B_{im}(\mathbf{q}) = 2sin(\chi(\mathbf{q}))$ contributes to the contrast transfer.

However, the geometrical lens aberrations are not the only contributors to the contrast transfer. Other factors are wave aberrations due to incoherent aberrations as well as the aperture. The Aperture function $A(\mathbf{q})$ describes the cutting of spatial frequencies above a certain value determined by the aperture size and semi-convergence angle. The incoherent wave aberrations are included as exponentially decaying envelope functions $E(\mathbf{q})$. These damping envelopes describe the limited temporal coherence that impose an information limit the microscope. The total envelope function $E(\mathbf{g})$ is the product of its components. $E_{vib}(\mathbf{q})$ describes the damping in dependence on the root mean square image displacement Δx introduced by vibrations. $E_{\Delta}(\mathbf{q})$ depends on the the focal spread Δ due to chromatic aberration [86, 87]. Altogether, these factors define the phase contrast transfer function (PCTF) to

$$PCTF(\mathbf{q}) = A(\mathbf{q})E(\mathbf{q})2sin(\chi(\mathbf{q}))\,. \tag{2.68}$$

The phase contrast transfer function depends on the spacial frequency $\mathbf{g}$. The highest spatial frequency with the same sign as all lower contributing frequencies defines the resolution of the microscope. This means, the first zero in $PCTF(\mathbf{g})$ defines the instrumental resolution limit. The information limit of the microscope is defined by the damping envelope functions that describe the limited spatial and temporal coherence.

Aberration correction in TEM

Spherical aberration is the geometrical aberration with the greatest influence on the resolution. If astigmatism is corrected, the third order approximation for the phase shift $\chi(\mathbf{q})$, which only takes into account the round aberrations, is $\chi(\mathbf{q}) = \pi\Delta f\lambda q^2 + \frac{1}{2}\pi C_s\lambda^3 q^4$. In this case, Scherzer [88] suggested to balance the defocus against the spherical aberration in order to achieve an optimal resolution. The defocus depends on the (positve) sperical aberration C_S and became known as the Scherzer defocus Δf_{Sch}

$$\Delta f_{Sch} = -\sqrt{\frac{4}{3}C_s\lambda}\,. \tag{2.69}$$

The correction of geometrical lens aberrations can be accomplished by using magnetic multipole lenses. These lenses and their magnetic fields are displayed in figure 2.22. Multipole lenses consist of an even number of alternating North and South poles that are arranged symmetrically around the optical axis. As illustrated in the figure, the magnetic fields of these multipole lenses are perpendicular to the electron beam so the Lorentz force will deflect the beam instead of rotating it, as it is the case for round lenses.

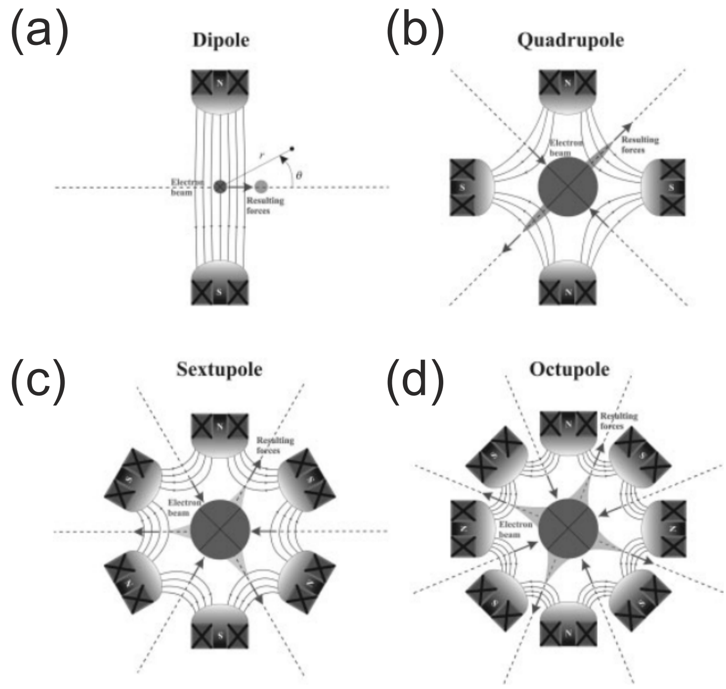

Figure 2.22: Schematic illustration of the four lowest order multipole lenses with their magnet fields effecting the round electron beam of a perfect lens. In (a) the electron beam travels from left to right and in (b)-(d) out of the paper plane. (a) The dipole lens shifts the beam traveling from left to right upwards. (b) The quadropole lens focuses the round beam into an line. (c) The sextupole lens produces a triangular distortion. (d) The octupole lens introduces a square distortion to the beam. [84]

The magnetic fields of the lenses consisting of $2N$ poles can be obtained by solving the Laplace's equations for the corresponding multipoles. The resulting magnetic scalar potential Φ with a radial (r) and azimuthal (θ) dependency defined in 2.22 (a) is

$$\Phi = r^N(p_N cos(N\theta) + q_N sin(N\theta)) \tag{2.70}$$

$$\mathbf{B} = \nabla\Phi \,. \tag{2.71}$$

In figure 2.22, the first order effect of the multipole lenses that distort the (dark gray) round beam are illustrated as light gray shapes. The dipole lens introduces a beam shift so it can be used easily to correct the radial distortion of coma. The quadrupole lens introduces a line focus that can correct the perpendicular line distortion due to astigmatism. Since this is quite simple to realize, it has already been used to correct the astigmatism in TEM for decades. The sextupole (or hexapole) lens produces a triangular distortion to the beam and the octupole lens introduces a square distortion to the beam.

However, the correction of spherical aberration is not as straightforward. There exist two different correctors, the quadrupole-octupole corrector as well as the hexapole

corrector. Since the (S)TEM investigations in this study have been performed with the latter, only the hexapole corrector will be explained in the following. In order to correct the positive C_s of the round lens, it is necessary to introduce a negative C_s by the corrector.

The hexapole corrector is based on the use of long instead of thin lenses. In this way, the lens does not affect a single plane but introduces a second-order effect that is one power higher in the radial direction on the magnetic strength. According to equations 2.70 and 2.71, the first-order effect of a hexapole lens has a r^2 and three-fold azimuthal dependency that leads to the triangular distortion. The second-order effect has a r^3 and an uniform azimuthal dependency, which is equal to an negative spherical aberration. The hexapol corrector now consist of tow long hexapole lenses that are arranged in such a way that the second hexapole cancels out the first-order effect of the first hexapol lens but leaves twice the second-order effect with an overall negative spherical aberration.

The first ideas of an aberration corrector go back to Scherzer [89] who suggested to use octopole lenses to correct spherical aberrations. However, it took nearly 50 years until the first correctors for TEM and STEM have been implemented successful by Haider et al. [90, 91] and Krivanek et al. [92], respectively. Earlier attempts to built correctors failed because the computers of that time were not fast and powerful enough to operate them effectively [93]. The aberrations need to be diagnosed directly and fast with implemented routines to ensure that the correction process converges. Additional challenges are introduced by the fact that the corrector consists of magnetic lenses that are, of course, not perfect themselves. They introduce lower-order parasitic aberrations that also need be corrected.

2.6.4 Contrast in (S)TEM

So far, this section has described the interaction of the accelerated electrons in the TEM with the specimen, considering electron scattering and diffraction, which each form different kinds of contrast that strongly depend on the imaging conditions that are defined by the electron beam, lenses and apertures of the microscope as well as the used detector, which will be described in section 3. Fundamentally, contrast C is defined by different intensities I_1 and I_2 in neighboring areas causing the appearance of a feature in the image:

$$C = \frac{I_1 - I_2}{I_1} = \frac{\Delta I}{I_1} \ . \tag{2.72}$$

Mass-thickness contrast

The intensity due to the Rutherford-like scattering in equation 2.42 gives rise to the mass-thickness contrast that increases with a higher atomic number Z and decreases with

sample thickness due to absorption or inelastic scattering in thicker specimen. However, for crystalline materials it is mixed with diffraction contrast.

Diffraction contrast

The diffraction intensity at the diffraction condition $\Delta\mathbf{k} = \mathbf{g} - \mathbf{s}$ has been given by equation 2.58. This equation shows that the diffraction intensity will oscillate with a variation of the specimen thickness t or the deviation parameter s. This gives rise to contrast reversals known as thickness fringes and bend contours. The diffraction contrast only depends on the amplitude of the wave function and is therefore an amplitude contrast. By selecting only the direct beam for imaging, using an aperture as described in 3.4.3, the arising contrast is named bright-field (BF) contrast. dark-field (DF) contrast is based on the selection of a certain diffraction spot using only electrons scattered in that specific direction for imaging. These two imaging conditions are complementary to each other in the two-beam condition that can be achieved by a certain beam tilt. The diffraction contrast is mixed with the mass-thickness contrast so for the BF images thinner and/or lower-mass areas will appear brighter than thicker and/or higher-mass areas. The opposite will be true for a DF image.

So far, only the kinematic diffraction with one scattering event has been considered for $I_{\mathbf{g}}$. This only holds true for thin samples, when $I_{\mathbf{g}} \ll I_0$. Hereby, I_0 is the intensity of the direct beam. This condition is usually fulfilled when the deviation parameter s is large and the diffraction remains weak throughout the sample. For thicker samples, the scattered wave can be described by the dynamical diffraction theory that uses the Bloch wave function [94] to calculate the diffracted intensity to

$$I_{\mathbf{g}} = \left(\frac{\lambda \mathcal{F}_{\mathbf{g}}}{\pi V_c}\right)^2 \frac{sin^2(\pi s_{eff} t)}{(s_{eff})^2} = \frac{sin^2(\pi s_{eff} t)}{(\xi_{\mathbf{g}} s_{eff})^2} \,, \tag{2.73}$$

where $\xi_{\mathbf{g}} = \frac{\pi V_c}{\lambda \mathcal{F}_{\mathbf{g}}}$ is defined as the extinction length and $s_{eff} = \sqrt{s^2 + \xi_{\mathbf{g}}^{-2}}$ as the effective deviation parameter. The kinematic diffraction theory is a special case of the dynamic diffraction, since s_{eff} equals s for large deviation parameter s. For the BF and DF imaging conditions, the diffraction contrast is treated as a two beam condition, where only the direct beam with an intensity I_0 and a diffracted beam with intensity $I_{\mathbf{g}}$ are considered for contrast formation. When the incident intensity is normalized to 1, the intensities are contingent upon each other by

$$I_{\mathbf{0}} = 1 - I_{\mathbf{g}} \,. \tag{2.74}$$

This means there is an periodic intensity transfer from the diffracted beam to the direct beam over the extinction length $\xi_{\mathbf{g}}$.

However, the scattered wave treated so far only considers a perfect crystal with deviating diffraction conditions. In order to include displacements of the atoms from their ideal positions due to lattice defects like dislocations, the scattered wave of equation 2.45 has to include an distortion vector $\delta\mathbf{r}_g$. Then the vector product of the exponential function of 2.45 becomes

$$\begin{aligned}\Delta\mathbf{k}\cdot\mathbf{R}_j &= (\mathbf{g}-\mathbf{s})\cdot(\mathbf{R_g}+\mathbf{r}_j+\delta\mathbf{r}_g) = \mathbf{g}\cdot\mathbf{R_g}+\mathbf{g}\cdot\mathbf{r}_j+\mathbf{g}\cdot\delta\mathbf{r}_g-\mathbf{s}\cdot\mathbf{R_g}-\mathbf{s}\cdot\mathbf{r}_j-\mathbf{s}\cdot\delta\mathbf{r}_g \\ &\simeq \text{integer}+\mathbf{g}\cdot\mathbf{r}_j+\mathbf{g}\cdot\delta\mathbf{r}_g-\mathbf{s}\cdot\mathbf{R_g}\end{aligned} \tag{2.75}$$

because $|\mathbf{s}| < |\mathbf{g}|$ and $\mathbf{s}\cdot\delta\mathbf{r}_g$ is very small. Inserting the result of 2.75 into 2.45 results in

$$\begin{aligned}\Psi_{scatt}(\Delta\mathbf{k}) &= \sum_{\mathbf{R_g}}^{lattice}\sum_{\mathbf{r}_j}^{basis} f_{el}(\mathbf{r}_j)e^{-2\pi i\Delta\mathbf{g}\cdot\mathbf{r}_j}e^{-2\pi i\Delta(\mathbf{g}\cdot\delta\mathbf{r}_g-\mathbf{s}\cdot\mathbf{R_g})} \\ &= \mathcal{F}(\Delta\mathbf{g})\sum_{\mathbf{R_g}} e^{-2\pi i\Delta(\mathbf{g}\cdot\delta\mathbf{r}_g-\mathbf{s}\cdot\mathbf{R_g})}\,.\end{aligned} \tag{2.76}$$

The diffracted intensity is influenced by lattice defects (see section 2.4) that tilt the crystal orientation locally and change the diffraction conditions in that region. Therefore, diffraction contrast is very useful for defect imaging.

Phase contrast

If more than one diffracted beam is used for image formation, this will give rise to intensity variations due to the interference of the scattered electron waves with different phases. The formation of fringes in the two-beam condition or low magnification images, moiré patterns as well as the contrast in high-resolution TEM (HRTEM) images can be explained by this phenomena. The intensity in phase contrast images is influenced by the thickness, orientation, and scattering factor of the sample as well as by the lens aberrations described by the phase contrast transfer function of equation 2.68.

Z-contrast

The modified Rutherford differential cross-section in equation 2.42 describes the scattering into high angles sufficiently well and can explain the Z-contrast in high-angle annular HAADF STEM imaging. STEM imaging is based on a coherent, convergent probe scanning over the sample specimen. The Rutherford-like scattered electrons are collected by an annular detector as explained in section 3.4.6. However, the Z^2-dependency in equation 2.42

does not agree with experimental observations quantitatively. Therefore, the scattering factors are usually fitted by simulations [81]. The image intensity in annular dark-field STEM is often regarded with a Z^c dependency, where $1 \leq c \leq 2$, depending on the electron screening of the nucleus and detector angles [95, 96] as well as the sample thickness [96].

For crystalline samples oriented in low-indexed zone-axis, the atoms are aligned in columns that focus the incident electron beam into a narrow peak where the electrons channell [97–99], because the probe of the convergent beam mainly excites columnar 1s-Bloch states of the atoms [100]. This prevents a beam broadening through the channelling of the electrons parallel to the atomic columns. Introducing a beam or sample tilt of a few $mrad$ will spread the beam until the channelling disappears and the specimen will act like an amorphous material. Dechannelling can also occur due to disorder or defects in the crystal.

The annular detector collects the scattered electrons over a large angular range defined by the inner and outer detector angles θ_{min} and θ_{max} determined by the detector size. Since the detector geometry is large compared to the scattering range, this gives rise to the incoherent nature of annular dark-field imaging [101, 102]. A large detector will average over the interference features produced by the coherently scattered electrons so any coherent phase information will get lost. This means that the transfer function only depends on the aperture and not on the interference between spatially separated positions of the sample. In consequence, neither sample thickness nor defocus will introduce contrast reversals like in conventional TEM [101, 103, 104].

The inner detector angle can be varied by changing the focus of the projector lenses as explained in section 3.4.6. By lowering θ_{min}, the detection becomes more sensitive to strain [105] as well as to lighter elements [106]. At low detector angles, the high-angle Rutherford scattering is superimposed by the effects of screened low-angle or Bragg scattering [96]. Strain due to lattice defects or static atomic displacements of atoms with different covalent radii than their neighbors introduce diffuse scattering [107] as well as dechannelling [99]. This gives rise to a strain contrast at lower scattering angles.

In addition to Rutherford scattering, thermal diffuse scattering (TDS) has to be taken into account because it causes a diffuse background in the diffraction pattern and is the main contributor to HAADF STEM contrast. TDS is caused by thermal vibrations in a crystal at finite temperatures. To model TDS, thermal vibrations can be described by the Einstein model that regards the atoms in the lattice as independent oscillators [108]. The mean square displacement of an atom from its equilibrium position defines the vibration amplitude $\bar{u}^2$. These vibrations modify the scattering cross section [107–109], which will be explained further in section 3.4.7 describing the simulation of HAADF images.

Quantum-mechanically, the vibration in a lattice define quasi-particles, the phonons. The electron-phonon scattering, or TDS, is a quasi-elastic process since the interaction between an electron and a phonon leads to the transfer of momentum while the energy transfer is negligible.

3 Experimental Methods

This chapter introduces the experimental methods that have been used to produce and characterize the samples of this study. The first section 3.1 explains the sample growth by metal organic vapor phase epitaxy (MOVPE). After the growth, all samples have been investigated by atomic force microscopy (AFM) in order to analyze their surfaces and by high-resolution x-ray diffraction (XRD) to analyze the composition. These two methods are presented in section 3.2 and 3.3. The last section of this chapter 3.4 deals with transmission electron microscopy (TEM) that is used to gain an understanding of the sample structure at an atomic scale. The applied TEM methods, which are presented in this section, included conventional techniques like dark-field (DF) and weak-beam (WB) imaging, convergent beam electron diffraction (CBED), and conventional high-resolution TEM (HRTEM) as well as high angle annular dark-field (HAADF) imaging in scanning transmission electron microscopy (STEM) in an aberration corrected microscope. In the case of GaSb on GaP, it is possible to compare the experimental HAADF images to simulations which are introduced in section 3.4.7. As explained in the previous chapter, strain plays a crucial role during the growth of Sb-based layers on GaP/Si. It is possible to calculate the theoretical strain from the model which is introduced in section 3.4.8. The strain in the obtained STEM images is investigated using well established methods such as the peak pairs (PP) algorithm as well as geometric phase analysis (GPA) explained in section 3.4.9.

3.1 Metal organic vapor phase epitaxy

The investigated samples of this study have been grown by metal organic vapor phase epitaxy. Hereby, a MOVPE machine from the company *Aixtron*, an *AIX-200* with a horizontal reactor, has been used. A schematic overview of the machine is illustrated in figure 3.1 (a).

The different metal organic precursors are each stored in stainless steel reservoirs, the bubblers, within the gas-mixing cabinet. The aggregate state of the precursors is usually liquid, apart from a few exceptions such as trimethylindium, which are solid. Each bubbler is connected by a stainless steel pipe to the hydrogen carrier gas supply. The hydrogen carrier gas supply line dips into the liquid precursor (which is why it is also named dip-

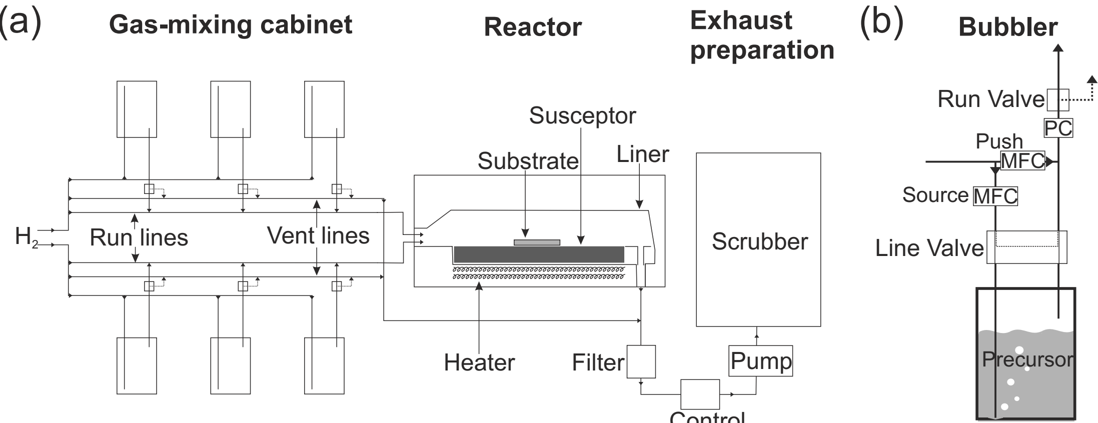

Figure 3.1: (a) Schematic illustration of a MOVPE reactor system with its gas-mixing cabinet, reactor and exhaust preparation. (b) The precursors are stored in bubblers in the gas-mixing cabinet. [110]

tube), produces bubbles (hence the name bubbler) and saturates the H_2 carrier gas with the precursor molecules as shown in figure 3.1 (b). The bubblers are stored in water bath of defined temperatures in order the regulate the vapor pressure p_S of the metal organic sources. The pressure p_C in the bubbler is regulated by the pressure controller (PC). The push-line can hereby dilute the saturated carrier gas subsequently. Different mass flow controller (MFC) monitor the gas flow of the carrier gas source Q_S as well as the total gas flow Q_{total} of the saturated carrier gas and keep it on a constant level for all bubblers before they are guided into one line to the reactor (run line) or bypassing the reactor (vent line). Afterwards, the exhaust gases are filtered by a scrubber that binds the partially toxic reaction productions of the growth before the exhaust is emitted to the free air.

It is important to note that there are separate lines for the group III and group V precursors. Otherwise the chemical reactions might take place within the lines instead of the reactor. Due to the vent line, the gas flow is kept constant during growth without opening or closing further valves if a certain gas is not needed.

The crystal growth is taking place in the reactor. The reactor is a quartz glass case, the liner, that contains a graphite pad, the suszeptor, onto which the substrate is placed. In order to obtain a homogeneous growth, the liner provides a laminar gas flow of the group III and group V gases over the substrate. Additionally, the suszeptor contains a rotary plate for the substrate. The suszeptor, and therefore the substrate, can be heated by infrared lamps so the growth temperate can be controlled. The growth temperate is an important growth parameter since the decomposition and incorporation of the different precursors is temperature dependent. The pressure in the reactor p_R is kept constant.

The crystal growth has been described in section 2.3. An important growth parameter has been the partial pressure p_P of the precursors, since they determine the growth rate as well as the composition of the grown material. The partial pressure for each precursor can be calculated by

$$p_P = \frac{Q_S}{Q_{total}} \cdot \frac{p_S}{p_C - p_S} \cdot p_R \,, \tag{3.1}$$

using the carrier gas flow Q_S, the vapor pressure p_S, and the pressure p_C in the respective bubbler as well as the total gas flow Q_{total} and pressure p_R in the reactor that are each controlled by the according MFC, PC and temperature of the water bath of the bubbler.

3.2 Atomic force microscopy

Atomic force microscopy AFM is a simple, non-destructive method to investigate the surface morphology of epitaxial grown samples. The method is based on scanning an tip, which is fixed on a flexible cantilever, over the sample surface and measuring the resulting short distance interactions, such as van-der-Waals and electrostatic forces. These interactions deflect the cantilever to a small amount. The deflection of the cantilever is detected by monitoring an laser beam being reflected from rear side of the cantilever onto a photo-diode array. All samples in this study have been investigated with a *Nanoscope IIIa Scanning Probe Microscope* of the company *Digital Instruments* using the non-contact tapping mode. In the tapping mode, the cantilever is stimulated to oscillate close to its resonance frequency. The interaction of the sample surface with the tip alters its resonance frequency changing the oscillation amplitude of the cantilever and the phase between stimulation and oscillation. During scanning the sample along xy direction by using a set of piezo crystals that move the sample below the cantilever, the oscillation amplitude is kept constant by adjusting the distance between the cantilever and the sample using a third set of piezo crystals changing the z-direction. The changes z-height are displayed to image the surface morphology with a vertical resolution on the atomic scale. The resulting lateral resolution of the images is a few nm due to the radius of curvature of the tip.

3.3 X-ray diffraction

High-resolution X-ray diffraction (HR-XRD) is, like AFM, an important nondestructive characterization method of epitaxial grown samples. The diffraction of X-rays at the periodic crystal can be used to measure the lattice plane spacings d_{hkl}. Since the wavelength of X-rays have the same length scale as d_{hkl}, Bragg's law (equation 2.50), which relates every lattice plane spacings to a specific scattering angle, can be applied. According to equation 2.9, the lattice plane spacing d_{hkl} is directly related to the lattice constant a for

cubic crystals.

The lattice constant of mixed crystals depends on the composition of the material (see figure 1.1) and can be calculated by Vegards law for ternary materials (equation 2.16). However, the lattice plane spacings are not only influenced by the composition but also the tetragonal distortions due to pseudomorphic growth during epitaxy (see section 2.5). In addition, plastic relaxation (equation 2.29) has to be taken into account. Pseudomorphically grown layers have per definition a relaxation $R = 0\%$, so it is possible to determine the lattice constant by measuring the angular distance between the substrate and the layer peak in rocking-curves obtained along the distorted lattice spacing in growth direction. Rocking-curves are one-dimensional projections of the reciprocal space. In the case of plastic relaxation ($R > 0\%$), the in-plane lattice spacing as well as the lattice spacing in growth direction are unknown, so and additional information has to be taken into account. They can be obtained by reciprocal space map (RSM). RSM are two-dimensional projections of the reciprocal space that can be used to determine the lattice constant as well as the sample tilt and the plastic relaxation of a layer.

Setup of the XRD

The HR-XRD measurements have been conducted with a *X'Pert Pro - MRD Diffractometer* from the company *Pananalytical*. A schematic illustration of the x-ray diffractometer setup is displayed in figure 3.2.

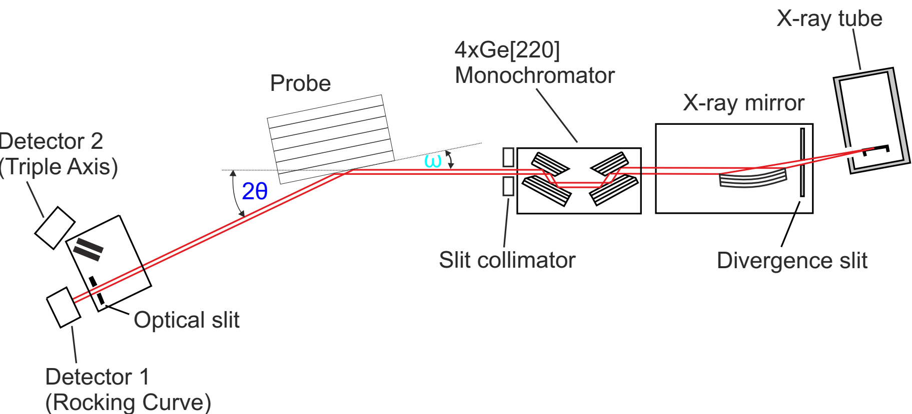

Figure 3.2: Schematic illustration of x-ray diffractometer setup. Modified from [76]

The x-rays are generated from the $K_{\alpha 1}$ emission line of a copper anode operated at 45 kV and 40 mA. The mirror, asymmetric 4-crystal Germanium monochomer and slits are used to focus the x-rays onto the sample. The sample can be aligned relative to the beam by changing the x, y, and z position of the sample as well as the angles Ψ, Φ, ω, and θ that are defined in figure 3.3. The diffracted x-rays are analyzed by one of the two proportional detectors that can be moved along the 2θ angle within the reciprocal space. The triple

axis detector is used to obtain RSM. It contains an analyzer crystal that only allows to pass scattered X-rays satisfying the Bragg condition of the analyzer. The alignment of the beam is particularly important for the measurement of a RSM to avoid projection errors that can occur if the incident and scattered beam are not in the same plane [111] or if the scattering plane is not normal to the sample rotation axis [112]. The technical alignment procedure has been conducted according to previously described instructions [55, 112, 113].

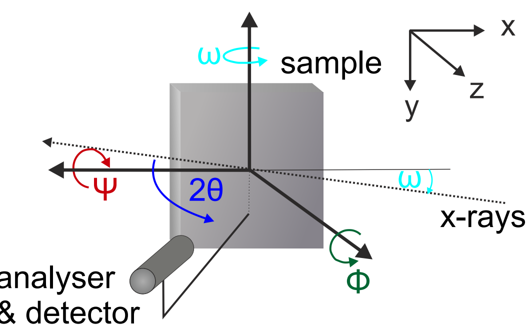

Figure 3.3: Schematic illustration of goniometer axes and relevant angles in XRD. Modified from [112]

3.3.1 Rocking-curve measurements

During the measurement of rocking-curves, the angle 2θ is varied twice as fast as the ω angle to stay in the Bragg condition of the chosen reflection. These ω-2θ-scans make a line through the origin of the reciprocal space as illustrated in figure 3.4. Due to energy and momentum conversion, it is only possible to measure the reflections within the radius q_{max} determined by the incoming wavevector: $q_{max} = 2|\mathbf{k}_0| = 2/\lambda$. The reflections within the gray areas of this semicircle are not accessible since they correspond to a transmission setup.

By measuring a rocking-curve of the symmetric 004 reflection, it is possible to determine the lattice spacing d_{004} along the (001) growth direction using Bragg's law. The symmetry of the setup and the measured reflection hold the condition $\omega = \theta$. For a pseudomorphically grown layer, the lattice mismatch of the epitaxial layer in growth direction $\frac{\Delta d^{\perp}}{d} = \frac{d_{\perp} - a_S}{a_S}$ can be calculated from the derivative of Bragg's law [111] using the angular difference between the substrate and layer peak $\Delta\theta = \theta_L - \theta_S$ as well as the Bragg angle of the substrate peak θ_S as illustrated in figure 3.5:

$$\frac{\Delta d_{hkl}}{\Delta\theta} = \frac{\lambda(-cos\theta)}{2sin^2\theta} = -d_{hkl}cot\theta \quad \Leftrightarrow \quad \frac{\Delta d_{hkl}}{d_{hkl}} = \frac{d_{\perp} - a_S}{a_S} = -\Delta\theta cot\theta_S \, . \tag{3.2}$$

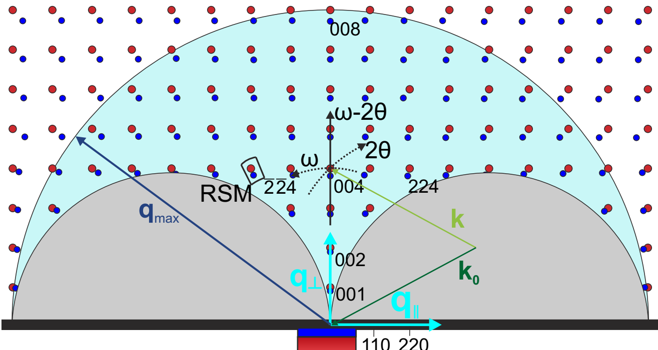

Figure 3.4: The scattering geometry in reciprocal space. The measuring directions for the line scans are indicated by the black arrows. The rocking curve corresponds to a $\omega - 2\theta$ scan. The black square marks a region used for reciprocal space mapping. The red and blue dots are the hkl reflections of the substrate and a layer peak, respectively. $\mathbf{k}_0$ and $\mathbf{k}$ are the incoming and scattered wavevectors. $q_\parallel$ and $q_\perp$ are the projections of the reciprocal lattice vector in-plane and in growth direction. [76]

The result can be used to calculate the relaxed layer constant according to equation 2.32. For a pseudomorphically grown layer, the in-plane lattice spacing $d_\parallel$ is adapted to the substrate layer constant a_S, so equation 2.32 simplifies to

$$a_L = \frac{c_{11}}{c_{11} + 2c_{12}}(d_\perp - a_S) + a_S \,. \tag{3.3}$$

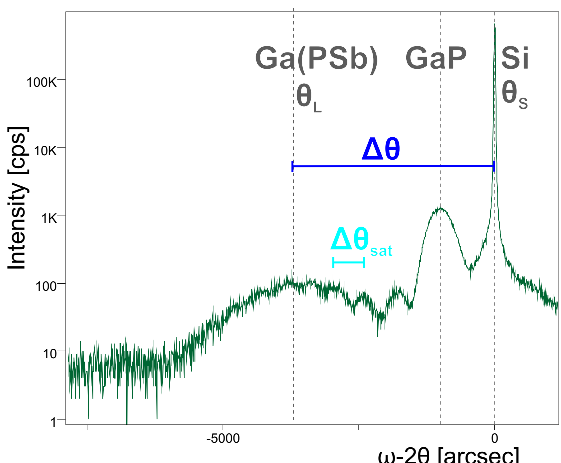

Figure 3.5: XRD rocking curve of the 004 reflection of the a thin, pseudomorphically grown Ga(PSb) layer on GaP/Si. The angular difference between the substrate and layer peak $\Delta\theta = \theta_L - \theta_S$ can be used to calculate the lattice spacing d_{004} and the relaxed layer constant a_L. The layer thickness t_{layer} can be obtained from the separation $\Delta\theta_{sat}$ between the satellite fringes.

The XRD-curve of the ω-2θ-scan not only contains the substrate peak as well as the layer peaks due to the constructive interference of the crystal lattice spacings but also thickness fringes or satellite peaks due to constructive interference at the epitaxial layers itself. The

thickness t_{layer} of the epitaxial layer is much larger than the lattice plane spacings which results in much smaller constructive interference angles. The layer thickness can then be calculated from Bragg's law using the Bragg angle of the substrate peak θ_S and the separation $\Delta\theta_{sat}$ between two neighboring maxima of the fringes shown in figure 3.5, so

$$d_{layer} = \frac{\lambda}{2\Delta\theta_{sat} cos\theta_S} \, . \tag{3.4}$$

3.3.2 Reciprocal space maps

As indicated in figure 3.4, reciprocal space maps show a detail of the reciprocal space around a certain reflection. They are obtained by measuring several individual rocking-curves with varying incidence angles ω. In order to determine the composition as well as the plastic relaxation or misfit of a relaxed or partially relaxed sample, not only the symmetric 004 reflection, which only contains information in growth direction, but also the asymmetric $\bar{2}\bar{2}4$ reflection, which gives additional information about the in-plane lattice spacing in (110) direction, has been detected. The measured angles ω and 2θ are rewritten into coordinates of the reciprocal lattice vector $\mathbf{q}$ according to the geometrical relationship illustrated in figure 3.6, so

$$\begin{aligned} q_{\|} &= \frac{1}{\lambda}(cos(\omega) - cos(\omega - 2\theta)) \\ q_{\perp} &= \frac{1}{\lambda}(sin(\omega) + sin(\omega - 2\theta)) \, . \end{aligned} \tag{3.5}$$

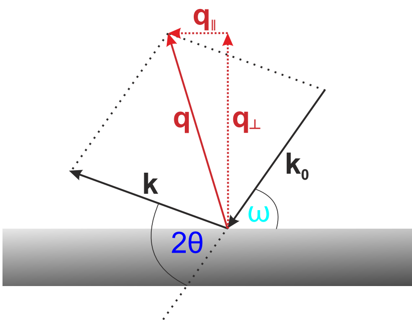

Figure 3.6: Schematic illustration of geometric relation between the incoming and scattered wavevectors $\mathbf{k}_0$ and $\mathbf{k}$, the angles ω and 2θ, and the projections $q_{\|}$ and $q_{\perp}$ of the reciprocal lattice vector $\mathbf{q}$ in-plane and in growth direction. Modified from [55].

Figure 3.7 (a) displays the substrate and layer peak positions of the 004 and $\bar{2}\bar{2}4$ reflections in dependence on the projections $q_{\|}$ and $q_{\perp}$ of the reciprocal lattice vector as defined in figure 3.6. A schematic illustration of the different layers with varying plastic relaxation is displayed in 3.7 (b)-(e). The layers are drawn in the same color as the corresponding layer peak reflections. The substrate and substrate peak is drawn in red. The substrate has a high quality and is therefore represented by a sharp, circular peak. For thin layers or a variation of the lattice spacing with layer depth, the layer peak is

broadened normal to the surface. A mosaic structure, a sample curvature or dislocations cause a peak broadening parallel to the surface.

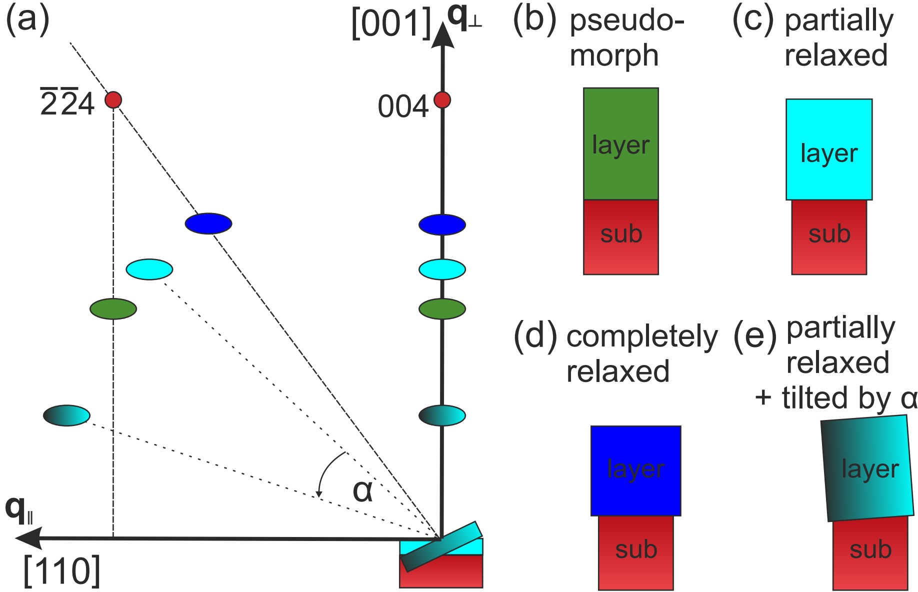

Figure 3.7: Schematic overview of the relationship between the XRD diffraction pattern and the epitaxial layer growth. The plastic relaxation and layer tilt change the positions of the $\bar{2}\bar{2}4$ peaks relative to the projections $q_{||}$ and $q_{\perp}$ of the reciprocal lattice vector $\mathbf{q}$ in-plane and in growth direction. The reflections and associated layers have the same colors, respectively. Modified from [55].

For a pseudomorphically grown layer with compressive strain, illustrated in image (b) as a green layer, the corresponding green $\bar{2}\bar{2}4$ and 004 layer peaks in (a) have the $q_{\perp}$ component is the same for both reflections. The $q_{||}$ component of the $\bar{2}\bar{2}4$ reflection is equal to the corresponding substrate peak. For a partially relaxed layer, depicted in image (c) as a turquoise layer, the in-plane lattice plane spacing increases while the lattice plane spacing decreases in growth direction. This leads to a diagonal displacement of the corresponding $\bar{2}\bar{2}4$ layer peak position in reciprocal space. For a completely relaxed layer shown in image (c) as a blue layer, the blue $\bar{2}\bar{2}4$ layer peak position in (a) is on the line through the origin and the substrate peak. A tilt α of the lattice planes rotates the $\bar{2}\bar{2}4$ peak position by α in reciprocal space as shown by the turquoise-black layer in image (e) and the corresponding peak in (a).

However, the tilt can be calculated from the symmetric 004 reflection, since in this case $q_{||}$ equals 0. The result can be used to correct the $q_{||}$ values of the asymmetric $\bar{2}\bar{2}4$ reflection. The $q_{\perp}$ values are the same for both reflections, which is why they are employed to calculate the lattice plane spacing in growth condition using again the symmetry relationship $\omega = 2\theta/2$ in equation 3.5. Through careful alignment, the absolute zero of the angle 2θ can be obtained and the projection error can be minimized. The lattice plane

spacings $d_{\|}$ and $d_{\perp}$ are calculated from the projected reciprocal lattice vector values $q_{\|}$ and $q_{\perp}$ taking into account that

$$d_{\|} = \frac{\left|\begin{pmatrix}1\\1\\0\end{pmatrix} \cdot \begin{pmatrix}\bar{2}\\\bar{2}\\4\end{pmatrix}\right|}{q_{\|}} = \frac{2\sqrt{2}}{q_{\|}}$$
$$d_{\perp} = \frac{\left|\begin{pmatrix}0\\0\\1\end{pmatrix} \cdot \begin{pmatrix}0\\0\\4\end{pmatrix}\right|}{q_{\perp}} = \frac{4}{q_{\perp}} \,. \tag{3.6}$$

These measured lattice plane spacing can be used to calculate the layer constant a_L using equation 2.32. In order to obtain the composition of the ternary layer material, Vegard's law should be included for the lattice constant as well as the elastic constants c_{11} and c_{12}. Additionally, the calculated layer constant a_L and the in-plane spacing allow the determination of the plastic relaxation R according to equation 2.29.

3.4 Transmission electron microscopy

The electron thinned samples have been investigated by TEM using different methods with two different instruments from the company *JEOL*. Dark-field and weak-beam imaging in combination with convergent beam electron diffraction have been conducted with a *JEOL JEM 3010* TEM that is operated at 300 kV and supplied with a LaB_6 crystal as electron gun. For high-resolution TEM and scanning transmission electron microscopy, a double-corrected *JEOL 2200 FS* (S)TEM with a field emission gun (FEG) operated at 200 kV has been used.

3.4.1 Sample preparation

In order to investigate any material by TEM, it has to be electron transparent. For crystalline materials, there are several methods for sample preparation. They are based on mechanical grinding or ion thinning. For this study, the conventional sample preparation, which combines both methods, has been used. The six most important steps are illustrated in figure 3.8.

At first (3.8 (a)), the silicon wafer with the epitaxial grown thin layers on top (indicated by the yellow color in the figure), are broken into 5 x 5 mm pieces by making a scratch at the corner of the wafer and applying some pressure. The cleavage planes of the silicon wafer run straight along the energetically favorable {111} planes, which have the least amount of dangling bonds. The direction of the edges should be <110> since this study is

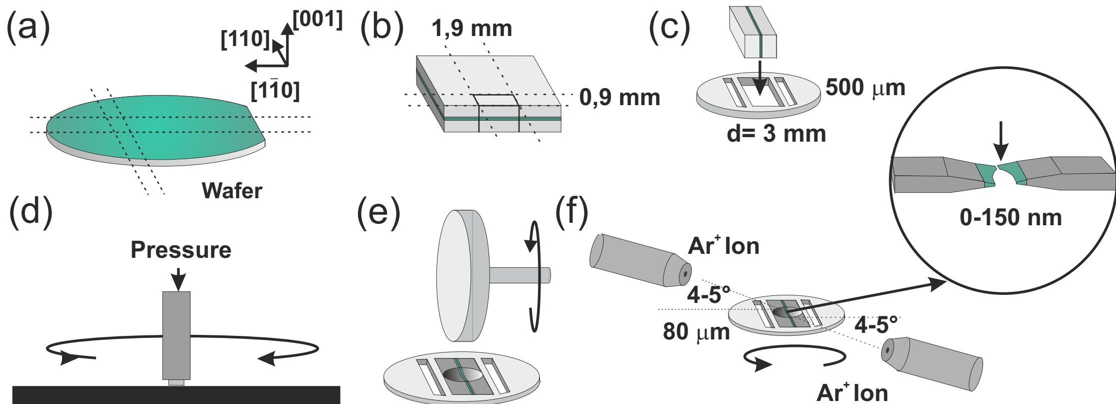

Figure 3.8: Schematic illustration of the conventional sample preparation by mechanical grinding and argon milling. Modified from [69].

interested in the dislocation lines that follow this direction. In the second step (3.8 (b)), two of the wafer pieces are glued together top on top using a heat sensitive glue and cut into 1.9 x 0.9 mm pieces by a diamond saw. These pieces are again glued into special titan rings of 3 mm diameter with a hole in the size of the cut pieces (3.8 (c)). In the fourth step, these rings are mechanically grounded and polished on both sides by gluing the sample ring on a steel sample holder and move them with some pressure over sand paper with different grain sizes from 15 μm to 3 μm until the sample is 80 μm thick and shiny (3.8 (d)). The center of the sample is even further thinned by grinding a dimple from both sides using a grain size of 3 μm to 250 nm in a dimple machine from the company *Fishione* (3.8 (e)). In the last step (3.8 (f)), the center of the sample is thinned by a focused argon ion beam of 5 kV under an angle of 5° - 3.5° until a hole becomes visible using a *precision ion polishing system* from the company *Gatan*. Finally, the sample is polished at lower kV to get rid of some of the amorphous material. Before the electron thin sample is investigated in TEM, organic rest groups on the surfaces are removed using high-frequency generated Argon-Oxygen plasma in the *plasmacleaner* of the company *Fishione*. For the preparation of a plan-view sample, steps (a)-(c)are substituted by sewing a round piece with a diameter of 3 mm out of the wafer. The following steps are practically the same with the only difference that only the rear side of the wafer is treated and the epitaxial grown layer is protected during the preparation. In the *precision ion polishing system*, the generation of the hole is conducted only at 4 - 3 kV and an angle of 4° since the metamorphic buffer layer in the plan-view sample has to withstand great stress when the substrate milled away.

3.4.2 Optics of a transmission electron microscope

This section introduces the setup of a transmission electron microscope using the schematic illustration of a TEM and double-corrected (S)TEM in figure 3.9 (a) and (b). The TEM can

be roughly divided into the illumination system with the electron gun and probe forming lenses, the sample that is located in the objective lens, and the imaging system. The beam path is not only determined by the magnetic lenses (section 2.6.3) but also by magnetic coils to shift or deflect the beam as well as apertures that allow only certain electrons to pass through a lens. Apertures are usually circular holes with different diameters in movable metal plates, so apertures with different sizes can be selected.

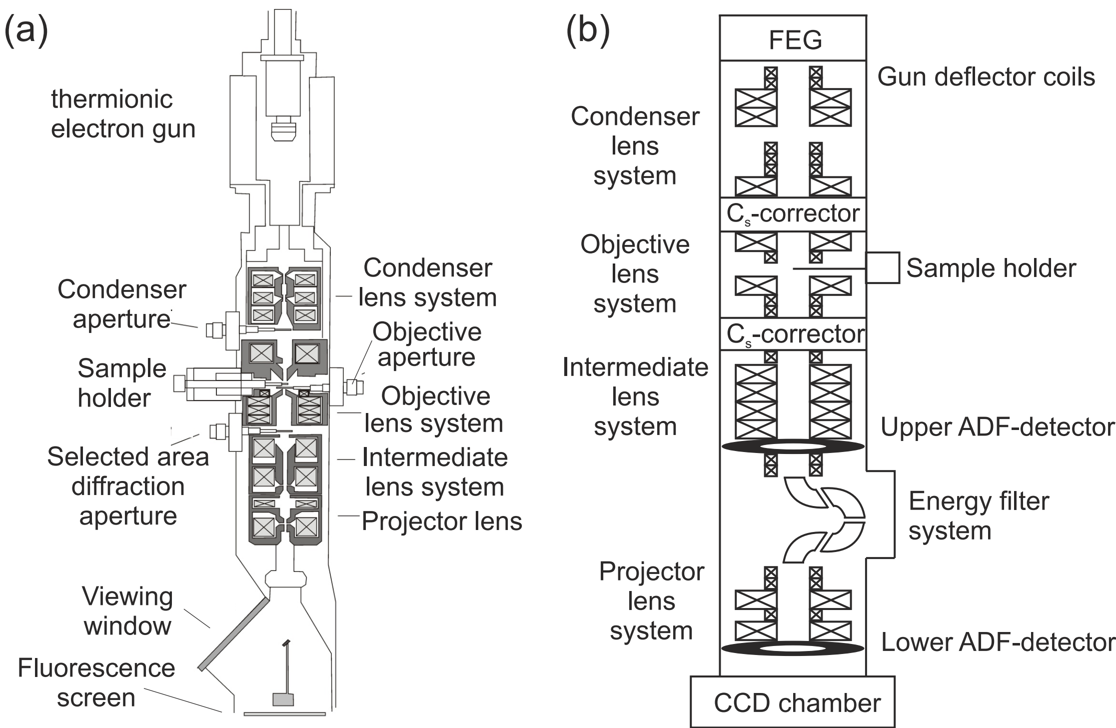

Figure 3.9: Schematic illustration of the (a) *JEOL JEM 3010* for conventional imaging methods and (b) double C_s-corrected *JEOL 2200 FS* (S)TEM for HRTEM and HAADF imaging. Modified from [114].

The electron gun generates the incident electrons either by thermionic emission, as in the case of the LaB_6 filament that is heated to (2000-2700) K, or by using the tunneling effect in a field emission gun (FEG). In a FEG, a strong electric field is applied to lower the potential barrier between filament tip and the vacuum to allow the tunneling of the electrons. In both cases, the filament is a cathode. The field between the filament and the anode not only extracts and accelerates the electrons, but it also acts as an electrostatic lens that focuses the electrons into its first crossover on the optic axis. Altogether, the FEG exhibits improved properties compared to the thermionic LaB_6 filament. The FEG has a higher emission current density and gun brightness, a smaller energy width of the accelerated electrons, and a reduced crossover diameter. These improved properties of the FEG offer a better resolution in STEM and HRTEM as well as for analytical measurements.

The condenser lens system controls the intensity and angular divergence of the beam by changing the foci of the condenser lenses and introducing a condenser aperture. The condenser aperture defines the semi-convergence angle α for illumination and limits off-axis rays that introduce aberrations to the image, as explained in section 2.6.3. The illumination of the sample can be adjusted by the condenser lens system. For CBED and STEM, a convergent beam is necessary, while HRTEM, DF and WB diffraction contrast require a parallel sample illumination.

The specimen is located between the upper and lower pole piece of the objective lens in a goniometer stage that can control the sample position and height as well as the tilt in relation to the beam. In TEM-modus, the objective lens forms a magnified image of the illuminated sample in its image plane. In the back focal plane (BFP) of the objective lens, the diffraction pattern (DP) is generated since parallel rays that are scattered from a set of lattice planes of the sample with the same angle are focused into one point. By changing the focus of the intermediate lenses, either the image or the DP can be selected for a further magnification by the projector lens system onto the fluorescence screen or the charge-coupled device (CCD) camera. The magnification of the image is mainly determined by the magnification of the objective lens. The magnification of the DP is set only by varying the focus of the projector lens system that defines an effective, virtual camera length (CL).

It is possible to detect the diffraction pattern only from a certain area in the image by using the selected area aperture located in the image plane. In analogy, the objective aperture located in the BFP allows the image formation with only selected reflections of the diffraction pattern.

In STEM operation, the image is generated by scanning the convergent beam over the sample and collecting the scattered electrons with the upper or lower annular detector to determine the image intensity pixel per pixel. The collection angle can be modified by varying the focus of the intermediate and projector lens systems. This alters the effective CL that determines the collection angle by simple trigonometry.

The JEOL 2200 FS (S)TEM is equipped with two C_S-correctors. The first one is located behind the condenser lens system to correct the probe-forming beam. The second corrector behind the objective lens corrects the aberrations of the high-resolution images in TEM mode. Additionally, the JEOL 2200 FS (S)TEM allows analytical evaluations of the sample by energy dispersive X-ray spectroscopy (EDX) and electron energy loss spectroscopy (EELS) through an energy filter which is positioned in front of the projector lens system.

3.4.3 Conventional dark-field and weak-beam imaging

Dark-field (DF) imaging is a well established TEM method to investigate defects, composition or strain within a sample. Hereby, the objective aperture is used to select one diffracted beam to form an image. The different reflections in the DP can be sensitive to strain or composition due to sample geometry and the structure factor introduced in 2.47 and evaluated for the zinc blende structure in equation 2.59. Lattice distortions due to defects also introduce a diffraction contrast according to equation 2.76.

For optimal diffraction contrast, the specimen is tilted in such a way that the chosen reflection **g** that is used to form the dark-field image is maximally excited. This procedure establishes the two beam condition that has been explained in section 2.6.4. If the direct beam instead of a diffracted beam is chosen for imaging, this condition is called bright-field (BF) imaging, which is illustrated in figure 3.10 (a). Usually, the microscope is aligned with the direct beam on the optic axis. If the objective aperture is used to select a diffracted reflection for the DF condition, the image will be formed by off-axis rays that suffer more severely from aberrations. This "dirty" dark-field is displayed in 3.10 (b). The image formation with off-axis rays can be circumvented by tilting the beam so the chosen reflection is located on the optic axis as shown in 3.10 (c) for the axial dark-field mode. The Ewald sphere constructions for the two beam condition of the BF and axial DF are illustrated in figure 3.11 (a) and (b).

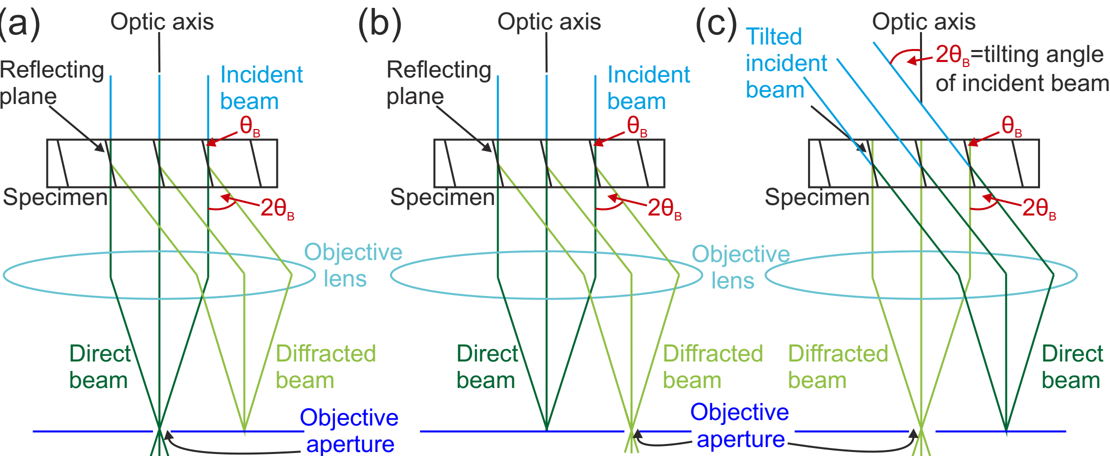

Figure 3.10: Beam path in (a) bright-field (BF) mode, (b) "dirty" dark-field (DF) mode and (c) axial dark-field mode. [77]

Weak-beam (WB) imaging is a special case of DF imaging to detect defects in a higher contrast and high spatial resolution. Since the DF technique is based on imaging with only one diffracted beam, the intensity and often the contrast is very low. For the weak-beam dark-field condition, the reflection **g** that is chosen for imaging by the objective aperture is only weakly excited, hence the name weak-beam. According to practical experience

[77], it has been shown that the weak-beam condition for the reflection **g** can be fulfilled if the 3**g** reflection is strongly excited as depicted in figure 3.11 (c). The Ewald sphere construction shows that the reflection **g** on the optic axis is not excited if the sample is tilted by θ into the two beam conditions. However, the direct beam and the 3**g** reflection lie on the Ewald sphere and are excited. This became known as the **g**(3**g**) WB condition. However, this condition can only serve as a guide to set up the WB dark-field and some experiments might require a stronger or even weaker excitement of the reflection **g**.

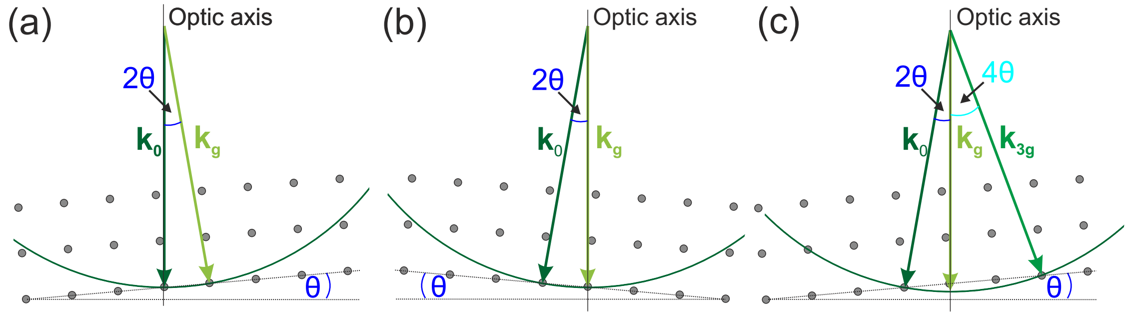

Figure 3.11: Ewald sphere construction for (a) bright-field (BF), (b) dark-field (DF), and (c) **g**(3**g**) weak-beam (WB) imaging. The reflection **g** on the optic axis is chosen for imaging using the objective aperture, respectively. For BF and DF imaging, the chosen reflection **g** is strongly excited while for WB imaging the axial reflection **g** is only weakly excited and the 3**g** reflection is strongly excited instead.

Due to the weak excitement of the imaging reflection **g**, the intensity of the sample is also weak. Defects like dislocations or stacking faults disturb the perfect crystal structure. If the lattice planes in close proximity to the defects are bent back into the Bragg condition the defect will show a high contrast in the WB image. The WB technique is commonly used to study dislocations [115, 116], however, stacking faults and twins also can be made visible in WB images. Stacking faults and twins distort the lattice in {111} direction and define a wedge-shaped volume that generates a thickness contrast in WB images [77]. The lattice distortion of a dislocation depends on its Burgers vector **b**. The dislocations will be invisible if the Burgers vector is parallel to the diffracting planes. This gives the visibility criterion for the imaging reflection **g** to

$$\mathbf{g} \cdot \mathbf{b} \neq 0\,. \tag{3.7}$$

The reverse argument for an invisibility criterion is only fulfilled if

$$\mathbf{g} \cdot \mathbf{b} \times \mathbf{l} = 0\,, \tag{3.8}$$

where **l** is the dislocation line vector. These two criteria can be used to determine the Burgers vector of dislocations in plan-view samples. For the cross section samples in this

study, the 004 and 220 reflections have been used for WB imaging to detect stacking faults and threading dislocations.

3.4.4 Convergent beam electron diffraction

Convergent beam electron diffraction (CBED) is a versatile TEM technique with a much higher spatial resolution than selected area diffraction, because the investigated area is not limited by the selected area aperture but the illuminated area of the convergent beam. CBED patterns contain crystallographic information about the unit cell, the Bravais lattice or the crystal symmetry. CBED offers the possibility to measure the sample thickness, lattice constants, or strain. Additionally, line and planar defects as well as the crystal polarity can be characterized. In this study, the CBED technique has been used to determine the crystal polarity that defines the viewing direction of the sample grown on InP or GaP/Si substrate. The following explanations will focus thereon.

As a consequence of the convergent beam, the incident wave cannot be described as plane wave with a single wave vector $\mathbf{k}_0$ anymore, but the incoming wave vectors lie within an angular range defined by the semi-convergence angle α that determine a continuum of Ewald spheres in reciprocal space as shown in 3.12 (a). As result, the diffraction pattern displays discs instead of the spots that are observed with a parallel beam. The size and overlap of the discs is determined by the semi-convergence angle α specified by the condenser aperture as shown in figure 3.12 (b). In the experiments of this study, the camera length and semi-convergence angle have been chosen to (80-120) cm and $\alpha = 5$ mrad so the discs overlap just slightly.

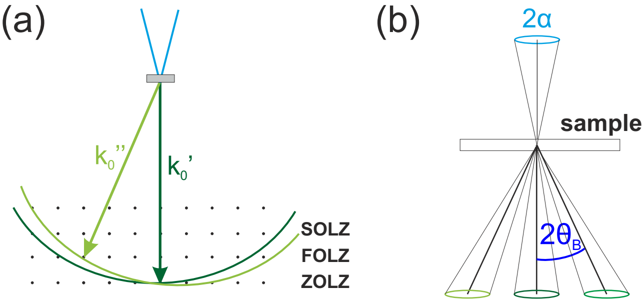

Figure 3.12: (a) The convergent beam with semi-convergence angle α defines various $\mathbf{k}$ vectors and Ewald spheres in reciprocal space. (b) The beam path in convergent beam electron diffraction leads to the formation of diffraction discs. Modified from [117]

In order to determine the polarity of non-centrosymmetric III-V semiconductor structures, it is necessary to tilt the sample away from the symmetric zone-axis orientation into two complementary Bragg conditions that each excite one of the $\pm$ 002 reflections as well as two weak, high odd-indexed reflections, respectively. These two conditions are illustrated in figure 3.13. The method has been developed by Taftø and Spence [118] for

GaAs, but it has been shown that it is also applicable for other polar III-V materials such as InP and GaP [119, 120].

The asymmetric tilt conditions lead to Bragg contrast lines in the ± 002 discs. These Bragg lines occur due to the interference of a singly scattered wave (000 → 002) with doubly scattered waves (000 → hkl → 002), where hkl denote the high odd-indexed reflections that are weakly excited. For non-polar crystals, this interference is always constructive so the 002 discs look alike [118]. For non-centrosymmetric III-V structures the interference can be either constructive or destructive depending on the polarity as well as the value of hkl. This leads to the formation of Bragg lines in the ± 002 discs with bright or dark contrast, accordingly. The interference conditions and therefore the contrast of these Bragg lines are reversed between the two complementary 002 and $00\bar{2}$ discs as well as for reversed polarity. According to findings of Spiecker et al.[119], the structure factor of the ± 002 reflections should be similar to the hkl reflections in order to obtain constructive as well as destructive interference. The sample should be thick enough for the appearance of the Bragg lines due to multiple scattering.

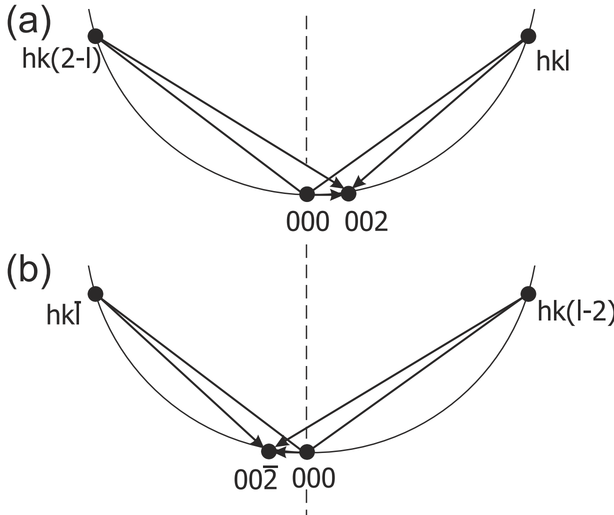

Figure 3.13: Excitation conditions and scattering paths for polarity determination in CBED in <110> projections. The sample is tilted so the Ewald sphere excites the ± 002 as well as two high odd-indexed reflections. The doubly scattered high odd-indexed reflections interfere (a) with the 002 and (b) with the $00\bar{2}$ reflection.

The convenience of this method is based on the fact that a qualitative interpretation of the CBED pattern is adequate enough to determine the polarity. Therefore, the experimental CBED patterns are compared to computer simulations that are only needed to be performed once to obtain the correct tilt conditions [121]. For GaP and InP, which have a larger difference of the atomic number than GaAs, the set of 115 and 117 reflections have been proven useful for the polarity determination [69, 117, 119, 120]. For the Ga-polar direction, the Bragg lines form a cross with bright or faded contrast in the 002 and a

dark contrast in the $00\bar{2}$ disc. For the In- and P-polarity, the contrast of these Bragg line crosses are reversed [117, 120].

3.4.5 High-resolution TEM

In high-resolution transmission electron microscopy (HRTEM), the image is formed by several diffracted beams by choosing a larger or no objective aperture in the BFP than for DF imaging. The interference of these diffracted beams gives rise to phase contrast. In order to resolve atomic periodicities, a high magnification should be chosen and the sample should be oriented into exact zone-axis. Since the spatial resolution depends inversely on the range of $\mathbf{k}$ vectors selected for imaging, the aperture should be large enough to show these low range spatial features. As described in section 2.6.4, the phase contrast also depends on the lens aberrations described by the phase contrast transfer function (PCTF). Figure 3.14 displays the $PCTF(\mathbf{q})$ for an uncorrected TEM at Scherzer defocus in (a) and for a C_S-corrected TEM in (b). The information limit of the microscope is defined through the cutoff frequency $\mathbf{q}_{max}$ of the damping envelope functions that describe the limited spatial and temporal coherence due to the aberration. The cutoff frequency is set by $E(\mathbf{q}_{max}) = e^{-2}$ [86]. The envelope function of spatial coherence due to the cutoff frequency of the aperture and geometric aberrations only imposes an information limit for the uncorrected microscope while the information limit of the C_S-corrected microscope is only determined by the limited temporal coherence due to the incoherent wave aberrations.

If the $PCTF(\mathbf{q})$ has a negative value, the atoms will appear dark against a bright background for HRTEM images. In case of a positive value for the phase contrast transfer function, the opposite will be true so the atoms will appear bright against a dark background. If $PTFC(\mathbf{q})$ is equal to 0, there will be no detail visible in the image for this value of $\mathbf{q}$). The $PCTF$ of the uncorrected TEM shows several zeros in figure reffig:PCTF (a). This will lead to contrast reversals in high-resolution TEM images. The contrast reversals depend on the defocus and spherical aberrations since they change the shape and zeros of the $PCTF$. The first zero defines the resolution limit.

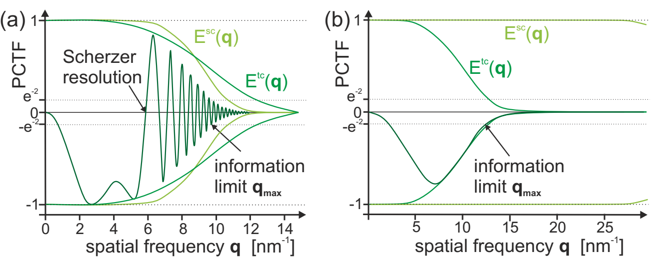

Figure 3.14: $PTFC(\mathbf{q})$ for (a) an uncorrected TEM at Scherzer defocus and (b) a C_S-corrected TEM operated. Images modified from [122] and [123], respectively.

3.4.6 High-angle annular dark-field STEM

As described before in section 3.4.2 and 2.6.4, annular dark-field (ADF) imaging is based on scanning a convergent, coherent electron beam over the sample and collecting the scattered electrons with the upper or lower annular detector. For high-angle annular dark-field (HAADF) imaging, the lower detector is used since its detector angle can be varied over a larger range. The corresponding imaging process is depicted in figure 3.15. Electrons scattered into very low angles can also be detected using a annular or disc-shaped bright-field detector for bright-field imaging.

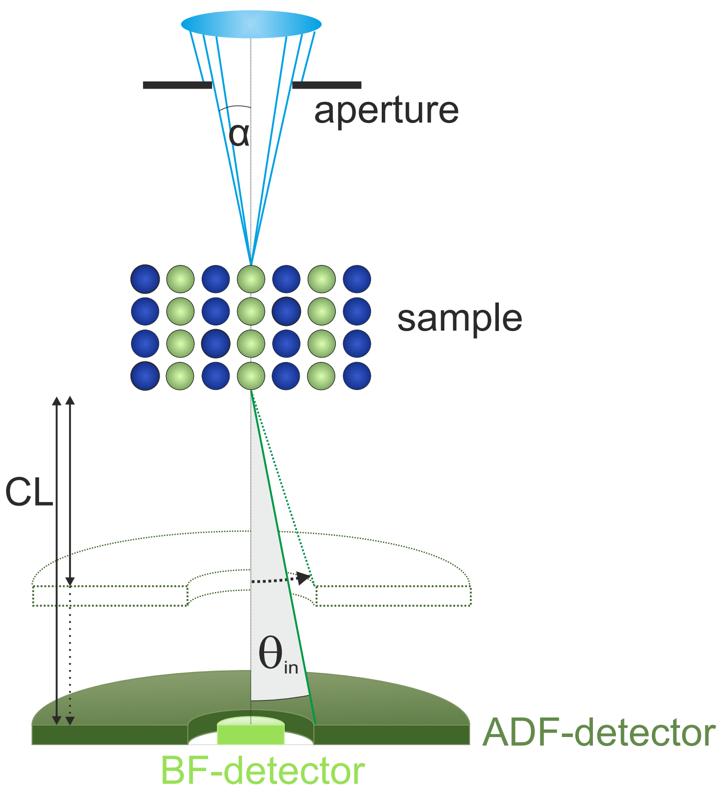

Figure 3.15: Schematic beam path in scanning electron transmission microscope. The convergent beam has a semi-convergence angle α defined by the condenser aperture. The electrons scattered by the sample are collected with an annular dark-field (ADF) detector or a disc-shaped BF-detector. The collection angle can be changed by varying the camera length (CL).

The condenser aperture limits aberrated off-axis rays and defines the semi-convergence angle α and therefore the intensity of the beam. The aberration correction of the probe-forming beam allows the use of a larger condenser aperture, which minimizes the probe size and increases the intensity. For the experiments of this study, α has been chosen to 24 mrad. The probe size, and therefore the degree of aberration correction, determines the resolution of the STEM. The magnification of the image is set by the scanned area of the beam.

Changing the foci of the intermediate and projector lenses can vary the camera length and therefore the inner detector angle θ_{in}. A larger CL increases the collection angle so the arising contrast becomes more sensitive to material with a lower atomic number as well as strain (section 2.6.4).

In order to avoid image distortions due to sample or stage drift as well as low-frequency scanning-distortions, it is possible to record a stack of successive images. The image acquisition for each image is increased compared to a single image to reduce the scanning distortion. The final image is obtained by summing over the image stack. The individual images are aligned to each other to correct the linear shear distortions due to sample drift as well as the non-linear scanning-distortions using the *Smart Align* software tool in *MATLAB* from Jones et al. [124].

3.4.7 Simulation of HAADF images

Simulating HAADF images plays an important role in the interpretation and quantitative evaluation of experimental HAADF images. The interaction of the electron beam with the sample is calculated using a crystal model of the sample that describes the atom positions as exactly as possible. In this study, simulation of STEM images of the GaSb/GaP interface has been carried out with the STEMsim package [125] using the multislice method with an absorptive potential (AP) approximation [109].

Relaxation of atom positions

The crystal model of the sample is a supercell that is constructed from atoms at their undisturbed lattice sites. In the following step, these supercells are structurally relaxed by varying the atom positions until the total energy of the supercell as a function of atomic bond-lengths and angles is minimal. In this study, the relaxation of the supercell followed the method of Wang and coworkers [126] using a molecular dynamics (MD) algorithm, which employed Stillinger-Weber potentials [127] and periodic boundary conditions along [110] and [1-10] direction.The first six monolayers in GaP were kept fixed in order to provide a reference area for the strain evaluation by peak pairs and geometric phase analysis.

Stillinger-Weber potentials are modified Lennard-Jones-type potentials that take into account the short-range nature and the angle stiffness of covalent bonds. They have been used for the MD simulation of crystal growth [128], study of defects [129, 130] or the calculation of structural properties [131, 132]. During the MD simulations, only nearest neighbor bonds are considered. The covalent bonds are approximated by a combination of pair and triplet potentials. The two-body interaction term depends on the bond length d_{ij} between neighboring atoms i and j and the three-body interaction term depends on the angle θ between the bonds as well as the cohesive energy per bond, and bond strength

factors that have to be determined by reproducing basic properties of the material. In this study, the values have been taken from the publication of Ichimura [133] who determined bond strength factors for several III-V compounds using their cohesive energy, equilibrium lattice constants and elastic properties.

For the model of the GaSb/GaP interface, the dislocations should be included into the unrelaxed supercell. Therefore, the constructed supercells contained four glide set and shuffle set Lomer dislocations perpendicular to each other along the <110> directions. The ratio of the number n of {110} lattice planes between the dislocations is determined by the lattice constants of the two materials through

$$n_{GaP}a_{GaP} = n_{GaSb}a_{GaSb} \rightarrow \frac{n_{GaP}}{n_{GaSb}} = \frac{a_{GaP}}{a_{GaSb}} = 1.118\,. \tag{3.9}$$

The closest ratios with natural numbers are $\frac{9}{8} = 1.125$ and $\frac{10}{9} = 1.111$, which are equally spaced from the desired value of 1.118. However, since the number (n) of {111} GaP lattice planes between the dislocations is $n = \frac{1+mf}{mf} = 9.48$ according to equation 4.4, n_{GaP} has been chosen to be 9.

Multislice method with absorptive potential

The multislice approach has been developed by Cowley and Moodie [134] to simulate conventional TEM images before it has also been applied for the computation of HAADF intensities by Kirkland [135] thirty years later. The multislice method is based on the division of the simulated supercell into thin slices. Each slice, one after the other, interacts with the respective incident electron beam. The outgoing wave function $\psi_{out}(\mathbf{r})$ from each slice can be calculated from the incoming wave function $\psi_{in}(\mathbf{r})$ by using a propagator function $p(\mathbf{r})$, that describes the evolution of the wave between the slices, and a transmission function $t(\mathbf{b})$ that determines the interactions between the electrons and projected atomic potentials.

$$\psi_{out}(\mathbf{r}) = (\psi_{in}(\mathbf{r})t(\mathbf{r})) \otimes p(\mathbf{r})\,. \tag{3.10}$$

The transmission function $t(\mathbf{r})$ is based on a phase grating. This phase grating is the projection of the atom potential along the incident beam direction at position $\mathbf{r}$ of the considered slice. The projection is denoted by the index p on the potential $V(\mathbf{r})$.

$$t(\mathbf{r}) = e^{-\frac{i}{\hbar v}V_p(\mathbf{r})}\,, \tag{3.11}$$

where v is the electron velocity and $\hbar$ the reduced Plank constant.

The thermal diffuse scattering (TDS) introduced in section 2.6.4 has to be taken into account into the simulation of HAADF images since it is the main contributor to the HAADF intensity. Therefore, either the absorptive potential (AP) [109] or the frozen lattice [136, 137] approach are employed to determine the projected potential $V_p(\mathbf{r})$ of the phase grating.

In this study, the AP has been used for the multislice simulation of the relaxed supercells due to the much lower computation time compared to the frozen lattice method. The relaxed supercells contained four dislocations along each <110> direction and therefore had a dimension of (13.7 nm, 13.8 nm, 4.1 nm).

The AP approach includes the TDS as an absorptive potential $V''(\mathbf{r})$ by extending the normal electrostatic scattering potential $V'(\mathbf{r})$ from equation 2.35 to a complex total potential $V(\mathbf{r})$ with $V''(\mathbf{r})$ as imaginary component, so

$$V(\mathbf{r}) = V'(\mathbf{r}) + iV''(\mathbf{r})\,. \tag{3.12}$$

According to Ishizuka [109], the intensity I that will be lost during the transmission of a slice can be calculated to

$$\begin{aligned} I &= \int \left(|\psi_{out}(\mathbf{r})|^2 - |\psi_{in}(\mathbf{r})|^2 \right) d\mathbf{r} \\ &= \int |\psi_{in}(\mathbf{r})|^2 \left[e^{\frac{2\pi}{\hbar v} V_p''(\mathbf{r})} - 1 \right] d\mathbf{r} \\ &\approx \int \frac{2}{\hbar v} |\psi_{in}(\mathbf{r})|^2 \, V_p''(\mathbf{r}) d\mathbf{r}\,. \end{aligned} \tag{3.13}$$

The total intensity I_n after the transmission of n slices can then be calculated by summing up the contributions of the single slices, so

$$I_n = \sum_{i=1}^{n} \frac{2}{\hbar v} \int |\psi_i(\mathbf{r})|^2 \, V_{p,i}''(\mathbf{r}) d\mathbf{r}\,. \tag{3.14}$$

In order to obtain the total intensity for an HAADF image, it is necessary to determine the absorptive potential $V_p''(\mathbf{r})$ that accounts for the thermal diffuse scattering into high angles. The scattering potential can be obtained from the inverse FT of of its Fourier components $V_{\mathbf{g}}$.

$$V_{\mathbf{g}} = \frac{2\pi\hbar^2}{m_0} \frac{1}{\Omega} \sum_k f_k(\mathbf{s}, M_k)\; e^{-M_k \mathbf{s}^2} e^{-2\pi i \mathbf{g}\cdot\mathbf{r}_k}\;, \tag{3.15}$$

where f_k are the atomic form factors of the scattering atoms at the positions $\mathbf{r}_k$ (equation 2.38), m_0 is the electron mass, Ω the unit cell volume and $e^{-M_k \vec{s}^2}$ the Debye-Waller factors. The Debye-Waller factors and atomic form factors depend on the vector $\mathbf{s} = \mathbf{g}/2$,

whose magnitude is defined by the Bragg angle θ_B and the electron wave length λ to $|\mathbf{s}| = sin(\theta_B)/\lambda$.

The real part of the scattering potential, $V'(\mathbf{r}')$, can be calculated by taking into account the atomic form factors from equation 2.38 evaluated by Doyle and Turner [80]. The imaginary part of the the scattering potential, $V''(\mathbf{r}')$, which describes the TDS, is evaluated by considering the absorptive form factors f''_k that have been given by Hall and Hirsch in [138] to

$$f''_k(\mathbf{s}, M_k) = \frac{4\pi\hbar}{m_0 v} \int_{\theta_{min}}^{\theta_{max}} f_k(|\mathbf{s}'|) f_k(|\mathbf{s} - \mathbf{s}'|) \left[1 - e^{(-2M_k(\mathbf{s}'^2 - \mathbf{s}\cdot\mathbf{s}'))}\right] d\mathbf{s}' \;, \tag{3.16}$$

where the integration is performed only over the detector range defined by the inner and outer detector angles θ_{min} and θ_{max}. In this case, the atomic form factors f_k should be calculated from the analytical expression from Weickenmeier and Kohl [81] since the scattering into high angles has to be considered.

3.4.8 Theoretical strain mapping

The constructed supercells are not only useful for the simulation the intensities in HAADF image, but also to determine the strain within the model [139].

There are three different approaches to obtain theoretical strain maps. The first two methods calculate the 3D strain tensor as defined in equation 2.23 in each atom position of the relaxed supercell before these values are projected to generate two-dimensional strain maps. The third approach takes the desired projection plane and determines the mean positions of atom columns on this plane. In the next step, the 2D-strain tensor is calculated at these atom column positions. The theoretical strain map is then obtained by constructing a 2D-mash grid for a 2D interpolation of the determined strain values. In this study, only the third approach has been used to generate the theoretical strain maps, because its work-flow is most comparable to the strain maps obtained from experimental images. The experimental images are also projections of the the atom columns into two-dimensional images that are used to calculate 2D strain maps using the PP or GPA algorithms explained in the following section 3.4.9.

To construct the theoretical 2D-strain maps, the nearest neighbor atom columns should be defined for any arbitrary atom column in the two-dimensional projection of the relaxed supercells. This is realized by using the distances R_i and corresponding 2D angles α_i from each given atom column to its neighboring atom columns as defined in figure 3.16. Since

the equilibrium values R_0 and α_0 are known from the ideal structure, it is possible to determine the nearest neighbor atom column positions by minimizing the sum

$$\frac{|R_i - R_0|}{R_0} + \frac{|\alpha_i - \alpha_0|}{\alpha_0} \,. \tag{3.17}$$

For the <100> projections, the equilibrium values are the same for all four neighbors, while for the <110> projections the distance and angle is different for the neighboring column position within the dumbbell compared to the other two neighbors.

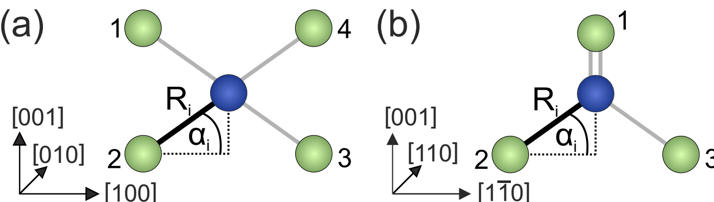

Figure 3.16: Nearest neighbor positions in dependence on the distances R_i and corresponding angles α_i for (a) <100> projections and (b) <110> projections.

For each given atom column position in the <100> projections, the relative coordinates of its arbitrary chosen three nearest neighbor positions relative to the fourth nearest neighbor positions (see figure 3.16 (a)) are calculated, so

$$\begin{aligned}(X,Y)_{21} =& (x_2 - x_1, y_2 - y_1)\\ (X,Y)_{31} =& (x_3 - x_1, y_3 - y_1)\\ (X,Y)_{41} =& (x_4 - x_1, y_4 - y_1)\,.\end{aligned} \tag{3.18}$$

For the <110> projections, only two relative coordinates between two arbitrary chosen nearest neighbor positions relative to the third nearest neighbor positions are calculated for each give column position, accordingly.

These relative coordinates are determined for the positions in the relaxed supercell as well as for the ideal positions in a supercell with defined lattice constant a_0. The ideal lattice should have the same size as the relaxed supercell and acts as a reference lattice to determine the distortion tensor e_{ij} as defined in equation 2.22, using the definition only in two instead of three dimensions. Therefore, the following coordinate transformation between the ideal lattice and the relaxed model is used

$$\begin{aligned}x' =& (1 + e_{xx})x + e_{xy}y\\ y' =& e_{yx}x + (1 + e_{yy})y\,.\end{aligned} \tag{3.19}$$

The dash denotes the relative coordinates in the relaxed supercell and the undashed values are the relative coordinates in the ideal lattice. The two-dimensional distortion tensor has four entries that define the two-dimensional strain tensor accordingly to equation 2.23 to

$$\varepsilon = \begin{pmatrix} \varepsilon_{xx} & \varepsilon_{xy} \\ \varepsilon_{yx} & \varepsilon_{yy} \end{pmatrix} = \begin{pmatrix} e_{xx} & e_{xy} + e_{yx} \\ e_{yx} + e_{xy} & e_{yy} \end{pmatrix} . \tag{3.20}$$

If the relative coordinates for each column position are inserted in equation 3.19, the deformation and strain tensor can be evaluated for each position. In case of the <100> projections, there are three relative coordinates giving six equations to determine the four entries of the distortion tensor. This over-determined problem is solved in *MATLAB* by computing the least squared mean from the possible solutions.

3.4.9 Strain mapping by geometric phase analysis and peak pairs analysis

There are two well established methods to evaluate the the strain in high-resolution TEM or HAADF images are geometric phase analysis (GPA) [140, 141] and peak pairs (PP) analysis [142] using a reciprocal and real space approach, respectively. They are both commercially available as plug-ins for the *Gatan Microscopy Suite Software* that drive the digital cameras in the TEM instruments.

Geometric phase analysis

The geometric phase analysis is based on choosing two non-collinear Bragg reflections $\mathbf{g}_1$ and $\mathbf{g}_2$ in the Fourier transform (FT) of the high-resolution image and performing inverse Fourier transforms, respectively. The resulting complex images are determined by the local Fourier components $I_{g_1}(\mathbf{r})$ and $I_{g_1}(\mathbf{r})$. The local contrast and and positions of the lattice fringes in the inverse FT images depend on the amplitude, $A_g(\mathbf{r})$, and phase, $P_g(\mathbf{r})$ according to

$$I_g(\mathbf{r}) = A_g(\mathbf{r}) e^{iP_g(\mathbf{r})} . \tag{3.21}$$

Since the phase $P_g(\mathbf{r})$ describes the fringe positions, it determines the local displacements of the atomic lattice planes and has a simple relationship to the displacement field $\mathbf{u}$ through $P_g(\mathbf{r}) = -2\pi\mathbf{g} \cdot \mathbf{u}$. Therefore, the two-dimensional displacement field $\mathbf{u}$, whose partial derivatives are used to calculate the local distortion field of the lattice according to equations 2.22, can be obtained from the two phases:

$$\mathbf{u} = -\frac{1}{2\pi} [P_{g_1}(\mathbf{r})\mathbf{a}_1 + P_{g_2}(\mathbf{r})\mathbf{a}_2] , \tag{3.22}$$

where $\mathbf{a}_1$ and $\mathbf{a}_2$ define the real space lattice corresponding to the reciprocal lattice vectors $\mathbf{g}_1$ and $\mathbf{g}_2$. The distortion of the lattice are determined by defining a reference phase from an chosen, undistorted area within the image, e.g. the substrate.

Peak pairs analysis

In contrast to GPA, peak pairs analysis is based on the evaluation of the real-space high-resolution images by detecting the atom positions through the maximum intensity of the peaks. A sub-pixel resolution can be achieved by using a 2D-interpolation or a 2D quadratic fitting function and maximization to determine the position (x,y) with maximum intensity. Inverse Fourier filtering with several Bragg reflections or the application of a low-pass Wiener filter can be used in a preliminary step to reduce the noise.

Similar to GPA, it is necessary to choose a reference area in the image. This reference is used to define two non-collinear basis vectors $\mathbf{a}_1$ and $\mathbf{a}_2$. For each maximum peak position (x,y) the nearest neighbor peak in direction of the basis vectors and at the distances $|\mathbf{a}_1|$ and $|\mathbf{a}_2|$ are identified. This identification is simplified by an affine transformation of the (x,y) peak positions to a square grid with orthogonal basis vectors and integer coordinate values for the reference area. The nearest neighbor peaks can then be found by using the Euklidean distance. The neighboring positions are connected to pairs by single lines along the two non-collinear directions of the two basis vectors. These peak pairs are used to calculate the two-dimensional displacement field $\mathbf{u}$ relative to the reference lattice defined by $\mathbf{a}_1$ and $\mathbf{a}_2$. The resulting displacement field $\mathbf{u}$ can be used to determine the strain tensor for each maximum position. A continuous distortion field for a strain map is obtained by applying a 2D-interpolation to the strain values obtained at the (x,y) positions.

Separated sublattices

For images in the <110> projections, the two basis vectors are not sufficient to connect every peak in the image so the peaks pairs algorithm can not be used to obtain strain maps for this case. In order to overcome this problem, the atom positions detected by PP are evaluated with a self-written *MATLAB* program of the group. Missing peaks that have not been found by the PP algorithm are added and the group III and group V sublattices are separated. For each sublattice, a new image is generated using a quadratic function to generate a peak at each determined position. These sublattice-peak images are then used to generate strain maps using PP analysis.

4 Results and discussion

This chapter presents the results of this study in two parts. The first section 4.1 deals with the growth optimization of Ga(PSb) and Ga(AsSb) buffer layers on Si with the main focus on the former. Starting with the characterization of lattice-matched growth on InP substrate in section 4.1.1, the transfer onto the GaP/Si substrate is described in the following section 4.1.2. The samples were investigated by AFM, XRD and (scanning) transmission electron microscopy ((S)TEM) to gain insight on the surface, the morphology and the relaxation. In order to improve the Ga(PSb) buffer layer, three different approaches were applied: interlayer of low-Sb content lattice matched to GaP/Si described in 4.1.4, a flow modulated epitaxy of Ga(PSb) presented in section 4.1.5, and an InP interlayer, whose results are shown in 4.1.6). The second part of this chapter 4.2 is a thorough investigation by STEM of three different Sb-based buffer layers, namely GaSb, Ga(PSb) and Ga(AsSb), at the beginning of their growth on GaP/Si. Particular attention is paid to the interface with its dislocations. In the case of the binary material, GaSb, it was possible to compare the experimental HAADF images and their evaluation by strain mapping with simulations obtained by molecular dynamics calculations.

4.1 Growth optimization of Sb-based buffer layers

4.1.1 Pseudomorphic growth of Sb-based buffer layers on InP-substrate

The aim of this study has been the growth of Sb-based buffer layers with the lattice constant of InP on Si substrate. The lattice constant in dependence on the composition can be determined by measuring rocking curves in the XRD and compare them to simulations. However, in the case of a ternary material like Ga(PSb) grown strained on Si this determination is ambiguous since strain as well as the composition determine the measured lattice constant. In the preliminary step, the buffer layers were therefore grown lattice-matched on InP substrate to obtain the growth conditions for the buffer layers at the desired lattice constant and composition. In the following, the layer quality of the pseudomorphically grown Sb-based buffer layers on InP substrate have been observed.

The Sb-based buffer layers were not grown directly on the InP substrate. Instead a (GaIn)As interlayer was embedded to achieve a smoother layer growth of the Sb-based buffer on the InP substrate. Two different Sb-based buffer layers grown pseudomorphically

on InP were realized, Ga(PSb) and Ga(AsSb). The Ga(PSb) buffer layer epitaxy were achieved by using the following growth parameter: TEGa = $7.1 \cdot 10^{-3}$ mbar, TBP = 0.1 mbar, TESb = 0.0176 mbar, V/III = 17, Sb/V = 0.15. The growth temperate was $T_{growth} = 475°C$ and the growth rate had been determined to $v_{growth} = 0.3\, nm/s$. Under the assumption of pseudomorphic growth, the XRD measurement gave a composition of $Ga(P_{33.3}Sb_{66.7})$ for this sample. The sample was investigated by AFM and TEM to analyze the surface and structural morphology. The results are displayed in figure 4.1.

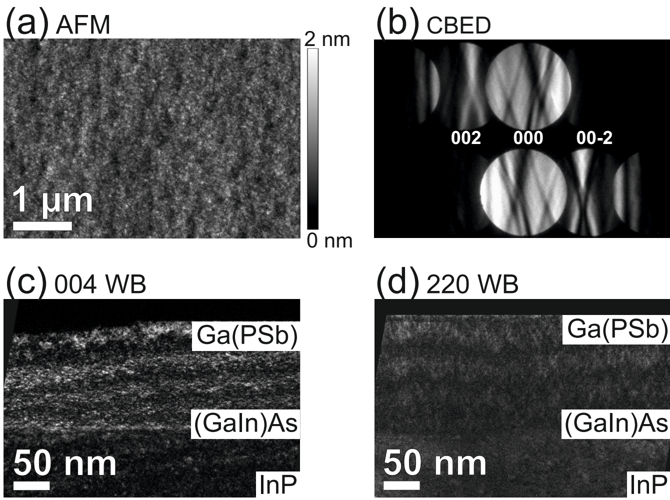

Figure 4.1: (a) shows the surface of a Ga(PSb) buffer layer on InP substrate by AFM. Images (b)-(d) are TEM investigation of the same sample. (b) CEBD image to determine polarity and (c) (004) and (d) (220) weak-beam images.

The AFM image in 4.1 (a) shows a very smooth surface. The height scale was only 2 nm and the root mean square (rms) average of the height deviation, which is a measure for the degree of roughness, was 0.24 nm. The sample has also been investigated by TEM using CBED in 4.1 (b) to determine the polarity and by (004) and (220) weak-beam imaging in images (c) and (d) to gain insight on the layer quality.

The CBED image demonstrates that the investigated sample was Ga-polar and therefore viewed in [110] projection. The weak beam images showed no signs of stacking faults (SF), twins or threading dislocations (TD). The contrast variation of bright and dark lines are thickness fringes that result from the changing thickness due to the wedge shape of sample preparation. The corresponding [$\bar{1}$10] projection had also been investigated and looked accordingly (not shown here). No lattice defects such as SF or TD have been observed in TEM. Since 3 μm of the sample with an presumed average thickness of 300 nm have been analyzed, the upper limit for the SF and TD defect densities can be estimated to $\frac{1}{3 \cdot 10^{-4} cm \cdot 3 \cdot 10^{-5} cm} = 10^8\, cm^{-2}$, respectively. This number is still very large due to the very small area that can be investigated by TEM. However, the sample surface investigated by AFM in figure 4.1 (a) shows no sign of cross-hatching due to the generation of misfit

dislocations [143, 144] so it can be assumed that no misfit dislocations, and therefore no TD, had been generated in a much larger area than investigated by TEM. The density in the order of $10^8\,cm^{-2}$ then was an overestimated upper limit. The real density is expected to be much lower. This showed that the pseudomorphic grown Ga(PSb) layer had a high structural quality.

A pseudomorphically grown Ga(AsSb) buffer layer on the InP substrate had also been realized. In this case, the lattice constant of InP was reached with an composition of $Ga(As_{48.6}Sb_{51.4})$. Hereby, the following growth conditions were used: TEGa = $14.2 \cdot 10^{-3}$ mbar, TBAs = 0.0249 mbar, TESb = 0.0167 mbar, V/III = 2.9, Sb/V = 0.4, keeping the growth temperature of $475°C$. The same analysis in AFM and TEM have been performed (not shown here). The results were similar to the Ga(PSb) buffer layer. The AFM micrograph showed a flat surface with a rms of 0.23 nm, while in TEM images no lattice defects could be observed.

In summary, it has been shown that the Sb-based buffer layers were grown on the InP substrate as smooth 2D layers as exhibited by AFM and TEM investigations. The lattice constant of InP had been reached with a composition of $Ga(P_{33.3}Sb_{66.7})$ and $Ga(As_{48.6}Sb_{51.4})$. In the following, this study is concentrating on the Ga(PSb) buffer while the results of Ga(AsSb) are consulted as a comparison to the Ga(PSb) findings.

4.1.2 Metamorphic growth of Sb-based buffer layers on GaP/Si pseudosubstrate

Investigation of Ga(PSb) buffer layers of different thicknesses by atomic force microscopy and scanning transmision electron microscopy

The previous section has shown that it was possible to grow a high quality Sb-based buffer layers on InP substrate. This was the starting point for the transfer onto Si substrate. As explained in the introduction, the Sb-based buffer layer was not grown directly on Si but on a GaP/Si pseudosubstrate to avoid antiphase boundaries within the Sb-buffer. Previous work has proven that there are certain growth conditions at which the antiphase boundaries annihilate when the polar GaP is grown on the non-polar Si substrate [19]. The GaP/Si pseudosubstrate was overgrown with GaP at $675°C$ to supply a flat and clean surface for the following growth of the Sb-based buffer layer. Hereby, it should be taken care that the overall GaP layer thickness does not exceed its critical thickness. Otherwise, the GaP will start to relax by generating misfit dislocations along [110] and [$\bar{1}$10] at the GaP/Si interface. The dislocation formation is connected to plastic strain relaxation due to the dislocation glide process during nucleation which leads to rippled surface morphology [143, 144]. The generated misfit dislocation network causes a nonuniform elastic strain field. This results in surface roughening that becomes visible in AFM images as cross-hatch pattern [145]

because the growth rate is enhanced at the surface above the misfit dislocations [144] by strain-driven adatom diffusion or because atoms are more easily incorporated into these regions. In this way, strain energy is compensated by surface energy and surface roughness [146]. The cross-hatch pattern is characteristic for a lattice mismatch lower than 2 %. A completely relaxed layer has a nearly flat surface [144]. In case of highly mismatched layers, no surface crosshatch pattern can be observed because the stress fields of the threading dislocations overlap and dominate the surface morphology [143]. At the beginning of this study, the GaP layers had exceeded their critical thickness and started to relax which was visible as a cross-hatch pattern in the AFM images in figure 4.2. Misfit dislocations at the GaP/Si interface had been observed in TEM images for these cases.

The Sb-based buffer layer was now grown onto the GaP/Si template using the same growth conditions that had been determined by the pseudomorphic growth on the InP substrate. In case of the Ga(PSb) buffer layers, cooling down from $T^{GaP}_{growth} = 675°C$ to $T^{Ga(PSb)}_{growth} = 475°C$ was conducted with and without stabilization by TBP. However, this stabilization did not lead to different results for the Ga(PSb) buffer in all succeeding investigations by AFM, RSM and TEM. In the following, the results are shown for samples with TBP stabilization. Figure 4.2 displays AFM images of the Ga(PSb) surface at different nominal thicknesses.

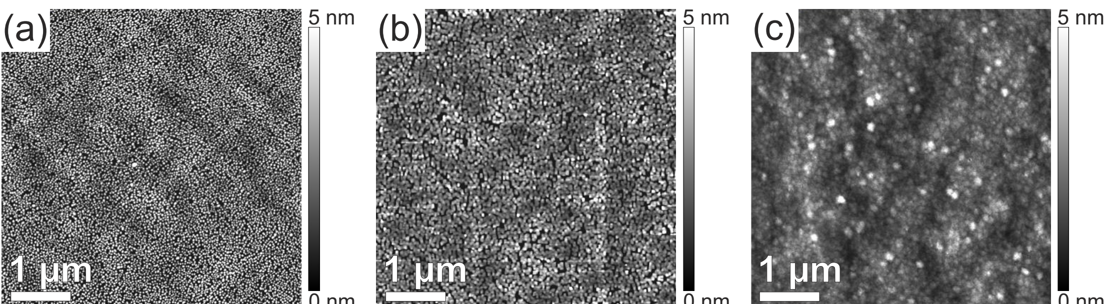

Figure 4.2: AFM micrographs of Ga(PSb) layers on GaP/Si substrate at (a) 2 nm (b) 20 nm and (c) 100 nm nominal thickness.

Figure 4.2 (a) reveals that at the beginning of growth the Ga(PSb) is growing in island-like structures. With increasing growth time these islands expanded and grew together 4.2 (b) until a cohesive film was formed. The trenches were overgrown and a smooth surface could be observed for thick samples in 4.2 (c). This qualitative observation was supported by the rms that changed thereby from (a) 1.68 nm over (b) 1.83 nm to (c) 0.70 nm.

The observed island-like structures at the beginning of growth had a round shape. They were neither elongated nor show a particular facetting. The latter point is proven by STEM investigations as in figure 4.4 (b). This means they had no preferred direction of growth. El Kazzi et al. [126, 147, 148] have shown that the growth of GaSb on an Sb-rich

GaP-surface resulted in {111}-facetted islands that have been relaxed by a network of Lomer dislocations at the interface. Due to their Sb-rich surface treatment the strain has been relaxed by a higher fraction of 90° dislocations along the Ga-polar orientation so the island have been elongated in the perpendicular direction. However, the shape of the Ga(PSb) islands on GaP/Si did not change during nucleation when a 1 s TESb pre-run was introduced before the Ga(PSb) growth in order to offer a Sb-rich surface. This can be seen in figure 4.3, where AFM images of Ga(PSb) at nominal thicknesses of 2 nm and 20 nm without TESb pre-run figure (a) and (b) are compared to samples of same nominal thicknesses with TESb pre-run figure (c) and (d). TEM investigations that are presented in the following support this assumption.

Figure 4.4 presents HAADF images of Ga(PSb) with 1 s TESb pre-run after its island-like nucleation. Figure 4.4 (a) shows that the islands were randomly distributed as already indicated in the AFM image of 4.3. In addition to that a blurred film of a few nm thickness on top and between the islands was visible. This becomes even more distinguishable in higher magnification in figure 4.4 (b) on one of the islands and between the islands in figure 4.4 (c). This blurry contrast might be attributed to hydrocarbon groups floating on the surface during growth or undissipated TESb originating from the cooling down of the sample after growth with TESb. It could also be Sb covering the surface similar to Bi that segregates at the surface during growth [149]. Antimony is a well known surfactant

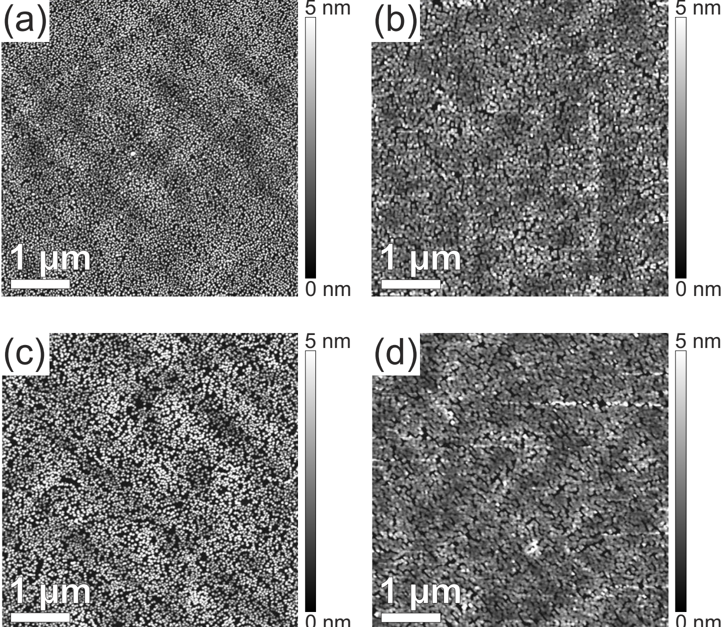

Figure 4.3: Comparison by AFM of Ga(PSb) layers with nominal thicknesses of 2 nm (a) and 20 nm (b) grown without TESb pre-run to Ga(PSb) layers with nominal thicknesses of 2 nm (c) and 20 nm (d) grown with TESb pre-run.

that accumulates at the surface during growth and increase the group III ad-atom surface diffusion and modulates the band gap energy [150, 151] or alters the growth rates and facet formation [152]. These assumptions could not be confirmed by energy dispersive X-ray spectroscopy, but this might be attributed to the fact that this layer is very thin so that not enough X-ray signal is generated to detect Sb. This blurry film is observed on every Sb-based buffer layer, in every TEM investigation. Another explanation for these blurred film on top of each layer could be an amorphous oxidation layer on top of the material. The amorphization by argon milling during sample preparation is a well investigated effect. Previous studies have reported a surface amorphization of 2 - 4 nm by argon ion milling [153–156]. However, one does not exclude the other and a combination of all might be true.

In addition, figure 4.4 (c) revealed that the GaP layer was of high quality and that there was no wetting layer between the islands because otherwise the group V positions would be brighter than the group III positions in this Z-contrast HAADF image. This means that no Stranski-Krastanow growth (see section 2.3.2) was taking place.

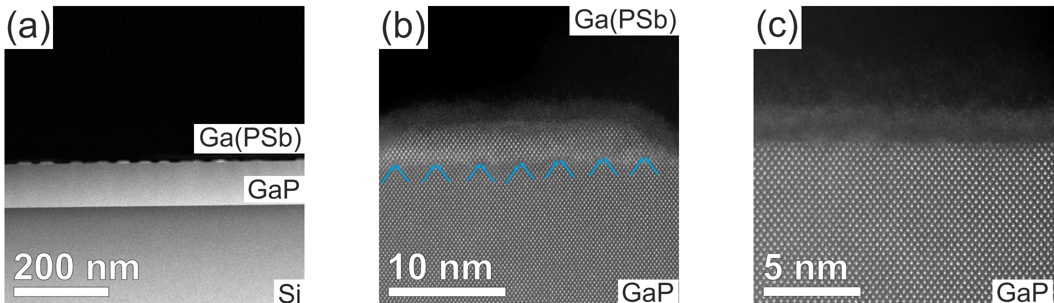

Figure 4.4: HAADF STEM images of Ga(PSb) on GaP/Si after the island-like nucleation at the beginning of growth. The blue arrows indicate the additional {111} lattice planes that form the dislocations at the interface between GaP and Ga(PSb).

The facets of the islands were higher-indexed lattice planes such as {112}, {123}, or {133} that have inclination angles between 32° - 47° to the (001) plane in growth direction. The height of the islands had been measured to 3 - 4 nm. This exceeds the expected critical thickness which is only a few monolayers for this highly mismatched material system [34, 157], so misfit dislocations are generated at the interface. According to Dunstan [34], the growth at high mismatch often results in island growth, where the equilibrium critical thickness theory is inapplicable. The islands do not need dislocation multiplication for relaxation, because surface relaxation and dislocation—dislocation interaction dominate. The additional {111} lattice planes in the smaller lattice constant material GaP, that form the dislocations, are marked with blue arrows. They indicate that the arising misfit dislocations were mainly Lomer dislocations or 60° pairs. However, especially at the verge

of the islands, 60° misfit dislocations were also observed. This might be explained by the plastic relaxation at the free surface of the island [34]. A further explanation is given by the model for the generation of misfit dislocations whereat dislocations are generated as 60° dislocation half loop at the edges of the island [29, 54, 158, 159]. With increasing thickness a second 60° dislocation half loop is generated and glides along {111} planes to merge with the first 60° to form a Lomer [160] or 60° dislocation pair, depending on whether the 60° dislocations have opposite (Lomer) or parallel (pair) screw components of the Burgers vector [56–58]. Since the Lomer dislocation reduces strain most efficiently, their generation is the most favorable, [157, 161]. 60° dislocations are a highly active sources for the generation of threading dislocations [56, 157, 162]. However, the strain is not only reduced by the generation of misfit dislocations, but also by the formation of stacking faults that have been observed in some islands. In most cases, the origin of stacking faults is associated with the dissociation of a 60° dislocation into its 30° and 90° partials under stress [54, 61, 163, 164]. Narayan and Oktyabrsky [56] have shown that this also holds true when the 60° dislocations form pairs. However, the stacking faults might not only arise due to strain relaxation and the dissociation of 60° dislocations but also due to a stacking disorder caused by the presence of impurities or surface steps [165] or too rapid deposition rates [63, 64] during growth. The presence threading dislocations and stacking faults is of cause undesired since they degrade the quality of the buffer layer and therefore the active material that will be grown on top of it.

When the islands coalesced with increasing growth time, the degree of relaxation of neighboring islands not necessary matched each other. This leads to the creation of further lattice defects such as TD [29, 34] or SF [166]. The HAADF investigations of a Ga(PSb) buffer layer of 20 nm nominal thickness with TBP stabilization and 1 s TESb pre-run is displayed in figure 4.5.

Like the island in 4.4 (b), the strain of the thin Ga(PSb) was compensated by Lomer and 60° pair dislocations. However, 60° dislocations as well as numerous stacking faults and microtwins were observed in 4.5 (a)-(c). Having a closer look at the SFs in figure 4.5, it was noticeable that not all of them continued to the surface, but some annihilated each other when they intersected. In most cases, one SF continued like in image (a), but the case of both annihilating each other has also been observed in 4.5 (b). It is possible that this observed effect occured due to the thickness gradient of the sample preparation and the rest of the stacking fault had been milled away. However, this annihilation of SFs has been observed in every investigated sample and much more often than the disappearance of an SF due to sample preparation which makes this explanation statistically unlikely, especially for the case of double annihilation like in image (b). In addition, this annihilation of stacking faults has been observed and investigated before, like in 3C-SiC/Si by Yamasaki

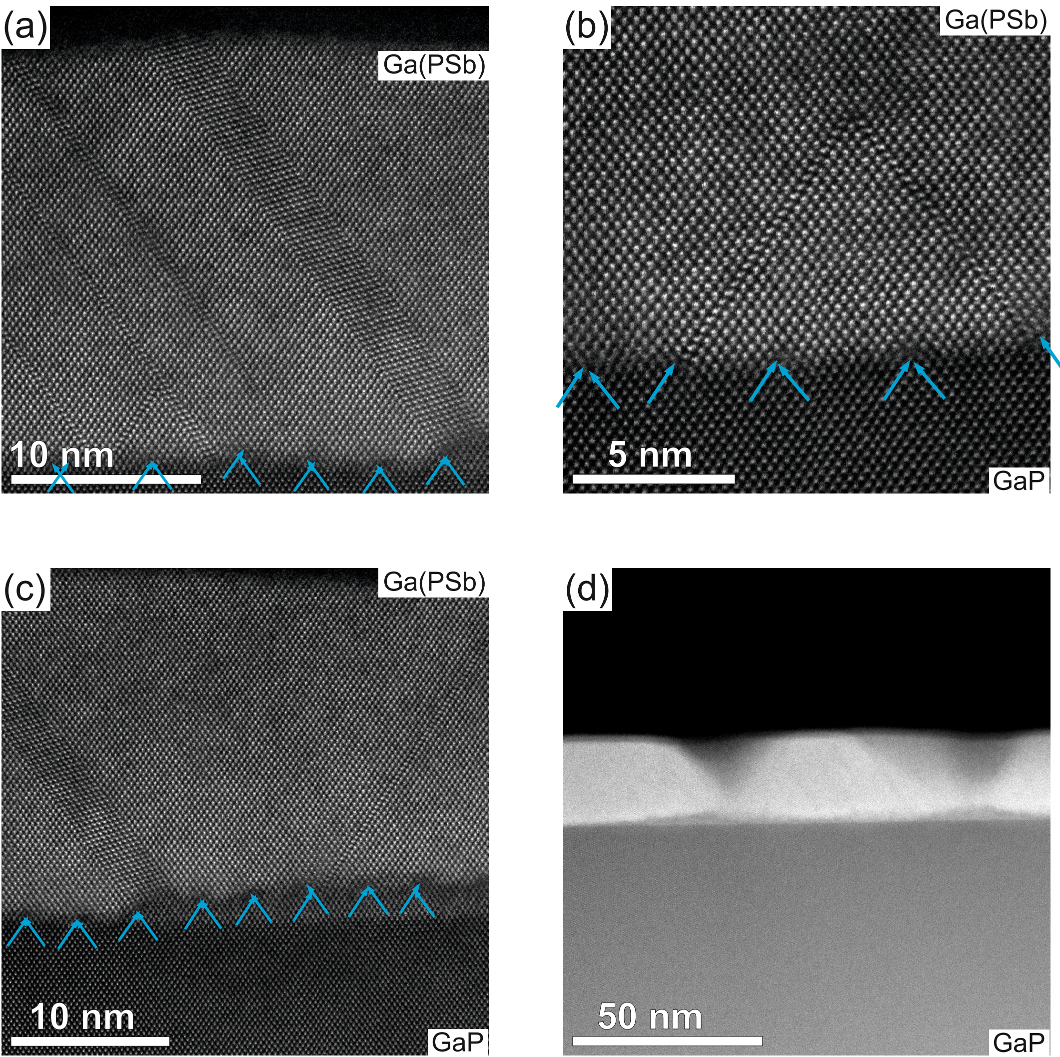

Figure 4.5: HAADF STEM images of a Ga(PSb) coalesced buffer layer of 20 nm nominal thickness grown on GaP/Si. The blue arrows indicate again the additional {111} lattice planes that form the dislocations. Image (c) and (d) reveal an interlayer between the GaP and metamorphic Ga(PSb) buffer layer.

et al. [165] or in GaP/Si by Narayanan et al [167].

Figure 4.5 (c) revealed a striking difference to the images (a) & (b) related to the interface. Here, there was no sharp transition between GaP and Ga(PSb) but an interlayer, which had grown pseudomorphically to GaP, could be observed. The contrast of this interlayer is brighter than GaP but much darker than Ga(PSb). This has to be attributed to the group V element, since Ga is the only group III source. This leads to the assumption, that a Ga(PSb) layer with a much lower Sb-content and a lattice constant of GaP has formed. The dislocations as well as SFs and twins were generated at the interface between the pseudomorphic low-Sb-content Ga(PSb) layer and the metamorphic grown high-Sb-content Ga(PSb) layer. In 4.5 (d), an overview image of the sample revealed that

these pseudomorphic interlayers mainly appeared in the trenches of the buffer layer where the sample has not coalesced yet. These trenches have already been observed in the AFM investigations as shown in figure 4.3. Since no pseudomorphic low-Sb content Ga(PSb) islands or layers between the islands have been observed in samples with island-like structures, it means that they appear at a later stage of growth. Either this is attributed to the high mismatch between Ga(PSb)/GaP or to the growth conditions. It could be, that the gas phase within the trenches is different from the reactor in such a way that the Sb-integration is hindered, for example, by offering not enough Sb or providing too much P. In the Ga(AsSb) layers, no such pseudomorphic interlayer was observed. This might be hint that this pseudomorphic interlayer appears due to growth conditions and not due to strain.

After coalescence, figure 4.2 has shown that thick samples offer a smooth surface that could be used as buffer layer for the integration of an active (GaIn)As channel. Figures 4.6 and 4.7 show the results of the investigations of a Ga(PSb) buffer layer of 100 nm nominal thickness by ADF imaging. The ADF imaging collects the intensity scattered to low angles and is therefore more sensitive to strain within layer. This strain can be caused by threading dislocations or stacking faults. The <110> overview images in figure 4.6 have been obtained by stitching together several individual images, which leads to slight contrast changes and sharp borders within the single figures. The polarities have been determined by high-resolution imaging. SF appear as bright straight lines with a 54.7° inclination angle to the GaP interface since they run along the {111} lattice planes, while all other bright lines are attributed to threading dislocations. TD not only form during the coalescence of the islands but are connected to the misfit dislocation network [40, 42]. Wang et al. [157] showed that imperfections in the Lomer dislocation network are unavoidable and lead to edge or mixed type threading dislocations. Figure 4.6 shows that some of the TD formed loops, but the majority followed the growth direction along [001] and end at the surface. These vertical threading dislocations have previously been reported in the highly mismatched SiGe/Si material system [168–170]. According to the Burgers vector analysis of Marzegalli et al. [170], the vertical TD can be either edge type or screw type.

The sample thickness in viewing direction was determined in the GaP buffer layer. Hereby, the GaP intensity in the experimental image is normalized to the total beam intensity and then compared to normalized, simulated GaP intensities of known thicknesses. The Ga-polar side in (a) had a thickness of 39 nm ± 8 nm to 72 nm ± 9 nm while the P-polar side was less steep with 40 nm ± 7 nm to 60 nm ± 9 nm. The high standard deviations result from the low signal-to-noise ratios in the large field of view images with a size of 1024x1024 pixels. Assuming an average thickness of 55 and 50 nm for the Ga-polar and P-polar viewing directions, the stacking fault densities were $1.7 \cdot 10^{10}\,cm^{-2}$

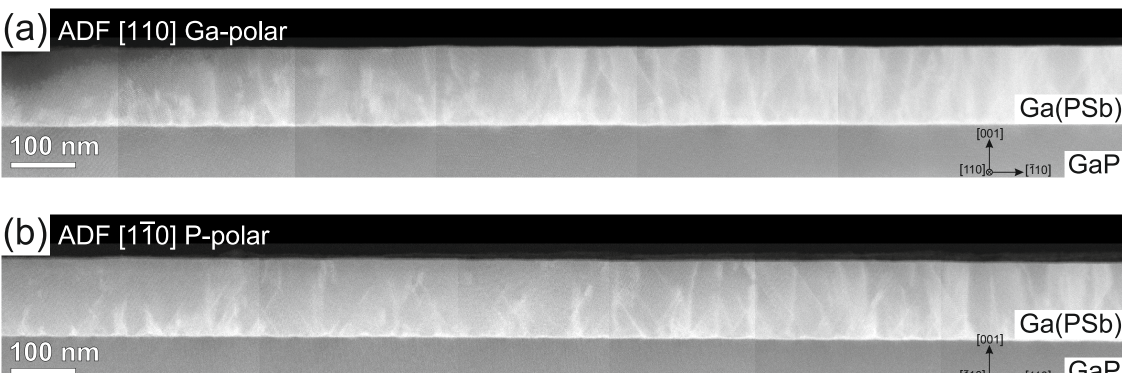

Figure 4.6: Overview ADF images of Ga(PSb) of 100 nm nominal thickness on GaP/Si. Image (a) shows the Ga-polar [110] projection and (b) the P-polar [$\bar{1}$10] projection. Stacking faults appear as bright straight lines with a 54.7° inclination angle to the GaP interface and all other bright lines are attributed to threading dislocations.

and $3.7 \cdot 10^{10}\, cm^{-2}$, respectively. The sample thickness in the Ga-polar viewing direction was higher, which led to an intensity increase so that the stacking fault were less visible and the density of SF in the Ga-polar direction might be slightly underestimated. However, the SF density in the P-polar [$\bar{1}$10] projection is more than twice as high as in the Ga-polar direction, so the SF density in the Ga-polar layer would probably still be lower. It should be considered that TEM only investigates a very small area and this result does not have to apply for a larger area. However, it is possible that the generation of stacking faults is favored in one direction due to the growth conditions. This has been observed for the island nucleation of GaP on Si before [64, 167].

The threading dislocation densities were evaluated to $4.1 \cdot 10^{10}\, cm^{-2}$ and $3.7 \cdot 10^{10}\, cm^{-2}$ for the [110] and [$\bar{1}$10] projection, respectively. This estimation was supported by the ADF plan-view image in figure 4.7. Here, a network of threading dislocations can be observed. The green spots mark lattice defects forcing through the surface. They will continue in any active material grown onto the buffer layer. Their density could be calculated to $3 \cdot 10^{10}\, cm^{-2}$ which fits to the estimations of the cross section samples. The estimated defect densities for this layer were extremely high. The maximal tolerable threading dislocation density for electronic [171, 172], optoelectronic [173] or solar cell devices [174] is several orders of magnitude lower, in the range of $10^5\, cm^{-2}$ - $10^7\, cm^{-2}$. A high density of TD as well as SF and twins, as observed for the investigated Ga(PSb) sample, are highly unfavorable since they degrade the performance and lifetime of those devices.

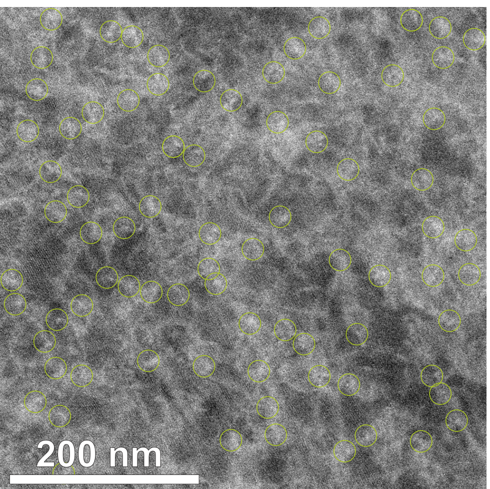

Figure 4.7: Plan-view ADF image of Ga(PSb) of 100 nm nominal thickness on GaP/Si. The green spots mark lattice defects forcing through the surface.

Composition and strain evaluation by reciprocal space mapping in comparison to high-resolution (S)TEM imaging

In addition to the (S)TEM investigations that have given insight into the morphology, the sample of 100 nm nominal thickness has also been investigated by recording reciprocal space maps in XRD as shown in figure 4.8. The figure displays the $\bar{2}\bar{2}4$ reflection. The 004 reflection has also been measured to correct the results with this symmetric peak as described in section 3.3. The narrow peak with the highest intensity in figure 4.8 is the Si substrate peak with the GaP peak next to it. The GaP peak is at $q_x = 0$, showing that GaP was grown pseudomorphically on Si. The broad peak with low intensity is the Ga(PSb) layer peak. It is inclined to the substrate peak, showing that the layer has relaxed as already shown by the (S)TEM investigations. The high defect densities that have been observed in TEM are responsible for the high full width at half maximum (FWHM) of the Ga(PSb) peak in the RSM. This high FWHM makes the reading of the maximum peak position difficult. Therefore, the reading had been conducted at different times with different presentations of the RSM as bitmap, contour map and RSM contour map. The results presented in the following are the mean values and standard deviations of these different measurements, respectively. The broadening is more severe for ω than for 2Θ. This justifies the approach of using the RSM of the symmetric 004 reflection to correct the measured ω of the $\bar{2}\bar{2}4$ reflection under the assumption that the 2Θ have been measured well. The different readings of the angles showed indeed a wider variation in ω compared to the 2Θ values.

Reciprocal space mapping allows to gather information about the composition of the sample as well as its strain at the same time. Hence, it is possible to calculate the relaxed

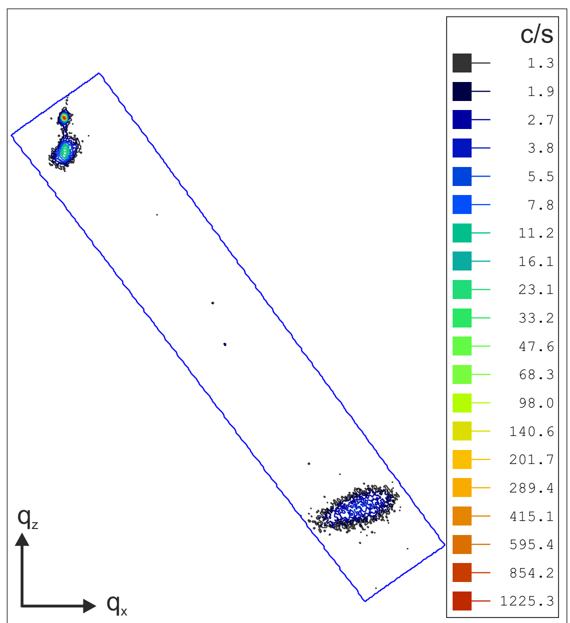

Figure 4.8: XRD-RSM of the $\bar{2}\bar{2}4$ reflection of Ga(PSb) of 100 nm nominal thickness on GaP/Si.

lattice constant of the Ga(PSb) layer according to equation 2.32 as well as its composition using Vegard's law. The resulting composition and the relaxed lattice constant of the 100 nm nominal thickness samples of Ga(PSb) are compared to its corresponding Ga(AsSb) sample in table 4.1.

	25639 Ga(PSb) 100 nm	**25576 Ga(AsSb) 100 nm**
Sb-fraction (group V) / [%]	67.3 ± 0.3	55.7 ± 0.4
lattice constant a_L / [nm]	0.589 ± 0.0002	0.590 ± 0.0002

Table 4.1: Sb-concentration (group V) and lattice constant of Ga(PSb) and Ga(AsSb) buffer layers of 100nm nominal thickness grown on GaP/Si calculated from $\bar{2}\bar{2}4$ and 004 reciprocal space maps.

The table shows that the percentage of Sb (measured on group V) in the Ga(AsSb) layer differed from in the respective buffer layer grown under the same conditions on InP substrate in section 4.1.1. The pseudomorphically grown buffer layers on InP have a Sb fraction of 66.7 % in Ga(PSb) and 51.4 % in Ga(AsSb). Within the precision of the measurement, the Sb fraction in the Ga(PSb) layer on the GaP/Si stayed the same, while it increased for the Ga(AsSb) layer. However, changing the substrate alters the growth conditions so variations in the composition can be expected. This change in composition leads to an increase of the buffer layer lattice constant. However, the much

higher composition difference in Ga(AsSb) did not have an as strong impact on the lattice constant. This can be explained by the different covalent radius of the atoms which is larger for the As than for P. The resulting lattice constants of both samples were slightly larger than 0.58687 nm [175], the lattice constant of InP. The relative deviation, or rather the misfit $mf = \frac{a_{layer} - a_{InP}}{a_{InP}}$, was 0.27 % for the Ga(PSb) and 0.53 % for the Ga(AsSb) layer. The aim to grow a Sb-based buffer layer with the lattice constant of InP on a Si substrate has thereby been reached with a slight mismatch. However, the initial, pseudomorphic buffer layers grown on InP, $Ga(P_{66.7}Sb_{33.3})$ and $Ga(As_{48.6}Sb_{51.4})$, were also both slightly mismatched by 0.2 % to InP, whereby the calculated lattice constant was 0.588 nm in both cases.

The results of the RSM could then be used to calculate the misfit $mf = \frac{a_L - a_{Si}}{a_{Si}}$ of the buffer layers to the silicon substrate using the relaxed layer lattice constant a_L of table 4.1 and the lattice constant of Si, $a_{Si} = 0.543105\, nm$ [175]. The residual strain to the relaxed layer lattice constant in-plane ($\varepsilon_{\parallel}^{res}$) and in growth direction ($\varepsilon_{\perp}^{res}$) could also be calculated using the measured lattice spacings in-plane $d_{\parallel}$ and in growth-direction $d_{\perp}$ in $\varepsilon_i^{res} = \frac{d_i - a_L}{a_L}$. The measured lattice spacings d_i could also be used to evaluate the in-plane and perpendicular misfit $mf_i = \frac{d_i - a_{Si}}{a_{Si}}$. The measured in-plane lattice spacings $d_{\parallel}$ can be used to calculate the plastic relaxation $R = \frac{d_{\parallel} - a_{Si}}{a_L - a_{Si}} \cdot 100\%$. These findings are presented in table 4.2.

	25639 Ga(PSb) 100 nm	**25576 Ga(AsSb) 100 nm**
misfit / [%]	8.4	8.6
$\varepsilon_{\parallel}^{res}$ / [%]	-0.13	-0.28
$\varepsilon_{\perp}^{res}$ / [%]	0.12	0.25
$mf_{\parallel}$ / [%]	8.2	8.3
$mf_{\perp}$ / [%]	8.5	8.9
R / [%]	98.3	96.5

Table 4.2: Misfit, strain and residual strain components in-plane and in growth direction of Ga(PSb) and Ga(AsSb) layers of 100nm nominal thickness grown on GaP/Si calculated from $\bar{2}\bar{2}4$ and 004 reciprocal space maps.

As presented in table 4.1, the relaxed lattice constant of Ga(AsSb) was slightly higher than Ga(PSb). This leads, by definition, to a higher mismatch of 8.6 % compared to 8.4 %. The lattice mismatch mf between InP and Si is 8.1 %. More important, however, were the findings of the residual strain in-plane and in growth direction. They state that the buffer layers are nearly completely relaxed. The Ga(PSb) layer showed a residual strain of -0.13 % in-plane and 0.12 % perpendicular to it, while the residual strain of the Ga(AsSb) layer was twice as high: -0.28 % in-plane and 0.25 % in growth direction. This means that for both cases the in-plane lattice spacing $d_{||}$ was slightly compressed compared to a_L. The plastic relaxation R gave the same result. It states that Ga(PSb) is nearly completely relaxed to 98.3 % while Ga(AsSb) is relaxed to 96.5 %. Since both buffer layers have a slight residual compressive strain in-plane and tensile strain in the perpendicular growth direction, the in-plane misfit ($mf_{||}$) is smaller than mf and the misfit in growth direction ($mf_{\perp}$) is larger, respectively.

In addition to the results derived from the RSM in XRD, (S)TEM measurements were conducted to evaluate relaxation and strain by a further method. Hereby, high-resolution HAADF and TEM images were evaluated by measuring the distance between the dislocations as shown in figure 4.9. The dislocations are recognizable as inserted {111} planes in GaP. This recognition will be much easier if only the filtered {111} lattice planes are examined. Therefore, the fast Fourier transformation of the HR images were taken (inset of 4.9 (a)), the {111} spots in the FFT were masked (insets of 4.9 (b) & (c)) and an inverse FFT was performed (4.9 (b) & (c)). The additional {111} planes in GaP are clearly visible in images (b) & (c) and have been marked by blue arrows. Overlaying these arrows onto the original image like in 4.9 (d), 60° dislocation, Lomer dislocations and 60° dislocation pairs could be distinguished.

The image shown in figure 4.9 is Ga(PSb) of 100 nm nominal thickness on GaP/Si. The dislocations were again mainly Lomer and 60° pair dislocations. Similar to figure 4.5, a low-antimony content layer grown pseudomorphically to GaP could be observed again. The spacing between the dislocations can be calculated by counting the number (n) of {111} lattice planes between the dislocations and multiply them with the lattice distance between two {111} lattice planes. Since the inserted lattice planes belong to GaP grown pseudomorphically on Si substrate and the samples are observed in <110> projection in a zinc blende crystal, this distance is $\frac{a_{Si}}{\sqrt{2}}$ for geometrical reasons, so the misfit dislocation spacing can be evaluated by

$$d_{MD} = n \cdot \frac{a_{Si}}{\sqrt{2}} \,. \tag{4.1}$$

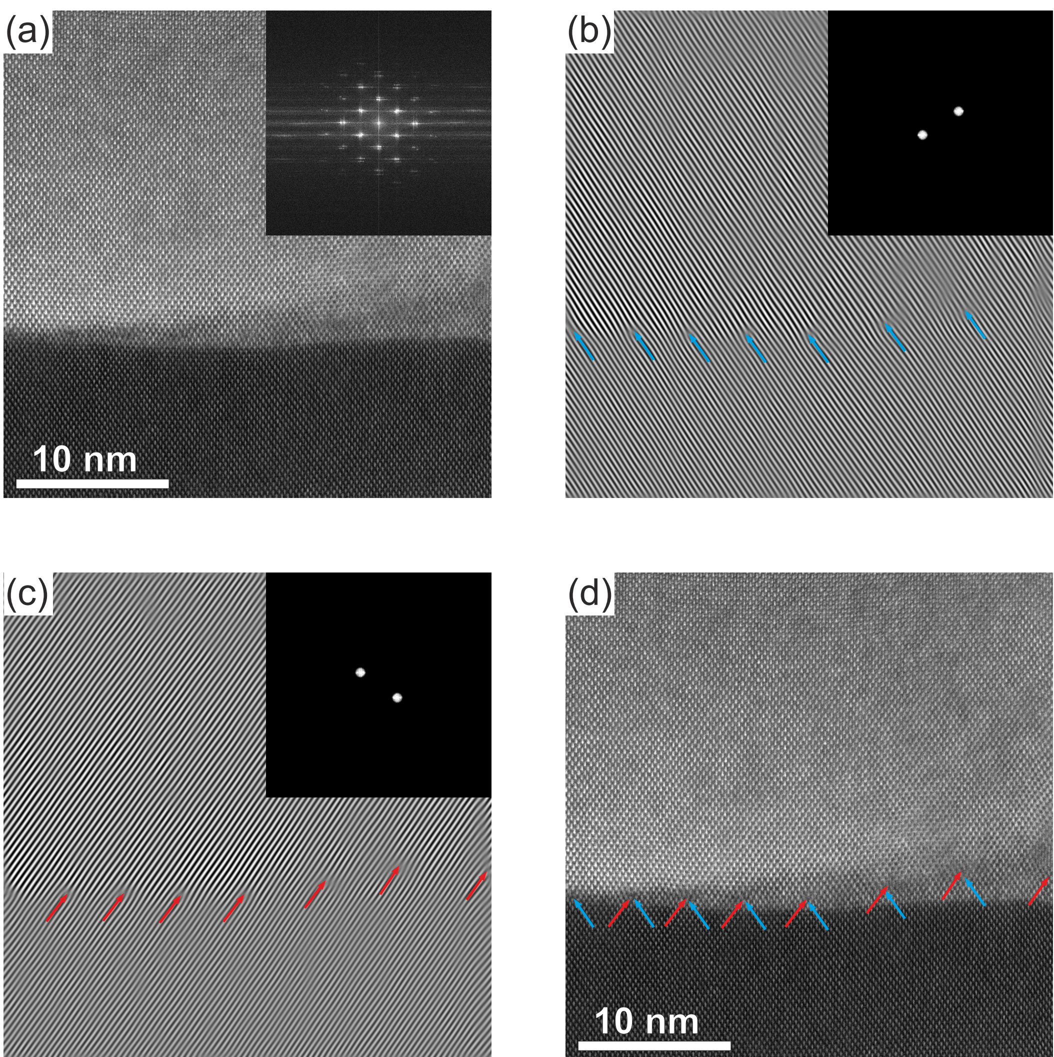

Figure 4.9: Work flow to demonstrate evaluation of dislocations in high-resolution (S)TEM images (a), using FFT and inverse FFT (images (b) and (c)) to localize dislocations at the interface of the buffer layer to GaP as shown in image (d). The example image displayed here is Ga(PSb) layer of 100 nm nominal thickness on GaP/Si.

The average dislocation distances d_{MD} of several Ga(PSb) and Ga(AsSb) samples are presented in table 4.3.

According to Dunstan [34], the average dislocation distance is related to the misfit-reliving component of the Burgers vector $|\vec{b_{mf}}|$ (in the projection perpendicular to the dislocation line) and the in-plane components of the plastic strain tensor e_{xx} and e_{yy} along the two (110) directions, parallel to the misfit dislocations by

$$d_{MD_x} = \frac{|\vec{b_{mf}}|}{e_{xx}} \quad \& \quad d_{MD_y} = \frac{|\vec{b_r}|}{e_{yy}} \,. \tag{4.2}$$

In anisotropic relaxed layers, the two plastic in-plane strain components and therefore the dislocation distances will differ from each other. The plastic strain components are related to the misfit and elastic stress by $e_{xx} = mf - \varepsilon_1$ and $e_{yy} = mf - \varepsilon_2$ and will range from zero for a pseudomorphic layer to mf for a fully relaxed layer with vanishing stresses. For completely relaxed layer with arrays of 90° edge dislocations, where the Burgers vector is $|\vec{b}| = |\vec{b_{mf}}| = |\frac{a_L}{2}[110]|$ and the stress vanishes, the misfit dislocation distance in equation 4.2 can be reformulated to

$$d_{MD} = \frac{a_L}{\sqrt{2}} \cdot \frac{1}{mf} = \frac{a_{Si} \cdot a_L}{(a_L - a_{Si}) \cdot \sqrt{2}} \,. \tag{4.3}$$

By comparing equation 4.1 and 4.3 and using the definition of the misfit, the average number n of lattice planes between dislocations becomes a direct measure of the misfit mf with

$$mf = \frac{1}{n-1} \,. \tag{4.4}$$

The misfit has been calculated for several samples under these assumptions and are also presented in table 4.3.

Table 4.3 shows not only results of the thick buffer layers that have already been investigated by RSM but also of thinner layers of 20 nm nominal thickness and the island-like structures. Several noticeable conclusions can be drawn from this list.

Firstly, the table shows that the average dislocation distance increased with increasing layer thickness in Ga(PSb) while in Ga(AsSb) the nominal 20 nm thick sample had the same d_{MD} as the nominal 100 nm buffer and only the islands had a decreased dislocation spacing. An increase in dislocation spacing leads to an decrease in the calculated lattice mismatch which can be explained by the according math of the evaluation. Secondly, the standard deviation of the average dislocation distance was very high, up to one nm. This is 20 - 25 % of the measured mean values. This evaluation has been performed on a comparably small number of dislocations so that the standard error of the mean dislocation spacings ($SE_{\bar{x}}$) are also listed to give a measure for the accuracy of the measured mean. Samples for which HRTEM as well as HAADF investigations have been conducted, the mean dislocation distances lie within their standard errors. However, these high standard deviations can not only be explained by the low statistics of the measurement, but it should be attributed to the inhomogeneous relaxation during the island-like nucleation and the consequent incomplete coalescence of the thin layers. Thirdly, the evaluated misfit of the nominal 100 nm thick buffer layers for Ga(PSb) and Ga(AsSb) did not give the same results like the evaluation of the RSM.

sample	**thickness**	**polarity**	**method**	d_{MD} / **[nm]**	$d_{MD}\ SE_{\bar{x}}$	mf / **[%]**
25639 Ga(PSb)	**100 nm**	**Ga-polar**	HAADF	4.84 ± 0.90	0.08	8.6
25639 Ga(PSb)	**100 nm**	**P-polar**	HAADF	4.91 ± 0.89	0.10	8.5
25641 Ga(PSb)	**20 nm**	**Ga-polar**	HAADF	4.28 ± 0.34	0.07	9.8
25641 Ga(PSb)	**20 nm**	**P-polar**	HAADF	4.40 ± 0.52	0.10	9.5
25641 Ga(PSb)	**20 nm**	-	HRTEM	4.53 ± 0.74	0.08	9.3
25843 Ga(PSb)	**20 nm**	**Ga-polar**	HRTEM	4.07 ± 1.09	0.10	10.4
25843 Ga(PSb)	**20 nm**	**P-polar**	HAADF	4.32 ± 0.67	0.10	9.7
25843 Ga(PSb)	**20 nm**	**P-polar**	HRTEM	4.19 ± 0.99	0.04	10.1
25842 Ga(PSb)	**island**	**Ga-polar**	HAADF	3.96 ± 0.28	0.05	10.7
25842 Ga(PSb)	**island**	**Ga-polar**	HRTEM	4.11 ± 0.90	0.11	10.3
25842 Ga(PSb)	**island**	**P-polar**	HRTEM	4.20 ± 0.78	0.07	10.1
25576 Ga(AsSb)	**100 nm**	**Ga-polar**	HAADF	4.97 ± 0.87	0.18	8.4
25576 Ga(AsSb)	**100 nm**	**P-polar**	HAADF	5.00 ± 0.67	0.09	8.3
25576 Ga(AsSb)	**100 nm**	**P-polar**	HRTEM	4.73 ± 0.51	0.24	8.5
25836 Ga(AsSb)	**20 nm**	**Ga-polar**	HAADF	4.92 ± 0.92	0.15	8.5
25536 Ga(AsSb)	**20 nm**	**P-polar**	HAADF	4.93 ± 0.51	0.08	8.5
25838 Ga(AsSb)	**island**	**Ga-polar**	HAADF	4.30 ± 0.54	0.11	9.8
25538 Ga(AsSb)	**island**	**P-polar**	HAADF	4.37 ± 0.50	0.07	9.6

Table 4.3: Average dislocation spacing ± standard deviation and its standard error of the mean dislocation spacing, misfit, and strain of Ga(PSb) and Ga(AsSb) layers grown on GaP/Si of different thicknesses investigated in [110] and [$\bar{1}$10] projection by TEM and STEM.

Several considerations had to be taken into account for these results. Especially the evaluation of misfit had to be treated carefully. The misfit was calculated under the assumption of perfect relaxation by arrays of Lomer dislocations. However, the RSM showed that even the 100 nm thick samples were not perfectly relaxed. Moreover, the (S)TEM images revealed that the dislocations were not only 90° Lomer dislocations but also 60° dislocation pairs and some 60° dislocations. The Burgers vector of a 60° dislocation is e.g $\vec{b} = (a_L/2)[101] = (a_L/4)[1\bar{1}0] + (a_L/4)[110] + (a_L/2)[001] = \vec{b_{mf}} + \vec{b_{screw}} + \vec{b_{tilt}}$ [46]. The misfit-relieving value $|\vec{b_{mf}}|$ is half the amount of an edge dislocation. In case of a 60° dislocation pair, two 60° dislocations with parallel screw component react with each other. The resulting Burgers vector has no tilt component, a non-vanishing screw component and the same misfit-relieving component as a Lomer dislocation. So in case of the Ga(PSb) and Ga(AsSb) 100 nm thick buffer layers, that were relaxed by Lomer and 60° dislocation pairs to 98.3 and 96.5 %, the assumption to calculate misfit from the dislocation distance was justifiable. However, the dislocations were not equidistant to each other, leading to the high standard deviation of d_{MD} that can explain the deviations for the mf from the results in table 4.2. The high standard deviation can be explained by the fact that the layers were, for one, not relaxed perfectly and, for two, relaxed under the presence of a high TD and SF density as well as 60° dislocations. Using equation 4.2 with the a_L values of table 4.1, the expected dislocation spacings were 4.97 nm for Ga(PSb) and 4.92 nm for Ga(AsSb). These values were within the standard errors of the mean dislocation spacings of each of the measured samples.

The thin Ga(AsSb) buffer layer of 20 nm nominal thickness had, within the standard error of the mean, the same average dislocation distance as the thick buffer layer. This means that they were nearly completely relaxed as well. The lattice mismatch, that was calculated from the mean number of lattice planes between the dislocations, was 8.5 %. The thin Ga(PSb) layers on the other hand showed significant smaller mean dislocation distances. This implies, that these layers were not fully relaxed. That actually means that the calculated misfit did not really hold true because the underlying assumption of perfect relaxation was not fulfilled. The misfit dislocations at the interface had been identified in figure 4.5 to be mainly Lomer and 60° dislocation pairs so that $b_{mf} = \frac{a_L}{\sqrt{2}}$. Using $d_{MD} = \frac{b_{mf}}{e_{xx}}$ in order to calculate e_{xx} is, however, not possible because the values for a_L were unknown and cannot be measured by RSM since the sample thickness was too small. Since the mean dislocation distance was decreased, e_{xx} must be increased and/or a_L smaller than 0.5890 nm. The difference between the thin Ga(AsSb) and Ga(PSb) in relaxation can be explained by looking back at the AFM images in figure 4.3 (b) and (d). They showed that the surfaces of the two thin Ga(PSb) layers were not completely coalescent and had deep trenches. The AFM micrographs of the thin Ga(AsSb) on the other hand (not shown here) displays a smooth surface that is completely coalescent,

without trenches, looking similar to the thick Ga(AsSb) layer. That shows that only samples with a closed layer can relax completely. The islands have different degrees of relaxation due to plastic relaxation at the free island surface. The island-like structures were, similar to the thin Ga(PSb) layers, not completely relaxed for both buffer layers. This is in line with the just discussed results for the thin layers and the same conclusions about strain and misfit apply. It is, however, noticeable that the results for d_{MD} of Ga(AsSb) were larger than for Ga(PSb). That might also been explained by the corresponding AFM images. They show that the Ga(AsSb) island already started to coalesce. This could mean that the Ga(AsSb) islands had reached a higher degree of relaxation and therefore an increased mean dislocation spacing.

The samples were investigated along the Ga-polar [110] and the P-polar [$\bar{1}$10] projection. The average dislocation spacings of the Ga(PSb) samples were slightly increased for the P-polar direction. A difference in d_{MD} means a difference in relaxation. However, considering the high standard deviation and standard error of the mean, this deviation was not highly significant. An anisotropic relaxation should go along with an elongation of the islands which have neither been observed in TEM nor in AFM images. The differing mean dislocation spacings in Ga(PSb) can therefore be attributed to the statistical variations of the results. These variations are smaller for the Ga(AsSb) results where the mean values were very close to each other.

In the next step, the strain of the buffer layers have been investigated in the HRTEM images using the two conventional strain mapping approaches geometric phase analysis and peak pair analysis that have been introduced in section 3.4.9. Figure 4.10 shows the results for the thin Ga(PSb) layer (#25641). Image (a) is a high-resolution TEM image of the GaP/Ga(PSb) interface, where the blue arrows mark the dislocations. 4.10 (b) displays the $e_{\parallel}$ strain image from GPA with a mask size of 0.3 $\mathbf{g}$, $\mathbf{g}$ being the (111) reciprocal lattice vector. It showed that the epitaxial Ga(PSb) layer was highly strained compared to the GaP where the mapped strain was zero because of the GPA method of choosing a reference region where the strain is set to zero. The cores of the dislocations were visible as highly strained areas at the interface. The colored rectangles in image (a) show different areas where the mean strain and their standard deviation have been measured, in GaP for the reference and in Ga(PSb), the strained layer. These measurements have been performed for different mask sizes in GPA as well as PP for the in-plane strain $e_{\parallel}$ and in growth direction $e_{\perp}$. Hereby, $e_{\parallel}$ and $e_{\perp}$ were the difference of the mean strain measured in the reference area, where the strain should be zero, subtracted from the epitaxial area. The results are pesented in the graphs in figure 4.10 (c)-(f) and table 4.4. Figure 4.10 (c) and (d) showed the influence on the mean in-plane strain $e_{\parallel}$ when a different area to measure the mean in the reference (c) and in the epitaxial area (d) were chosen in dependence on the mask size.

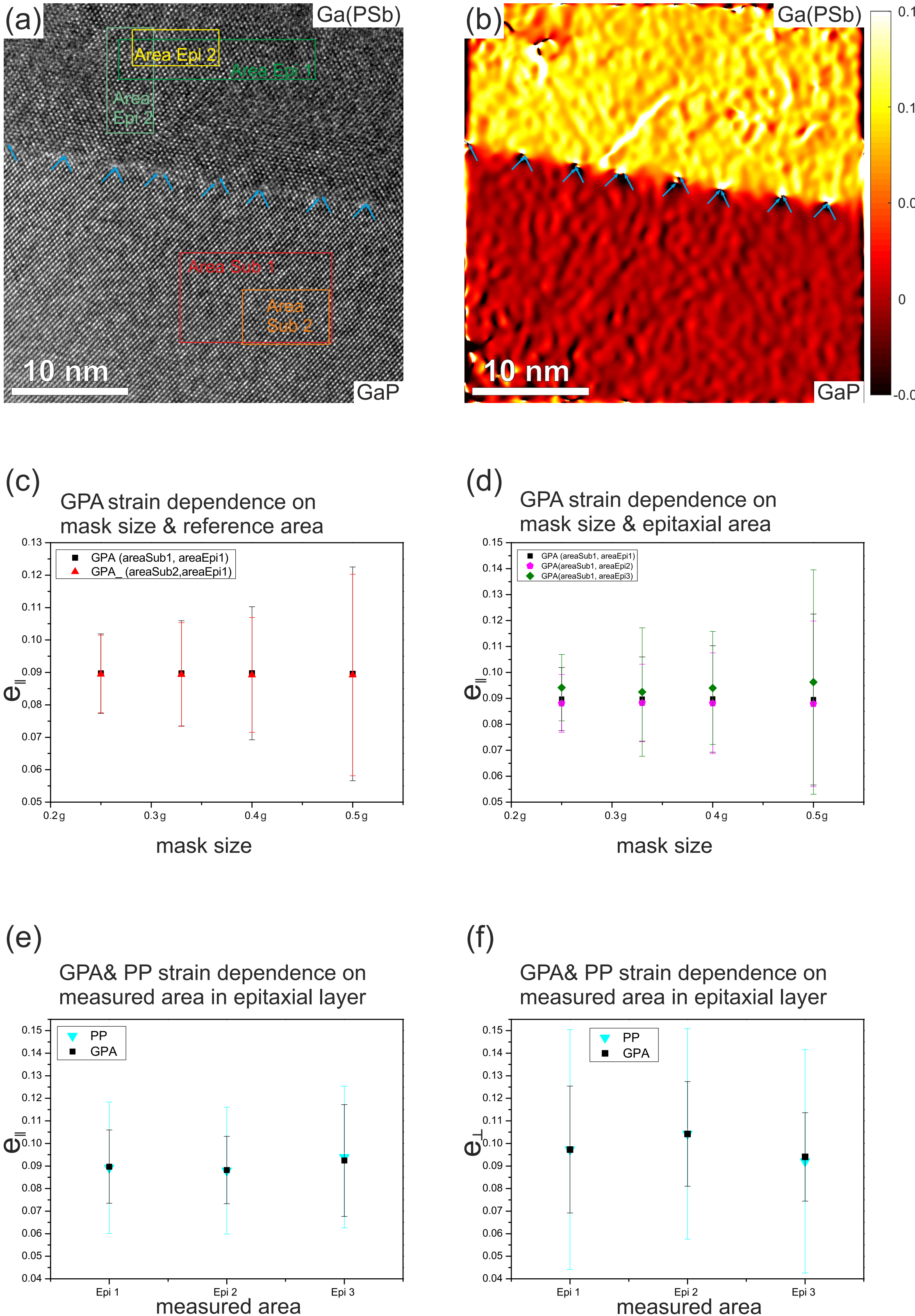

Figure 4.10: (a) HRTEM image of a thin Ga(PSb) buffer layer grown on GaP/Si. The rectangles indicate positions of strain evaluation. (b) $e_{\|}$ of GPA at mask size 0.3g. (c) GPA $e_{\|}$ in dependence on the strain in GaP and mask size, (d) GPA $e_{\|}$ in dependence on the strain in epitaxial layer and mask size, (e) GPA and PP $e_{\|}$, (e) GPA and PP $e_{\perp}$.

As expected, the first graph showed that choosing a different reference area did not change the resulting in-plane strain. The mean $e_{\|}$ also did not change with choosing a different mask size to obtain the GPA image. However, with increasing mask size the standard deviation increased due to artifacts caused by the specimen, electron source and the detector in accordance with Li et al. [176]. The second graph in image (d) showed that choosing a different area in the strained epitaxial layer changes the results for $e_{\|}$ which is not surprising considering that the standard deviations measured in the strained layer was up to twice as high as in the reference area. This means, the strain changes locally considerable. This can be again explained by the high density of threading dislocations and stacking faults in this layer.

The third graph in (e) shows in principle the same results as (d) with the added results of PP analysis. However, the strain is now plotted against the measured area in the epitaxial area instead of the mask size. Here, the mask size is kept at 0.3 g, as suggested by [176] in order to balance spacial resolution against noise. Image (f) presents the corresponding results for $e_{\perp}$. The two graphs showed that in both cases the mean strain measured by PP and GPA were the same. That means, the measured strain depended more on the measured area than on the method. However, the standard deviation for PP was higher than for GPA since at the same mask size, PP produced noisier images compared to GPA. Additionally, the standard deviations for $e_{\|}$ was lower compared to $e_{\perp}$.

Table 4.4 presents the strain evaluated at mask size 0.3 g by GPA, as in 4.10 (e) and (f). It was measured in different images for a thin Ga(PSb) and the thick Ga(AsSb) buffer layer. The mean strain and its standard deviation was evaluated in different areas for each image and the presented values are the mean thereof. As expected from the just discussed results, the standard deviations were quite high and the mean strain deviates within it since it had been measured in very different areas.

However, two conclusions can be taken from these findings. First, the mean strain of the thick Ga(AsSb) buffer layer was in two of the three images nearly the same in both directions and fitted to the previous conclusions that this layer is nearly completely relaxed. The third image shows a higher mean strain in growth direction, but it was taken in a higher magnification than the other two images, close to two stacking faults and a threading dislocation. This led to the increase in $e_{\perp}$ due to the high distortions in this image. The second observation is that the strain of the thin Ga(PSb) layer is higher than the thick Ga(AsSb) layer. This also fitted to the results already presented in in 4.3, showing that this layer was not fully relaxed yet.

This section has shown that it was possible to grow nearly fully relaxed Sb-based buffer layers onto the GaP/Si pseudosubstrate. However, the beginning the growth started with

	$e_{\parallel}$ TEM / [%]	$e_{\perp}$ TEM / [%]
25641 Ga(PSb) 20 nm image 1	9.0 ± 1.8	9.8 ± 2.5
25641 Ga(PSb) 20 nm image 2	8.8 ± 1.6	10.2± 2.6
25576 Ga(AsSb) 100 nm image 1	7.8 ± 2.7	8.0 ± 2.4
25576 Ga(AsSb) 100 nm image 2	8.0 ± 2.0	8.0 ± 2.5
25576 Ga(AsSb) 100 nm image 3	7.9 ± 1.9	8.9 ± 2.3

Table 4.4: In-plane and perpendicular strain measured by GPA in different HRTEM images of the thin Ga(PSb) and the thick Ga(AsSb) layers grown on GaP/Si.

island-like structures which coalesced with continuing growth time. The layers were not relaxed as long as they have not grown together. In consequence of stacking faults in the islands and a different degree of relaxation of these island, stacking faults, twins, microtwins and threading dislocations were generated in a high density after coalescence. Moreover, a low Sb-content layer that had grown pseudomorphically onto GaP has been observed for Ga(PSb) in the trenches of the uncoalescent thin samples. The following sections deal with several approach to overcome these problems in Ga(PSb) buffer in order to achieve high quality buffer layers with low defect densities.

4.1.3 Variation of growth parameters

The previous parts have dealt with the growth of the Sb-based buffer layers on InP substrate and their transfer on GaP/Si pseudosubstrate. Hereby, the growth conditions for the buffer layers on GaP/Si have been determined on the InP substrate. The only varied growth parameter has been a pre-run of TESb that has not shown any influence on the nucleation. The resulting buffer layers were grown in different thicknesses and investigated thoroughly in the last section with the focus on Ga(PSb). This section presents the investigations of Ga(PSb) buffer layers grown under changing growth conditions. The gas phase during growth was varied by changing the partial pressures of TEGa, TBP and TESb.

The resulting samples have been investigated by XRD rocking curves in order to determine their composition. However, since the degree of relaxation is unknown, the evaluated composition can only be specified within a certain range. This could be solved by recording reciprocal space maps in XRD, but most of the samples were too thin. Figure 4.11 shows the $Ga(P_{(1-x)}Sb_x)$ composition in dependence on different gas phase ratios of the

TEGa, TBP and TESb partial pressures. The phosphorous incorporation in Ga(PSb) was analyzed in dependence on the $P/III = p_P(TBP)/p_P(TEGa)$ ratio while the antimony incorporation was investigated in dependence on the $Sb/III = p_P(TESb)/p_P(TEGa)$ and the $Sb/V = p_P(TESb)/(p_P(TESb)/ + p_P(TBP))$ ratios. Since the p_P of TBP was much higher than $p_P(TESb)$, the P/III ratio was close to the V/III ratio and Sb/V was nearly the Sb/P ratio.

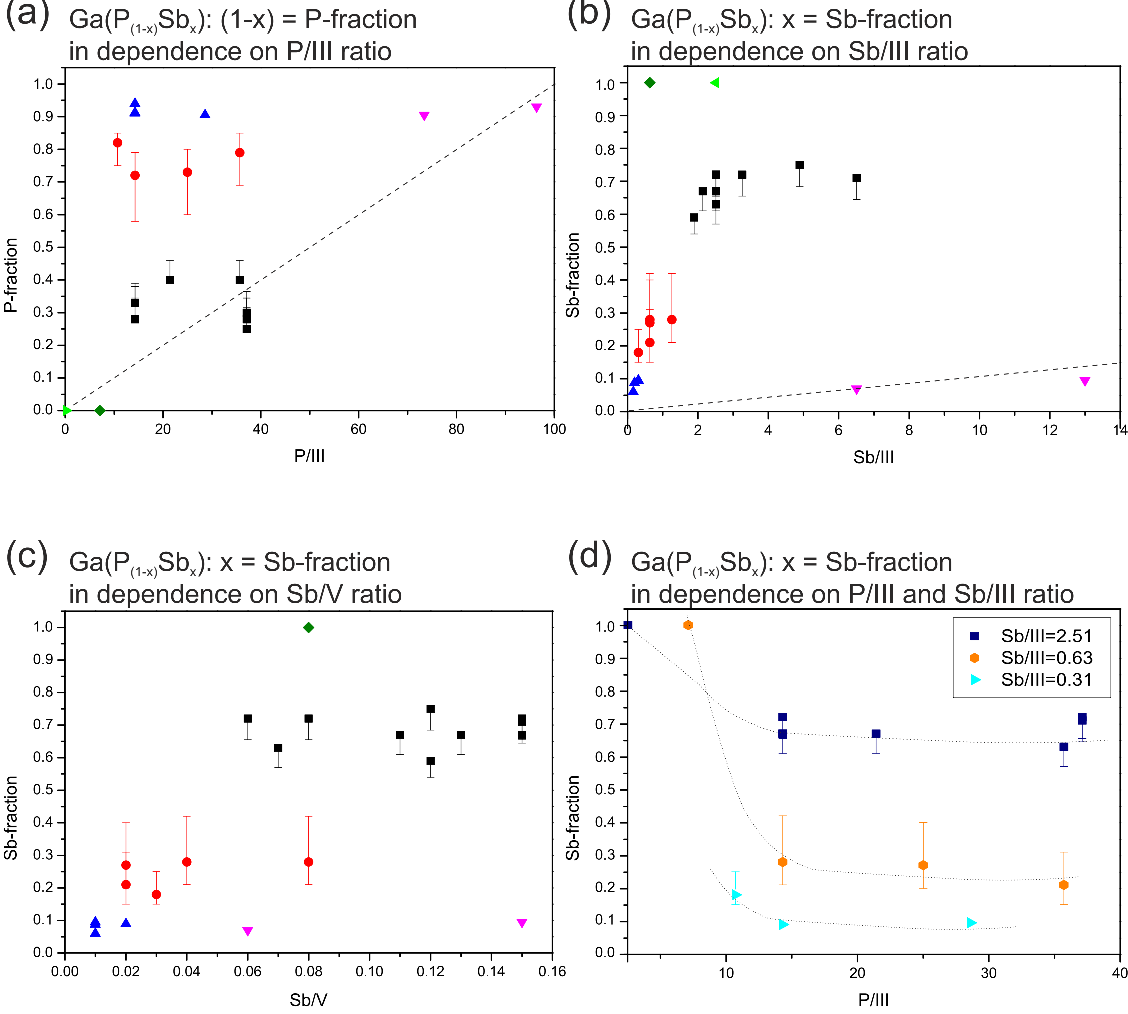

Figure 4.11: Composition of $Ga(P_{(1-x)}Sb_x)$ on GaP/Si in dependence on (a) P/III ratio, (b) Sb/III ratio, (c) Sb/V ratio and (d) P/III ratio in dependence on constant Sb/III ratio. The black dotted lines are only guides to the eye, not fits.

It is quite noticeable, that the data points have different colors and error bars. The black squares had compositions comparable to the already investigated metamorphic buffer layer with $Ga(P_{33}Sb_{67})$. In fact, one of the data points at $P/III = 14.3$ with $Ga(P_{33}Sb_{67})$ belongs to this sample. Since this sample was relaxed to 98 % according to the rms analysis, there is no error bar. For the other samples with black squares, the degree of relaxation has not been evaluated and they are plotted at the composition at 100 % relaxation.

This is most probable not true, so the error bars up to 90 % relaxation are drawn in the graph. Reproducing the already investigated sample with $Ga(P_{33}Sb_{67})$ at a different epitaxy machine at the same growth conditions gave a result of $Ga(P_{28}Sb_{72})$ at 100 % relaxation which fits within the error bar to the previous result. The green data points belong to binary GaSb. There is no error bar, because there is no uncertainty. The sample represented by a light green triangle was grown as binary GaSb, so phosphorous was not offered at all. The blue and magenta triangles belong to samples with less than 10 % of antimony, similar to the low-antimony regions that have been observed in figure 4.5. Two different colors have been chosen due to the very different growth conditions resulting in a similar Sb-fraction in Ga(PSb). They were assumed to grow pseudomorphically to GaP and be maximally 10 % relaxed, which would mean a change of composition of about 1 %. The error bars would be as high as the data point and have not been plotted for reasons of presentation. The assumption for the pseudomorphic growth with less than 10 % of relaxation has been built on the results of $Ga(P_{91.5}Sb_{9.5})$ (blue triangle) at $P/III = 14.3$. This sample was grown at 10 nm as well as 50 nm thickness and has been evaluated by XRD and AFM as shown in figure 4.12.

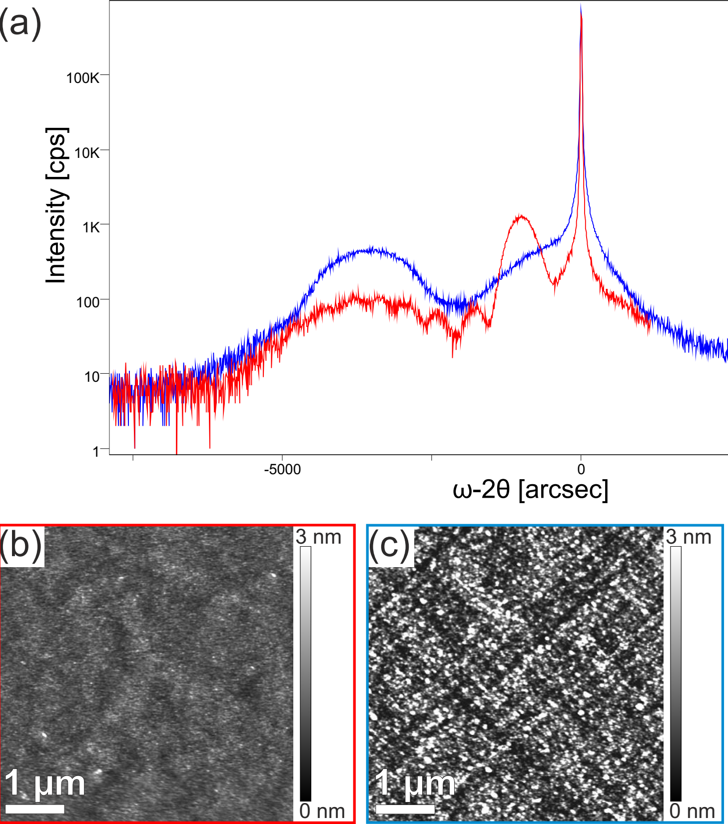

Figure 4.12: (a) XRD curves of low antimony content Ga(PSb) layers with 10 nm (red curve) and 50 nm thickness (blue curve) grown on GaP/Si. The corresponding AFM images are shown in (b) for the sample with 10 nm layer thickness and in (c) for the 50 nm layer thick sample.

If the thin 10 nm sample had 9.5 % of Sb at 0 % relaxation, the thick 50 nm sample would be 20 % relaxed, assuming that the composition has not changed. If the thin sample was relaxed to 100 % or 50 %, the thick sample would be 100 % or 60 % relaxed, respectively. However, this does not fit to the AFM results. The thin sample had a very smooth surface with a rms of 0.31 nm as shown in image (b), while the 50 nm sample had a cross-hatched surface as shown in 4.12 (c). The cross-hatch pattern is characteristic for a lattice mismatch lower than 2 % and is connected to the plastic and elastic strain relaxation by the misfit dislocation generation for incompletely relaxed samples [144]. This means that the thick sample was partly relaxed while the thin sample was below the critical thickness, before the onset of misfit dislocations and therefore pseudomorphic to GaP with less than 10 % of relaxation. The samples plotted as red data points have a higher amount of Sb than the ones plotted as blue triangle but a lower Sb-fraction than the samples represented by black squares. Since their degree of relaxation is unknown, they are plotted with the composition at 50 % relaxation and the error bars cover the whole composition range from completely relaxed to completely strained. However, the latter is more unlikely since the lattice mismatch to silicon is lower than 2 % for samples with less than 30 % relaxation . In this case, the 50 nm thick samples should show the cross-hatch pattern in AFM micrographs, which was not the case.

In figure 4.11 (a), the P-fraction is plotted against the P/III ratio. The graph can be divided into three different areas: a low P/III ratio regime from $0 - 10$, medium P/III ratios from $10 - 40$, and very high P/III ratios up to 100. In the low P/III ratio regime, only pure GaSb has been grown. The dark green diamond belongs to a sample with $P/III = 7.7$. Even though TBP is offered, no phosphorous was incorporated. This can be explained by the findings of Stegmüller et al [177]. They have calculated the decomposition pathways of TBP and have come to the conclusion that most of the TBP arrives undecomposed at the surface because the reaction channels exhibit either large energy barriers or unfavorable thermodynamics. These barriers might be changed by adsorption or reactions on the surface. For example, Stegmüller [178] has also shown that the barriers of $P(C_4H_9)H$ adsorbed on a hydrogen passivated Si(001) surface in the β-hydrogen elimination is decreased compared to the gas phase. It might be possible that TBP needs to react with TEGa or TESb to be decomposed. The higher the P/III ratio, the more P is available for incorporation. At high P/III ratios, larger than 40, the P dominated the gas phase as well as the composition of the buffer layer. The magenta triangles show buffer layers with less than 10 % of Sb. However, if as much as P had been incorporated in the buffer layer as TBP is contained in the gas phase, the P-fraction in Ga(PSb) would follow the black, dotted, straight line. This again shows, that the incorporation of P does not follow a linear behavior due to the low amount of decomposed TBP. Only at very high P/III ratios, the phosphorous incorporation followed this trend. In the medium P/III ratio range, the composition of Ga(PSb) could not be explained by the

P/III ratio any more. At the same P/III ratio, samples with very different compositions have been grown, for example at $P/III = 14.3$, there was $Ga(P_{91.5}Sb_{9.5})$ (blue triangle), $Ga(P_{72}Sb_{28})$ (red dot), and $Ga(P_{33}Sb_{67})$ (black square).

This behavior becomes understandable when considering the Sb/III and Sb/V in (b) and (c), respectively. In both graphs, the Sb content in the Ga(PSb) increased with the increasing offer of TESb until it saturated at a Sb-fraction of about 70 %. In (c), there was a outlier at Sb/V = 0.08, where at the same Sb/V ratio a sample with high antimony content of $Ga(P_{28}Sb_{72})$ (black square) was grown as expected as well as a sample with medium Sb-content, $Ga(P_{72}Sb_{28})$ (red dot). This showed, that the incorporation of Sb not only depends on the Sb/V ratio but also on the V/III ratio, since this data point was not an outlier in the first two graphs. In (b), the bisection line is indicating again the line at which the amount of Sb incorporated in Ga(PSb) compares to the amount of Sb in the gas phase. Consequently to the decreased phosphorous incorporation due to the inefficient decomposition and adsorption of TBP, the antimony incorporated into Ga(PSb) was much higher than TESb ratio in the gas phase. Similar to the the first graph, only the purple data points, that were grown at very high P/III ratios, followed this trend line. In addition to the mostly undecomposed TBP, this might also be explained by the assumption that antimony is behaving similar to bismuth (Bi). Ludewig et al. [149] reported that the Bi incorporation in dependence on the Bi/V ratio follows a linear trend until it reaches saturation level that can be explained by the amount of Bi at the surface. According to their model, Bi only acts as a surfactant below a minimum surface coverage, before it is incorporated into the layer by following a linear trend, and saturates at a certain Bi-fraction above a maximum critical surface coverage. The saturation level depends on the growth conditions and occurs with the formation of droplets. However, since antimony has a higher vapor pressure and therefore desorbs more easily from the surface, and a much higher amount of Sb is incorporated into the layer, no droplets are formed at the surface of Ga(PSb).

The last graph is a summary of the already presented results. It is complementary to (a), displaying the antimony instead of the phosphorous-fraction of the buffer layer in dependence on the P/III ratio in the low and medium P/III ratio range. The graph only contains data points of three different, constant Sb/III ratios, namely 2.51 (dark blue curve), 0.63 (orange curve) and 0.31 (cyan curve). The black, dotted lines are guides to the eye that show that the Sb-fractions declined, i.e. the P-fraction increased, with increasing P/III ratio. However, with increasing Sb/III ratio, the amount of Sb in the Ga(PSb) buffer layer increased, as demonstrated by the three different curves.

The investigation of the growth conditions of Ga(PSb) has shown that it is possible to incorporate Sb over a wide rage, from 7 % Sb to a saturation level of about 70 % in

dependence on the amount of TESb offered. Since most of the TBP was not decomposed, the amount of antimony incorporated into the Ga(PSb) layer was much higher than in the gas phase, except at very high P/III ratios.

4.1.4 Intentional growth of pseudomorphic interlayer

Section 4.1.2 has shown that the nucleation on GaP took place by the growth of island-like structures. One reason for this island-like nucleation could be a missing wetting layer on GaP. The first approach to improve the Ga(PSb) buffer layers made use of the low Sb-content layers that grows pseudomorphically to GaP and have been observed during the coalescence of the Ga(PSb) layers. The previous section (4.1.3) revealed that it is possible to grow these pseudomorphic low-Sb content layers deliberately by changing the growth conditions. This section investigates these layers further and uses them as a pseudomorphic interlayer at which the actual buffer layer is grown onto. It might be possible to achieve a 2D nucleation on this antimony containing interlayer in order to avoid the island nucleation and its undesirable consequences.

It has been possible to grow these pseudomorphic low-Sb content layers under very different growth conditions. In the first case, the partial pressures of TEGa and TBP were increased compared to the metamorphic grown buffer in 4.1.2 so that TEGa = $2.725 \cdot 10^{-3}$ mbar, TBP = 0.2626 mbar and TESb = 0.0176 mbar. This led to a V/III = 107, Sb/III = 6.51, Sb/P = 0.068 and P/V = 0.94. The growth temperature was kept to $T_{growth} = 475°C$. The AFM micrographs of this sample showed a smooth surface with a rms average of height deviations of 0.35 nm. The XRD profile gave a composition of $Ga(P_{93}Sb_7)$. Figure 4.13 shows the STEM investigations of this sample. The overview (a) as well as the high-resolution image in (b) of the interface showed a smooth 2D layer of high structural quality without defects. The presented high-resolution image in (b) and (c) is the sum of an aligned stack of 10 images to increase the signal-to-noise ratio and correct scanning distortions. The image intensity has been normalized to the intensity of the direct beam.

The HAADF images show that the interface between GaP and and the pseudomorphic Ga(PSb) layer is clearly visible as a bright line. Since the intensity in HAADF STEM images is sensitive to the atomic number of the observed material, this leads to the assumption of an increased amount of Sb at this interface. The intensity in dependence on the position across the interface can be evaluated by finding the positions of the group III and group V atom columns as well as the background positions in between the columns using the peak pairs algorithm. Line scans along the (001) lattice planes were used to obtain the mean intensity and standard deviation for each marked (001) lattice plane in dependence on the position in growth direction as shown for the group III positions in

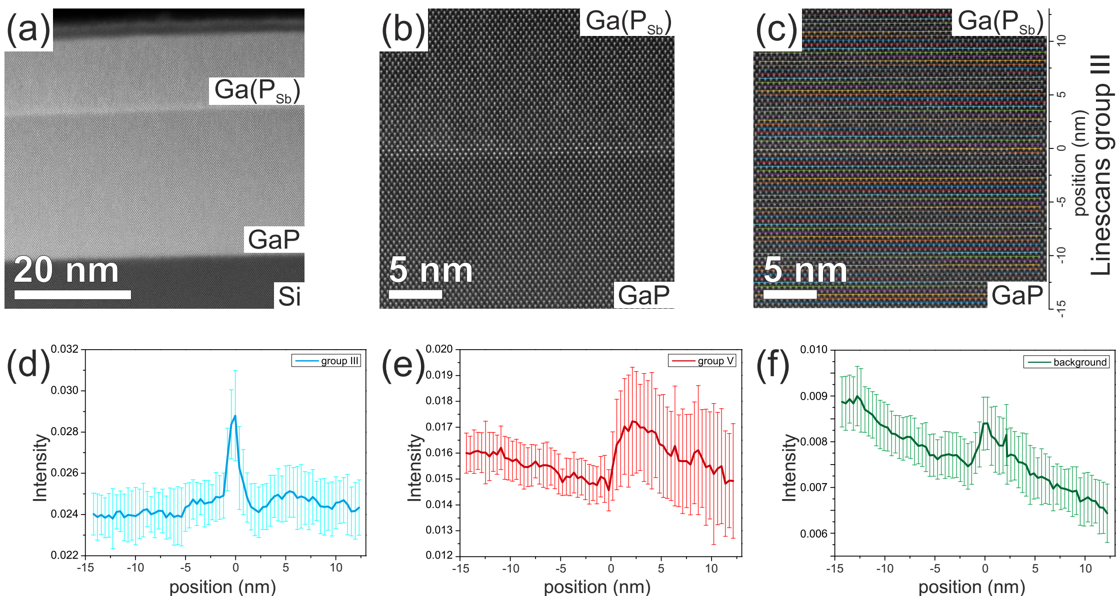

Figure 4.13: (a) Overview and (b) high-resolution HAADF STEM images of pseudomorphically grown $Ga(P_{93}Sb_7)$ on GaP/Si. The subscript Sb in $Ga(P_{Sb})$ denotes the low Sb-content in the pseudomorphically grown layer. (c) Same as high-resolution micrograph as in (b), where the [001] lattice planes of the group III atom columns are marked. The corresponding averaged mean intensity and standard deviation of each (001) lattice plane is plotted in (d) in dependence on its position in growth direction. The interface has been chosen as position 0 nm. The intensity plots in dependence of the positions (e) for the group V positions and (f) the background positions.

image (c). The intensity plots for the group III, group V and background positions are displayed in 4.13 (d)-(f). The plots are centered at the interface, which has been chosen as the position 0 nm. The plotted intensities show a gradient that have a different slope for all three graphs, so this can not only be attributed to a thickness gradient due to sample preparation. The thin, pseudomorphically strained sample probably also exhibits plastic relaxation that causes lattice plane bending and influences the intensity [100, 107]. The graphs reveal that the increased intensity at the interface cannot be explained by an increased amount of Sb at the interface. The intensity at the interface shows a spike for the group III and the background and not the group V intensity as expected. The group V intensity at the interface rises abruptly to a value higher than GaP due to the incorporation of a low amount of antimony. The intensity peak of the group III atoms at the interface was very localized with a FWHM of 1.2 nm and a maximum intensity of 0.0284. This means an intensity increase of 0.004, while it was only 0.001 for the background intensity. So this effect was not only caused by an increased background intensity at the interface. The increased group III intensity at the interface might be explained by dechannelling due to plastic relaxation at the interface. Another possible explanation are antimony antisites on the group III positions due to the triethylantimony (TESb) pre-run before the growth of the Ga(PSb) layer. Altogether, further investigations are necessary to explain this

effect. They should include comparison to simulations, the investigation of the P-polar direction and electron energy loss spectroscopy (EELS) to investigate the plasmon and surface plasmon peak. EELS or EDX should be used to investigate antimony antisites at the interface.

However, growing a low Sb-content pseudomorphic layer has also been possible by decreasing only the TESb partial pressure. In this case the samples were grown at $475°C$ at TEGa = $7 \cdot 10^{-3}$ mbar, TBP = 0.1 mbar and TESb = $2.2 \cdot 10^{-3}$ mbar. This led to a V/III = 14.6, Sb/III = 0.31, Sb/P = 0.022 and P/V = 0.98. The resulting sample also displayed a very smooth surface in AFM measurement with an rms of 0.31 nm. The XRD revealed a slightly higher Sb content, with a layer composition of $Ga(P_{91.5}Sb_{9.5})$. The low-Sb content Ga(PSb) layer of the second sample has been used as a pseudomorphic interlayer to grow the metamorphic Ga(PSb) buffer layer on top of it. The resulting sample is investigated by HAADF as shown in figure 4.14. The interface between GaP and the pseudomorphically grown Ga(PSb) interlayer does not shown the bright contrast that had been observed in figure 4.13. This might be attributed to the different growth conditions which lead to a different antimony content, or the effect might depend on the polarity. Figure 4.13 shows the bright contrast at the Ga monolayer at interface of the Ga-polar projection while figure 4.14 shows the results for the P-polar direction.

The HAADF overview image in figure 4.14 (a) showed a rough surface, which has also been revealed by AFM micrographs, where the rms has been measured to 0.75nm. The overview image not only revealed a rougher surface but also a rough interface between the pseudomorphic and the metamorphic buffer layers. This is remarkable since the pseudomorphic interlayer have shown very smooth surfaces before. This shows, that the pseudomorphic interlayer did not lead to a 2D nucleation due to a continuous wetting layer on GaP. Figure 4.14 (a) showed that the pseudomorphic interlayer was particularly thick when the metamorphic Ga(PSb) was thin or, more precisely, had trenches. This observation suggests, that the same growth as without the interlayer took place. The Ga(PSb) nucleated in islands on the smooth, pseudomorphic Ga(PSb) interlayer and with continuing epitaxy, the islands grew larger and coalesced. In the trenches between the islands, the pseudomorphic layer continued to grow. Images (b) and (c) are high-resolution images where the additional {111} GaP lattice planes of the dislocations have been marked by blue arrows. In contrast to the previously investigated metamorphic buffers, these samples exhibited a higher number of 60° dislocations. In addition, stacking faults and microtwins could be observed in these images.

All in all, the pseudomorphic interlayer did not provide a better surface for the metamorphic buffer layers. The resulting layer showed a lower quality than the original buffer layers grown directly on GaP/Si. The island-like nucleation has not been overcome, instead a

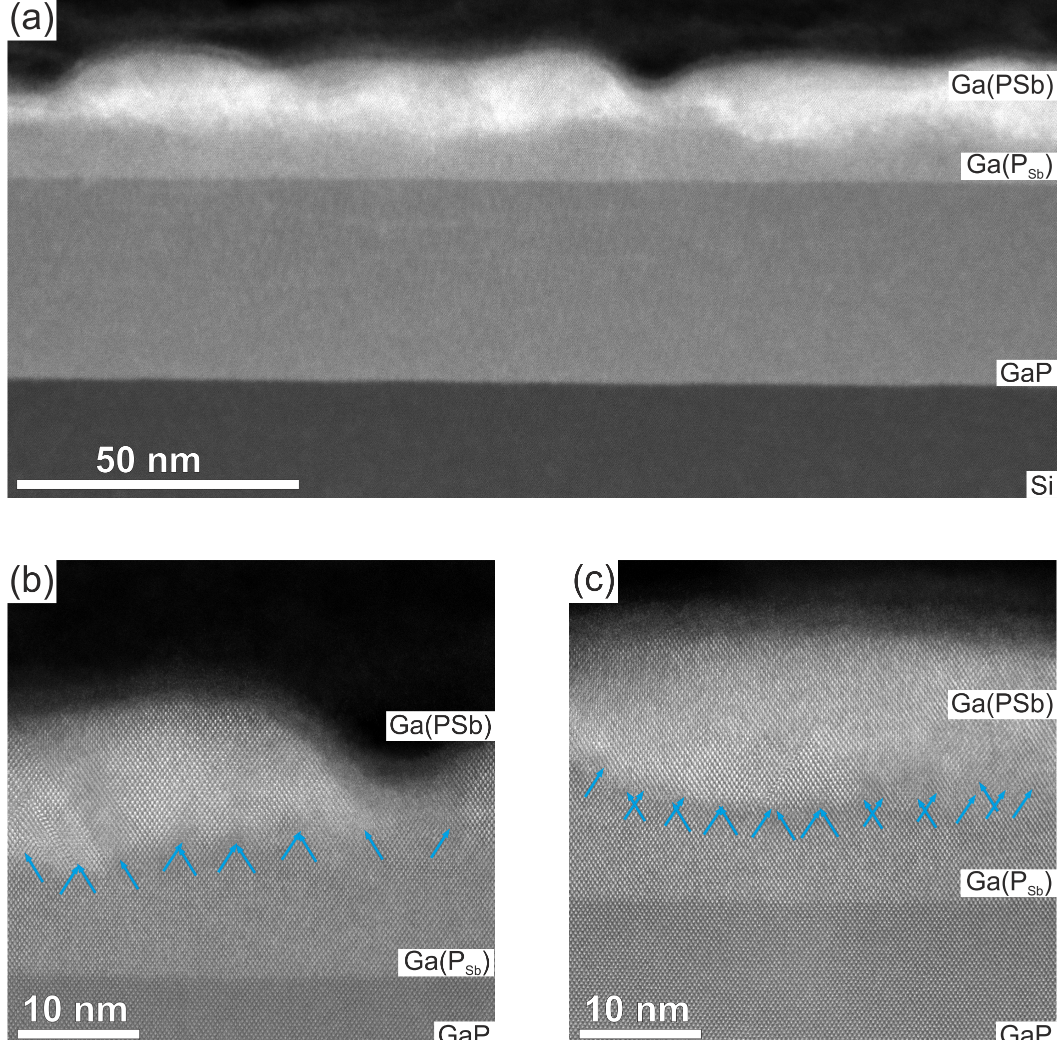

Figure 4.14: HAADF investigation of Ga(PSb) metamorphic buffer layer on low Sb-content pseudomorphic Ga(PSb) interlayer on GaP/Si. The subscript Sb in $Ga(P_{Sb})$ denotes the low Sb-content in the pseudomorphically grown interlayer. The blue arrows indicate the additional {111} lattice that form the dislocations.

rougher surface and interface between the interlayer and the metamorphic Ga(PSb) layer could be observed.

4.1.5 Pulsed growth of Ga(PSb) on GaP/Si

As shown in the previous section, an pseudomorphic interlayer did not provide a better substrate to avoid island nucleation. Therefore, a different strategy needed to be found. Previous studies on GaP [69, 117] have shown that GaP also has an island-like nucleation that leads to a high density of stacking faults and twins due to the coalescence of these islands. In this case, the island nucleation could be overcome by changing the growth mode from a continuous growth to a flow rate modulated epitaxy (FME) at $450°C$. This

means changing the supply of the two precursors TEGa and TBP from a continuous flow to an alternating offer of only one precursor at a time as illustrated in figure 4.15 (a) and (b), respectively. Image (b) shows that there has been a growth interruption between the supply of each precursor and that the time step of the flow modulation is one second. This increases the mobility of the Ga and P atoms so that they have enough time to diffuse towards the optimal incorporation sites.

The aim is now to achieve similar results for the Ga(PSb) buffer layers. Ga(PSb) is a ternary material with three instead of two precursors. Changing from the continuous epitaxy to the FME mode is therefore not as unambiguous as shown for GaP. Instead, two different nucleation sequences have been applied. In the one case, TEGa is alternated with both group V precursors offered at the same time as illustrated in image (c). In the the other case, only one group V precursor is offered at a time. Since the $Ga(P_{32.3}Sb_{67.3})$ buffer contains twice as much Sb as P, TESb was offered twice as often as shown in image (d). TEGa is supplied between each group V precursor. There was no growth interruption between the alternating offer of the precursors.

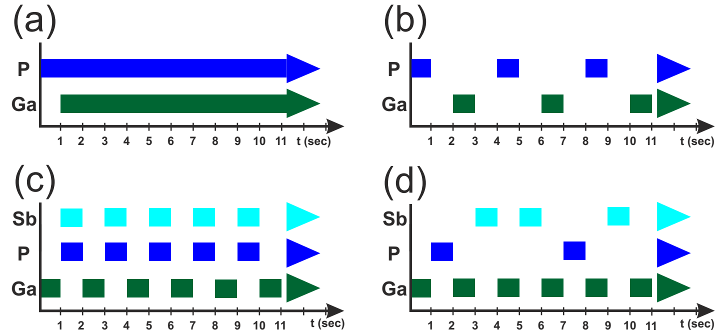

Figure 4.15: Illustration of the different growth modi for (a) continuous epitaxy and (b) FME of GaP, as well as FME of Ga(PSb) with (c) both group V precursors at a time and (d) one group V precursor at a time.

First, the results for the samples grown with FME of only one group V precursors at a time, as illustrated in figure 4.15 (d), are discussed. Figure 4.16 shows the XRD profiles and the corresponding AFM images of four different samples. Hereby, the AFM images have frames in the same color as the according XRD profiles. The black curve belongs to a Ga(PSb) buffer of 50 nm nominal thickness grown with continuous flow under the same growth conditions as the Ga(PSb) buffer layers investigated in section 4.1.2, namely TEGa $= 7.1 \cdot 10^{-3}$ mbar, TBP $= 0.1$ mbar and TESb $= 0.0176$ mbar so that Sb/III $= 2.5$ and P/III $= 14.25$. The XRD peak in (a) is at the same position as previous investigated samples and the corresponding AFM image in figure 4.16 (b) shows a smooth, coalesced surface. The same partial pressures were used to grow a sample with FME with one second pulses of TEGa:TBP:TESb = 3:1:2. The resulting XRD profile is shown in (a) in purple. It is striking that the peak of the sample is at the position of pure GaSb. The phosphorous

has not been incorporated. The surface of the sample is very rough as shown in (c). Notice the scale bar of 15 nm. This can again be explained by the study of Stegmüller et al [177] which stated that most of the TBP arriving at the surface is not decomposed.

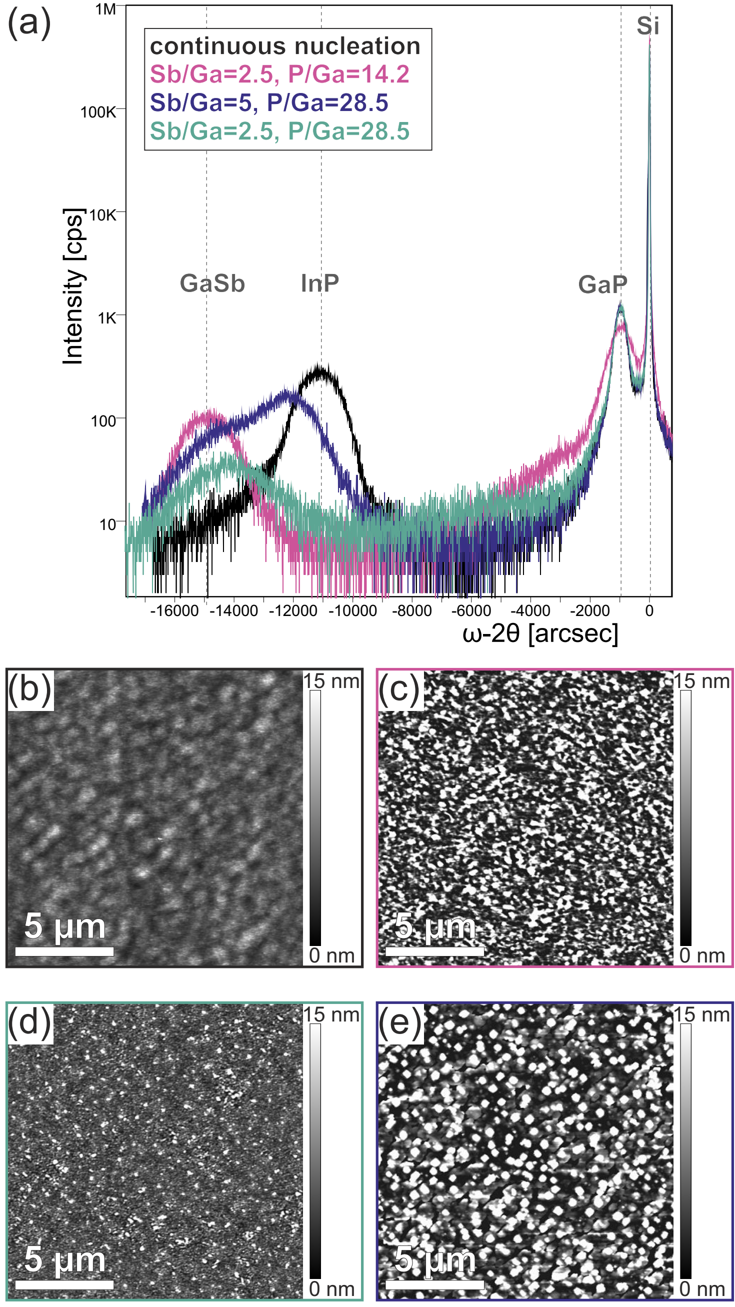

Figure 4.16: Flow rate modulated epitaxy of Ga(PSb) using one precursor at a time: Ga-P-Ga-Sb-Ga-Sb. (a) shows the XRD curves for several samples with different growth conditions, (b)-(e) the corresponding AFM images. The colors of the frames around the AFM images match to the XRD curves.

On the basis of these results, the flux of TBP was doubled so that Sb/III = 2.5 and P/III = 28.5. The results are displayed in green and show, that the main peak still lies at the GaSb position. This peak is, however, smaller and a weak, broad second peak at becomes visible. This corresponded to a lattice constant much smaller than the desired InP lattice constant. The according AFM micrograph in (d) showed a layer with small trenches and islands. Doubling the p_P of TBP led to a higher amount of P at the surface which led in turn to the growth of Ga(PSb), however, at the wrong composition. For the third FME grown sample, both group V fluxes were doubled compared to the first one so that Sb/III = 5 and P/III = 28.5. The XRD profile in blue shows now a main peak at a lattice constant higher than the one of InP. This means that more Sb than desired has been incorporated or the Ga(PSb) layer was not relaxed. Probably it is a combination of both. In addition, the XRD peak has a shoulder at the GaSb position. The surface of the sample exhibited deep trenches and large islands as demonstrated by the AFM measurment in (e).

The AFM in combination with the XRD results indicate that the trenched surfaces correspond to the Ga(PSb) layers while the islands probably are islands of binary GaSb. The islands only appeared in the AFM images when a shoulder at the GaSb was observed in XRD while thin Ga(PSb) layers with trenches have been observed in 4.1.2 before. This also means that the island-like nucleation was still taking place, leading to a Ga(PSb) layer with trenches.

All in all, it was not possible to achieve the growth of Ga(PSb) at the desired lattice constant. Not enough P was incorporated by this flow rate modulated epitaxy of separated pulses. Hereby, Sb was offered twice as often as P since the the aim was to grow Ga(PSb) with one third of P and two thirds of Sb. Since most of the TPB does not decompose in the gas phase, it was necessary to increase the offer of phosphorous in order to grow Ga(PSb) instead of pure GaSb. However, it has not been possible to grow Ga(PSb) in the right composition using a pulse sequence of separated group V precursors.

In the next step, the pulse sequence was changed so that both group V precursors were offered at the same time as shown in figure 4.15 (c). The results are shown in figure 4.17. Again, the samples were compared to the already discussed Ga(PSb) grown with continuous flow, that is demonstrated by the black XRD profile in 4.17 (a). The corresponding AFM image is not shown again. The first sample grown with this pulse sequence by FME nearly had the same partial pressures as the continuous grown sample, namely TEGa = $6.9 \cdot 10^{-3}$ mbar, TBP = 0.1 mbar and TESb = 0.0176 mbar so that Sb/III = 2.5 and P/III = 15. The p_P of TEGa has been reduced slightly so that it matched the TEGa partial pressure of the FME of GaP at $475°C$ with a growth rate of 1 ML/s. Using the previous partial pressure of TEGa = $7.1 \cdot 10^{-3}$ to grow the Ga(PSb), the AFM

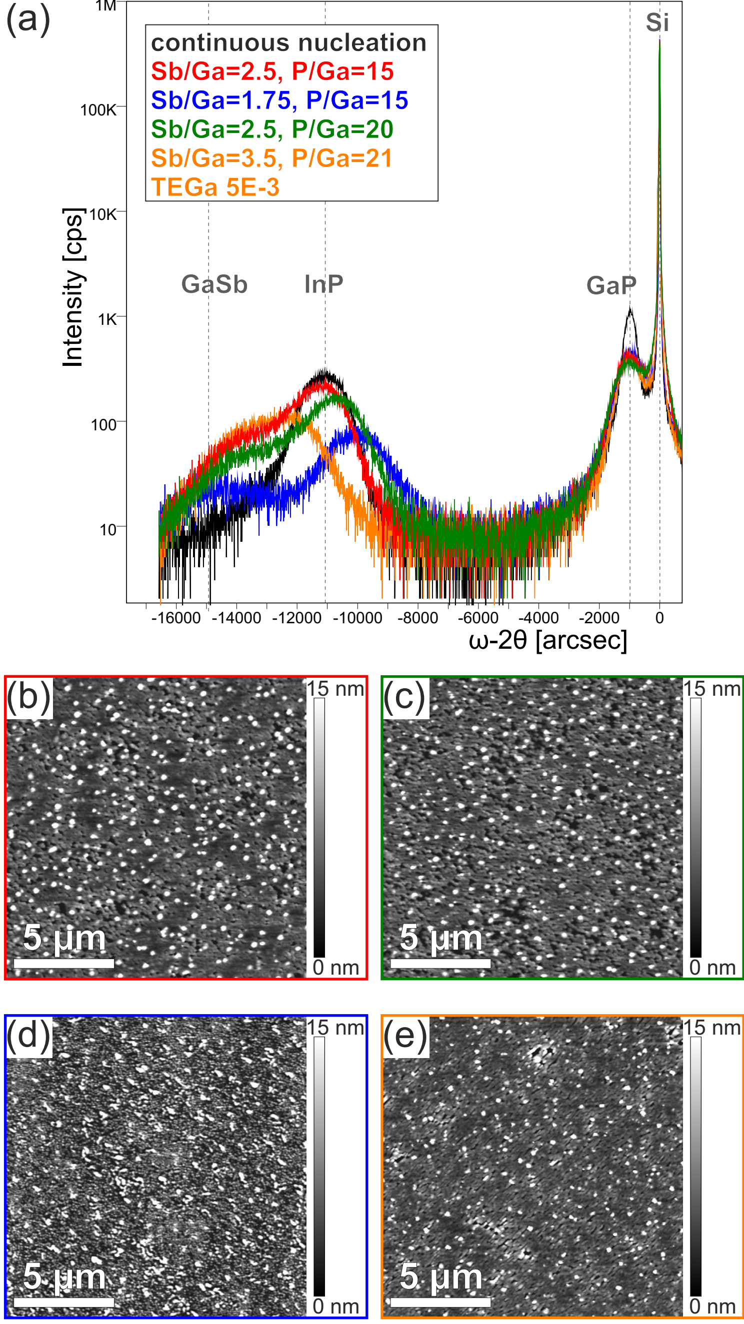

Figure 4.17: Flow rate modulated epitaxy of Ga(PSb) with alternating group III and group V precursors: Ga-P+Sb. (a) shows the XRD curves for several samples with different growth conditions, (b)-(e) the corresponding AFM images marked by matching the colors of the AFM frames to the XRD curves.

results presented in figure 4.17 (b) and the red XRD profile in (a) were unchanged (not shown here). The red XRD curve shows, that the resulting sample had its main peak at the desired lattice constant of InP. However, there is a small shoulder at the GaSb lattice constant. The red framed AFM measurment in image (b) shows that the surface had trenches and small islands similar to 4.16 (e), which have been assigned to the presence of GaSb. In order to decrease the surface roughness and prevent the growth of binary GaSb islands, the partial pressures of TBP, TESb and TEGa were changed successively.

Firstly, the TBP flow was increased so that Sb/III = 2.5 and P/III = 20. This only led to slight changes in the XRD and AFM results as indicated by the green colored curve in (a) and AFM in (c), respectively. The surface still exhibited islands on a trenched surface. The green XRD curve shows that that the buffer layer had a lower Sb content or was not relaxed completely. The shoulder at GaSb was slightly more pronounced. The next step, decreasing the p_P of TESb so that Sb/III = 1.75 and P/III = 15 resulted in an even further shift of the main peak in the XRD to a smaller lattice constant with a lower Sb content and a stronger GaSb shoulder as shown by the blue curve. The blue framed AFM micrograph in (d) fits well to the XRD results as it shows smaller islands between the trenches that probably belong to the Ga(PSb) with lower Sb content while the GaSb islands on top of the smaller Ga(PSb) islands are larger than in (b) and (c). A lower amount of Sb in Ga(PSb) due to a decreased Sb/III ratio agreed well to the results of figure 4.11 (b) in section 4.1.3, where the Sb incorporation decreased with decreasing Sb/III. The smaller Ga(PSb) islands can probably be attributed to a decreased growth rate. The decreased growth rate was also demonstrated by the XRD intensity of this sample that is lower compared to the other layers, although all samples have had 170 cycles of pulses. This indicated that not only Ga but also Sb was a driving force for the growth. It is possible, that TBP is not only decomposed in the presence of Ga but also by Sb. In the last step, the TEGa was decreased so that TEGa = $5 \cdot 10^{-3}$ mbar and the Sb/III and P/III are increased simultaneously to 3.5 and 21, respectively. The orange framed AFM image in (e) displays a surface with less islands and smaller trenches. The orange XRD profile in (a) looks similar to the blue one in figure 4.17 (a), where probably too much Sb is incorporated. This similarity is consistent since in both cases, the Sb/III and P/III have been increased simultaneously. The direct comparison of the two XRD curves showed a more pronounced shoulder at the GaSb peak position in 4.17, for the FME grown sample with separated group V pulses . In this case, the Sb/III ratio was 2.5 and therefore lower than 3.5, however, Sb is offered twice as often, leading a higher amount of GaSb. The XRD results fitted well to the AFM results, since the islands in 4.17 (e) were larger than in 4.18 (e).

Altogether, this means that the most promising result was the "red" sample with alternating TEGa and group V pulses with Sb/III = 2.5 and P/III = 15 since it had the right lattice constant with the lowest amount of binary GaSb. However, the AFM

measurment revealed that the surface was not coalescent and the GaSb islands were still present. The previous experiments have shown that increasing the amount of P does not change much, while changing the amount of Sb led either to more GaSb islands when increasing it or a lower composition of Sb in the Ga(PSb) layers when decreasing it. The surface with the trenches showed, that the island-like nucleation had not been overcome by FME. The higher mobility did not have the same effect as for the growth of GaP on Si. Therefore, the growth rate was increased by doubling all partial pressures and setting the lowest possible pulse rate of 0.5 s. In this way, the same layer thickness should be reached, however, the system was given less time to form islands. Figure 4.18 (a) presents the resulting XRD curve in blue. The curve is again compared to the continuous grown sample shown in black and the initial sample in red.

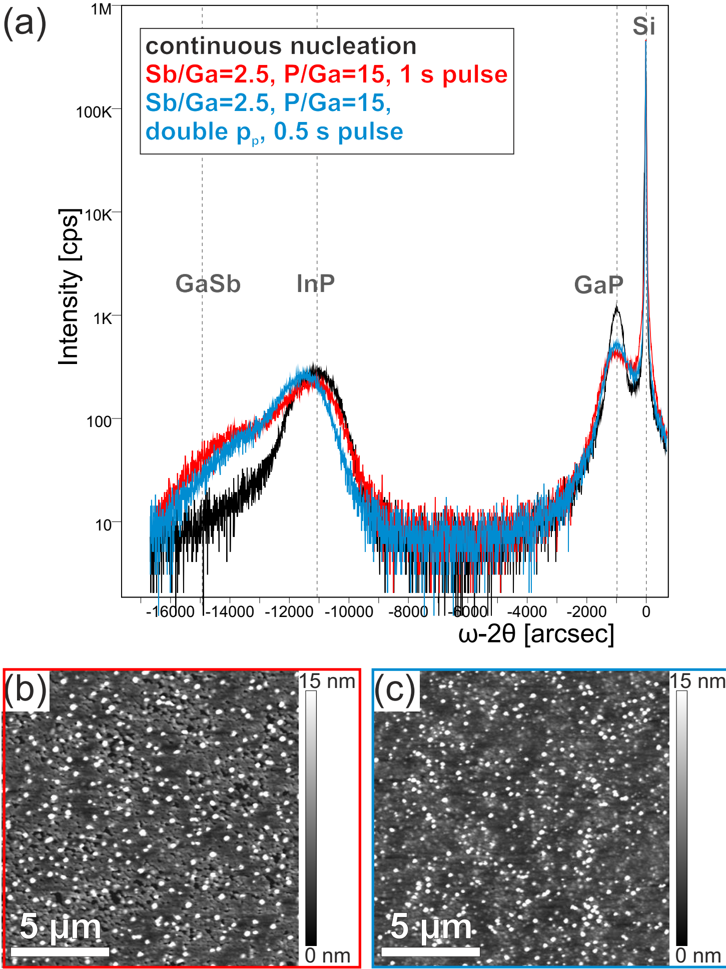

Figure 4.18: Flow rate modulated epitaxy of Ga(PSb) with alternating group III and group V precursors: Ga-P+Sb. (a) shows the XRD curves for the two best results in comparison to the continuous growth. The corresponding AFM images with matching frame colors are shown in (b) and (c).

The comparison showed that the peak position was slightly shifted so it had not the lattice constant of InP anymore. However, the goal to reduce the shoulder at GaSb had

been achieved. Comparing the blue framed AFM image in (c) to the initial one in (b), it is noticeable that the trenches as well as the islands were smaller. The smaller trenches might be explained by the higher growth rate that led to an increased sample thickness within the same growth time and therefore to a higher degree of coalescence. The smaller GaSb islands could be attributed to the decreased shoulder at the GaSb peak position in the XRD. Since this sample showed the smoothest surface in AFM image and has, according to the XRD, nearly the right lattice constant of InP as well as the lowest amount of GaSb, it was investigated by STEM.

Figure 4.19 (a) and (b) show ADF overview images in both <110> projections. Similar to figure 4.6, high densities of stacking faults and threading dislocations were visible. The P-polar [$\bar{1}$10] projection was perpendicular to the trenches. In accordance with the observations made in 4.5 (d), a pile up of low-Sb content Ga(PSb) grown pseudomorphically to GaP could be observed in the trenches. A closer look of the Ga(PSb)/GaP interface was made in images (c) and (d). They were also ADF images from the P-polar side.

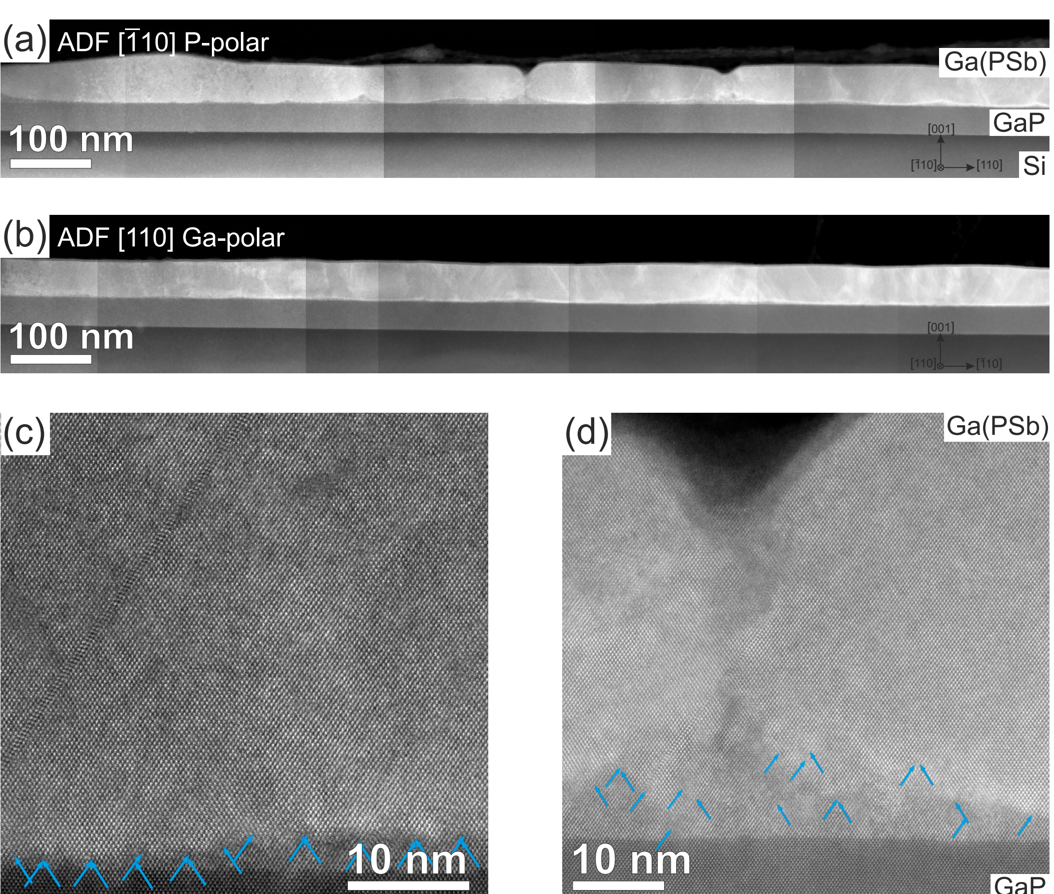

Figure 4.19: Structural characterization by ADF of Ga(PSb) grown by FME. (a) and (b) are ADF overview images in [$\bar{1}$10] and [110] projection. (c) and (d) are high-resolution ADF images at the GaP/Ga(PSb) interface in [$\bar{1}$10] projection. The blue arrows indicate the additional {111} lattice that form the dislocations.

In (c), it became apparent that the pseudomorphic low-Sb content layer not only appeared in the trenches, but continued over a wide range with a few ML. However, there were also areas without this pseudomorphic layer (not shown here). The pseudomorphic layer had an inhomogeneous thickness which led to the formation of 60° dislocations instead of Lomer or 60° dislocation pairs. This was visible in image (c) and particularly in the trenches as shown in image (d). Here, nearly no Lomer or 60° dislocation pairs could be observed. A threading dislocation passed from the tip of the piled up pseudomorphic layer to the dip of the trench. This supports the assumption that the growth of Ga(PSb) by FME has not changed compared to the continuous one. The Ga(PSb) nucleated in islands at GaP. Between the islands pseudomorphic Ga(PSb) with low content Sb was grown. Comparing the TEM investigations of the FME grown Ga(PSb) layers to the continuous grown ones in 4.6 and 4.5, the pseudomorphic layers were larger for the FME grown samples.

Altogether, the flow rate modulated epitaxy did not overcome the problem of the island-like nucleation and the resulting issues of high SF and TD densities as well as the formation of trenches and of low Sb-content pseudomorphic Ga(PSb) layers at the interface to GaP. Instead, a new issue arised: the formation of GaSb islands on the surface.

4.1.6 InP interlayer

The previous sections have shown that neither the pseudomorphic Ga(PSb) interlayer nor the FME growth have led to an significant improvement of the Ga(PSb) buffer layer quality. The island-like nucleation of this ternary material on the GaP/Si pseudosubstrate could not be circumvented with these strategies. High quality 2D layers have only been achieved by pseudomorphic growth on InP substrate. Therefore, the strategy for this section has been changed to avoid the direct growth of Ga(PSb) on GaP/Si. Instead, an InP interlayer is employed onto the GaP/Si pseudosubstrate.

Up to now it has not been possible to achieve a better wetting of the ternary Ga(PSb) on GaP by changing the pre-flow, the pseudosubstrate, partial pressures, growth temperature or growth mode. Therefore, it is tested whether the binary material InP has different growth conditions in such a way that a better wetting layer leading to a 2D nucleation can be achieved. This approach can not work if the large lattice mismatch between GaP/Si and the buffer layer is the constraining effect hindering the 2D nucleation due to strain. Previous attempts to grow InP on Si substrate relied on wafer bonding [179–181], GaAs [182, 183] or graded (GaIn)As [184] buffer layers in the range of μm, strained superlattices [185, 186], or epitaxial lateral overgrowth (ELO) methods with lithography-patterned buffer layers [187–189]. Direct hetero-epitaxial growth of InP on Si has been conducted in the late 1980s using low pressure MOVPE [190] or low temperature and high V/III ratios [191] in combination with a thin GaAs buffer layer [192]. However, the structural investi-

gation of these samples has not been conducted by TEM but AFM, photoluminescence and XRD.

In this study, a thin InP layer was grown onto the GaP/Si pseudosubstrate. The growth conditions were adopted according to the growth of GaP on Si, using $T_{growth} = 450°C$ and a high V/III ratio used in [19], since most of the TBP is not decomposed. In this case, the partial pressures were TMIn $= 5.8 \cdot 10^{-3}$ mbar and TBP $= 0.58$ mbar so that V/III $= 100$. The AFM images revealed a smooth surface with a rms of 0.39 nm as shown in 4.20 (a). This observation was supported by the HAADF STEM investigation in 4.20 (b) and (c).

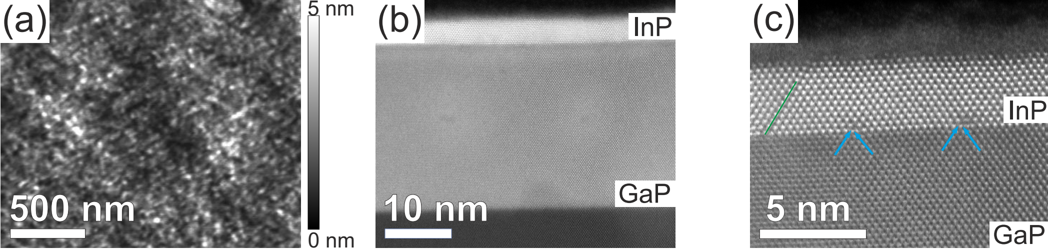

Figure 4.20: (a) AFM surface as well as (b) overview and (b) high-resolution STEM investigation of a thin InP layer grown on GaP/Si. The green line marks a SF and the blue arrows indicate the additional {111} lattice that form the dislocations.

The HAADF overview image in (b) also showed a smooth surface as well as an abrupt interface to GaP. The high-resolution images, as presented in 4.20 (c), exhibited mainly edge dislocations or 60° dislocation pairs at this interface. However, a stacking fault, marked by the green line, is also visible in (c). But the SF density was much lower than in the Ga(PSb) layers and no threading dislocations were observed. The thin 3.5 nm InP layer on GaP/Si was a smooth 2D layer without any trenches or interface roughness. This suggests that the InP layer did not nucleate in island-like structures but from a 2D nucleation as desired. However, the XRD as well as the large dislocation spacing in the HAADF images revealed that the layer was not completely relaxed, the lattice constant of InP had not been reached.

In the next step, a thicker InP layer was prepared with the same growth conditions as the previous sample in order to find out whether a thicker layer would relax completely and how. Moreover, a very thin Ga(PSb) layer is grown on top of the InP using the same growth conditions as determined in section 4.1.1. The growth time was as short as the layers that revealed the island-like structures during nucleation to investigate whether the Ga(PSb) had a 2D or island-like nucleation on top of the InP. The XRD revealed that the thick layer was now relaxed to 95 %, similar to the thick Ga(AsSb) layer investigated before. The morphology of the sample was again analyzed by STEM and the results are presented in figure 4.21.

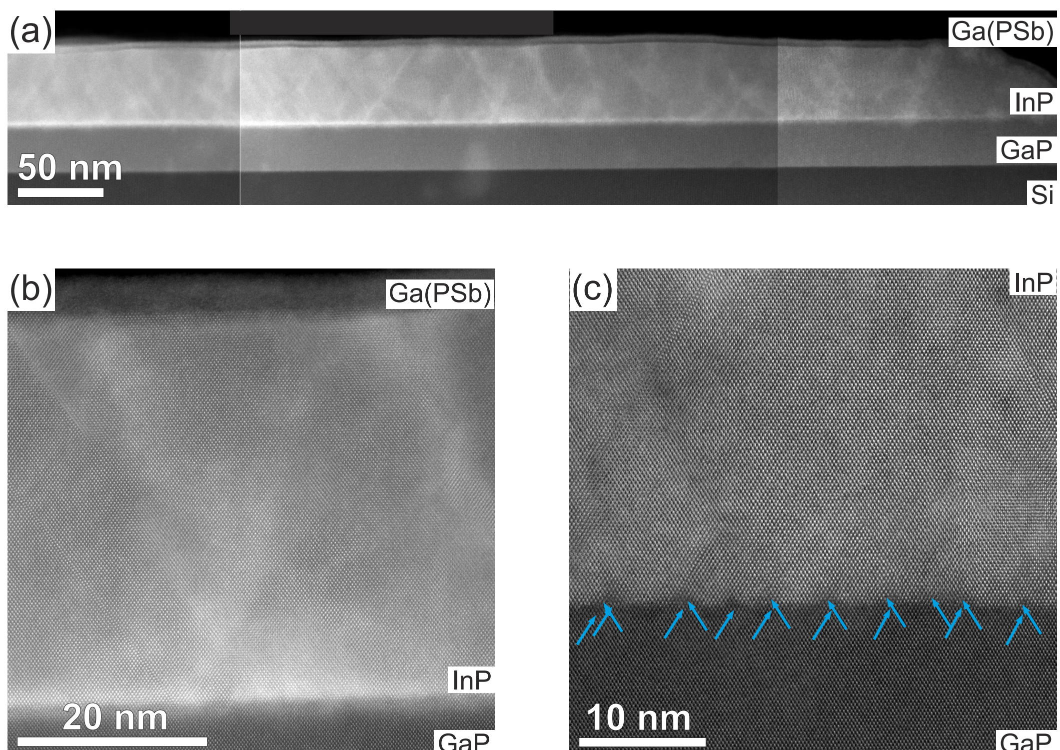

Figure 4.21: STEM investigation of a Ga(PSb) nucleation layer on a thick InP interlayer grown on GaP/Si. (a) and (b) are ADF overview images at different magnifications, (c) a high-resolution HAADF image of the InP/GaP interface. The blue arrows indicate the additional {111} lattice that form the dislocations.

The ADF overview images in (a) and (b) (under different magnifications) revealed that the thick InP layer had again a high density of stacking faults and threading dislocations present in the sample. The high density of SF was not unexpected since the thin unrelaxed sample in 4.20 already had SFs to relax the layer. Image (c) is a high-resolution image of the InP/GaP interface that showed that the relaxation of the thick layer not only took place by the generation of 90° dislocations or 60° dislocation pairs but also by 60° dislocations. They are a known source for the generation of threading dislocations and can explain the presence thereof. The other issue investigated in this sample is the nucleation of a thin Ga(PSb) on the InP interlayer. The overview images in (a) and (b) showed now sign of island nucleation. This satisfies the expectations since the InP interlayer was nearly relaxed to its own lattice constant and the $Ga(P_{33.3}Sb_{66.7})$ should grow pseudomorphically to InP with a 2D nucleation as already shown in section 4.1.1. This can be explained either by the vanished mismatch and strain or a better wetting of the Ga(PSb) on the InP layer, whereat the two explanation do not exclude each other so both effects could contribute.

The HAADF investigations showed that it was possible to grow InP interlayers for the Ga(PSb) buffers in order to avoid the island-like nucleation. However, these interlayers

relaxed with the generation of SF, 60° dislocations and TD. The thin Ga(PSb) layer grown on top of it did not show any sign of island nucleation. If it is possible to grow the InP interlayer in a better quality, this will be a promising approach. Therefore, the growth of GaP on Si was consulted again [19]. Here, a homogenous 2D nucleation without stacking faults has been achieved by using the flow rate modulated epitaxy for the nucleation. InP is, like GaP, a binary material so that the FME might be more successful than for the ternary material Ga(PSb) presented in section 4.1.5. The growth conditions for the InP have been varied successively in order to improve the InP layer quality. The surfaces analyzed by AFM are presented in figure 4.22.

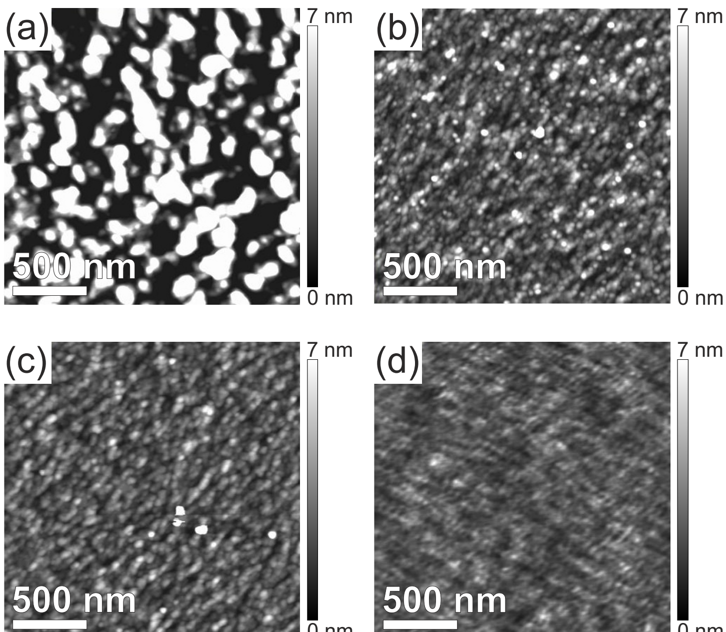

Figure 4.22: AFM images of InP layers grown on GaP/Si by flow rate modulated epitaxy under different growth conditions.

Figure 4.22 (a) shows the AFM investigated sample surface of an FME grown InP layer with the same growth conditions as the continuous grown sample investigated before, that was T_{growth} = 450°C and V/III = 100. The AFM results show that the surface was very rough, there were large islands visible. The scale bar was 7 nm and the rms was 5.6 nm. Apparently, the increased mobility of the In and P atoms did not lead to an diffusion towards the optimal incorporation sites but to the formation of islands. Therefore, the growth temperature was decreased to 400°C in the next step. The according AFM image in (b) showed a smoother surface with much smaller islands. The rms average of the height deviation was decreased to 1.3 nm. The appearance of the small islands might be attributed to too much indium in the gas phase. This might be explained by the decrease of the the growth temperature to 400°C, since the decomposition of TBP is less effective at lower temperatures. Therefore, the V/III ratio was increased to 126 by decreasing the partial

pressure of TMIn in the next step. Since the group III element determines the growth rate, the number of pulse cycles is increased by 25 % to compensate for the drop of growth rate due to the decrease of the p_P of TMIn. This approach was more complicated than increasing the the partial pressure of TBP but had to be realized due to technical reasons. The mass flow controller of the TBP has been at the upper limit. The resulting surface morphology is shown by the AFM image in 4.22 (c). In comparison to the sample surface in (b), the surface seemed to be smoother again. This subjective observation is supported by a decreased rms of 1.1 nm. An even smoother surface with rms = 0.76 nm is presented in image (d). It has been grown by decreasing the TMIn partial pressure further so that V/III = 185.

The last two samples of figure 4.22, (c) and (d), were also investigated in the STEM to find out whether less SF are present in the FME grown sample in comparison to the continuous grow one. The ADF micrographs of the two different samples are presented in the same magnification in figure 4.23. The stacking faults are marked by green lines while the threading dislocations are indicated by dark blue arrows. The stacking fault density was still very high. The thickness of the two images has been determined to 18 nm (a) and 52 nm (b), so the stacking fault density was $2.7 \cdot 10^{11}\,cm^{-2}$ and $1.3 \cdot 10^{11}\,cm^{-2}$, respectively.

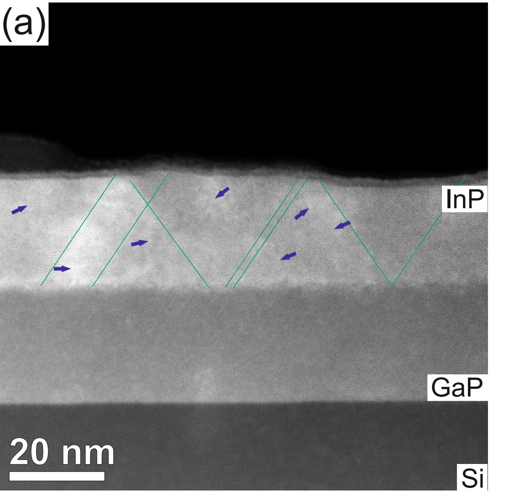

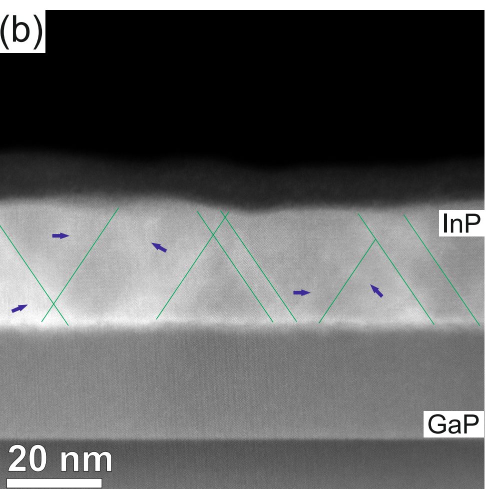

Figure 4.23: STEM investigation of two different FME grown samples of InP/GaP/Si. The corresponding AFM investigated surfaces are shown in 4.22 (c) and (d), respectively. Green lines mark the stacking faults and blue arrows the threading dislocations.

This means that the relaxation of the InP takes place with undesirable lattice defects instead of a pure network of Lomer dislocations at the interface. This might be explained by non-optimized growth conditions. The growth rate has not been adjusted to 1 ML/pulse, which leads to the formation of islands during the growth since too much or not enough

atoms are incorporated at higher or rather lower growth rates. Again, this causes the formation of TD and SF when the islands coalescent. In literature, e.g. [180, 183, 187], not only the high mismatch between InP and Si is named as a problem for the formation of lattice defects but also the different thermal expansion coefficient of the two materials, namely $2.6 \cdot 10^{-6}/K$ for Si and $4.65 \cdot 10^{-6}/K$ for InP [175]. However, the investigated sample contained a GaP buffer layer between the Si substrate and the InP layer. Since the thermal expansion coefficient of GaP is $4.6 \cdot 10^{-6}/K$, it is very close to InP, so this problem should be circumvented and has not proven to be a problem during the growth of GaP on Si. It is possible to grow high quality GaP layers on Si using flow rate modulated epitaxy [19].

In summary, the InP interlayer has probably been grown with a 2D-nucleation onto the GaP/Si pseudosubstrate. The resulting surfaces were very smooth with rms below 1 nm. They provided a good substrate for a 2D nucleation of the Ga(PSb) buffer layers. The InP interlayer has been grown with continuous as well as flow rate modulated epitaxy. In both cases, the InP layer was not relaxed completely. The relaxation took place under the generation of stacking faults, twins, 60° dislocations and, consequential, threading dislocations. The TD and SF densities are again in the order of $10^{11}\,cm^{-2}$. These problems might be circumvented by optimizing the growth rate of the layers.

4.1.7 Summary of the growth optimization of Sb-based buffer layers

The first part of this study dealt with the growth of Ga(PSb) and Ga(AsSb) buffer layers lattice matched on InP substrate and their transfer onto the GaP/Si pseudosubstrate. Hereby, the investigation was focused on Ga(PSb). The pseudomorphic growth on InP substrate succeeded with the growth of $Ga(P_{33.3}Sb_{66.7})$ and $Ga(As_{48.6}Sb_{51.4})$ as smooth 2D layers with defect densities lower than $10^{8}\,cm^{-2}$. In the following, it has been shown that the transfer of these layers onto the GaP/Si by using the same growth conditions as on InP was attended by an island-like nucleation. These islands increased in size with longer growth time until they coalesced to form continuous layers with a smooth surface and rms smaller than 1 nm. These Ga(PSb) and Ga(AsSb) coalescent layers with a nominal thickness of 100 nm and smooth surfaces were investigated by RSM in XRD. Their evaluation resulted in a composition of $Ga(P_{32.73}Sb_{67.3})$ and $Ga(As_{44.3}Sb_{55.7})$ with a plastic relaxation of 98.3 % and 96.5 %, respectively. The misfit has been determined to 8.4 % for Ga(PSb) and 8.6 % for Ga(AsSb). These findings were supported by evaluating the dislocation spacing and misfit by counting the number (n) of {111} lattice planes between the dislocations in Fourier filtered high-resolution images as well as GPA strain mapping of high-resolution TEM imaging in case of the Ga(AsSb) layer. The misfit dislocation spacing of the islands was decreased compared to the thick coalsecent layers showed that the islands of both buffer layers were not completely relaxed by the formation

of dislocations. It is assumed that plastic relaxation due to the free surface is the reason behind this. AFM investigations revealed that the thin Ga(PSb) layers were less coalescent compared the thin Ga(AsSb) layers. The dislocation spacing of these thin Ga(PSb) layers was lower, so that the calculated misfit was higher. The latter has also been confirmed by GPA strain mapping. With increasing layer thickness and island coalescence, the dislocations spacing increased and therefore the calculated mismatch decreased.

STEM investigations of the Ga(PSb) layers showed that the dislocations at the interface were not only Lomer dislocations but also 60° dislocation pairs as well as single 60° dislocations. In addition to the formation of dislocations and plastic relaxation, some island were also relaxed by the formation of stacking faults. Additional stacking faults as well as twins and threading dislocations were formed during the coalescence of the islands for increasing layer thicknesses because the island have different degrees of relaxation. In consequence, the stacking fault as well as threading dislocation densities were in the order of $10^{10}\,cm^{-2}$ for the thick Ga(PSb) buffer layers. Additionally, a low Sb-content Ga(PSb) layer that grows pseudomorphically onto GaP was observed in the trenches of the thin Ga(PSb) samples that have not coalescent yet. In consequence, they could also be observed in the thick, coalescent layers.

In order to gain a better understanding of the growth of Ga(PSb) on GaP/Si, the growth parameters were varied by changing the partial pressures (p_P) of the three precursors triethylgallium (TEGa), tert-butylphosphine (TBP) and triethylantimony (TESb). It has been shown that the P-fraction increased, with increasing P/III ratio. Hereby, three different P/III ratio regimes have been identified. For low P/III ratios of 0 - 10, only pure GaSb has been grown. This has been explained by the low decomposition of TBP. At high P/III ratios, well above 40, layers with less than 10 % of Sb have been grown since more P is available at such high P/III ratios. In-between, for P/III ratios between 7 - 40, it has been shown that the composition depends on the amount of TESb offered which can be understood by investigating the dependence of the Sb-content in the Ga(PSb) layers on the Sb/III and Sb/V ratios. They showed that increasing the offer of TESb increased the Sb-content until it saturated at a Sb-fraction of about 70 %.

Varying the growth parameters led to changes in composition but did not change the island-like nucleation and layer quality. In order to reduce the defect density of the Ga(PSb) buffer layer by changing the nucleation, three different approaches have been applied. The first approach made use of the low Sb-content layers that were grown either at very high P/III ratios or low Sb/V with medium P/III ratios and have been observed in the trenches of coalescent thin layers before. They were grown intentionally as a pseudomorphic interlayer onto the GaP/Si in order to provide a better surface for a continuous wetting layer of the metamorphic Ga(PSb) buffer layer. However, the island-like nucleation could

not be eliminated in this way. Instead, a rougher surface resulting from a rougher interface between the interlayer and the metamorphic Ga(PSb) layer can be observed. This interface also contained much more 60° dislocations than the original buffer layers grown directly on GaP/Si. The second approach applied a flow rate modulated epitaxy (FME) that had also been used for the GaP layers to overcome the island-nucleation, reducing the stacking fault density and providing the annihilation of antiphase boundaries. However, the island-like nucleation and the resulting issues of high stacking fault and threading dislocation densities as well as the formation of trenches and of low Sb-content pseudomorphic Ga(PSb) layers at the interface to GaP were not resolved by FME. Additionally, GaSb islands were formed on the surface. The third approach to improve the buffer layer quality was of the growth of an InP interlayer. It has been shown in this study that the InP had a 2D-nucleation on the GaP/Si pseudosubstrate. AFM and STEM investigations have proven that the surface was very flat and provided a good substrate for a 2D nucleation of the Ga(PSb) buffer layers. The InP layer was grown with continuous as well as flow rate modulated epitaxy. However, STEM investigations revealed that the InP layer were relaxed not only by Lomer dislocations but also by 60° dislocations and lattice defects such as stacking faults, twins, and threading dislocations. These defects did not arise due to an island nucleation but due to unoptimized growth conditions.

4.2 Structural investigation of GaSb, Ga(PSb) and Ga(AsSb) islands on GaP

In the previous section, 4.1.2, it has been shown that the Ga(PSb) as well as the Ga(AsSb) nucleate in island-like structures on the GaP/Si pseudosubstrate. These islands were mainly relaxing by the generation of Lomer dislocations as well as 60° dislocation pairs. This section presents a further investigation of this island nucleation by HAADF scanning transmission electron microscopy. Only a small number of dislocations have been investigated due to the limited statstics of this method. (S)TEM, particularly high-resolution (S)TEM, is a method that only investigates small areas of interest. The examined Ga(PSb)/GaP and Ga(AsSb)/GaP interface areas were even smaller, since in these cases only islands and not a continuous layer were investigated. Hereby, strain mapping and the intensity ratio of the two sublattices were applied to study the differences and similarities of these two buffer layers at the beginning of their growth. In addition to these two ternary material systems, GaSb on GaP/Si has also been investigated. This binary material system has also been observed to grow in island-like structures on GaP and Si, respectively [148, 193, 194]. The mismatch between Si and GaSb of 12 % is higher than for the ternary Sb-based buffer layers and is also mainly accommodated by 90° dislocations as well 60° dislocation pairs [126, 193]. The investigations of the GaSb/GaP interface have been the basis for

the comparison of the two ternary Sb-based buffer layers later in this section. Hereby, simulations supported the experimental analysis of this interface.

4.2.1 GaSb/GaP interface - Comparison of simulation and experiment

At first, the interface of GaSb islands grown on GaP has been investigated by HAADF STEM along the dislocation lines in [$\bar{1}$10] and [110] projection as shown in figure 4.24 (a) and (b). The sample was grown at a temperature of 475°C using TEGa = $7.1 \cdot 10^{-3}$ mbar and TESb = 0.0176 mbar, so that V/III = 2.5. Before the growth of the islands, a 1 s pre-run of the antimony precursor TESb was introduced to provide a Sb wetting of the surface [57, 126]. The images presented here are the sum of an aligned stack of 30 images to increase the signal-to-noise ratio and correct scanning distortions. The image intensity has been normalized to the intensity of the direct beam. The sample thickness in viewing direction was determined to 18.7 nm in the P-polar image in (a) and 13.9 nm in the Ga-polar image in (b) using the normalized intensity of the GaP pseudosubstrate and comparing it the the normalized intensities of simulated GaP supercells of known thicknesses. The background intensity is much higher in image (a) compared to (b) due to the increased thickness. Unfortunately, thinner islands of the P-polar layer had become amorphous by ion sputtering during sample preparation. A surface amorphization of 2 - 4 nm [155, 156] significantly influences the total intensity.

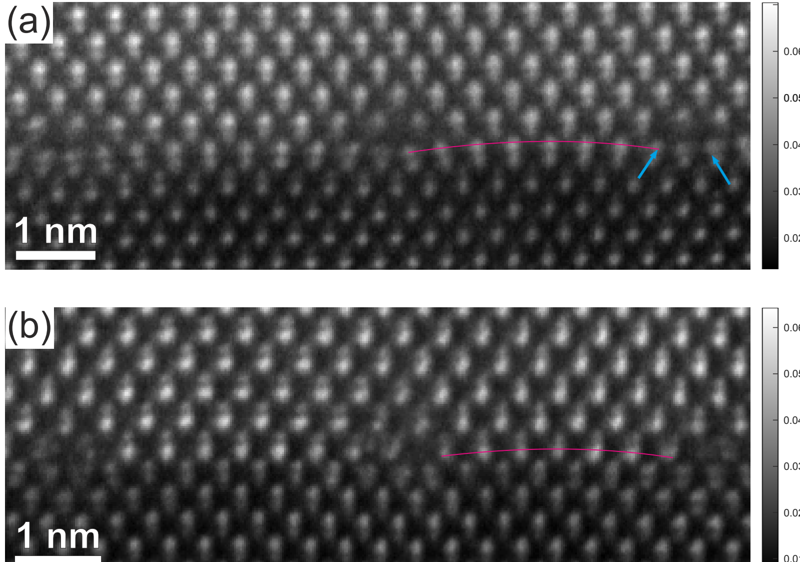

Figure 4.24: HAADF STEM images of the GaSb/GaP interface in (a) [$\bar{1}$10] (P-polar) and (b) [110] (Ga-polar) viewing direction. The magenta line is a guide to the eye for the lattice bowing. The blue arrows indicate the inserted {111} lattice planes that form a closely space 60° dislocation pair.

The analysis of figure 4.24 gave several interesting results. Firstly, the figure showed that the atom positions close to the dislocations were not able to be determined unambigu-

ously because the atoms were not perfectly aligned. Secondly, the high-resolution images revealed the type of dislocations. The P-polar projection was dominated by Sb-terminated shuffle set dislocations as shown in (a). However, some 60° dislocation pairs have been observed, like the right dislocation in (a). The two additional {111} lattice planes that form the closely spaced 60° dislocation pair are marked by blue arrows in the figure. The perpendicular [110] Ga-polar projection in image (b) had, as expected from theory, glide set dislocations at the interface. Again, 60° dislocation pairs have also been observed but are not displayed here. Thirdly, the dislocation cores were not at the exact interface of GaP/GaSb as it has been also observed by Wang et al. [57]. The shuffle set dislocation cores were located in the first monolayer of GaSb instead of the last monolayer of GaP. This might be connected to the assumption in section 4.1.2 concerning the deposition of Sb on the surface. Wang et al. [195] have also observed that an Sb-treatment of the surface before the growth of GaSb led to the formation of dislocations in the first monolayer of GaSb during the investigation of the GaSb/GaAs interface. Fourthly, the first monolayers of GaSb, between the dislocations, were bowed as indicated by the magenta line. This bowing was much more pronounced for the shuffle set dislocations in the P-polar projection in image (a). This effect might be connected to the third observation of the shifted dislocation cores, where the Sb atoms with a much higher covalent radius were sitting on the positions of P atoms. This bowing of the first monolayer has not been reported by Wang et al. This can probably be attributed to the fact that the lattice mismatch of GaSb is lower to GaAs compared to GaP. Fifthly, it has been noticeable that core atoms of the glide set dislocations had a very low contrast. This is unexpected since the shuffle set dislocations were Sb-terminated. Therefore, the glide set dislocation should also have a antimony core atom with a much brighter contrast in the Z-contrast HAADF micrographs. In order to evaluate the core intensity, the atom column positions were determined using the peak pairs algorithm. The intensity of the atoms was then determined by an integration with a radius of 1/3 of the nearest neighbor distance around the peak positions. The results for the Ga-polar sample with glide set dislocations are displayed in figure 4.25.

The intensity of the glide set core atoms was indeed only in the range of the P atoms or even lower. This can be denoted to a phosphor core atoms. This is unexpected due to the antimony-terminated shuffle set dislocations. It was, however, noticeable that at the core region and the GaP columns at the interface, the intensity of all atoms was about 20 % lower than in the bulk region. This can be explained by the displacement of the atoms in the columns which leads to a dechannelling effect of the electron beam. The glide set core atoms had the lowest intensity in this image. It might be the case that the core atoms were so displaced to each other that the dechannelling effect was so severe that at the center of the glide set dislocations were Sb or a mixture of Sb

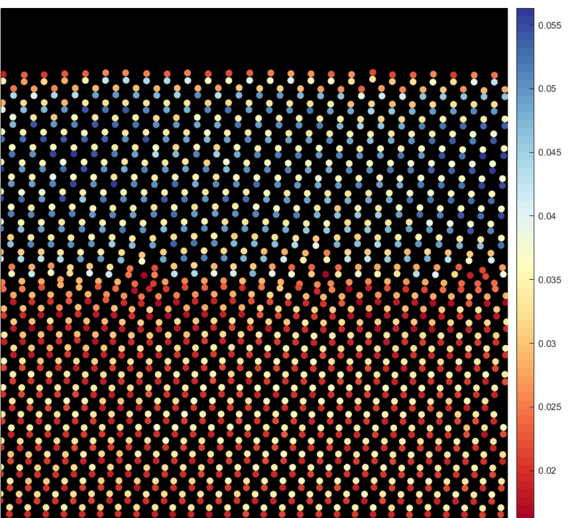

Figure 4.25: Averaged intensity map of [110] GaSb/GaP HAADF image with glide set dislocations at the interface.

and P atoms that could not be detected by the evaluation of the intensity. Considering that the intensity of all neighboring atoms suffered from the dechannelling, this effect certainly played a role. It explains why the core atom intensity was 20 % lower than the phosphor intensity. This is consistent with the neighboring atoms that also show an intensity drop of 20 - 35 %. However, the presence of Sb core atoms would mean an intensity drop of more than 60 %. It is therefore assumed that the core atom is a P atom, indeed.

In order to investigate this effect further, theoretical considerations were carried out by simulating different models of the GaSb/GaP interface. Hereby, the work of Wang and coworkers [57] has been followed. The investigated material, GaSb/GaP, with its Lomer dislocations at the interface were modeled using molecular dynamics simulations with Stillinger-Weber potentials. The model contained four dislocations and had a thickness of 13.7 nm in [$\bar{1}$10] and 13.8 nm in [110] viewing direction. This fitted well to the Ga-polar sample shown in 4.24 (b). The resulting ball-and-stick model of the simulations are displayed in figure 4.26.

There are four different models displayed. Similar to the experimental images in figure 4.24, both <110> projections are displayed and the images are cropped to the same size as in 4.24 for a better presentation. The left column shows the shuffle set dislocations, the right column the glide set dislocations. Figure 4.24 (a) presents the model of Ga-terminated dislocations and (b) the P-terminated dislocations, which have also been simulated in [57]. However, both models clearly do not fit to the observed dislocations in 4.24 where the dislocations were located in the first monolayer of GaSb. Hereby, the shuffle set dislocations were observed in [$\bar{1}$10] and the glide set dislocations in [110] projection. This corresponds

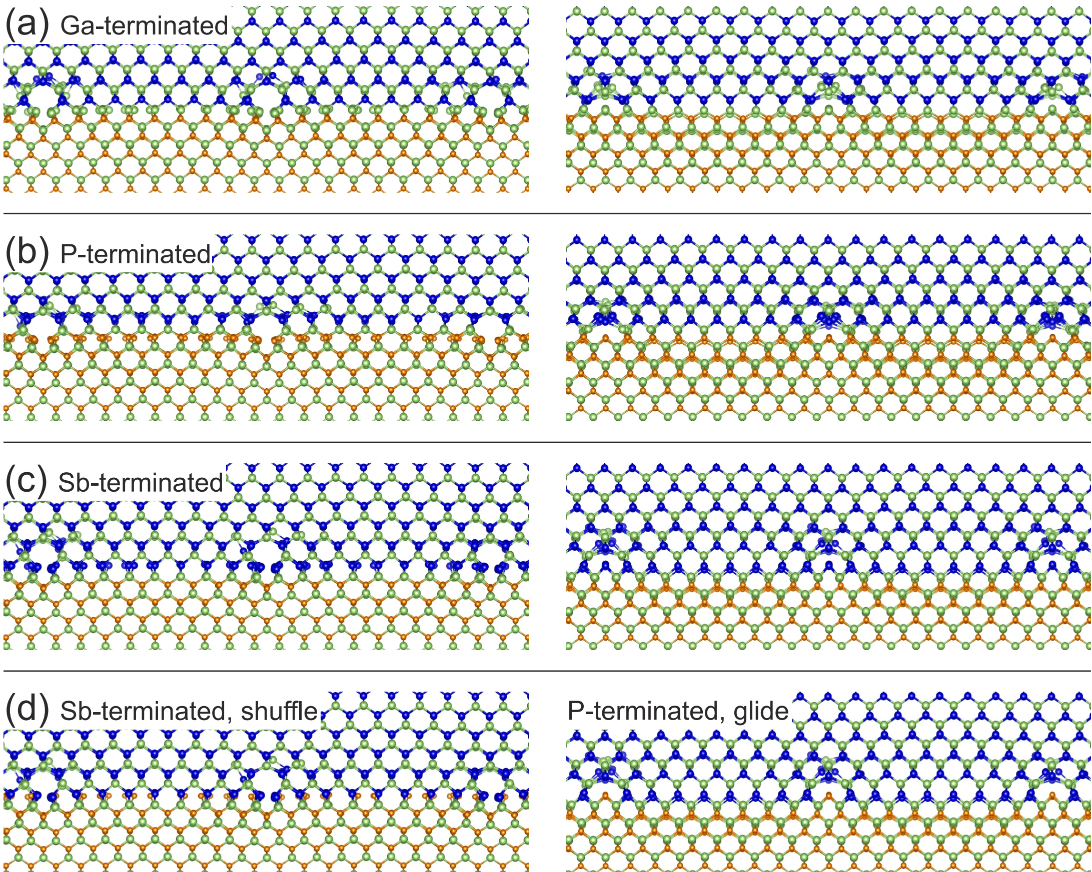

Figure 4.26: Four different models of the GaSb/GaP interface displayed in four columns viewed along both <110> directions. Ga atoms are represented in green, P atoms in orange and Sb atoms in blue. The left column shows the shuffle set dislocations, the right column the glide set dislocations in the perpendicular <110> direction. The model of the Ga-terminated dislocation cores are displayed in (a), the P-terminated cores in (b) , the Sb-terminated cores in (c) and the Sb-terminated shuffle set dislocation with a P-terminated glide set dislocation is shown in (d).

to the P-terminated model where the last ML of P is substituted by Sb atoms as shown in 4.26 (c). As previously mentioned, Wang et al. [195] have also observed dislocations in the first monolayer of GaSb in the GaSb/GaAs interface. However, in this interface, the Sb atoms replaced the As atoms in the Ga-terminated model. According to their analysis, this results in more confined dislocations with a lower core energy. Image (d) shows the same model as the previous one, but the core atoms of the glide set dislocation were substituted by P atoms. A striking observation regards the atom positions forming the dislocations in all four models: the atoms were not perfectly aligned in their column. This fits to the observation made in xperimental images displayed in figure 4.25, where this effect led to lower intensities due to dechannelling.

These models have been used to calculate their elastic energy per atom using sub-supercells that contained a glide-set and shuffle-set dislocation line, respectively. The

results showed, that the P-terminated glide set dislocation within the model of dislocations in the first monolayer of GaSb have a lower elastic energy per atom than the corresponding Sb-terminated glide set dislocations. This might explain the formation of the P-terminated glide set core within the GaSb monolayer. Additionally, P has a smaller covalent radius than Sb so its presence might be sterically favorable as well. The elastic energies of the four supercells showed the following hierarchy in dependence on the type of dislocation (glide-set and shuffle-set) and termination of the core (Ga, P, Sb, and Sb-P) as displayed for the four models in figure 4.26 (a)-(d):
$E_{Sb}^{glide} > E_{Sb-P}^{glide} > E_{Sb-P}^{shuffle} > E_{Sb}^{shuffle} > E_{Ga}^{glide} > E_{Ga}^{shuffle} > E_{P}^{glide} > E_{P}^{shuffle}$.
The elastic energy of the Lomer set dislocation within the first ML of GaSb (with Sb- as well as P-terminated glide set dislocation) is higher than for the corresponding P- or Ga-terminated Lomer set dislocations located at the interface. However, the fomation in the first ML of GaSb instead of the interface might be explained by the Sb-rich pretreatment and the kinetics during growth. The models do not include any kinetics. Wang et al. reported a lower core energy for the 90° dislocations with one monolayer of Sb in the GaSb/GaAs model [195] compared to the Ga-terminated dislocations at the interface. The comparison between the the Ga-terminated and P-terminated Lomer dislocations by Wang et al. [57] also showed a slightly different hierarchy for the elastic energies:
$E_{P}^{glide} > E_{Ga}^{glide} > E_{Ga}^{shuffle} > E_{P}^{shuffle}$.
This might be attributed to different initial conditions for the calculations of the models that have not been reported in their papers. However, all calculations showed that the shuffle-set dislocations are energetically favorable compared to their associated glide-set dislocations.

Since the last model in figure 4.26 (d) fitted best to the experimental results in 4.24, it was the basis for the simulation of HAADF STEM images using the multislice approach of the STEMsim software [125]. The STEMsim package only accounts for the geometrical aberrations. The effect of the finite source size was included by the convolution of a Lorentz function onto the simulated image. The FWHM was fitted to the experimental image in 4.24 (b), because their thicknesses fitted well to each other. The resulting simulated HAADF images are presented in figure 4.27. The Ga-polar image in (b) agrees very well to its corresponding experimental image in 4.24 (b). For the P-polar image in 4.27 (a) and 4.24 (a), the difference due to the diverging thickness and the resulting background intensity and different Lorentz fitting becomes apparent. However, the similarity is still noticeable. The bowing of the first monolayers of GaSb between the dislocations is clearly visible as indicated by the magenta line which serves as a guide to the eye. This bowing was much less pronounced in the [110] projection between the glide set dislocations, probably because they were located at the interface and not within the first ML of GaSb.

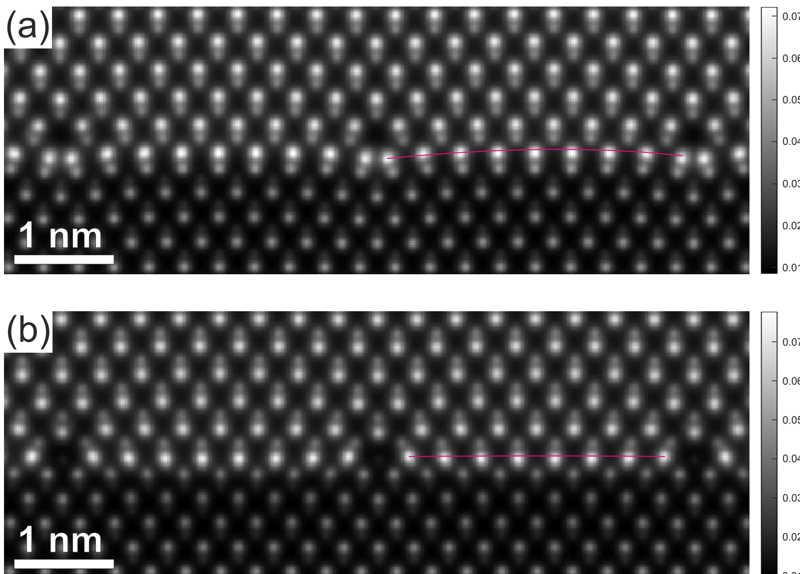

Figure 4.27: Simulated HAADF image of the GaSb/GaP interface in (a) $[\bar{1}10]$ (P-polar) and (b) [110] (Ga-polar) viewing direction. The magenta line is a guide to the eye for the lattice bowing.

So far, the interface of GaSb/GaP has been investigated by HAADF scanning transmission electron microscopy and comparing the results to four different models of the interface that were generated by MD simulations. The best fitting model is the one with Sb-terminated shuffle set dislocation in $[\bar{1}10]$ direction and glide set dislocation with a P core perpendicular to it, as shown in 4.26 (d). This model has been used to simulate HAADF images of the same interface and are in good agreement to the experimental micrographs. In the following, these simulated HAADF images are used for strain mapping. The results will be compared to the experiment.

Strain mapping

The first step to investigate the strain at the GaSb/GaP interface was to use the simulation of this interface to calculate the strain theoretically. The procedure has been explained in section 3.4.8. The resulting strain maps are presented in figure 4.28. The first row shows the shuffle set dislocations in $[\bar{1}10]$ direction whereat image (a) is the in-plane strain component and image (b) the strain in growth direction. Images (c) and (d) display the corresponding strain maps of $e_{\parallel}$and $e_{\perp}$ of the glide set dislocation in [110] projection.

Since the calculations used GaP as the reference lattice constant a_0, the strain in the GaP layer is zero. The dislocation cores were, as anticipated, highly strained in all four strain maps. The strain at the core was confined in the $e_{\parallel}$ map and had a very high

positive strain component in the GaSb layer and a negative value in the GaP layer. The $e_\perp$ map showed an even higher positive strain in GaSb while the strain in GaP was close to zero at the dislocation core. It is noticeable that only the in-plane strain component differs for the two dislocations while the perpendicular strain maps look very similar to each other. However, it should be considered that the program had some difficulties calculating the strain at the core of the shuffle set dislocations, because there were no nearest neighbors present due to the nature of the dislocations. Each dislocation displayed in (a) had a slightly different strain at the core because the determined nearest neighbors were not uniquely defined. An interesting observation could be made for the two $e_\perp$ strain maps: at the interface between the dislocation cores, a band of high positive strain was observable. This might be explained by the lattice bowing of the first ML between the dislocations that have been observed in the HAADF images.

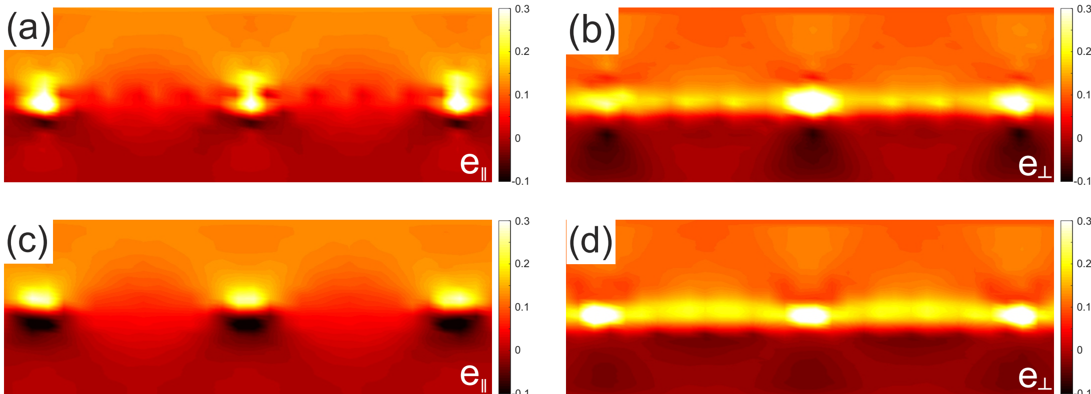

Figure 4.28: Theoretical strain maps of the GaSb/GaP interface based on the model in figure 4.26 (g) and (h). Images (a) and (b) show the strain in-plane and in growth direction of the shuffle set dislocation in [$\bar{1}$10] and (c) and (d) for the glide set dislocation in [110], accordingly.

The theoretical strain maps showed very interesting findings that should be compared to strain maps constructed by well-established methods like GPA and PP. Thereby, the strain mapping will be applied first to the simulated HAADF images since the HAADF images and the theoretical strain maps were both calculated from the same model. At first, GPA was applied. The resulting strain maps are displayed in figure 4.29. As in figure 4.27, the first row shows the shuffle set and the second row the glide set dislocations in [$\bar{1}$10] and [110] projection where the first column displays the respective in-plane strain component and the second column the perpendicular strain component.

The in-plane strain maps of both dislocations were hardly distinguishable from each other. They looked very similar to the theoretical in-plane strain map of the glide set dislocations in figure 4.28 (c), where the strain at the dislocation core was confined and had a very high positive strain component in the GaSb layer and a negative value in the GaP layer. This might be another hint that the calculations of the theoretical strain

had some problems with the calculations of the shuffle set dislocation. The strain maps in growth direction looked different from the theoretical strain maps. Here, $e_{\perp}$ of the shuffle set dislocation in the $[\bar{1}10]$ direction in image (b) was negatively strained at the dislocation core and had a band of high positive strain between the dislocations. Image (d) shows $e_{\perp}$ of the glide set dislocation in [110] direction vice versa to (b): the strain at the dislocation core was positively strained with a band of negative strain between the dislocations. However, this observation can be attributed to the <110> viewing direction.

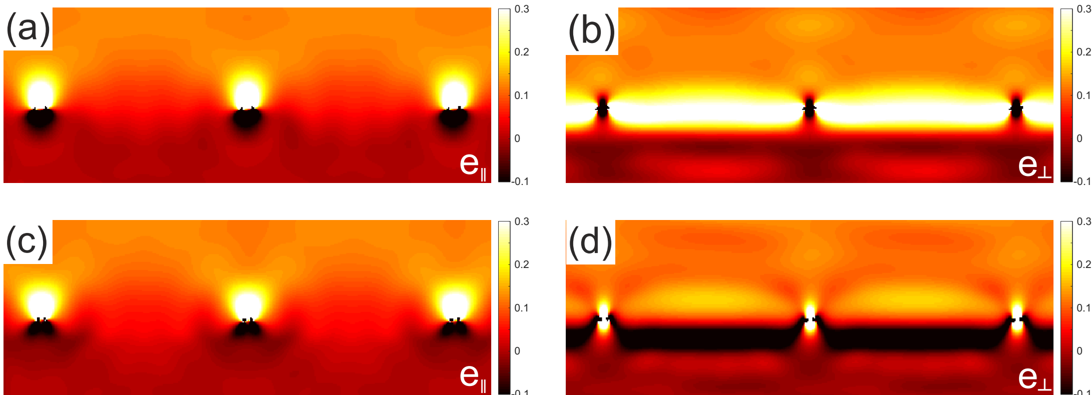

Figure 4.29: GPA strain maps of the GaSb/GaP interface of the simulated HAADF images from figure 4.27. (a) and (b) show the $e_{\parallel}$ and $e_{\perp}$ strain maps of the Sb-terminated shuffle set dislocation in $[\bar{1}10]$ projection and (c) and (d) the respective P-terminated glide set dislocation in [110] projection.

The GPA strain mapping has also been applied to the simulated HAADF images of Ga-terminated as well as the P-terminated cores as shown in figure 4.30. Each image shows the detail of the simulated HAADF image in combination with a detail of the corresponding, adjacent perpendicular GPA strain maps between the dislocations. The first row shows the $[\bar{1}10]$ viewing direction and the second row the corresponding [110] projection. The first column, images (a) and (d), belongs to the already discussed model of Sb-terminated shuffle set dislocations in $[\bar{1}10]$ direction and P-terminated glide set dislocations. The presented HAADF and GPA strain map images are details of figures 4.27 and 4.29. The second column presents the Ga-terminated glide set dislocation in $[\bar{1}10]$ and shuffle set in [110] direction in images (b) and (e). The third row shows the P-terminated shuffle set dislocation in $[\bar{1}10]$ and glide set in [110] projection in images (c) and (f).

The perpendicular strain maps with the negatively strained dislocation cores and the band of positive strain between the dislocations like in 4.29 (b) and 4.30 (a) could also be observed for the Ga-terminated glide set dislocation in 4.30 (b) and the P-terminated shuffle set dislocation in 4.30 (c). Both of them were observed in $[\bar{1}10]$ projection like the Sb-terminated shuffle set dislocation. The Ga-terminated shuffle set dislocation in 4.30 (e) and the P-terminated glide set dislocation in 4.30 (f) in [110] projection both showed $e_{\perp}$

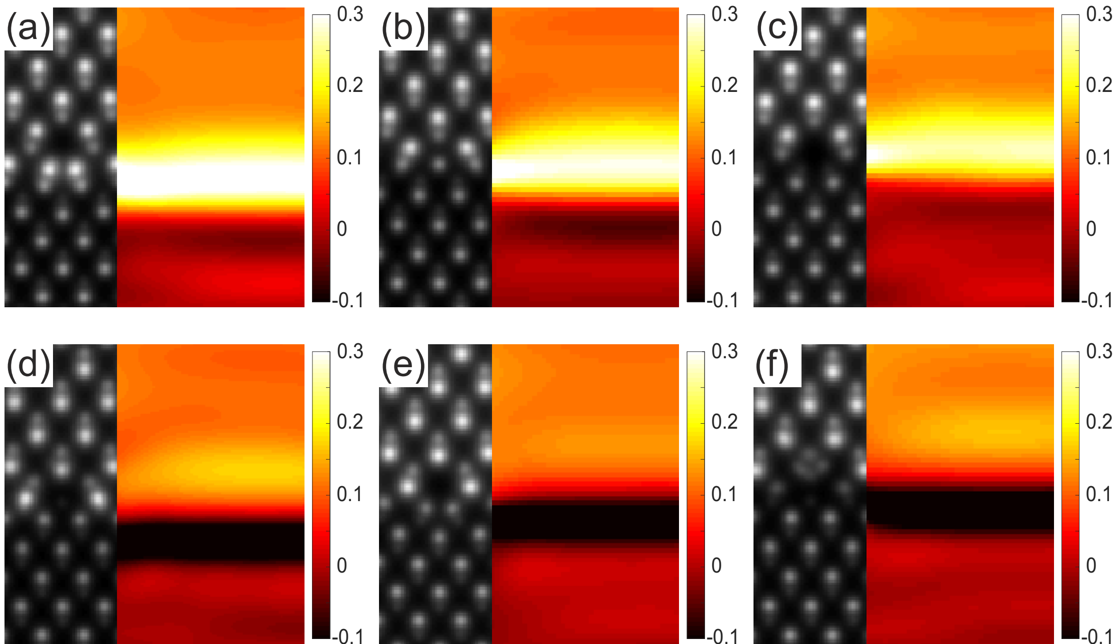

Figure 4.30: Details of the simulated HAADF images of the Sb-terminated, Ga-terminated and P-terminated dislocation cores in combination with the corresponding, adjacent $e_\perp$ GPA strain maps between the dislocations. (a) Sb-terminated shuffle set dislocation, (b) Ga-terminated glide set dislocation and (c) P-terminated shuffle set dislocation, each in [$\bar{1}$10] projection and the respective (d) P-terminated glide set dislocation, (e) Ga-terminated glide set dislocation and (f) P-terminated glide set dislocation in [110] projection.

maps with a band of negative strain between the positively strained dislocations like in figure 4.29 (d) and 4.30 (d) for the P-terminated glide set dislocation in [110] projection.

This means, that the observed GPA $e_\perp$ strain depends on the polarity of the viewing direction and is therefore not comparable to the theoretical strain maps. This can be explained by the contrast change within the dumbbells at the GaP/GaSb interface given that the contrast in STEM images is depending on the atomic number and $Z_P < Z_{Ga} < Z_{Sb}$. In the GaP layer, the intensity is brighter at Ga atom positions, the group III sublattice, in the GaSb layer, it is brighter at the Sb atom positions, the group V sublattice. The center of mass, or rather center of intensity of the dumbbell has therefore been changing from a position closer to group III to a position closer to group V position leading to the observed dependency of the $e_\perp$ strain component on the polarity. This means that the $e_\perp$ strain at the interface cannot be analyzed by GPA. It is not possible to observe the band of high positive strain between the dislocations that has been calculated for the theoretical strain in figure 4.28.

For this reasons, peak pairs strain analysis was applied to the same HAADF images simulated from the model shown in 4.26 (g) and (h). Due to the dumbbell structure in

<110> projection, it was necessary to separate the group III and group V sublattices to be able to perform the peak pairs analysis. Hereby, the difficulties of the intensity change at the interface were overcome since then not the mean positions of the dumbbells but each sublattice for itself is considered. After all peaks had been detected and the sublattices had been separated, new images that just display one sublattice were generated for the PP analysis, as described in section 3.4.9. The resulting PP strain maps are presented in figure 4.31. Again, $e_{\parallel}$ is displayed in the first column and $e_{\perp}$ in the second column. The Sb-terminated shuffle set dislocation in $[\bar{1}10]$ projection are separated into the group III strain maps in images (a) and (b) and group V strain maps in (c) and (d). Correspondingly, group III strain maps of the P-terminated glide set dislocations in [110] projection are displayed in (e) and (f) and the group V strain maps in (g) and (h).

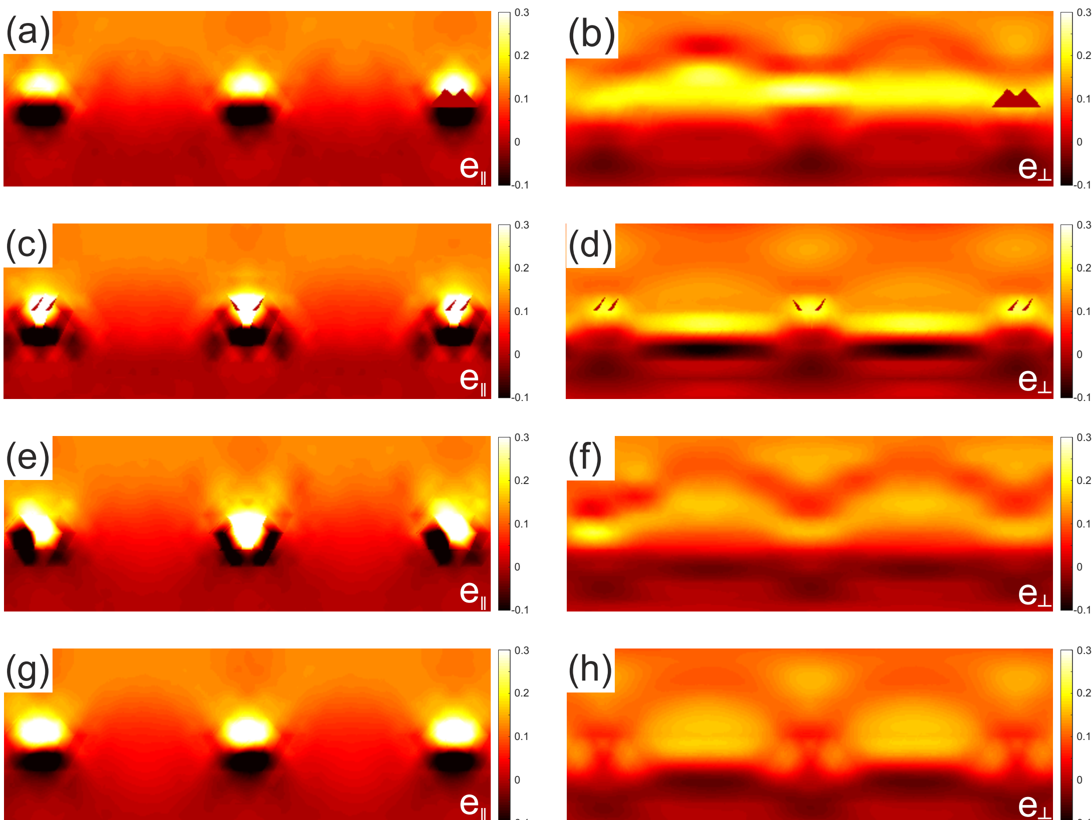

Figure 4.31: PP strain maps of the GaSb/GaP interface of the simulated HAADF images from figure 4.27. (a) and (b) show the $e_{\parallel}$ and $e_{\perp}$ strain maps of the Sb-terminated shuffle set dislocation in $[\bar{1}10]$ projection of the group III positions and (c) and (d) the respective group V positions. (e) and (f) show the $e_{\parallel}$ and $e_{\perp}$ strain maps P-terminated glide set dislocations in [110] projection of the group III positions and (g) and (h) the respective group V positions.

Similar to 4.28 and 4.29, the in-plane strain at the dislocation core (left column) was highly positive in the GaSb layer and a negatively strained in the GaP layer. However, the strain was less confined for the group V shuffle set (c) and group III glide set (e)

dislocations. It is conspicuous that some dislocation cores display areas of unevaluated strain in each strain component. This is caused by the PP algorithm. Similar to the theoretical strain maps in 4.28, PP could not determine the nearest neighbor at the core unambiguously because the nearest neighbor distances were too large. In case of the strain in growth direction, it is noticeable that the band of positive strain was very strong for the shuffle set dislocations and weak for the glide set dislocations. Additionally, the group V $e_{\perp}$ of the shuffle set dislocation in image (d) had a band of negative strain next to the band of positive strain at the interface. The higher strained interface between the shuffle set dislocations makes sense insofar as the high-resolution HAADF images have shown that the first monolayers of GaSb were bowed much stronger between the shuffle set dislocations than the glide set dislocations which leads to the expectation of higher strain at the interface. The perpendicular strain maps of theoretical strain maps in 4.28 (b) and (d) also showed this band of high positive strain between the dislocations. However, in this case, the band of high positive strains seemed to be more pronounced for the glide set dislocations in 4.28 (d). The PP analysis can only consider one sublattice at a time so the results presented by the theoretical strain maps in 4.28 cannot be excluded.

So far, the strain of the GaSb/GaP interface has been investigated for the case of the simulated model of the interface by theoretical calculations, GPA and PP analysis. The comparison of these models showed that they are similar to each other. They revealed that the dislocation cores were highly positively strained in the GaSb layer and a negatively strained in the GaP layer for the in-plane strain while in growth direction they were mainly strained in the GaSb layer. The results were similar but not the same and thereby showed the weaknesses of each method. Particularly the strain in growth direction revealed the biggest differences. It has hence been shown that the GPA is not suitable for the strain analysis of these highly strained interfaces in <110> direction and should therefore not be used for the evaluation of the experimental images. Due to the nature of the dislocations, the theoretical strain calculations as well as PP analysis could not determine the nearest neighbors at the highly strained cores unambiguously. The nearest neighbor distances were too large. In comparison, the two methods showed a slightly different strain in growth direction for the glide set dislocations which might be caused by the separation of the sublattices.

The strain analysis of the experimental images from figure 4.24 has also been conducted by PP analysis. The results are presented in figure 4.32 and will be compared to the results of the simulation in the following. The order of the images is analogous to the PP analysis of the simulated images in figure 4.31.

The comparison of the PP strain maps of the experimental with the simulated HAADF images showed a very good agreement. Again, the $e_{\parallel}$ at the dislocation cores was positively strained in GaSb and negatively strained in the GaP layer. However, the strain was less

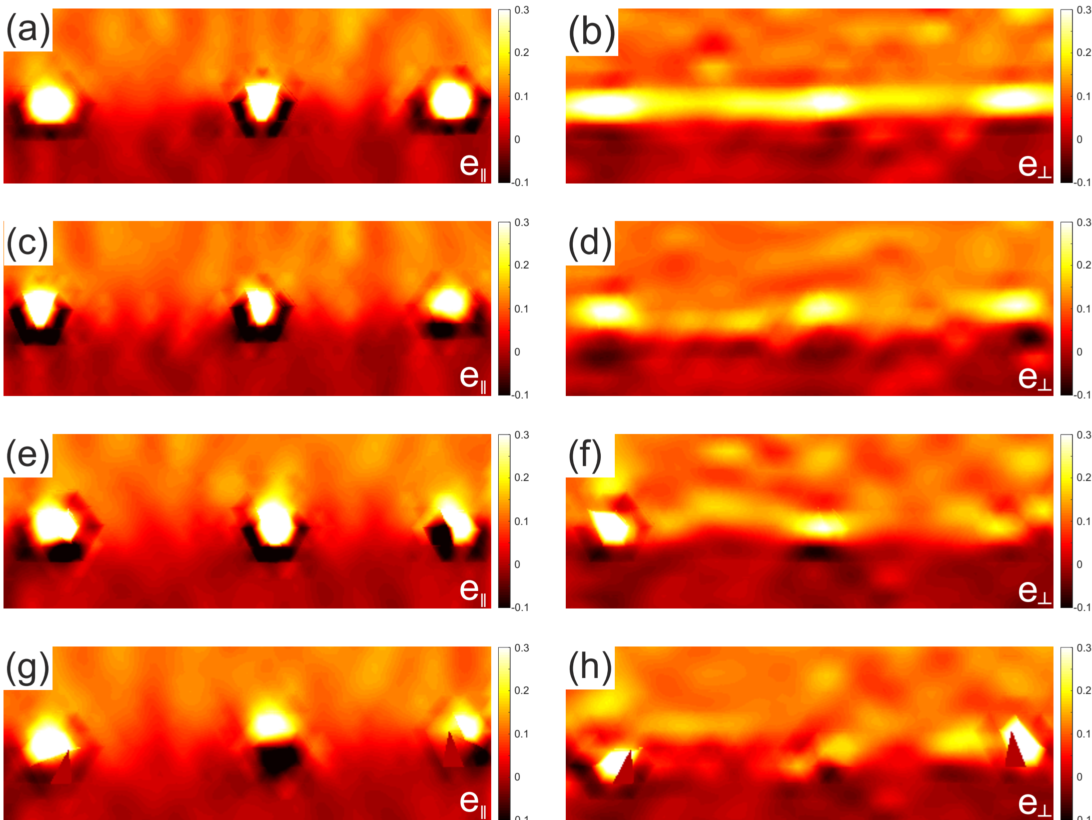

Figure 4.32: PP strain maps of the GaSb/GaP interface of the experimental HAADF images from figure 4.24. (a) and (b) show the $e_{\parallel}$ and $e_{\perp}$ strain maps of the Sb-terminated shuffle set dislocation in [$\bar{1}$10] projection of the group III positions and (c) and (d) the respective group V positions. (e) and (f) show the $e_{\parallel}$ and $e_{\perp}$ strain maps P-terminated glide set dislocations in [110] projection of the group III positions and (g) and (h) the respective group V positions.

confined and looked slightly different within one map of the same dislocation and evaluated sublattice. This emphasizes again the previous conclusion that the peak positions at the dislocation cores cannot be determined unambiguously. This means that PP strain mapping is not suitable to determine whether it is a glide or shuffle set dislocation. Viewing the $e_{\perp}$ strain maps, it is noticeable that the dislocation cores were more strained than in 4.31, looking more similar to the theoretical strain maps in 4.28. The group III strain map of the shuffle set dislocations in 4.32 (b) showed again the band of high positive strain at the interface between the dislocations. The band of positive strain at the interface can be observed in outlines for the remaining $e_{\perp}$ strain maps, similar to the PP analysis of the simulated HAADF images in 4.31 (f) and (h). This band of positive strain can be attributed to the lattice bowing observed in the experimental as well as simulated HAADF images in 4.24 and 4.27.

Altogether, it has been shown that the PP strain maps with separated sublattices of the experimental and simulated HAADF STEM images were in very good compliance.

They were also very similar to the theoretical strain maps of the simulated model except for the band of high positive strain in growth direction between the glide set dislocations. This band of positive strain in $e_\perp$ was much weaker when the two sublattices are treated separately in the PP analysis. All in all, these results show a good basis to compare the strain maps to the respective PP strain maps of Ga(PSb) and Ga(AsSb) in the following subsections 4.2.2 and 4.2.3. As a next step, the abruptness of the GaSb/GaP interface is investigated.

Dumbbell Ratio

In the following, the abruptness of the GaSb/GaP interface is discussed by comparing once again the simulated HAADF images to the experimental ones. The evaluation was carried out by determining the intensity of the atom columns as described for figure 4.25. In the next step, the ratio of the group III intensity to the group V intensity was calculated for each dumbbell and the corresponding dumbbell ratios are plotted on the corresponding group III positions. These dumbbell ratio maps are displayed in figure 4.33 for the simulated HAADF images of figure 4.27 and in figure 4.34 for the according experimental HAADF images of 4.24. Hereby, the complete images are shown in contrast to the cropped part that have been chosen in the previous figures for reasons of presentation.

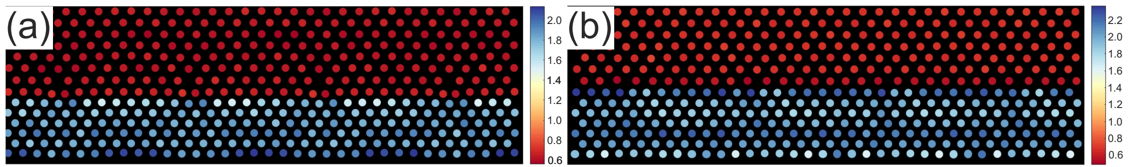

Figure 4.33: Intensity ratio of each dumbbell plotted on the corresponding group III positions for the simulated HAADF images of GaSb on GaP of figure 4.27. (a) $[\bar{1}10]$ (P-polar) and (b) [110] (Ga-polar) viewing direction.

In GaP, the intensity of gallium is much higher than phosphorous due to their atomic numbers 31 and 15, so that the (group III)/(group V) intensity ratio at each dumbbell should be higher than one. In the chosen color map, this corresponds to blue. Since the atom number of antimony is 51, the intensity ratio in GaSb is lower than one, which corresponds to red in the color map. It is noticeable, that the intensity scale bars of the different color maps do not have same range, they differ for the simulated compared to the experimental maps as well as for the each viewing direction. This is due to slightly different intensities, that not only depend on the atomic number but also on the sample thickness in STEM imaging. The thickness of the simulated model differed by one atom layer for the two viewing directions, causing different intensity scales. As explained earlier, the sample thickness of the experimental layers in $[\bar{1}10]$ direction in 4.34 (a) was 18.7 nm and therefore much higher than 13.9 nm along the [110] direction in 4.34 (b). The sample thickness of the latter sample was comparable to the simulations. However, the scale bar

is much lower. This is most likely due to the chromatic aberration which reduces the experimental contrast by ~20 % [196, 197].

The dumbbell ratio maps of the simulated images in 4.33 show that the shuffle set dislocations were located within the first monolayers of GaSb, while the glide set dislocations are directly at the interface. The interface is very abrupt. The color changes promptly from blue to red in both images. However, the maps display a slight color gradient at the interface. This can be attributed to the intensity change of the columns due to the dechannelling by the displacements of the atoms as explained before for the intensity map of the experimental HAADF image in figure 4.25. All these effects can be expected from the model of 4.26 (d).

The dumbbell ratio maps of the experimental images in figure 4.34 display a slightly stronger color gradient in the GaP layer at the interface than the corresponding dumbbell ratio maps of the simulated HAADF images in 4.33. The atom columns in the GaP display a lighter blue to yellow color compared to bulk region.

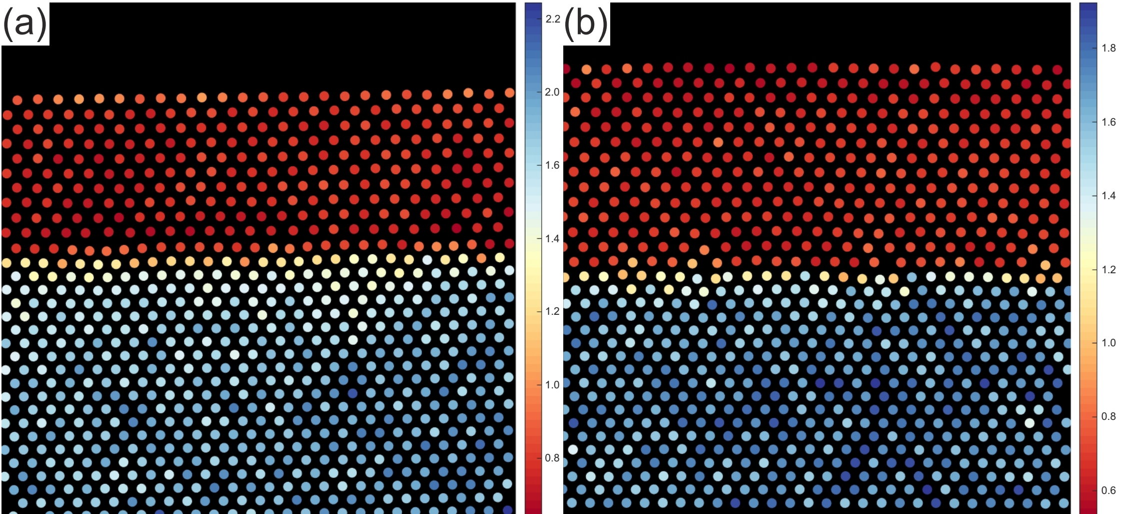

Figure 4.34: Intensity ratio of each dumbbell plotted on the corresponding group III positions for the experimental HAADF images of GaSb on GaP of figure 4.24. (a) [$\bar{1}$10] (P-polar) and (b) [110] (Ga-polar) viewing direction.

This can again be explained to some extent by the dechannelling due to the displacements of the atoms. Additionally, plastic relaxation that leads to a bending of the lattice planes close to the interface and adds to the dechannelling should be taken into account [100]. If intermixing of the GaP and GaSb had been taking place at the interface by the formation of Ga(PSb) columns, this would be expected as an yellow/orange color gradient with an (group III)/(group V) dumbbell ratio close to one in the GaSb layer, not before the interface, in the GaP layer. The transition to the GaSb layer was very abrupt, in accordance with the simulation. No roughness or structuring of the interface,

such as the formation of small islands or pyramidal structures as found for the growth of GaP on Si [198], could be observed. The experimental intensity dumbbell ratio maps show an abrupt interfaces with sharp composition profiles in both <110> viewing direction.

Altogether, it has been shown that the dumbbell ratio maps of the simulated and experimental images were in reasonable agreement. Apart from slight, explainable discrepancies of dumbbell ratio intensities in GaP, the dumbbell ratio maps of the experimental HAADF images of the GaSb/GaP interface match the dumbbell ratio maps of the simulated HAADF images. Both figures showed an abrupt interface without intermixing on the atom columns in GaSb or structuring of the interface.

The investigation of the GaSb islands on GaP/Si has shown that the strain is mainly accommodated by 90° dislocations at the interface, however, 60° dislocation pairs have also been observed. In the $[\bar{1}10]$ projection, the Lomer dislocations were Sb-terminated shuffle set dislocations, that were located within the first ML of GaSb. In the Ga-polar [110] viewing direction, the Lomer dislocations were of glide set type. The core atom of the glide set dislocations was assumed to be phosphorous. The investigations of this interface had not only been conducted by the investigation of experimental HAADF images but also by modeling the interface and investigating the simulated HAADF images in the same manner as the experimental ones, using PP strain mapping and evaluating the intensity dumbbell ratios. In addition to the PP strain mapping, it was possible to calculate theoretical strain maps from the simulated model. The experimental as well as simulated HAADF images showed that the position of the Lomer dislocations within the first ML of GaSb caused a lattice bowing between the dislocations. This led to a band of positive strain in the $e_{\perp}$ theoretical and PP strain maps. The intensity dumbbell ratio maps showed that the interface was abrupt, without intermixing. Altogether, the comparison between the experiment and the simulation showed a good agreement.

4.2.2 Ga(PSb)/GaP interface

In this section, the previous results obtained for the the GaSb/GaP interface is compared to the result of the Ga(PSb)/GaP interface. The investigated Ga(PSb) islands were grown under similar growth conditions as the sample presented in figure 4.4, however, without a TESb preflow. The partial pressures were again TEGa = $7.1 \cdot 10^{-3}$ mbar, TBP = 0.1 mbar, TESb = 0.0176 mbar, V/III = 17, Sb/V = 0.15 at a growth temperature of $475°C$. Before the growth of the islands, a 1 s pre-run of the antimony precursor TESb was introduced to provide a Sb wetting of the surface [57, 126]. Figure 4.35 presents the HAADF STEM investigations of the Ga(PSb)/GaP interface, using again the sum of an aligned stack of 30 images to minimize the scan noise. The sample thicknesses of the two images in viewing direction was determined to 12.6 nm and 15.8 nm, respectively.

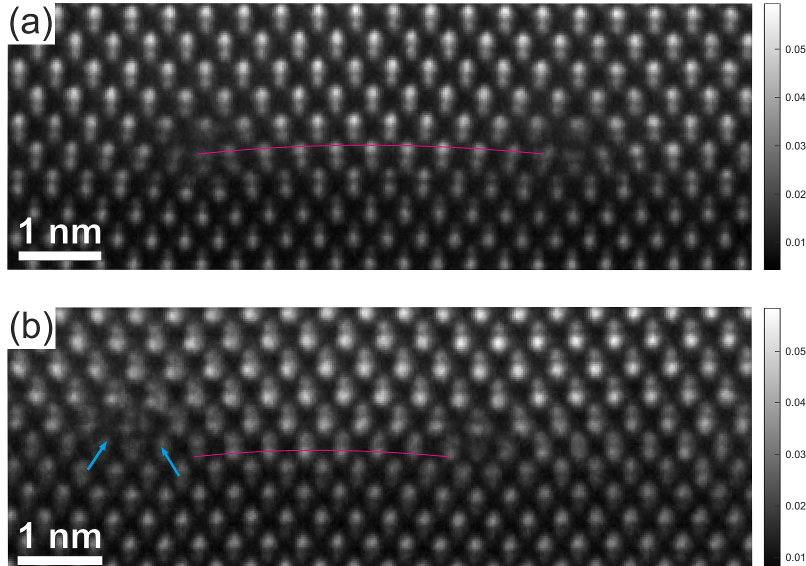

Figure 4.35: HAADF STEM images of the Ga(PSb)/GaP interface in (a) [$\bar{1}$10] (P-polar) and (b) [110] (Ga-polar) viewing direction. The magenta line is a guide to the eye for the lattice bowing. The blue arrows indicate the inserted {111} lattice planes that form a closely space 60° dislocation pair.

Figure 4.35 (a) displays Sb-terminated shuffle set dislocations along the P-polar [$\bar{1}$10] projection. Similar to the GaSb/GaP interface, the dislocations cores were located within the first ML of GaSb, causing again a bowing of the first ML in GaSb between the islands. Since the lattice mismatch is reduced from 12 % for the GaSb islands to 8 % for the Ga(PSb) islands, the dislocation spacing has been larger and the bowing less severe. Figure 4.35 has the same magnification as 4.24, showing only two instead of three dislocations. Accordingly, the Ga-polar [110] viewing direction in image (b) shows a glide set dislocation on the right. The left dislocation is a 60° dislocation pair, because the inserted {111} lattice planes do not terminate at the same atom column. Altogether, the two images are in accordance with the HAADF results obtained for the GaSb/GaP interface.

In the next step, the peak pair analysis on the separated sublattices of the HAADF images was performed in the same manner as for figure 4.24. The resulting strain maps are displayed in figure 4.36. The order of the images is the same as in figure 4.24.

Again, some dislocations showed areas of unevaluated strain due to the missing nearest neighbor at the core. The left column shows the in-plane strain maps. In accordance with figure 4.24, the in-plane strain component at the dislocation cores was highly positive in the Ga(PSb) layer and a negative in the GaP layer. The band of positive strain in the perpendicular strain maps of the right column was only clearly visible for the group III strain shuffle set dislocation in image (b) but much weaker than the according image in 4.24 (b). This is reasonable since the bowing of the first ML of Ga(PSb) between the

dislocations was much weaker compared to GaSb due to the higher dislocation spacing as shown by the HAADF images in the figures 4.35 and 4.24.

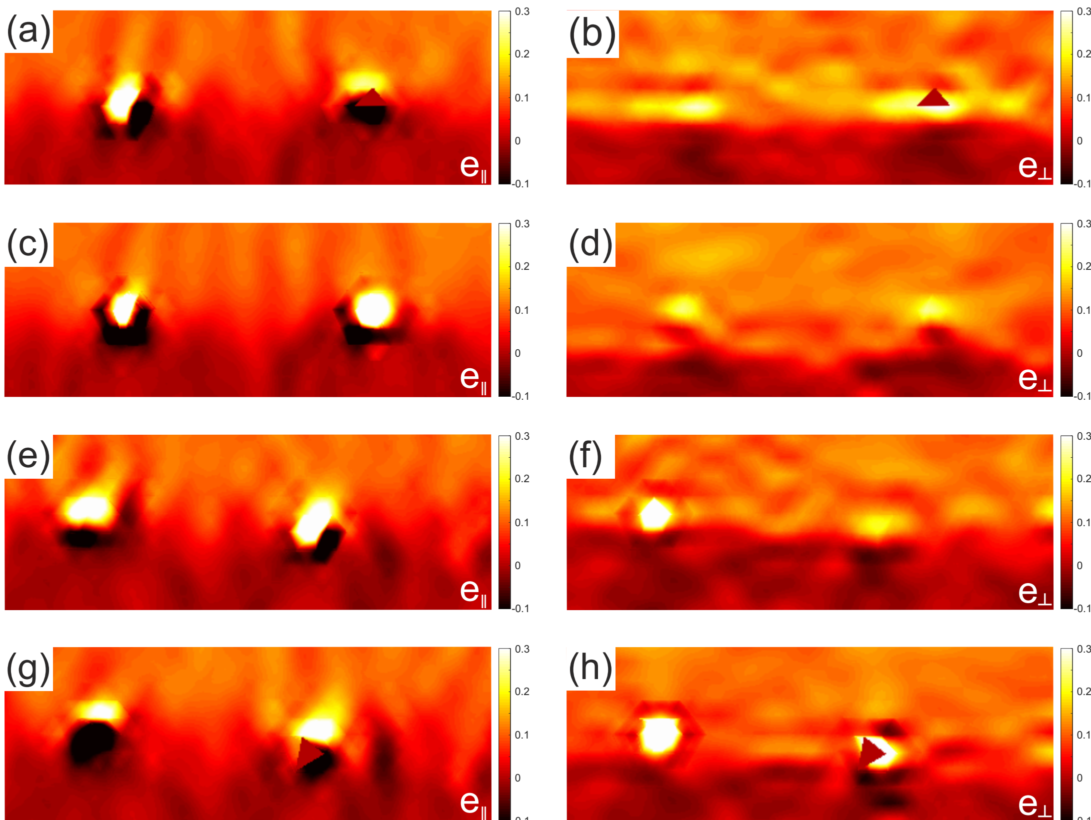

Figure 4.36: PP strain maps of the Ga(PSb)/GaP interface of the experimental HAADF images from figure 4.35. (a) and (b) show the $e_\parallel$ and $e_\perp$ strain maps of the Sb-terminated shuffle set dislocation in $[\bar{1}10]$ projection of the group III positions and (c) and (d) the respective group V positions. (e) and (f) show the $e_\parallel$ and $e_\perp$ strain maps P-terminated glide set dislocations in [110] projection of the group III positions and (g) and (h) the respective group V positions.

The high-resolution HAADF STEM images in figure 4.35 only show a detail of larger images that have been cropped to the same size as the GaSb/GaP HAADF images and their simulation for reasons of presentation. The large image of figure 4.35 (b) in the Ga-polar [110] viewing direction is displayed again in figure 4.37. On the left, there is the 60° dislocation pair and in the middle the glide set dislocation. The dislocation on the right, however, is a Ga-terminated shuffle set dislocation. Its presence can be explained by a double atomic step between the glide set and shuffle set dislocation. However, a missing core atom could also lead to the same result. The core of the shuffle set dislocation was located within the first monolayer of Ga(PSb) while the glide set Lomer dislocation was at the interface. This observation had been conducted at more than one occasion in this sample and is in agreement to the findings of Wang et al. [195], who also found shuffle set dislocations in both <110> directions. They explained their presence due to

the lower total elastic energy of the shuffle set dislocations compared to the glide set dislocations.This also fits for the calculated elastic energies of the GaSb/GaP models in the previous section. The shuffle set dislocations in the Ga-polar [110] direction have not been observed for the GaSb/GaP interface, but this might be due to the limits of statistics.

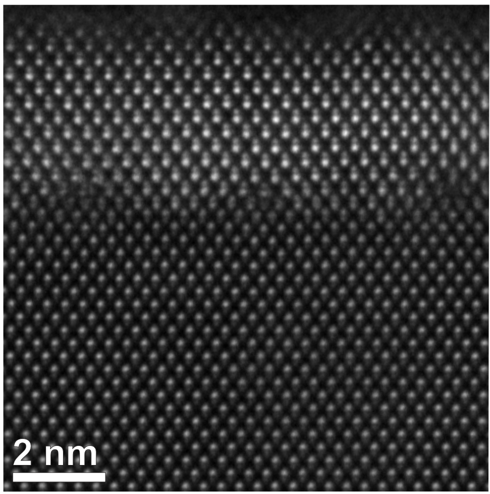

Figure 4.37: HAADF STEM image of the Ga(PSb)/GaP interface in [110] (Ga-polar) viewing direction.

The experimental HAADF images with a large field of view have been used to investigate the interface roughness using again the intensity dumbbell ratio maps as already conducted for the GaSb/GaP interface in figure 4.33 and 4.34. Figure 4.38 shows the corresponding (group III)/(group V) dumbbell intensity ratio maps for the two viewing directions. Image (b) presents the intensity dumbbell ratio map of the [110] viewing direction of figure 4.37. It is noticeable that the interface was not as smooth as GaSb/GaP interface in 4.34 (b), particularly at the atomic step between the shuffle set and glide set dislocations. There was intermixing of P and Sb at the atomic columns of the interface, leading to dumbbell ratios between 1 to 1.4, which became apparent as orange to yellow points in the map and as interface roughening in form of intermixed intensity ratios or rather intermixed blue, red or orange points at the interface. These two effects led to an intermixed layer in the perpendicular [$\bar{1}$10] projection in image (a) below the shuffle set dislocation cores, that were located in the first ML of Ga(PSb). This layer also had intensity dumbbell ratios between 1 to 1.6, so that the color ranged from orange over yellow to light blue, that were caused by the different Sb/P ratios and the average of the interface roughening in the perpendicular direction. This intermixing that had not been observed for the growth of GaSb on GaP can be explained by the growth of the ternary material. During the growth, the antimony and phosphorous compete for the group V lattice positions. Each atom column at the interface has a different amount of Sb/P ratio leading to a different intensity of the group V column and therefore to different intensity ratios compared to the group

III column. The different ratios of Sb to P can again be explained by the undecomposed TBP.

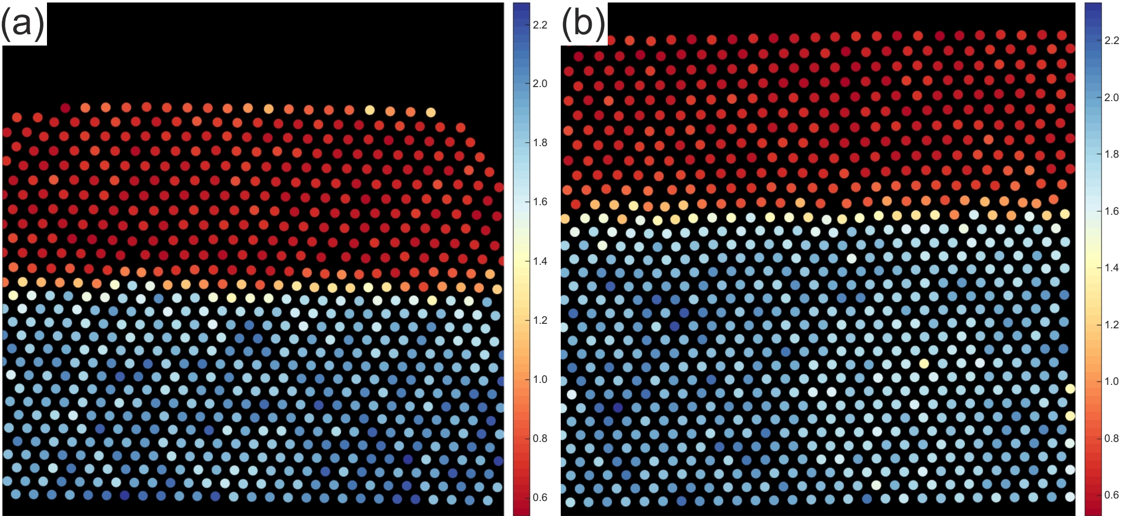

Figure 4.38: Intensity ratio of each dumbbell plotted on the corresponding group III positions for the experimental HAADF images of Ga(PSb) on GaP of figure 4.35. (a) [$\bar{1}$10] (P-polar) and (b) [110] (Ga-polar) viewing direction.

In summary, it has been shown that the Ga(PSb) islands grow in a similar way as GaSb on the GaP/Si pseudosubstrate. The strain was accommodated by the formation of Lomer shuffle set dislocations located in the first ML of the Ga(PSb) islands in the P-polar [$\bar{1}$10] direction and glide set dislocations at the Ga(PSb)/GaP interface in the perpendicular Ga-polar [110] viewing direction. Additionally, 60° dislocation pairs had also been observed in both directions. However, the presence of atomic steps at the GaP surface led to the formation of shuffle set dislocations in the [110] projection. The evaluation of the strain of the Ga(PSb)/GaP interface by PP strain mapping with separated sublattices showed very similar results to the GaSb/GaP strain maps. However, the band of positive strain at the interface was much weaker for the Ga(PSb)/GaP interface, which can be explained by the less pronounced bowing of the first ML in Ga(PSb) compared to GaSb due to the larger dislocation spacing caused by the lower lattice mismatch. Reducing the mismatch by including P into the growth GaSb-based buffer on GaP/Si changed little in the strain relaxation and formation of dislocations at the interface. However, growing a ternary material like Ga(PSb) instead of binary GaSb led to a competition between the incorporation of Sb or P on the group V lattice positions. The evaluation of the (group III)/(group V) intensity ratio at each dumbbell showed that the interface was slightly rougher than the GaSb/GaP interface due to this intermixing on the atom columns at the interface.

4.2.3 Ga(AsSb)/GaP interface

In the last part, the Ga(AsSb)/GaP interface is investigated and compared to the previous results of the GaSb/GaP and Ga(PSb)/GaP interfaces using the same techniques as before. The Ga(AsSb) islands were grown under similar growth conditions as the samples in section 4.1.1 and 4.1.2 using TEGa $= 14.2 \cdot 10^{-3}$ mbar, TBAs $= 0.0249$ mbar, TESb $=$ 0.0167 mbar, V/III $= 2.9$, Sb/V $= 0.4$, at a growth temperature of $475°C$. Before the growth of the islands, a 1 s pre-run of the antimony precursor TESb was introduced to provide a Sb wetting of the surface [57, 126]. Figure 4.39 shows the HAADF STEM micrographs of the Ga(AsSb)/GaP interface in the same magnification as the figures 4.35 and 4.24. The sample thicknesses of both images in viewing direction were determined to 11.9 nm and 15 nm.

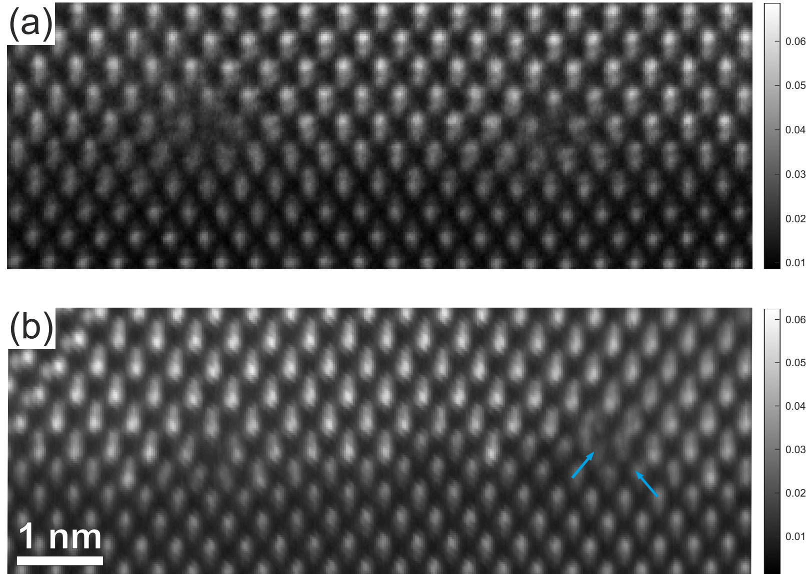

Figure 4.39: HAADF STEM images of the Ga(AsSb)/GaP interface in (a) $[\bar{1}10]$ (P-polar) and (b) [110] (Ga-polar) viewing direction. The blue arrows indicate the inserted {111} lattice planes that form a closely space 60° dislocation pair.

It is quite noticeable, that the HAADF images of the Ga(AsSb)/GaP differ from the HAADF investigations of the GaSb/GaP and Ga(PSb)/GaP interfaces. For the Ga(AsSb)/GaP interface, the Lomer glide set dislocations were observed in image (a) that show the P-polar $[\bar{1}10]$ viewing direction. The perpendicular Ga-polar [110] projection is displayed in image (b) and shows a shuffle set dislocation on the right as well as a 60° dislocation pair on the left. Of course, 60° dislocation pairs have also been found in $[\bar{1}10]$ viewing direction. According to the polarity, these dislocations had Ga-terminated cores and were located directly at the interface and not within the first ML of Ga(AsSb). In consequence, there was no lattice bowing between the dislocations apparent. This agrees with the model of the Ga-terminated Lomer dislocations at the GaSb/GaP interface in figure 4.26 (a) that also showed no lattice bowing between the dislocations. However, in

case of the P-polar [$\bar{1}$10] projection, P-terminated shuffle set Lomer dislocations had also been observed at the interface, similar to the Ga-terminated shuffle set dislocation in the [110] viewing direction of the Ga(PSb) islands in figure 4.37.

Figure 4.40 shows the PP strain maps of the Ga(AsSb)/GaP interface that have been generated analogously to the previous PP strain analysis of the other two material systems.

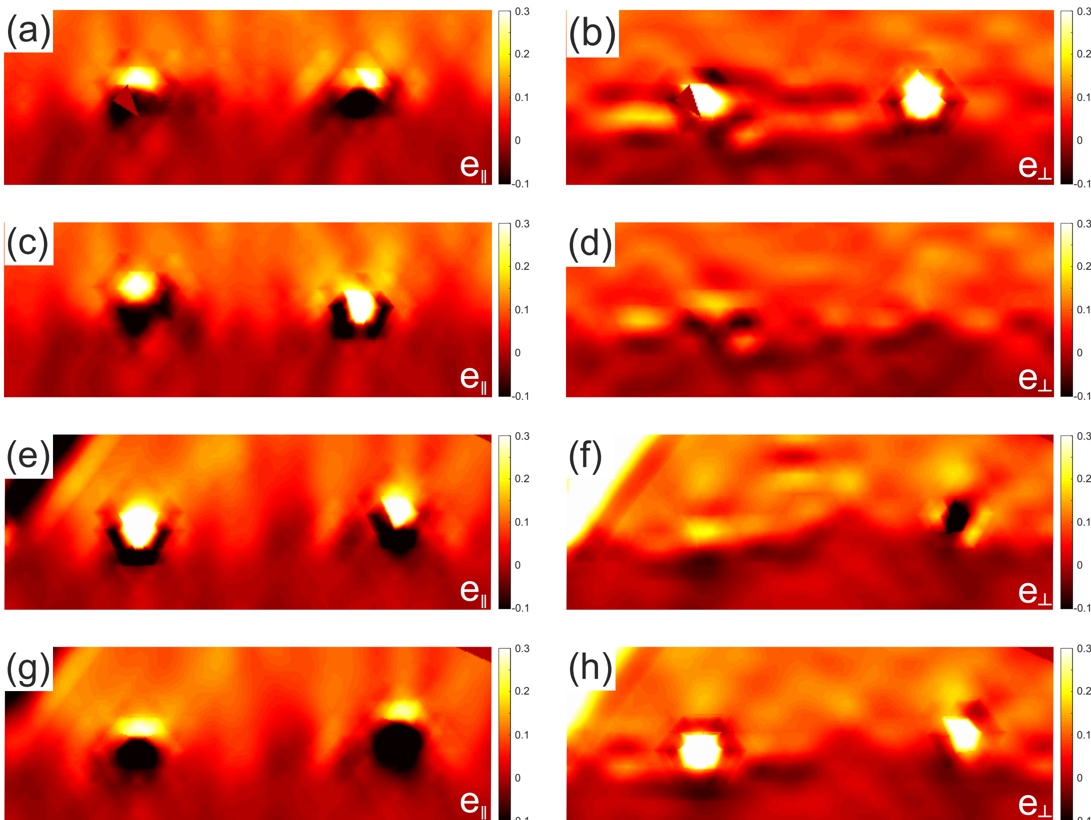

Figure 4.40: PP strain maps of the Ga(AsSb)/GaP interface of the experimental HAADF images from figure 4.39. (a) and (b) show the $e_{\parallel}$ and $e_{\perp}$ strain maps of the Sb-terminated shuffle set dislocation in [$\bar{1}$10] projection of the group III positions and (c) and (d) the respective group V positions. (e) and (f) show the $e_{\parallel}$ and $e_{\perp}$ strain maps P-terminated glide set dislocations in [110] projection of the group III positions and (g) and (h) the respective group V positions.

Images (a) - (d) show the strain analysis of the Ga-terminated glide set dislocations in [$\bar{1}$10] projection. Using the same order as before, the first row displays the group III sublattice strain maps and the second row of according group V sublattice maps, where the $e_{\parallel}$ are arranged on the left column and $e_{\perp}$ on the right. The strain analysis of the [110] viewing direction with the shuffle set dislocation is displayed in figure 4.40 (e) -(h), accordingly. The stacking fault, that is visible in the corresponding HAADF image of figure 4.39 (b), showed a highly positive strain in group III as well as group V $e_{\perp}$ maps and a highly negative strain in both $e_{\parallel}$ maps. As expected, the in-plane strain maps in

the right column were not different from the according results of the Ga(PSb)/GaP and GaSb/GaP interfaces. It was highly positively strained at the dislocation cores in the Ga(AsSb) layer and negatively strained in the GaP layer. The strain in growth direction in images (d) and (f) at the dislocation cores in the Ga(AsSb) layer is nearly the same or lower than in the GaP layer, which has also been observed in the simulated as well as experimental PP strain maps in figures 4.31 and 4.32. This might be explained in a similar way as the unevaluated areas at the cores due to the changing nearest neighbor distances at the core. It is important to notice that the band of high positive strain between the dislocations could not be observed in the perpendicular strain maps of the Ga(AsSb)/GaP interface. That is consistent with the observations made in the HAADF images in figure 4.39, where no lattice bowing within the first ML of Ga(AsSb) was apparent.

In the last step, the intensity (group III)/(group V) ratios were again evaluated for each dumbbell in the HAADF images of figure 4.39, using the whole, not the cropped part of the images. The corresponding dumbbell ratio maps are shown in figure 4.41. The [110] projection with the shuffle set dislocations in image (b) showed a very structured, rough interface. This was much more pronounced than the structuring at the Ga(PSb)/GaP interface in [110] viewing direction in figure 4.38 (b). In consequence of this highly structured interface in [110] projection, the interface in the perpendicular [$\bar{1}$10] projection showed a layer with ratios of 1 - 1.4 at the interface below and between the dislocations as an average of this roughening. This corresponds to a color range of orange to yellow in the chosen color bar. This can be explained again by the competition of Sb and P at the group V positions during growth. The effect at the Ga(AsSb)/GaP interface might be more pronounced because in this case the whole group V atoms are exchanged from P to As/Sb at the interface instead of just adding Sb to the GaP. Moreover, the composition of the $Ga(As_{48.6}Sb_{51.4})$ contained much less Sb compared to the $Ga(P_{33.3}Sb_{66.7})$ buffer layer or the binary GaSb. The incorporation of Sb was less efficient since a lower amount of Sb was incorporated using the same TESb partial pressure and a higher Sb/V ratio of 0.4 compared to 0.15 for Ga(PSb).

The investigation of the Ga(AsSb) islands grown on GaP/Si showed that the nucleation of this ternary Sb-based buffer is different to the growth of GaSb or Ga(PSb) on GaP. The HAADF STEM images revealed that the Lomer set dislocations were Ga-terminated and the glide and shuffle set dislocation lines ran along the opposite directions as for the other two material systems, namely glide set dislocations along the [$\bar{1}$10] direction and shuffle set along [110]. Due the their Ga-terminated character, the dislocations were located directly at the interface and not within the first monolayers of the Ga(AsSb) islands. In consequence, there was no lattice bowing between the dislocations so that the PP strain maps in growth direction showed no band of high positive strain between the dislocations.

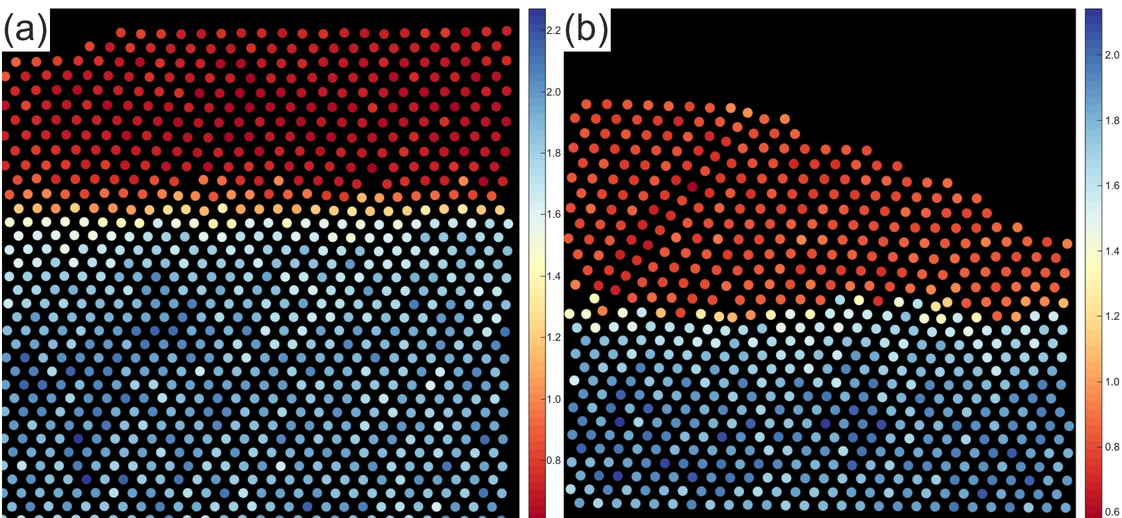

Figure 4.41: Intensity ratio of each dumbbell plotted on the corresponding group III positions for the experimental HAADF images of Ga(AsSb) on GaP of figure 4.39. (a) [$\bar{1}$10] (P-polar) and (b) [110] (Ga-polar) viewing direction.

In addition to the Lomer set dislocations, 60° dislocation pairs had been observed in both viewing direction. The [$\bar{1}$10] projection not only showed glide set dislocations at the interface but also shuffle set dislocations. The evaluation of the dumbbell intensity ratios showed that the interface roughening at the Ga(AsSb)/GaP interface is much more severe than for the corresponding Ga(PSb)/GaP. This interface roughening might be connected to the formation of Ga-terminated Lomer set locations located directly at the interface instead of the Sb-terminated dislocations in the first monolayer of the buffer layer. The rougher interface shows that the growth kinetics is different compared to the GaSb and Ga(PSb) buffer layers. The effect of the Sb wetting layer introduced by the TESb pre-run might be compensated by the TBAs precursor that has a more efficient dissociation than TBP.

4.2.4 Summary of the structural investigation of GaSb, Ga(PSb) and Ga(AsSb) islands on GaP

In the second part of this study, the island-like nucleation of GaSb, Ga(PSb) and Ga(AsSb) on the GaP/Si pseudosubstrate was investigated and compared to each other by high-angle annular dark-field (HAADF) STEM. The images revealed that all islands relaxed by forming Lomer dislocations at the interface, but 60° dislocation pairs were observed frequently. However, the observed 90° dislocations did not have the same atomic configuration in all three material systems. The GaSb and Ga(PSb) islands had shuffle set dislocations in [$\bar{1}$10] viewing direction and glide set dislocations in the perpendicular [110] projection. However, the shuffle set dislocations were not located directly at the interface like the glide

set dislocations but within the first monolayers (ML) of GaSb and Ga(PSb), respectively. As a consequence, a bowing of the first ML of the buffer layers between the dislocations could be observed. This bowing was much more severe in GaSb compared to Ga(PSb) since the dislocation spacing was much smaller in GaSb due to the higher mismatch of 12 % compared to 8.4 %. In the case of the binary GaSb, a model of GaSb/GaP interface had been calculated and used to simulate the HAADF images. These simulated HAADF images matched the experimental ones well. The comparison of the intensities showed that the core atom of the glide set dislocations were not Sb-terminated like the shuffle set dislocations, but they were P-terminated instead. The Ga(AsSb)/GaP interface on the other hand had Ga-terminated dislocations with glide set dislocations in [$\bar{1}$10] and shuffle set dislocations in [110] projection. The investigation of the Ga(PSb)/GaP and Ga(AsSb)/GaP showed that the presence of shuffle set dislocation between glide set dislocations was possible after a double atomic step or by a missing core atoms of the glide set dislocations. These shuffle set dislocations had the opposite atomic termination than the neighboring glide set dislocations and shuffle set dislocations in the perpendicular <110> direction.

In order to gain a further insight on the interfaces, the HAADF image have been investigated by strain mapping as well as by theoretical calculations of the strain in the model of the GaSb/GaP material system. These theoretical strain maps have been compared to geometric phase analysis (GPA) and peak pair (PP) analysis of the separated sublattices of the simulated HAADF images first. The in-plane strain maps of all three methods were very similar to each other and revealed that the dislocation cores had a high positive strain in the GaSb layer and a negative strain in the GaP layer. However, the perpendicular strain maps differed from one another. They showed that GPA was not suitable for an interface viewed in <110> direction. The change of the center of intensity in the dumbbells determines the $e_{\perp}$ strain at the interface in dependence on the viewing direction and not the actual strain. The theoretical as well as the PP $e_{\perp}$ strain maps showed a band of high positive strain at the interface in the GaSb layer between the dislocations. This could be attributed to the the lattice bowing observed in the HAADF images. However, this band of positive strain in $e_{\perp}$ was much weaker when the two sublattices were treated separately in the PP analysis, in particular for the [110] projection between the glide set dislocations. The comparison of the PP strain maps of the experimental HAADF images to the PP analysis of the simulated HAADF images of the GaSb/GaP interface showed a very good agreement. They were also very similar to the PP strain analysis of the Ga(PSb)/GaP interface. Here, the band of positive strain in the perpendicular strain maps was much weaker. This fitted well to the weaker bowing in the GaSb layers that had been observed in the corresponding HAADF images. The PP analysis of the Ga(AsSb)/GaP interface also fitted well to the results of the other two material systems. They still showed a high positive strain in the GaSb layer and negative strain in the GaP layer for the dislocation

cores of the in-plane strain component. The perpendicular PP strain maps did not show a the band of high positive strain at the interface which fitted to the Ga-terminated dislocations that were located at the interface and did not cause a lattice bowing.

The interfaces of the three different material systems have not only been analyzed by strain mapping but also by evaluating the (group III)/(group V) intensity ratios of the dumbbells in the HAADF images. In the case of the GaSb/GaP interface, the dumbbell ratio maps of the experimental and simulated HAADF images were in good agreement to one another showing an abrupt interface. In the case of the Ga(PSb)/GaP interface, which showed a similar dislocation formation to the GaSb/GaP interface, the intensity dumbbell ratio maps revealed different ratios of Sb to P on the atom columns at the interface which led to a rougher interface compared to GaSb/GaP. This could be explained by the competition between the incorporation of Sb or P on the group V lattice positions. In the case of the Ga(AsSb)/GaP interface, this interface roughening was even more severe since the competition for the group V lattice positions was between the three species P, As, Sb at the interface. This showed that the formation of the Ga(AsSb)/GaP interface differed from the Ga(PSb)/GaP and GaSb/GaP interfaces and might explain the different formation of Lomer dislocations and the lower degree of relaxation for the coalescent thick layers investigated by reciprocal space mapping.

5 Summary and Outlook

The aim of the present study was the growth of antimony-based buffer layers with the lattice constant of InP on a GaP/Si pseudosubstrate by metal organic vapor phase epitaxy (MOVPE) and their structural investigation by atomic force microscopy (AFM), X-ray diffraction (XRD), and (scanning) transmission electron microscopy ((S)TEM). The purpose of these buffer layers was to overcome the lattice mismatch between Si and InP and to provide a smooth surface for the growth of n-doped (GaIn)As channel layers with a lattice constant of InP on a Si substrate. In order to obtain (GaIn)As channel layers with high electron mobilities, it is necessary to grow buffer layers with low defect densities. Lattice defects such as threading dislocations, stacking faults or twins act as scattering and/or recombination centers for charge carriers leading to a degradation in performance and live time of devices. Therefore, a 2D-nucleation with the formation of a Lomer dislocation network at the interface between GaP and the buffer layer to compensate for the misfit strain would be favorable. Lomer dislocations are the most efficient dislocations for strain relaxation and the more perfect the dislocation network the less threading dislocations will be formed. A 2D-growth will prevent the formation of threading dislocations, stacking faults or twins that would be formed during the coalescence of islands after an island-like nucleation or Stranski-Krastanow growth. The Sb-based buffer layers were not grown directly onto the silicon substrate but on a GaP buffer layer instead, in order to avoid the formation of antiphase boundaries within Sb-based buffer layer. Previous studies have shown that certain growth conditions allow an annihilation of the antiphase boundaries during the growth of the polar GaP on the non-polar Si substrate.

This study has shown that the growth of Sb-based buffer layers on GaP/Si pseudosubstrate is very challenging. The main problem was the island-like nucleation that occurs for Ga(PSb), Ga(AsSb) as well as GaSb on GaP/Si. The islands had different degrees of relaxation. The atomic resolution HAADF investigations have shown that the islands not only have Lomer but also 60° dislocations and 60° dislocation pairs at the interface. Additionally, they were relaxed by plastic relaxation due to the free surface as well as by the formation of stacking faults. However, the presence of stacking fault might not only be attributed to strain relaxation but also to unoptimized growth conditions that led to a stacking disorder. It has been shown that the interface roughness increases for the ternary material system Ga(PSb)/GaP compared to the binary GaSb/GaP and is most severe for the Ga(AsSb)/GaP, where the group V atoms are completely exchanged

from P to (AsSb). This might explain the formation of Ga-terminated Lomer dislocations instead of Sb-terminated shuffle set dislocations in $[\bar{1}10]$ projection and P-terminated glide set dislocations in [110] projection, as it has been observed for the GaSb/GaP and Ga(PSb)/GaP interfaces. These Sb-terminated shuffle set dislocations were located within the first monolayers of the Sb-based buffer layers which led to an bowing of the lattice planes between the dislocations. In consequence, the peak pairs analysis as well as the theoretical GaSb/GaP strain maps in growth direction showed a band of high positive strain at the interface in the GaSb and Ga(PSb) layer between the dislocations.

With increasing growth time, the sizes of the islands increased until they coalesced. This generated additional lattice defects such as stacking faults, twins and threading dislocations. In consequence, the density of stacking fault as well as threading dislocation densities were in the order of $10^{10}\,cm^{-2}$ for the thick Ga(PSb) buffer layers. In addition, a low Sb-content layer that grew pseudomorphically onto GaP was observed for Ga(PSb) in the trenches of the thin samples that have not coalescent yet as well as in thick, coalescent layers. Reciprocal space mapping (RSM) in XRD as well as the evaluating of the dislocation spacing and misfit in Fourier filtered high-resolution images and geometric phase analysis strain mapping of high-resolution TEM images showed that the degree of relaxations increased with an increasing degree of coalescence.

It was possible to grow Ga(PSb) layers of different composition by varying the partial pressures of the precursors, but this did not change the island-like nucleation and layer quality for Ga(PSb) with high antimony-content. It was, however, possible to grow low Sb-content Ga(PSb) layers pseudomorphically to GaP by increasing P/III ratio above 40 or decreasing the offer of triethylantimony (TESb) so that the Sb/III and Sb/V ratio were decreased. The HAADF investigation of the low Sb-content Ga(PSb) layer grown with a P/III ratio above 40 showed an increased intensity for the Ga-layer at the interface between the GaP and Ga(PSb) layer for the Ga-polar viewing direction. This effect needs further investigations to be explained. These investigations should include comparison to simulations, the investigation of the P-polar direction, energy dispersive X-ray spectroscopy and electron energy loss spectroscopy to investigate the presence of antimony antisites as well as the plasmon and surface plasmon peak.

The island-like nucleation of Ga(PSb) could neither be overcome by introducing a pseudomorphically grown Ga(PSb) interlayer with a low Sb-content between the metamorphic Ga(PSb) and the GaP layer nor by utilizing a flow rate modulated epitaxy. The most promising approach had been the introduction of an InP layer that showed a 2D-nucleation on the GaP/Si pseudosubstrate. If the growth conditions are optimized so that the relaxation of the layer will take place without the formation of lattice defects such as stacking faults or threading dislocations, the InP/GaP/Si pseudosubstrate will be

a very promising growth template not only for the (GaIn)As channel layers but also other materials that are grown on InP substrate. These materials could also be integrated into the CMOS technology. Hereby, the flow rate modulated epitaxy should be investigated again under the aspect of the growth rate so that island formation due to a growth rate different from 1 ML/s is avoided.

For future work, the theoretical strain mapping has been proven to be a useful additional tool to evaluate strain and should be considered for other material systems as well. The software is available in this group and is easy to use due to its user-friendly interface. The peak pair (PP) analysis of the separated sublattices developed in this work made is possible to analyze the strain in the <110> directions with its dumbbell configuration. In this case, geometric phase analysis (GPA) strain mapping becomes problematic for materials with different atomic numbers due to the change of the center of intensity in the dumbbells, so that the PP analysis with separated sublattices offers an interesting alternative for such materials and should be applied in these cases.

6 Zusammenfassung

Ziel der vorliegenden Arbeit war das Wachstum von Antimon-basierten Puffer Strukturen mit der Gitterkonstante von InP auf einem GaP/Si Pseudosubstrat mittels metallorganischer Gasphasenepitaxie (MOVPE) und die anschließende strukturelle Untersuchung mit Rasterkraftmikroskopie (AFM), hochauflösender Röntgenbeugung (XRD) und (Raster-) Transmissionselektronenmikroskopie ((S)TEM). Der Zweck dieser Puffer war die Überbrückung der Gitterfehlanpassung zwischen Si und InP, sodass eine homogene Oberfläche für das Wachstum von n-gedopten (GaIn)As Kanalschichten mit der Gitterkonstante von InP auf einem Siliziumsubstratrat zur Verfügung steht. Um Kanalschichten mit einer hohen Elektronenmobilität zu erhalten ist es notwendig Pufferschichten mit einer geringen Defektdichte herzustellen. Kristalldefekte wie Fadenversetzungen, Stapelfehler oder Zwillinge wirken als Streu- und/oder Rekombinationszentren für Ladungsträger. Dies führt zu einer Verschlechterung in der Leistung und Lebenszeit von elektrischen Bauelementen. Daher wäre eine 2D-Nukleation, bei der ein Netzwerk von 90° Lomer-Versetzungen die Verspannung aufgrund der Gitterfehlanpassung an der Grenzfläche zwischen GaP und der Pufferschicht abbaut, vorteilhaft. 90° Versetzungen sind die effizientesten Versetzungen für die Relaxation von Verspannungen im Kristall. Dabei sollte das Netzwerk von Lomer-Versetzungen so perfekt wie möglich sein und die Ausbildung von Fadenversetzungen zu minimieren. Ein zweidimensionales Wachstum würde verhindern, dass sich beim Zusammenwachsen von Inseln im Stranski-Krastanow oder Vollmer-Weber Wachstum Fadenversetzungen, Stapelfehler und Zwillinge bilden. Um die Entstehung von Antiphasen in den Pufferschichten zu vermeiden, wurden die Sb-basierten Schichten nicht direkt auf das Silizium sondern auf einen GaP Puffer aufgewachsen. Vorherige Studien haben gezeigt, dass die Antiphasengrenzen bei dem Wachstum von polaren GaP auf das unpolare Siliziumsubstrat unter bestimmten Wachstumsbedingungen annihilieren.

Die zugrundeliegenden Untersuchungen dieser Arbeit haben gezeigt, dass das Wachstum von Sb-basierten Pufferschichten auf GaP/Si Pseudosubstrat mit vielen Herausforderungen verbunden ist. Das Hauptproblem lag in der Inselnukleation von GaSb, Ga(PSb) sowie Ga(AsSb) auf dem gewählten Substrat. Diese Inseln hatten jeweils verschiedene Relaxationsgrade. Die hochauflösenden Z-Kontrastbilder haben gezeigt, dass die Inseln nicht nur durch die Lomer-Versetzungen, sondern auch durch 60° Versetzungen und 60° Versetzungspaare and der Grenzfläche ausbilden. Zusätzlich relaxieren die Inseln über plastische Relaxation aufgrund der freien Oberfläche, sowie dem Einbau von Stapelfehlern. Allerd-

ings könnten die Stapelfehler auch auf nichtoptimierte Wachstumsbedingungen, die eine Unordnung der Stapelfolge begünstigen, zurückzuführen sein. Es wurde außerdem gezeigt, dass die Grenzflächenrauigkeit für Ga(PSb)/GaP im Vergleich zum binären GaSb/GaP Materialsystem zunahm und der Ga(AsSb)/GaP Grenzfläche, wo die Gruppe V Atome von P zu (AsSb) komplett ausgetauscht werden, am ausgeprägtesten war. Dies könnte die Entstehung von Ga-terminierten Lomerversetzngen erklären. An den GaSb/GaP und Ga(PSb)/GaP Grenzflächen entstanden stattdessen Sb-terminierten "shuffle set" Versetzungen in [$\bar{1}$10] Projektion and P-terminierten "glide set" Versetzungen in [110] Projektion. Diese Sb-terminierten "shuffle set" Versetzungen wurden in der ersten Monolage der Sb-basierten Pufferschicht gefunden. Dies führte zu einer Verbiegung der Gitterebenen der Pufferschicht zwischen den Versetzungen. In Konsequenz zu dieser Gitterverbiegung wurden bei der "Peak Pairs" Analyse sowie in den theoretischen Verspannungskarten von GaSb/GaP ein Band von hoher positiver Verspannung an der Grenzfläche in der GaSb und Ga(PSb) Schicht zwischen den Versetzungen in Wachstumsrichtung gefunden.

Mit zunehmender Wachstumszeit nimmt die Größe der Inseln zu, bis sie sich zu größeren Inseln verbinden und eine geschlossene Schicht bilden. In der dicken, geschlossenen Ga(PSb) Schicht betrug die Größenordnung für die Dichte an Stapelfehlern und Fadenversetzungen folglich $10^{10}/cm^2$. Zusätzlich wurde in dieser Schicht, sowie in den Gräben von dünneren, nicht-geschlossenen Ga(PSb) Schichten, Kristallbereiche mit geringen Sb-Gehalt, die pseudomorph an der Grenzfläche zu GaP wuchsen, beobachtet. Die Abbildung des reziproken Raumes mittels XRD sowie die Auswertung von den Versetzungsabständen und der Gitterfehlanpassung in Fourier gefilterten Hochauflösungsbildern und "geometric phase analysis" (GPA) der Verspannung in hochaufgelösten TEM-Aufnahmen hat gezeigt, dass der Relaxationsgrad mit wachsender Geschlossenheit der Schicht zunimmt.

Es war möglich Ga(PSb) Schichten mit verschiedenen Kompositionen zu wachsen indem die Partialdrücke der metalorganischen Präkursoren variiert wurden. Dies änderte aber nicht die inselartige Nukleation und Schichtqualität der Ga(PSb) Pufferstrukturen mit hohen Antimongehalt. Es war jedoch möglich Ga(PSb) Schichten mit geringem Antimongehalt pseudomorph auf GaP aufzuwachsen. Dafür wurde entweder das P/III Verhältnis über 40 erhöht oder das Angebot von Triethylantimon (TESb) verringert, sodass das Sb/III und Sb/V Verhältnis reduziert waren. Die HAADF STEM Untersuchung der Ga(PSb) Schichten mit geringem Antimongehalt, die mit einem P/III Verhältnis über 40 gewachsen wurden, ergaben eine erhöhte Intensität für the Galliumatomlage an der Grenzfläche zwischen GaP und Ga(PSb) in der Ga-polaren Untersuchungsrichtung. Dieser Effekt kann bisher noch nicht erklärt werden und sollte in Zukunft weiter untersucht werden. Dafür sollte die P-polare Richtung ebenfalls im STEM untersucht werden und energiedispersive Röntgenspektroskopie und Elektronenenergieverlustspektroskopie durchgeführt werden um die Presänz von Antimon Substitutionsatomen sowie den Plasmon-

und Oberflächenplasmom-Peak zu untersuchen. Außerdem sollte ein Vergleich zu Simulationen gezogen werden.

Die inselartige Nukleation von Ga(PSb) konnte weder durch die Anwendung eines gepulsten Wachstumsmodus noch durch das Einschieben einer pseudomorph gewachsenen Ga(PSb) Zwischenschicht mit einem geringen Sb-Gehalt zwischen der metamorph gewachsenen Ga(PSb) Pufferschicht und der GaP Schicht überwunden werden. Der vielversprechendste Ansatz zur Herstellung einer hochqualitativen Pufferschicht war die Einführung einer InP Schicht. Diese zeigte eine 2D-Nukleation auf dem GaP/Si Pseudosubstrat. Wenn die Wachstumsbedingungen so optimiert würden, dass die Relaxation der InP Schicht ohne die Bildung von Defekten wie Stapelfehlern oder Fadenversetzungen vonstatten geht, dann wäre das InP/GaP/Si Pseudosubstrat eine vielversprechende Grundlage für das Wachstum von (GaIn)As Kanalschichten. Darüber hinaus könnten andere Materialsysteme, die bisher auf InP Substrat gewachsen werden, ebenfalls auf Si gewachsen werden und möglicherweise in die CMOS Technologie integriert werden. Zur Verbesserung des InP-Wachstums auf GaP/Si sollte der gepulste Wachstumsmodus (*engl. flow rate modulated epitaxy*) nochmal unter dem Aspekt der Wachstumsrate untersucht werden. Inselwachstum durch Wachstumsraten abweichend von 1ML/s sollte dabei vermieden werden.

Diese Arbeit hat gezeigt, dass die Berechnung der theoretischen Verspannung ein nützliches Hilfsmittel ist um den Verspannungszustand einer Probe zu bestimmen. Es sollte daher zukünftig für andere Materialsysteme berücksichtigt werden. Die dafür notwendige Software ist in dieser Gruppe zugänglich und durch eine benutzerfreundliche Oberfläche einfach anzuwenden. Die "Peak Pair" (PP) Analyse an getrennten Untergittern, die während dieser Arbeit entwickelt wurde, ermöglichte die Bestimmung der Verspannung in den <110> Richtungen der Zinkblendestruktur mit seiner Hantel-artigen (*engl. dumbbell*) Anordnung der Atome. In diesem Fall ist die Bestimmung der Verspannung mittels GPA problematisch, da bei Materialen mit verschiedenen Ordnungszahlen sich der Intensitätsschwerpunkt innerhalb der "dumbbell" an der Grenzfläche verschieben kann. Daher bietet die PP Analyse mit getrennten Untergittern eine interessante Alternative und sollte für solche Fälle angewandt werden.

Bibliography

[1] F. L. Bauer. *Historische Notizen zur Informatik*. Springer (2009)

[2] J. Kilby. 'Miniaturized electronic circuits.' US 3138743 (1964). (filed Feb 1959)

[3] R. Noyce. 'Semiconductor device-and-lead structure.' US 2981877 (1961). (filed Jul 1959)

[4] F. Wanlass. 'Low stand-by power complementary field effect circuitry.' US 3387286 (1968). (filed Jul 1967)

[5] G. E. Moore. 'Cramming More Components onto Integrated Circuits.' *Electronics* **38**: 114 (1965)

[6] G. E. Moore. 'Progress in digital integrated electronics.' *Electron Devices Meeting* **21**: 11 (1975)

[7] IEEE spectrum, URL: http://spectrum.ieee.org/computing/hardware/gordon-moore-the-man-whose-name-means-progress. *Gordon Moore: The Man Whose Name Means Progress* (2015). Accessed 19.09.16

[8] *International Technology Roadmap for Semiconductors (ITRS)* . http://www.semiconductors.org/main/2015 _international_technology_roadmap_for_semiconductors_itrs (2015). Accessed 19.09.16

[9] heise online, URL: http://www.heise.de/newsticker/meldung/Intel-Chef-verabschiedet-sich-vom-bisherigen-Moore-s-Law-2751848.html. *Intel-Chef verabschiedet sich vom bisherigen "Moore's Law"* (2015). Accessed 19.09.16

[10] Frankfurter Allgemeine Zeitung, URL: http://www.faz.net/aktuell/wirtschaft/unternehmen/moore-s-law-ist-gefaehrdet-chips-aus-silizium-werden-ueberholt-13745555.html. *Das Silizium-Zeitalter geht zu Ende* (2015). Accessed 19.09.16

[11] MIT Technology Report, URL: https://www.technologyreview.com/s/601102/intel-puts-the-brakes-on-moores-law/. *Intel Puts the Brakes on Moore's Law* (2016). Accessed 19.09.16

[12] tom's HARDWARE, URL: http://www.tomshardware.com/reviews/intel-xeon-e5-2600-v4-broadwell-ep,4514-2.html. *Intel Xeon E5-2600 v4 Broadwell-EP Review* (2016). Accessed 19.09.16

[13] J. del Alamo. 'Nanometre-scale electronics with III–V compound semiconductors.' *Nature* **479**: 317 (2011)

[14] P. Win et al.. 'Metamorphic In0.3Ga0.7As/In0.29Al0.71As layer on GaAs: A new structure for high performance high electron mobility transistor realization.' *Applied Physics Letters* **61**: 922 (1992)

[15] J. M. Chauveau et al.. 'Indium content measurements in metamorphic high electron mobility transistor structures by combination of x-ray reciprocal space mapping and transmission electron microscopy.' *Journal of Applied Physics* **93**: 4219 (2003)

[16] I. Vurgaftman et al.. 'Band parameters for III–V compound semiconductors and their alloys.' *Journal of Applied Physics* **89, 11**: 5815 (2001)

[17] J. Massies et al.. 'High-mobility $Ga_{0.47}In_{0.53}As$ thin epitaxial layers grown by MBE, very closely lattice-matched to InP.' *Electron. Lett.* **18**: 758 (1982)

[18] X. Wallart et al.. 'High-mobility InGaAs/InAlAs pseudomorphic heterostructures on InP (001).' *Journal of Applied Physics* **97**: 053706 (2005)

[19] K. Volz et al.. 'GaP-nucleation on exact Si (001) substrates for III/V device integration.' *Journal of Crystal Growth* **315, 1**: 37 (2011)

[20] H. Ibach und H. Lüth. *Festkörperphysik.* Springer, fifth Auflage (2009)

[21] S. Hunklinger. *Festkörperphysik.* De Gruyter (2014)

[22] P. Y. Yu und M. Cardona. *Fumdamentals of Semiconductors.* Springer (1999)

[23] *URL: http://learn.crystallography.org.uk/learn-crystallography/what-is-a-crystal/.* Accessed 16.08.2016

[24] *URL: https://commons.wikimedia.org/wiki/File:Close_packing.svg.* Accessed 16.08.16

[25] G. B. Stringfellow. *Organometallic Vapor-Phase Epitaxy : theory and practice.* Academic Press (1999)

[26] J. H. van der Merwe. 'Crystal interfaces. Part II. Finite overgrowths.' *Journal of Applied Physics* **34**: 123 (1963)

[27] E. Bauer und J. H. van der Merwe. 'Structure and growth of crystalline superlattices: From monolayer to superlattice.' *Physical Review B* **33**: 3658 (1986)

[28] F. C. Frank und J. H. van der Merwe. 'One-Dimensional Dislocations. II. Misfitting Monolayers and Oriented Overgrowth.' *Proceedings of the Royal Society of London, A* **198**: 216 (1949)

[29] J. H. van der Merwe. 'Misfit Dislocation Generation in Epitaxial Layers.' *Critical Reviews in Solid State and Materials Sciences* **17**: 187 (1991)

[30] M. Volmer und A. Weber. 'Keimbildung in übersättigten Gebilden.' *Zeitschrift f. Phys. Chemie* **119**: 277 (1926)

[31] I. Stranski und L. Krastanow. 'Zur Theorie der orientierten Ausscheidung von Ionenkristallen aufeinander.' *Monatshefte für Chemie* **71**: 351 (1937)

[32] T. Torunski. 'Elektronenmikroskopische Untersuchungen zur quantitativen Analyse III / V-Halbleiterheterostrukturen Torsten Torunski.' Doktorarbeit, Universität Marburg (2005)

[33] R. Hull und J. C. Bean. 'Misfit dislocations in lattice-mismatched epitaxial films.' *Critical Reviews in Solid State and Materials Sciences* **17**: 507 (1992)

[34] D. J. Dunstan. 'Review Strain and strain relaxation in semiconductors.' *Journal of Materials Science: Materials in Electronics* **8**: 337 (1997)

[35] L. Vegard. 'Die Konstitution der Mischkristalle und die Raumfüllung der Atome.' *Zeitschrift für Physik* **5**: 17 (1921)

[36] S. C. Jain et al.. 'Misfit strain and misfit dislocations in lattice mismatched epitaxial layers and other systems.' *Philosophical Magazine A* **75**: 1461 (1997)

[37] J. W. Matthews und J. L. Crawford. 'Accomodation of misfit between single-crystal films of nickel and copper.' *Thin Solid Films* **5**: 187 (1970)

[38] J. W. Matthews und A. Blakeslee. 'Defects in epitaxial multilayers.' *Journal of Crystal Growth* **27**: 118 (1974)

[39] D. Holt und B. Yacobi. *Extended defects in semiconductors.* Cambridge University Press (2007)

[40] S. K. Mathis et al.. 'Threading dislocation reduction mechanisms in low-temperature-grown GaAs .' *Journal of Applied Physics* **86**: 4836 (1999)

[41] a. E. Romanov und J. S. Speck. 'Stress relaxation in mismatched layers due to threading dislocation inclination.' *Applied Physics Letters* **83**: 2569 (2003)

[42] P. Cantu et al.. 'Role of inclined threading dislocations in stress relaxation in mismatched layers.' *Journal of Applied Physics* **97**: 103534 (2005)

[43] J. Burgers. *Some considerations on the fields of stress connected with dislocations in a regular crystal lattice.* Kon.inklijke Nederlandse Akademie van Wetenschappen (1939)

[44] F. Nabarro. 'Mathematical theory of stationary dislocations.' *Advances in Physics* **1**: 269 (1952)

[45] W. Lomer. 'A dislocation reaction in the face-centred cubic lattice.' *The London, Edinburgh, and Dublin Philosophical Magazine and Journal of Science* **42:334**: 1327 (1951)

[46] E. Spiecker und W. Jäger. 'Burgers vector analysis of large area misfit dislocation arrays from bend contour contrast in transmission electron microscope images.' *Journal of Physics: Condensed Matter* **14**: 12767 (2002)

[47] F. C. Frank und J. Nicholas. 'CXXVIII. Stable dislocations in the common crystal lattices.' *The London, Edinburgh, and Dublin Philosophical Magazine and Journal of Science* **44:358**: 1213 (1953)

[48] J. Hornstra. 'Dislocation in the Diamond Lattice.' *J. Phys. Chem. Solids* **5**: 129 (1958)

[49] J. Hirth und J. Lothe. *Theory of Dislocations.* New York: McGraw-Hill (1969)

[50] D. Hull und D. Bacon. *Introduction to Dislocations.* Butterworth-Heinemann (2001)

[51] R. Heidenreich und W. Shockley. 'Report of a Conference on The Strength of Solids.' London: Physical Society (1948)

[52] F. C. Frank. 'Sessile Dislocations.' *Proc. Phys. Soc. A* **62**: 202 (1949)

[53] Z. Li und R. C. Picu. 'Shuffle-glide dislocation transformation in Si.' *Journal of Applied Physics* **113**: 083519 (2013)

[54] P. M. J. Marée et al.. 'Generation of misfit dislocations in semiconductors.' *Journal of Applied Physics* **62**: 4413 (1987)

[55] J. Ohlmann. 'Herstellung und Charakterisierung von metamorphen Pufferschichten für Ga(AsP)-Tandem-Solarzellen auf Si.' Dissertation, Philipps-Universität Marburg (2012)

[56] J. Narayan und S. Oktyabrsky. 'Formation of misfit dislocations in thin film heterostructures.' *Journal of Applied Physics* **92**: 7122 (2002)

[57] Y. Wang et al.. 'Mechanism of formation of the misfit dislocations at the cubic materials interfaces.' *Applied Physics Letters* **100**: 262110 (2012)

[58] A. Marzegalli et al.. 'Onset of plastic relaxation in the growth of Ge on Si(001) at low temperatures: Atomic-scale microscopy and dislocation modeling.' *Physical Review B - Condensed Matter and Materials Physics* **88**: 165418 (2013)

[59] P. Gallagher. 'The Influence of Aloying, Temperature, and Related Effects on the Stacking Fault Energy.' *Metallurgical Transactions* **1**: 2429 (1970)

[60] H. Gottschalk et al.. 'Stacking Fault Energy and Ionicity of Cubic III-V Compounds.' *Phys. Stat. Sol.* **45**: 207 (1978)

[61] W. Shockley. 'Dislocations and edge states in the diamond crystal structure.' *Physical Review* **91**: 228 (1953)

[62] S. M. Hu. 'Formation of stacking faults and enhanced diffusion in the oxidation of silicon.' *Journal of Applied Physics* **45**: 1567 (1974)

[63] V. Narayanan et al.. 'Origins of defects in self assembled GaP islands grown on Si (001) and Si (111).' *Thin Solid Films* **357, 1**: 53 (1999)

[64] A. Beyer et al.. 'Influence of crystal polarity on crystal defects in GaP grown on exact Si (001).' *Journal of Applied Physics* **109, 8**: 083529 (2011)

[65] D. Holt. 'Antiphase boundaries in semiconducting compounds.' *Journal of Physics and Chemistry of Solids* **30, 6**: 1297 (1969)

[66] S. F. Fang et al.. 'Gallium arsenide and other compound semiconductors on silicon.' *Journal of Applied Physics* **68, 7**: R31 (1990)

[67] M. Grundmann. 'Antiphase-domain-free InP on Si (001): optimization of MOCVD process.' *Journal of Crystal Growth* **115, 1-4**: 150 (1991)

[68] G. P. Tang et al.. 'Antiphase-Domain-Free InP on (100) Si.' *Japanese Journal of Applied Physics* **31, 8A**: L1126 (1992)

[69] A. Beyer. 'Hochaufgelöste transmissionselektronenmikroskopische Untersuchungen an Galliumphosphid auf Silizium.' Dissertation, Philipps-Universität Marburg (2012)

[70] E. P. O'Reilly. 'Valence band engineering in strained-layer structures.' *Semiconductor Science and Technology* **4**: 121 (1999)

[71] M. V. Fischetti und S. E. Laux. 'Band structure, deformation potentials, and carrier mobility in strained Si, Ge, and SiGe alloys.' *Journal of Applied Physics* **80**: 2234 (1996)

[72] F. Schäffler. 'High-mobility Si and Ge structures.' *Semiconductor Science and Technology* **12**: 1515 (1999)

[73] S. C. Jain et al.. ‘III–nitrides: Growth, characterization, and properties.’ *Journal of Applied Physics* **87**: 965 (2000)

[74] M. Grundmann. *The physics of semiconductors*. Springer (2010)

[75] W. Voigt. *Lehrbuch der Kristallphysik : mit Ausschluss d. Kristalloptik*. Teubner, Leipzig (1910)

[76] J. F. Woitok. ‘High-Resolution XRD: Analysis of Epitaxial Layers.’ PANalytical Manual (2005)

[77] D. Williams und C. Carter. *Transmission Electron Microscopy*. Springer, 1st Auflage (1996)

[78] B. Fultz und J. Howe. *Transmission Electron Microscopy and Diffractometry of Materials*. Springer (2008)

[79] E. Rutherford. ‘Scattering of Alpha and Beta Particles of Matter and the Structure of the Atom.’ *Philosophical Magazine* **21**: 669 (1911)

[80] P. A. Doyle und P. S. Turner. ‘Relativistic Hartree-Fock X-ray and electron scattering factors.’ *Acta Crystallographica Section A* **24, 3**: 390 (1968)

[81] A. Weickenmeier und H. Kohl. ‘Computation of absorptive form factors for high-energy electron diffraction.’ *Acta Crystallographica Section A Foundations of Crystallography* **47, 5**: 590 (1991)

[82] O. Scherzer. ‘Über einige Fehler von Elektronenlinsen.’ *Optik* **101**: 593 (1936)

[83] M. Haider et al.. ‘Information Transfer in a TEM Corrected for Spherical and Chromatic Aberration.’ *Microscopy and Microanalysis* **16**: 393 (2010)

[84] A. Bleloch und Q. Ramasse. *Aberration-Corrected Analytical Transmission Electron Microscopy*, Kapitel 4 - Lens Aberrations: Diagnosis and Correction, 55–89. Wiley (2011)

[85] O. Krivanek et al.. ‘Towards sub-Å electron beams.’ *Ultramicroscopy* **78, 1-4**: 1 (1999)

[86] M. A. O’Keefe. ‘Seeing atoms with aberration-corrected sub-Angström electron microscopy.’ *Ultramicroscopy* **108**: 196 (2008)

[87] P. C. Tiemeijer et al.. ‘Using a monochromator to improve the resolution in TEM to below 0.5 Å. Part I : Creating highly coherent monochromated illumination.’ *Ultramicroscopy* **114**: 72 (2012)

[88] O. Scherzer. 'The Theoretical Resolution Limit of the Electron Microscope.' *Journal of Applied Physics* **20, 1**: 20 (1949)

[89] O. Scherzer. 'Sphärische und chromatische Korrektur von Elektronen-Linsen.' *Optik* **2**: 114 (1947)

[90] M. Haider et al.. 'Correction of the spherical aberration of a 200kV TEM by means of a hexapole corrector.' *Optik* **99**: 167 (1995)

[91] M. Haider et al.. 'Electron microscopy image enhanced.' *Nature* **392**: 768 (1998)

[92] O. L. Krivanek et al.. 'Aberration correction in the STEM.' In J. M. Rodenburg (Herausgeber), 'In Proc. EMAG,' 35. Cambridge, UK (1997)

[93] P. Hawkes. 'Aberration correction past and present.' *Phil. Trans. R. Soc. A* **367**: 3637 (2009)

[94] H. Bethe. 'Theorie der Beugung von Elektronen an Kristallen.' *Annalen der Physik* **392, 17**: 55 (1928)

[95] P. Hartel et al.. 'Conditions and reasons for incoherent imaging in STEM.' *Ultramicroscopy* **63, 2**: 93 (1996)

[96] T. Walther et al.. 'Measuring the contrast in annular dark field STEM images as a function of camera length.' *Journal of Physics: Conference Series* **241**: 012068 (2010)

[97] J. Fertig und H. Rose. 'Resolution and contrast of crystalline objects in high-resolution scanning-transmission electron-microscopy.' *Optik* **59**: 407 (1981)

[98] R. F. Loane et al.. 'Visibility of single heavy atoms on thin crystalline silicon in simulated annular dark-field STEM images.' *Acta Crystallographica A* **44**: 912 (1988)

[99] J. M. Cowley und Y. Huang. 'De-channelling contrast in annular dark-field STEM.' *Ultramicroscopy* **40**: 171 (1992)

[100] V. Grillo. 'The effect of surface strain relaxation on HAADF imaging.' *Ultramicroscopy* **109, 12**: 1453 (2009)

[101] P. D. Nellist. *Aberration-Corrected Analytical Transmission Electron Microscopy*, Kapitel Theory and Simulations of STEM Imaging, 89–109. Wiley (2011)

[102] J. Spence et al.. 'On the Holz contribution to stem lattice images formed using high-angle dark-field detectors.' *Ultramicroscopy* **31, 2**: 233 (1989)

[103] S. J. Pennycook. 'Z-contrast STEM for Materials Science.' *Ultramicroscopy* **30**: 58 (1989)

[104] Z. Wang und J. M. Cowley. 'Simulating high-angle annular dark-field inelastic thermal diffuse scattering.' *Ultramicroscopy* **31**: 437 (1989)

[105] P. J. Phillips et al.. 'Atomic-resolution defect contrast in low angle annular dark-field STEM.' *Ultramicroscopy* **116**: 47 (2012)

[106] S. Hillyard und J. Silcox. 'Detector geometry, thermal diffuse scattering and strain effects in ADF STEM imaging.' *Ultramicroscopy* **58**: 6 (1995)

[107] V. Grillo et al.. 'Strain, composition and disorder in ADF imaging of semiconductors.' *Journal of Physics: Conference Series* **326**: 012006 (2011)

[108] S. J. Pennycook und D. Jesson. 'High-resolution Z-contrast imaging of crystals.' *Ultramicroscopy* **37, 1-4**: 14 (1991)

[109] K. Ishizuka. 'A practical approach for STEM image simulation based on the FFT multislice method.' *Ultramicroscopy* **90, 2-3**: 71 (2002)

[110] K. Werner. 'Chemical vapor deposition and physical characterization of gallium and carbon-related structures on Si (001) and GaP/Si (001) templates for the growth of graphene layers.' Dissertation, Philipps-Universität Marburg (2015)

[111] P. F. Fewster. 'Absolute lattice parameter measurement.' *Journal of Materials Science: Materials in Electronics* **10**: 175 (1999)

[112] P. F. Fewster. *X-ray scattering from semiconductors.* Imperial College Press (2003)

[113] R. Schmitt. 'Wachstum und Charakterisierung metamorpher Ga(AsP)-Pufferstrukturen für Tandem-Solarzellen auf Silizium.' Diplomarbeit, Philipps-Universität Marburg (2012)

[114] R. Fritz. 'Quantitative Untersuchungen der Zusammensetzung von kubischen III/V-Verbindungshalbleitern mittels HAADF-STEM.' Dissertation, Philipps-Universität Marburg (2013)

[115] D. J. H. Cockayne et al.. 'Investigations of dislocation strain fields using weak beams.' *Philosophical Magazine* **20**: 1265 (1969)

[116] G. Hug et al.. 'Weak-beam observation of a dissociation transition in TiAl.' *Philosophical Magazine* **57**: 499 (1988)

[117] I. Németh. 'Transmission electron microscopic investigations of hetero epitaxial III/V semiconductor thin layer and quantum well structures.' Doktorarbeit, Philipps-Universität Marburg (2008)

[118] J. Taftøund J. C. H. Spence. 'A simple method for the determination of structure-factor phase relationships and crystal polarity using electron diffraction.' *Journal of Applied Crystallography* **15, 1**: 60 (1982)

[119] E. Spiecker. 'Unified polarity analysis of <110> and <001> Sphalerite-type crystal samples using Bragg-line contrast rules.' *Inst. Phys. Conf. Ser.* **180**: 233 (2003)

[120] K. Marthinsen et al.. 'Non-centrosymmetry Effects and Polarity Determination in III/V Semiconductors.' *Acta Crystallographica Section A Foundations of Crystallography* **53, 3**: 366 (1997)

[121] E. Spiecker. 'Determination of crystal polarity from bend contours in transmission electron microscope images.' *Ultramicroscopy* **92**: 111 (2002)

[122] G. Lichte H. amd Geoger und M. Linck. 'Off-axis electron holography in an aberration-corrected transmission electron microscope.' *Phil. Trans. R. Soc. A* **367**: 3773 (2009)

[123] B. Kabius und H. Rose. *Aberration-Corrected Analytical Transmission Electron Microscopy*, Kapitel Novel Aberration Correction Concepts, 261. Wiley (2009)

[124] L. Jones et al.. 'Smart Align—a new tool for robust non-rigid registration of scanning microscope data.' *Advanced Structural and Chemical Imaging* **1**: 1 (2015)

[125] A. Rosenauer und M. Schowalter. 'STEMSIM - A New Software Tool for Simulation of STEM.' *Microscopy of Semiconducting Materials 2007* **120, 3**: 170 (2008)

[126] Y. Wang et al.. 'Investigation of the anisotropic strain relaxation in GaSb islands on GaP.' *Journal of Applied Physics* **110, 4**: 043509 (2011)

[127] F. H. Stillinger und T. A. Weber. 'Computer simulation of local order in condensed phases of silicon.' *Physical Review B* **31**: 5262 (1985)

[128] C. Roland und G. H. Gilmer. 'Epitaxy on surfaces vicinal to Si(001). I. Diffusion of silicon adatoms over the terraces.' *Physical Review B* **46**: 13428 (1992)

[129] A. S. Nandedkar und J. Narayan. 'Atomic structure of dislocations in silicon, germanium and diamond.' *Philosophical Magazine A* **61**: 873 (1990)

[130] A. Bere und A. Serra. 'Atomic structure of dislocation cores in GaN.' *Physical Review B* **65**: 205323 (2002)

[131] Y. H. Lee et al.. 'Molecular-dynamics simulation of thermal conductivity in amorphous silicon.' *Physical Review B* **43**: 6573 (1991)

[132] R. L. C. Vink et al.. 'Fitting the Stillinger-Weber potential to amorphous silicon.' *Journal of Non-Crystalline Solids* **282**: 248 (2001)

[133] M. Ichimura. 'Stillinger-Weber potentials for III–V compound semiconductors and their application to the critical thickness calculation for InAs/GaAs.' *Physica Status Solidi (a)* **153**: 431 (1996)

[134] J. M. Cowley und a. F. Moodie. 'The scattering of electrons by atoms and crystals. I. A new theoretical approach.' *Acta Crystallographica* **10, 10**: 609 (1957)

[135] E. J. Kirkland et al.. 'Simulation of annular dark field stem images using a modified multislice method.' *Ultramicroscopy* **23**: 77 (1987)

[136] R. F. Loane et al.. 'Thermal vibrations in convergent-beam electron diffraction.' *Acta Crystallographica Section A Foundations of Crystallography* **47, 3**: 267 (1991)

[137] R. F. Loane et al.. 'Incoherent imaging of zone axis crystals with ADF STEM.' *Ultramicroscopy* **40, 2**: 121 (1992)

[138] C. R. Hall und P. B. Hirsch. 'Effect of Thermal Diffuse Scattering on Propagation of High Energy Electrons Through Crystals.' *Proceedings of the Royal Society A: Mathematical, Physical and Engineering Sciences* **286, 1405**: 158 (1965)

[139] V. Haxha und M. Migliorato. 'Calculating strain using atomistic simulations: A review.' *J. Phys. Conf. Ser.* **242**: 012001 (2010)

[140] M. Hÿtch et al.. 'Quantitative measurement of displacement and strain fields from HREM micrographs.' *Ultramicroscopy* **74, 3**: 131 (1998)

[141] M. Hÿtch et al.. 'Measurement of the displacement field of dislocations to 0.03 Åby electron microscopy.' *Nature* **425**: 270 (2003)

[142] P. L. Galindo et al.. 'The Peak Pairs algorithm for strain mapping from HRTEM images.' *Ultramicroscopy* **107, 12**: 1186 (2007)

[143] S. Y. Shiryaev et al.. 'On the nature of cross-hatch patterns on compositionally graded SiGe alloy layers.' *Applied Physics Letters* **64**: 3305 (1994)

[144] M. Albrecht et al.. 'Surface ripples, crosshatch pattern, and dislocation formation: Cooperating mechanisms in lattice mismatch relaxation.' *Applied Physics Letters* **67**: 1232 (1995)

[145] H. Chen et al.. 'Crosshatching on a SiGe film grown on a Si (001) substrate studied by Raman mapping and atomic force microscopy.' *Physical Review B* **65**: 233303 (2002)

[146] E. Fitzgerald et al.. 'Relaxed GeSi structures for III/V integration with Si and high mobility two-dimensional electron gases in Si.' *Journal of Vacuum Science & Technology B* **10**: 1807 (1992)

[147] S. El Kazzi et al.. 'GaSb/GaP compliant interface for high electron mobility AlSb/InAs heterostructures on (001) GaP.' *Applied Physics Letters* **97, 19**: 192111 (2010)

[148] S. El Kazzi et al.. 'Interplay between Sb flux and growth temperature during the formation of GaSb islands on GaP.' *Journal of Applied Physics* **111**: 123506 (2012)

[149] P. Ludewig et al.. 'MOVPE growth mechanisms of dilute bismide III/V alloys.' *Semiconductor Science and Technology* **30**: 094017 (2015)

[150] G. B. Stringfellow et al.. 'Surface processes in OMVPE - the frontiers.' *Journal of Crystal Growth* **221**: 1 (2000)

[151] J. K. Shurtleff et al.. 'Band-gap control of GaInP using Sb as a surfactant.' *Applied Physics Letters* **75**: 1914 (1999)

[152] L. Zhang et al.. 'Effect of Sb as a surfactant during the lateral epitaxial overgrowth of GaN by metalorganic vapor phase epitaxy.' *Applied Physics Letters* **79**: 3059 (2001)

[153] *Á*. Barna et al.. 'TEM sample preparation by ion milling/amorphization.' *Micron* **30**: 267 (1999)

[154] J. P. McCaffrey et al.. 'Surface damage formation during ion-beam thinning of samples for transmission electron microscopy.' *Ultramicroscopy* **87**: 97 (2001)

[155] M. J. Süess et al.. 'Minimization of amorphous layer in Arþ ion milling for UHR-EM.' *Ultramicroscopy* **111**: 1224 (2011)

[156] J. Belz et al.. 'Direct investigation of (sub-) surface preparation artifacts in GaAs based materials by FIB sectioning.' *Ultramicroscopy* **163**: 19 (2016)

[157] Y. Wang et al.. 'The source of the threading dislocation in GaSb/GaAs heterostructures and their propagation mechanism.' *Applied Physics Letters* **102**: 052102 (2013)

[158] H. L. Tsai und R. J. Matyi. 'Generation of misfit dislocations in GaAs grown on Si.' *Applied Physics Letters* **55**: 265 (1989)

[159] A. Trampert et al.. 'Novel plastic strain-relaxation mode in highly mismatched III-V layers induced by two-dimensional epitaxial growth.' *Applied Physics Letters* **66**: 2265 (1995)

[160] E. A. Fitzgerald et al.. 'Structure and recombination in InGaAs/GaAs heterostructures.' *Journal of Applied Physics* **63**: 693 (1988)

[161] E. M. Trukhanov et al.. 'Influence of the misfit-dislocation screw component on the formation of threading dislocations in semiconductor heterostructures.' *Semiconductors* **36**: 290 (2002)

[162] N. Otsuka et al.. 'Study of heteroepitaxial interfaces by atomic resolution electron microscopy.' *Journal of Vacuum Science & Technology B* **4**: 896 (1986)

[163] J. M. Mills und P. Stadelmann. 'A study of the structure of Lomer and 60 degree dislocations in aluminium using high-resolution transmission electron microscopy.' *Philosophical Magazine A* **60**: 355 (1989)

[164] A. Vilà et al.. 'Structure of 60° dislocations at the GaAs/Si interface.' *Journal of Applied Physics* **79**: 676 (1996)

[165] J. Yamasaki et al.. 'Atomic structure analysis of stacking faults and misfit dislocations at 3C-SiC/Si(001) interfaces by aberration-corrected transmission electron microscopy.' *Journal of Physics D: Applied Physics* **45**: 494002 (2012)

[166] E. Peiner et al.. 'The effect of threading dislocations on optical absorption and electron scattering in strongly mismatched heteroepitaxial III/V compound semiconductors on silicon.' *Journal of Physics: Condensed Matter* **14**: 13195 (2002)

[167] V. Narayanan et al.. 'Stacking faults and twins in gallium phosphide layers grown on silicon.' *Philosophical Magazine A* **82**: 685 (2002)

[168] G. Capellini et al.. 'Strain relaxation in high Ge content SiGe layers deposited on Si.' *Journal of Applied Physics* **107**: 063504 (2010)

[169] F. Isa et al.. 'Onset of vertical threading dislocations in SiGe/ Si(001) at a critical Ge concentration.' *APL Materials* **1**: 052109 (2013)

[170] A. Marzegalli et al.. 'Unexpected dominance of vertical dislocations in high- misfit Ge/Si(001) films and their elimination by deep substrate patterning.' *Advanced Materials* **25**: 4408 (2013)

[171] V. a. Shah et al.. 'Reverse graded strain relaxed SiGe buffers for CMOS and optoelectronic integration.' *Thin Solid Films* **520**: 3227 (2012)

[172] S. Ghosh et al.. 'Effect of threading dislocation density and dielectric layer on temperature-dependent electrical characteristics of high-hole-mobility metal semiconductor field effect transistors fabricated from wafer-scale epitaxially grown p-type germanium on silicon substrates.' *Journal of Applied Physics* **115**: 094507 (2014)

[173] H.-C. Luan et al.. 'High-quality Ge epilayers on Si with low threading-dislocation densities.' *Applied Physics Letters* **75**: 2909 (1999)

[174] R. M. France et al.. 'Metamorphic epitaxy for multijunction solar cells.' *MRS Bulletin* **41**: 202 (2016)

[175] M. Levinshtein et al. (Herausgeber). *Handbook Series on Semiconductor Parameters, vol 1.* World Scientific (1996)

[176] J. Li et al.. 'Full-field strain mapping at a Ge/Si heterostructure interface.' *Materials* **6**: 2130 (2013)

[177] A. Stegmüller et al.. 'A quantum chemical study on gas phase decomposition pathways of triethylgallane (TEG, Ga(C2H5)3) and tert-butylphosphine (TBP, PH2(t-C4H9)) under MOVPE conditions.' *Phys.Chem.Chem.Phys* **16**: 17018 (2014)

[178] A. Stegmüller. 'Description of Gallium Phosphide Epitaxy Growth by Computational Chemistry.' Dissertation, Philipps-Universität Marburg (2015)

[179] D. Pasquariello und K. Hjort. 'Plasma-assisted InP-to-Si low temperature wafer bonding.' *IEEE Journal of selected topics in quantum electronics* **8**: 118 (2002)

[180] J. M. Zahler et al.. 'High efficiency InGaAs solar cells on Si by InP layer transfer.' *Applied Physics Letters* **91**: 012108 (2007)

[181] K. Matsumoto et al.. 'Growth of GaInAs/InP MQW using MOVPE on directly-bonded InP/Si substrate.' *Journal of Crystal Growth* **370**: 133 (2013)

[182] A. Seki et al.. 'MOCVD Growth of InP on 4-inch Si Substrate with GaAs Intermediate Layer.' *Japanese Journal of Applied Physics* **67**: L1587 (1987)

[183] M. Sugo et al.. 'Heteroepitaxial growth and characterization of InP on Si substrates.' *Journal of Applied Physics* **68**: 540 (1990)

[184] M. W. Wanlass et al.. 'High-efficiency, thin-film InP concentrator solar cells.' *Journal of Electronic Materials* **20**: 1019 (1991)

[185] T. E. Crumbaker et al.. 'Growth of InP on Si substrates by molecular beam epitaxy.' *Applied Physics Letters* **54**: 140 (1989)

[186] K. Samonji et al.. 'Reduction of threading dislocation density in InP-on-Si heteroepitaxy with strained short-period superlattices.' *Applied Physics Letters* **69**: 100 (1996)

[187] G. P. Tang et al.. 'A new maskless selective-growth process for InP on (100) Si.' *Journal of Applied Physics* **72**: 4366 (1992)

[188] H. Kataria et al.. 'Towards a monolithically integrated III-V laser on silicon: optimization of multi-quantum well growth on InP on Si.' *Semiconductor Science and Technology* **28**: 094008 (7pp) (2013)

[189] N. H. Julian et al.. 'Improvements in epitaxial lateral overgrowth of InP by MOVPE.' *Journal of Crystal Growth* **402**: 234 (2014)

[190] M. K. Lee et al.. 'Heteroepitaxial growth of InP directly on Si by low pressure metalorgani chemical vapor deposition.' *Applied Physics Letters* **50**: 1725 (1987)

[191] A. Yamamoto et al.. 'Optimization of InP/Si heteroepitaxial growth conditions using organometallic vapor phase epitaxy.' *Journal of Crystal Growth* **96**: 369 (1989)

[192] H. Horikawa et al.. 'Hetero-epitaxial growth of InP on Si substrates by LP-MOVPE.' *Journal of Crystal Growth* **93**: 523 (1988)

[193] S. H. Vajargah et al.. 'Strain relief and AlSb buffer layer morphology in GaSb heteroepitaxial films grown on Si as revealed by HAADF scanning transmission electron microscopy.' *Applied Physics Letters* **98**: 1 (2011)

[194] P. Treuherz. 'Elektronenmikroskopische Charakterisierung relaxierter Sb-basierter Kanalschichten auf Si(001).' Diplomarbeit, Philipps-Universität Marburg (2013)

[195] Y. Wang et al.. 'Antimony-mediated control of misfit dislocations and strain at the highly lattice mismatched GaSb/GaAs interface.' *ACS Applied Materials and Interfaces* **5**: 9760 (2013)

[196] K. Kuramochi et al.. 'Effect of chromatic aberration on atomic-resolved spherical aberration corrected STEM images.' *Ultramicroscopy* **110**: 36 (2009)

[197] C. Dwyer et al.. 'Sub-0.1 nm-resolution quantitative scanning transmission electron microscopy without adjustable parameters.' *Applied Physics Letters* **100**: 191915 (2012)

[198] A. Beyer et al.. 'Pyramidal Structure Formation at the Interface between III/V Semiconductors and Silicon.' *Chemistry of Materials* **28**: 3265 (2016)

List of Figures

1.1 The band gap in eV of various semiconductor materials in dependence on the lattice constant . . . 3

2.1 Schematic illustration of an direct and indirect semiconductor. . . . 6
2.2 The 14 Bravais lattices. . . . 8
2.3 Lattice planes in a simple cubic unit cell . . . 9
2.4 Illustration of the hexagonal close packing and the cubic closed packing . 9
2.5 The diamond and zinc blende structure . . . 10
2.6 Graphs of the Gibbs free energy as well as temperature in dependence on the composition x of the material $A_{1-x}B_x$ . . . 12
2.7 Frank van der Merwe, Stranski-Krastanow, and Volmer Weber growth modes 15
2.8 Schematic illustration of heteroepitaxial growth modes . . . 16
2.9 Burgers vector construction . . . 18
2.10 Screw dislocation . . . 19
2.11 60° dislocation . . . 20
2.12 "‘Shuffle"’ and "‘glide"’ slip planes in a diamond lattice . . . 22
2.13 Dissociation of perfect dislocation into Shockley partials . . . 23
2.14 Model of generation of misfit dislocations . . . 24
2.15 Model of antiphase domains . . . 26
2.16 Position vectors and wavevectors for electron scattering . . . 30
2.17 Scattering in the unit cell . . . 33
2.18 Bragg scattering . . . 34
2.19 Illustration of the Ewald construction . . . 35
2.20 Trajectory of an electron through a magnetic lens . . . 39
2.21 The spherical wavefront in relation to the aberrated wavefront . . . 40
2.22 Multipole lenses . . . 43

3.1 MOVPE reactor system . . . 50
3.2 Setup of a of x-ray diffractometer . . . 52
3.3 Goniometer axes and relevant angles in XRD . . . 53
3.4 Scattering geometry in reciprocal space in XRD . . . 54
3.5 XRD rocking curve . . . 54
3.6 Geometric relationship between wavevectors, angles and reciprocal lattice vector in XRD . . . 55

3.7 Relationship between XRD DP and the epitaxial layer growth 56
3.8 Conventional sample preparation 58
3.9 Schematic setup of the *JEOL JEM 3010* TEM and *JEOL 2200 FS* (S)TEM 59
3.10 Beam path in BF and DF mode 61
3.11 Tilting for BF, DF and WB imaging 62
3.12 Beam path in convergent beam electron diffraction 63
3.13 Polarity determination in CBED in <110> projections 64
3.14 PCTF of TEM 65
3.15 Schematic beam path in scanning electron transmission microscope 66
3.16 Nearest neighbor positions in <100> and <110> projections 71

4.1 AFM and TEM investigations of a Ga(PSb) buffer layer on InP substrate 76
4.2 AFM micrographs of Ga(PSb) on GaP/Si 78
4.3 Comparison by AFM of Ga(PSb) layers with and without TESb pre-run . 79
4.4 HAADF STEM images of Ga(PSb) on GaP/Si after the island-like nucleation 80
4.5 HAADF images of a coalesced Ga(PSb) buffer layer on GaP/Si 82
4.6 Overview ADF images of Ga(PSb) of 100 nm nominal thickness on GaP/Si 84
4.7 Plan-view ADF image of Ga(PSb) of 100 nm nominal thickness on GaP/Si. 85
4.8 XRD-RSM of the $\bar{2}\bar{2}4$ reflection of a Ga(PSb) layer on GaP/Si 86
4.9 Work flow to demonstrate evaluation of dislocations in high-resolution (S)TEM images 89
4.10 Strain evaluation of HRTEM images of thin Ga(PSb) buffer layer on GaP/Si 94
4.11 Composition of $Ga(P_{(1-x)}Sb_x)$ on GaP/Si in dependence on different partial pressure ratios 97
4.12 XRD and AFM investigations of low Sb-content Ga(PSb) layers on GaP/Si 98
4.13 HAADF STEM images of pseudomorphically grown $Ga(P_{93}Sb_7)$ on GaP/Si 102
4.14 HAADF investigation of Ga(PSb) metamorphic buffer layer on low Sb-content pseudomorphic Ga(PSb) interlayer on GaP/Si 104
4.15 Illustration of continuous epitaxy and FME growth modi 105
4.16 XRD and AFM investigation of Ga(PSb) layers grown by FME using one precursor at a time 106
4.17 XRD and AFM investigations of Ga(PSb) layers grown by FME using alternating group III and group V precursors 108
4.18 XRD and AFM of Ga(PSb) layers grown by FME using alternating group III and group V precursors showing the improved results 110
4.19 ADF STEM images of a Ga(PSb) layer on GaP/Si grown by FME 111
4.20 AFM and STEM investigation of a thin InP layer grown on GaP/Si . . . 113
4.21 STEM investigation of a Ga(PSb) nucleation layer on a thick InP layer grown on GaP/Si 114
4.22 AFM images of InP layers grown on GaP/Si by FME 115

4.23 STEM investigation of FME grown InP layers on GaP/Si 116
4.24 HAADF STEM images of the GaSb/GaP interface 120
4.25 Averaged intensity map of

110

GaSb/GaP HAADF image 122
4.26 Four different models of the GaSb/GaP interface 123
4.27 Simulated HAADF image of the GaSb/GaP interface 125
4.28 Theoretical strain maps of the GaSb/GaP interface 126
4.29 GPA strain maps of the GaSb/GaP interface of the simulated HAADF images 127
4.30 Details of the simulated HAADF images of the Sb-terminated, Ga-terminated and P-terminated dislocation cores in combination with the corresponding, adjacent $e_{\perp}$ GPA strain maps between the dislocations 128
4.31 PP strain maps of the GaSb/GaP interface of the simulated HAADF images 129
4.32 PP strain maps of the GaSb/GaP interface of the experimental HAADF images 131
4.33 Intensity ratio map for the simulated HAADF images of the GaSb/GaP interface 132
4.34 Intensity ratio map for the experimental HAADF images of the GaSb/GaP interface 133
4.35 HAADF STEM images of the Ga(PSb)/GaP interface 135
4.36 PP strain maps of the Ga(PSb)/GaP interface of the experimental HAADF images 136
4.37 HAADF STEM image of the Ga(PSb)/GaP interface in

110

projection 137
4.38 Intensity ratio map for the experimental HAADF images of the Ga(PSb)/GaP interface 138
4.39 HAADF STEM images of the Ga(AsSb)/GaP interface 139
4.40 PP strain maps of the Ga(AsSb)/GaP interface of the experimental HAADF images 140
4.41 Intensity ratio map for the experimental HAADF images of the Ga(AsSb)/GaP interface 142

List of Tables

4.1 Sb-concentration (group V) and lattice constant of Ga(PSb) and Ga(AsSb) buffer layers grown on GaP/Si 86
4.2 Misfit, strain and residual strain components of of Ga(PSb) and Ga(AsSb) buffer layers 87
4.3 Average dislocation spacing, misfit, and strain of Ga(PSb) and Ga(AsSb) layers grown on GaP/Si of different thicknesses 91
4.4 GPA strain mapping on the thin Ga(PSb) and the thick Ga(AsSb) layers grown on GaP/Si. 96

List of presented samples

Following samples were displayed in the individual figures in chapter 4:

Figure 4.1: # 25530

Figure 4.2: # 25835; # 25641; # 25639

Figure 4.3: # 25835; # 25641; # 25841; # 25843

Figure 4.4: # 25840

Figure 4.5: # 25843

Figure 4.6: # 25639

Figure 4.7: # 25639

Figure 4.8: # 25639

Figure 4.9: # 25639

Figure 4.10: # 25641

Figure 4.11: black: # 25639; # 18336; # 18338; # 18342; # 18354; # 25953; # 25962; # 25964; # 25969; red: # 18337; # 18339; # 18340; # 18343; # 18354; blue: # 18345; # 18347; # 18351; magenta: # 25957; # 25968; green: # 18346; # 25877

Figure 4.12: # 18345; # 18341

Figure 4.13: # 25968

Figure 4.14: # 18357

Figure 4.16: # 26321; # 26323; # 26324; # 26325

Figure 4.17: # 26321; # 26339; # 26347; # 26345; # 26343

Figure 4.18: # 26321; # 26339; # 26341

Figure 4.19: # 26341

Figure 4.20: # 25963

Figure 4.21: # 25966

Figure 4.22: # 25971; # 26005; # 26007; # 26020

Figure 4.23: # 26007; # 26020

Figure 4.24: # 25877

Figure 4.25: # 25877

Figure 4.32: # 25877

Figure 4.34: # 25877

Figure 4.35: # 25835

Figure 4.36: # 25835

Figure 4.37: # 25835

Figure 4.38: # 25835

Figure 4.39: # 26111

Figure 4.40: # 26111

Figure 4.41: # 26111

Danksagung

Als erstes möchte ich mich natürlich bei Prof. Kerstin Volz dafür bedanken mich als Doktorantin angenommen zu haben. Ich habe in den dreieinhalb Jahren viel gelernt und bin dankbar dabei so viele verschiedene Geräte zur Herstellung und Charakterisierung von Halbleitermaterialien kennen gelernt zu haben. Vielen Dank für die gute Betreuung, die Diskussionen sowie der Möglichkeit Konferenzen sowohl zum Thema der Elektronenmikroskopie als auch zur Epitaxie besucht haben zu dürfen.

Vielen Dank an Herrn Professor Heimbrodt für die freundliche Übernahme des Zweitgutachtens.

Bei Herrn Dr. Stolz möchte mich für das rege Interesse an meiner Arbeit und den diesbezüglichen hilfreichen Diskussionen bedanken.

Vielen Dank an Andreas Beyer für die Betreuung, Diskussionen und Hilfe bei kleinen und großen Problemen während meiner Arbeit, sowie der Korrektur der ersten Rohfassung von dieser Dissertation. An dieser Stelle möchte ich mich auch bei allen anderen fleißigen Korrekturlesern bedanken: Katharina Gries, Kevin zu Münser, Svenja Marx, Melanie Wagner, Jürgen Belz, Christian Fuchs, Antje Weber, Peter Ludewig, Eddi Sterzer, Lennart Duschek and Jürgen Volpp.

Bei Bernadette Kunert, Antje Weber und Peter Ludewig möchte ich mich für die vielen interessanten TEM Proben bedanken. Besonderer Dank geht hierbei an Antje Weber sowie Ulrieke Häuplik für die Einführung in die MOVPE, sowohl praktisch als auch das Programmieren neuer Rezepte. Danke Anjte für die anschließende Erklärung des XRD, nicht nur der „einfachen“ Rocking Curves und ihrer Simulation, sondern auch die wesentlich zeitaufwändigeren reciprocal space maps. Danke auch an Ulrike und Katharina Werner, dass ihr mir die Bedienung des AFM gezeigt habt sowie die einstimmigen Beschlüsse im Kuchenkommitee und die damit verbundenen vielen leckeren Kuchen.

Danke an meine Lehrer am TEM, besonders Jürgen Münzer am alten TEM und dem Einbläuen einer rigorosen, sinnvollen Benennung der Bilder sowie Addi Beyer am neuen TEM. Mein Dank gilt auch an Katharina Gries für die Einführung in das SEM und die FIB, sowie an Rainer Straubinger und Celina Bäcker für das geduldige Beibringen der

Probenpräparation.

Of course, I would like to thank the rest of the TEM Mafia for interesting discussion in and after the TEM seminar and help at the TEM or during sample preparation whenever needed, weather it was a technical problem or a user problem (a.k.a. me).

Many thanks to Kakhaber Jandieri for providing all the supercells needed for HAADF simulations (changing again and again their size or interface according to the latest results) as well as the user friendly program to evaluate the theoretical strain of interfaces with and without Lomer dislocations. I also would like to thank all the programmers on the STEMulator program to evaluate the STEM images, Addi Beyer, Lennart Duschek, Jürgen Münzner and Olli Oelerich. I hope you won't remember me as the girl who reported a new bug or was begging for a new feature (that nobody else needed), but the girl who gave you chocolate, instead.

Vielen Dank auch an das Sekretariat, Isabelle Kimmel, Marina Koch und ganz besonders bei Elke Vaupel bei der Hilfe von organisatorischen Dingen sowie an alle Technikern, Celina Bäcker, Michael Hellwig, Ulrike Häuplik, Stefan Rainer und Thomas Ochs bei technischen Problemen. Besonders möchte ich mich bei Celina Bäcker bedanken für das weiter-pipsen von so einigen Proben, dem Hervorzaubern von vermeintlich leeren Materialien und dem Einkühlen vom TEM, sodass ich morgens gleich loslegen konnte.

Many thanks to the whole group for the interesting and useful discussions about work and not so work related topics, fun in and after work, food (or money) when I forgot my lunch as well as the help when I moved out of my flat. I had a great time, most of the time, at least. (The actual writing of this thesis might have been a bit stressful, but I learned a lot.). Thanks to all of you (I don't want put down all the names, because the group is so big and I don't want to forget anybody).

Thanks to the "team Nord" for nice conversations during the countless bus rides to and from work. Dem "Team Süd" vielen Dank für das Fahren und vor allen Dingen dem Warten oder Abholen, wenn ich mal wieder zu spät dran war.

Even though it was by chance that we shared an office, I am so happy that we did. Thank you Katha and Rocio for the great time as well as the support or help when needed. I enjoyed the discussions and conversations, shared lunch times and nice walks in the woods a lot.

Zum Schluss möchte ich meinen Freunden und meiner Familie danken. Danke, dass ihr mich immer unterstützt habt, mich auffangt, antreibt, zum Lachen bringt, tolle Ideen habt und einfach großartig seid.